Tampere University

AAPO TERVONEN

Computational Modeling of Epithelial Barrier Properties and Biomechanics

Tampere University Dissertations 534

Tampere University Dissertations 534

AAPO TERVONEN

Computational Modeling of Epithelial Barrier Properties and Biomechanics

ACADEMIC DISSERTATION
To be presented, with the permission of
the Faculty of Medicine and Health Technology
of Tampere University,
for public discussion in the Jarmo Visakorpi auditorium
of the Arvo building, Arvo Ylpön katu 34, Tampere,
on 14 January 2022, at 12 o’clock.

ACADEMIC DISSERTATION
Tampere University, Faculty of Medicine and Health Technology
Finland

Responsible supervisor and Custos	Professor Jari Hyttinen Tampere University Finland	
Supervisors	Adjunct Professor Teemu Ihalainen Tampere University Finland	Adjunct Professor Soile Nymark Tampere University Finland
Pre-examiners	Lecturer Alexander Fletcher The University of Sheffield United Kingdom	Professor Dorothee Günzel Charité - Universitätsmedizin Berlin Germany
Opponent	Senior Lecturer Dawn Walker The University of Sheffield United Kingdom	

The originality of this thesis has been checked using the Turnitin OriginalityCheck service.

Cover design: Roihu Inc.

ISBN 978-952-03-2241-0 (print)
ISBN 978-952-03-2242-7 (pdf)
ISSN 2489-9860 (print)
ISSN 2490-0028 (pdf)
http://urn.fi/URN:ISBN:978-952-03-2242-7

PunaMusta Oy – Yliopistopaino
Joensuu 2022

Mummille

“Life kicks us in the teeth
Yet something makes us crawl back for more”
– *Sami Lopakka*

ACKNOWLEDGEMENTS

The work presented in this thesis was conducted during the years 2013-2021 in Computational Biophysics and Imaging Group (CBIG) at BioMediTech, Faculty of Medicine and Health Technology, Tampere University, as well as at the former Department of Biomedical Sciences and Engineering and Department of Electronics and Communications Engineering, Tampere University of Technology, Tampere, Finland.

First and foremost, I would like to thank my supervisor, Professor Jari Hyttinen, for his support, academic and scientific guidance, and the freedom that he has given me to follow my own interests. I owe Jari for sparking my interest in epithelia and computational modeling. I am also very grateful to my co-supervisors, Adjunct Professors Soile Nymark and Teemu Ihalainen, for partly adopting me to their groups and always being there if I needed help or support. Soile's seemingly unwavering positivity has been essential to bringing this thesis to an end. I am especially thankful to Teemu for introducing me to the mechanical side of cell biology. This supervisory team has helped me through the ups and downs of academia and life during these years. In addition, I am thankful to Docent Thomas Kühn for the valuable input as a member of my follow-up group as well as the pre-examiners Professor Dorothee Günzel and Lecturer Alexander Fletcher for the helpful comments and feedback.

I would like to thank the past and present colleagues at Tampere University, Tampere University of Technology, and the University of Tampere. I have had the privilege of working at the (tricellular) junction of three excellent and inspiring research groups – Jari's CBIG, Soile's Biophysics of the Eye, and Teemu's Cellular Biophysics. In particular, I would like to thank Kerstin Lenk, Julia Fadjukov, and Inkeri Välkki for not only being incredible and reliable colleagues but also good friends. In addition, I would like to acknowledge Iina Korkka, Lukas Tietz, Toni Montonen, Viivi Karema-Jokinen, and Antti Ahola for the fruitful discussion over the years about science and beyond. In addition, I would like to express my gratitude to Sanna Korpela for the experimental work on the last manuscript and Danial Garcia León for the collaboration with the initial tight junction model.

Furthermore, I would also like to thank Jari and Professor Minna Kellomäki for the opportunity to visit Tohoku University, Sendai, Japan, in early 2014, as well as Professor Tetsu Tanaka and his students for hosting me for two months. I am particularly grateful to Hiroko Sato, who was always ready to help me with anything at the moment notice during my stay in Sendai.

The thesis work was funded by Tampere University of Technology's Rector's Graduate School, The Ella and Georg Ehrnrooth Foundation, various projects of the Academy of Finland, and the Faculty of Medicine and Health Technology. I am highly grateful for all the funding sources that made this thesis possible.

Finally, I would like to express my deepest appreciation to my family and friends for their support over all these years. My parents, Leena and Antero, have always supported me in whatever I wanted to do in life. My sister Elina and brother Ate for reminding me that life is not only for work. I am extremely grateful to my friends, especially Tanja, Maria, Lauri, Hilla, and Sanna, for their support and for helping me enjoy life outside academia. Last but certainly not least, I would like to thank the little furballs Nurmu and Piimä for keeping me company (and distracted), especially in these previous, long 20 months.

Every time I have been banging my head against some problem over the years, I remember what Iina said to me when I was still doing my Master's thesis: "If this was easy, everybody would be doing it."

Aapo Tervonen
Tampere, December 2, 2021

ABSTRACT

Epithelial tissues consist of tightly connected cells that line all our organs and form barriers between the inside and outside of the body. Many of the epithelial functions are dependent on the junctions between the cells: e.g., the tight junctions that form the primary barrier and the adherens junctions that transmit forces between the cells. Due to their role as barriers, epithelia are subjected to many harmful stimuli and are thus prone to many diseases. These diseases usually lead to the failure of the barrier as well as changes in epithelial tissue biomechanics. Therefore, to better understand epithelial homeostasis and disease processes, more knowledge is required on the structure and regulation of the barrier and the factors affecting the transmission of forces between the cells.

The typical measurements of epithelial barrier reflect the epithelium-wide properties and thus lack the resolution to address the barrier at the cellular or subcellular level. More advanced methods have been developed, but they also have challenges mainly due to the small size scale of the barrier-forming structures. Likewise, while many methods exist to study epithelial biomechanics, they can only provide a partial view of the whole system by themselves. The field of computational modeling can provide tools to guide and support these experimental methods. While there are only a few detailed models of the epithelial barriers, there is an abundance of models describing the mechanics of these tissues. However, these models usually lack the description of the mechanical microenvironment of the cells.

This thesis aims to improve our understanding of the biophysical aspects of epithelial physiology by using computational modeling to develop tools to study the barrier-forming components in epithelial tissue barriers, the structural dynamics of the barrier-forming tight junctions, the measurement sensitivity of the transepithelial electrical measurements, and the effect of microenvironment stiffness on the force transmission between epithelial cells.

The thesis work resulted in three models and one study conducted using a finite element method software. The models use a variety of different modeling methods. The model describing the components of a tissue barrier, more specifically the blood-retinal barrier in the eye, was a steady-state model based on the serial and parallel connection between the barrier components. Stochastic multicompartmental and resistor network models were used to describe the structural dynamics of the tight junctions. The model of the transepithelial electrical measurements was built and solved using the finite element method. Finally, a cell-based model was developed to study epithelial biomechanics.

The epithelial tissue barrier model indicated that the paracellular pathway between the epithelial cells, specifically the tight junctions, formed the governing permeation route for diffusion through the whole tissue. The results from the more detailed tight junction model suggested that the so-called leak pathway utilized by larger molecules would be formed by both the large pores in the tricellular junctions and the step-by-step diffusion through the structural dynamics of the bicellular strand network. Furthermore, we found that the dynamic strand network described in this model affected the measured molecular permeability and transepithelial resistance values differently, enabling separate regulation of these two properties. The finite element model of the electrode placement showed that the electrode positioning and measurement frequency heavily affected the measured area of the epithelium, but not the obtained values themselves. The final model on the epithelial mechanics indicated that the propagation of forces between cells is highly dependent on the substrate stiffness and that cells in confluent epithelium can transmit information on the microenvironment stiffness and its heterogeneities depending on their ability to resist deformations.

The models developed in this thesis help to guide the experimental work by creating platforms to produce testable hypotheses, optimize measurements, and analyze and quantify experimental results. Together with experimental work, computational models of epithelia provide a more complete view of the properties and relationship of the epithelial barrier and biomechanics to help us understand these essential tissues in health and in disease.

TIIVISTELMÄ

Epiteelit ovat solukerroksia, jotka erottavat kudokset ympäristöstään ja säätelevät molekyylien ja ionien liikkumista kudosten välillä. Näiden kudosten toiminnan kannalta tärkeässä osassa ovat solujen väliset liitokset, erityisesti esteen muodostavat tiiviit liitokset sekä voimia solusta toiseen välittävät vyöliitokset. Koska epiteeleihin kohdistuu useita ulkoisia ärsykkeitä – kuten bakteerit suolessa ja ilman epäpuhtaudet keuhkoissa – ne ovat alttiita lukuisille sairauksille. Monet näistä sairauksista johtavat epiteeliesteen hajoamiseen sekä muutoksiin solujen biomekaniikassa. Aktiivisesta tutkimuksesta huolimatta, epiteelien muodostavan esteen rakennetta ja niiden biomekaanisia ominaisuuksia tai niissä tapahtuvien muutosten vaikutuksia ei vielä tunneta tarpeeksi hyvin tehokkaiden hoitojen kehittämiseksi.

Esteominaisuuksien ja epiteelin biomekaniikan tutkimiseen on monia kokeellisia menetelmiä, joilla on omat rajoitteensa. Epiteeliesteen, ja erityisesti solujen välisiä tiiviitä liitoksia, tutkivat menetelmät usein mittaavat epiteelinlaajuisia ominaisuuksia eivätkä aina kykene havaitsemaan paikallisia tai nopeita muutoksia. Epiteelin toimintaa ohjaavien voimien tutkimiseen puolestaan on useita kokeellisia menetelmiä, mutta ne eivät usein pysty luomaan täydellistä kokonaiskuvaa ilmiöstä. Laskennallinen mallinnus tarjoaa työkaluja tukemaan kokeellista tutkimusta yhdistämällä solubiologiaa, matematiikkaa, ja biofysiikan teoriaa laskennallisiin työkaluihin. Epiteelikudosten mallintaminen on aktiivisinta biomekaniikan osalta, mutta se on keskittynyt pääasiassa kudosten kehittymisen mallintamiseen, eikä solujen mekaanista ympäristöä usein huomioida. Epiteelin esteominaisuuksien mallintaminen on puolestaan harvinaista.

Väitöskirjani tavoite on matemaattisten mallien kautta parantaa ymmärrystämme epiteelin muodostamasta esteestä ja miten epiteelisolujen mekaaninen ympäristö vaikuttaa niiden toimintaan. Erityisesti tarkoituksena on tunnistaa esteiden pääkomponentit epiteelin muodostamissa kudoksissa, ymmärtää tiiviiden liitosten rakenteellista dynamiikkaa, tutkia epiteelien sähköfysiologisiin mittauksiin tarkoitettujen mittausjärjestelmien mittausherkkyyttä, ja selvittää epiteelin mekaanisen ympäristön vaikutusta solujen välisiin voimiin.

Väitöstutkimuksessani kehitin kolme uutta laskennallista mallia ja hyödynsin olemassa olevaa mallinnusalustaa yhteen tutkimukseen. Nämä mallit perustuvat moneen erilaiseen mallinnusmenetelmään. Epiteeliesteen, tarkemmin silmän takaosassa sijaitsevan veri-verkkokalvoesteen, pääkomponenttien tunnistamiseen hyödynnettiin niin sanottua steady-state mallia. Tiiviiden liitosten dynamiikkaa kuvattiin stokastisia kompartmentti- ja virtapiirimalleja hyödyntämällä. Epiteelin sähköfysiologista mittausjärjestelmää tutkittiin käyttäen elementtimenetelmää. Ympäristön mekaniikan vaikutusten selvittämistä varten kehitettiin solupohjainen malli.

Tulokset osoittivat, että epiteelin muodostamissa kudosesteissä läpäisevyyden määrittää pääasiassa solujen välissä sijaitsevat tiiviit liitokset. Tarkempaa tiivisliitosmallia hyödyntämällä ennustimme, että suurempien molekyylin epiteelin läpäisemisen mahdollistava vuotoreitti koostuu kahdesta komponentista eri osissa tiiviitä liitoksia. Lisäksi tarkastelimme tiiviiden liitosten rakenteellisen dynamiikan vaikutusta epiteelistä mitattuihin läpäisevyys- ja sähköresistanssiarvoihin ja havaitsimme, että dynaaminen rakenne vaikuttaa näihin mittasuureisiin eri tavalla. Mallimme sähköfysiologisesta mittausjärjestelmästä osoitti, että mittauselektrodien asettelu vaikuttaa epiteelistä mitattavaan kohtaan, mutta ei mittaustuloksiin. Viimeisen tutkimuksen tuloksien mukaan solujen ympäristön jäykkyydellä on merkittävä rooli voimien välittymisessä solujen välillä. Lisäksi solut kykenevät näiden voimien avulla viestimään tietoa muutoksista ympäristön jäykkyydessä pitkien etäisyyksien päähän.

Tässä väitöskirjassa kehittämäni mallit muodostavat laskennallisia alustoja, jotka kykenevät luomaan uutta tietoa epiteelien toiminnasta ja tukemaan kokeellista tutkimusta esimerkiksi luomalla uusia hypoteeseja ja mahdollistamalla tulosten kvantitatiivisen analysoinnin. Laskennallinen mallinnus yhdessä kokeellisten menetelmien kanssa muodostavat toisiaan tukevan tutkimustyökalun, joka parantaa ymmärrystämme epiteelien toiminnasta esteenä sekä niiden biomekaniikasta ja täten auttaa meitä ymmärtämään monia epiteelipohjaisia sairauksia.

CONTENTS

ABBREVIATIONS

AMD	Age-related macular degeneration
BRB	Blood-retinal barrier
ECM	Extracellular matrix
EMT	Epithelial-to-mesenchymal transition
FDM	Finite difference method
FEM	Finite element method
GTP	Guanosine triphosphate
GUI	Graphical user interface
IBD	Inflammatory bowel disease
JAM-A	Junctional adhesion molecule A
MDCK	Madin-Darby canine kidney epithelium
MLCK	Myosin light-chain kinase
ODE	Ordinary differential equation
PDE	Partial differential equation
PEG	Polyethylene glycol
RPE	Retinal pigment epithelium
TER	Transepithelial electrical resistance
TEZ	Transepithelial electrical impedance
TNF-α	Tumor necrosis factor alpha
ZO	Zonula occludens

ORIGINAL PUBLICATIONS

Publication I	Tervonen, A., Vainio, I., Nymark, S. & Hyttinen, J. 2014. Prediction of passive drug permeability across the blood-retinal barrier. Pharmaceutical Research, 31:2297–2311.
Publication II	Tervonen, A., Ihalainen, T.O., Nymark, S. & Hyttinen, J. 2019. Structural dynamics of tight junctions modulate the properties of the epithelial barrier. PLOS ONE, 14:e0214876.
Publication III	Tervonen A. & Hyttinen J. 2018. Sensitivity Distribution of Electrical Impedance Epithelial Measurement Systems. EMBEC & NBC 2017, Tampere, Finland, June 2017. IFMBE Proceedings, Springer, Singapore, 65:623–626.
Publication IV	Tervonen, A., Korpela, S., Nymark, S., Hyttinen, J. & Ihalainen, T.O. The effect of substrate stiffness on tensile force transduction in the epithelial monolayers. Manuscript. DOI: 10.1101/2021.09.06.459078

AUTHOR CONTRIBUTIONS

Publication I	Tervonen and Hyttinen conceived the original idea. Tervonen developed the model with the help of Vainio. Tervonen performed the simulations, analyzed the results, and drafted the manuscript with support from Vainio, Nymark, and Hyttinen. All authors discussed the results and contributed to the final manuscript.
Publication II	Tervonen, Ihalainen, Nymark, and Hyttinen conceptualized the model idea. Tervonen developed the model, performed the simulations, analyzed the results, and drafted the manuscript with the support of Ihalainen, Nymark, and Hyttinen. All authors discussed the results and contributed to the final manuscript.
Publication III	Tervonen and Hyttinen conceived the original idea. Tervonen developed the model, performed the simulations, analyzed the results, and drafted the manuscript. Both authors discussed the results and contributed to the final manuscript.
Publication IV	Tervonen and Ihalainen conceived the original idea. Tervonen developed the model, performed the simulations, and analyzed the results with the support of Nymark, Hyttinen, and Ihalainen. Korpela and Ihalainen created the hydrogels for the experiments, maintained the cells. Ihalainen performed the experiments. Tervonen drafted the manuscript, and all authors discussed the results and contributed to the final manuscript.

1 INTRODUCTION

Epithelia protect our bodies and organs from the external environment[1]. These tissues are made of thin cell layers that cover the external surface of our bodies and all our organs, forming active and adaptive cellular barriers that function as the gatekeepers of our bodies. Epithelia allow the passage of essential nutrients into our bodies by carefully regulating the transepithelial transport, for example, in the small intestine and in the lungs. On the other hand, they hinder the passage of harmful microorganisms, substances, and high-energy photons into our bodies. For example, the small intestine and the lung epithelium keep bacteria, viruses, toxins, and air pollutants outside while the skin and the retinal pigment epithelium (RPE) – an epithelium in the eye – absorb the high-energy ultraviolet light. However, being subjected to these adverse conditions make epithelial tissues prone to many diseases. Many of these pathogens manifest as dysfunction of the epithelia, usually leading to a breach of the barrier with an unregulated passage of substances and microorganisms through it. Moreover, due to the harmful environment, mutations in epithelial cells are common and may lead to cancers of epithelial origin.

First of all, since the epithelial tissues protect our bodies and organs, understanding their structure and function is essential to prevent and treat epithelial diseases. For example, inflammatory bowel disease (IBD) is a group of disorders that lead to a leaky intestinal epithelium[2], and age-related macular degeneration (AMD) is an ocular disease affecting the elderly in which dysfunction in the RPE results in visual impairment[3,4]. These diseases have become common in Western countries. The prevalence of IBD has rapidly increased in the industrialized countries during the last decades, with 2.5–3 million cases in Europe[5] and over 50,000 cases, or around 0.9 % of the population, in Finland[6]. On the other hand, AMD affects the lives of over 27 % of people aged over 85 in Europe[4]. In addition to the diseases that affect mainly the epithelium itself, cancers of epithelial origin, or carcinomas, accounted for the majority of new cancer cases worldwide in 2018 and included all the ten most common cancers[7,8].

Epithelia are common targets of research themselves, in addition to increasing our understanding related to epithelial diseases. Collective shape changes of epithelial cells have an essential role in embryonic development and the formation of organs[9–12]. Therefore, studying the collective behavior of epithelial cells provides us with a basic understanding of the development of our bodies. Moreover, epithelia have an important role when designing novel treatments for diseases affecting other tissues. Drugs have to be absorbed into the body, for example, through the epithelium in the intestine or through the skin. Therefore, the maximization of drug effectiveness requires good epithelial permeability, which further requires a good understanding of the components of the barrier and the pathways that these molecules take through it.

Many epithelial functions depend on the connections between the cells and their environment. Different cell-cell junctions form at the interface between neighboring cells, most notably the barrier-forming tight junctions and force transmitting adherens junctions. The tight junctions close the space between the cells and form a highly regulated barrier structure that is dynamic in its nature[13–15]. Understanding the structure and properties of this barrier is not only essential to facilitate drug design but also to help us treat diseases such as IBD and AMD. While our understanding of the structure of this barrier is constantly improving, the common imaging methods used to study it in most cases only provide a static view. On the other hand, a common method to study the functionality of this barrier is measuring the passage of solutes with different sizes and charges[16,17]. This has helped us to understand how the tight junctions regulate the passage of these molecules and ions and how this regulation is affected by various external stimuli. However, it is not fully understood how the suggested structure of the junctions produces the measured molecular and electrical barrier properties.

Multiple aspects of epithelial biology are connected to the mechanics inside the cells and their environment, including the formation and regulation of the epithelial barrier[18–21]. Cells sense forces and mechanical properties using so-called mechanosensitive proteins, located mainly in the adherens junctions and the connections between the cells and the extracellular matrix (ECM)[22]. These proteins change their function while under tension and thus enable the cells to respond to changes in their mechanical microenvironment, or in other words, signal by forces. Due to the high interconnectivity between the epithelial cells, forces can be transmitted between neighboring cells enabling long-distance mechanical signaling within the epithelial tissue[23]. Many diseases affecting epithelia, including IBD and tumors, are accompanied by changes in the mechanical properties of the cells and by an increase in ECM stiffness[24–26]. While the research on mechanical signaling is active, the effect of the ECM stiffness on the signaling between cells in the monolayer is not well known.

There are multiple excellent experimental methods to study both the epithelial barrier properties and biomechanics[16,27–29]. However, there are gaps in what these methods can show us about these properties. For example, measuring the global permeability of a drug molecule or the electrical resistance of the epithelium provide information related to the epithelial barrier but cannot describe the spatial differences in the barrier, pathways of the permeation, or the detailed structure of the barrier. On the other hand, while it is reasonably simple to image the movement of cells following some mechanical stimulus, it is more difficult to quantify the movement as the different forces felt by the cells.

Computational modeling provides a tool to fill these methodological gaps. These models can integrate the current biophysical knowledge into testable platforms that can be used to predict epithelial behavior and better quantify experimental results and optimize the design of experimental measurement systems. While epithelia have been a target of extensive modeling efforts due to their importance as a tissue, models investigating certain epithelial functions are lacking. Most computational models of the epithelial barrier are limited in studying only particular aspects of the barrier and often lack the resolution to characterize the barrier components in detail[30–35]. On the other hand, while there is a multitude of models that describe the interactions within the epithelia at the cell level[36–41], most have concentrated on epithelial morphogenesis and cell migration and usually lack a deformable ECM.

In my thesis, I aimed to improve our understanding of the epithelial barrier and mechanics. This was done by developing novel computational models to describe the main barrier components in epithelial tissues, optimize electrical barrier measurement setup, and study the role of the biomechanical environment in mechanical signaling between cells by developing computational models. My models will provide platforms for further experimental and computational studies related to these topics. The thesis includes a review of the relevant literature, a statement of the specific aims, a summary of the methods used in the studies and the results, a discussion of the results in the context of the literature, conclusions, and, finally, the four original publications.

2 LITERATURE REVIEW

In this chapter, I will describe the structure and function of epithelial tissues as well as their barrier function and biomechanics in more detail. Furthermore, I will give examples of how these properties relate to common epithelial diseases and can be measured experimentally. Finally, I will outline the basics of computational modeling in biological research and the existing models of epithelia related to their barrier function and biomechanics.

2.1 Introduction to epithelial structure and function

Epithelia are one of the four types of primary animal tissue, along with muscle, nervous, and connective tissues. They cover and line the tissues in our bodies and are formed by multicellular sheets of tightly packed cells. Epithelia can be categorized based on their primary function as 1) Covering epithelia, which form barriers between body compartments, and 2) glandular epithelia, which form the glands in our bodies[1]. The skin, the intestinal epithelium, and the lung epithelium are examples of covering epithelia, whereas the secreting components in glands such as thyroid, sweat glands, and liver are glandular epithelia[1]. Endothelia, cell layers that cover blood and lymphatic vessels, are closely related to epithelial tissues and sometimes considered a special type of epithelium. In this thesis, I will focus on covering epithelia, and therefore the term epithelium is used to refer to them from here onwards.

By forming the barrier and separating compartments, covering epithelia regulate the transfer of energy and substances across themselves. They prevent the passage of harmful things, such as light, air pollutants, and microbes, while allowing the transport of nutrients and waste products. Correct regulation of the transepithelial transport is essential for the proper functioning of many tissues. For example, in different sections of the renal tubules in the kidneys, certain solutes are either filtrated from, reabsorbed to, or secreted from the tubular fluid in a specific order. This happens by modifying the protein expression in the different parts of the tubules. Some specialized epithelia can also have functions outside the regulation of transport. For example, the RPE located under the retina in the posterior eye has multiple specialized functions, including the phagocytosis of the photoreceptor cell outer segments and the participation in the visual cycle[42].

An essential feature of the epithelial tissues is their polarity, meaning that they have two distinct surfaces[1,43]. The apical surface is usually facing the body exterior or the lumen of the organs. The apical side usually contains extensions called microvilli that increase the apical surface area[1]. On the other hand, the basal surface is towards the connective tissue and is connected to the basal lamina, a thin ECM sheet under the epithelium. The RPE is also exceptional because its apical side does not face a lumen but the retinal tissue[42]. The sides of the cells facing each other are known as lateral surfaces, and the narrow space between these surfaces is called the lateral space.

Epithelia can be classified based on the number of cell layers and the shape of cells, as shown in Fig. 1A and B[44]. There is only a single layer of cells in a simple epithelium, i.e., an epithelial monolayer, whereas a stratified epithelium has multiple cell layers. Furthermore, the cell shape is used to classify an epithelium as either squamous (flattened), cuboidal (cube-like), or columnar (tall). The focus of this thesis is on the simple cuboidal epithelia.

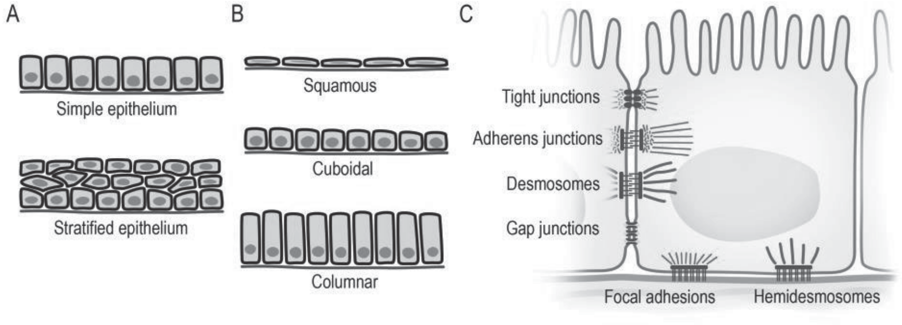

Figure 1. A) Classification of epithelia based on the number of cell layers. B) Classification of epithelia based on cell shape. C) A schematic representation of the cell-cell junctions and cell-ECM connections. Note that the locations of the cell-cell junctions along the lateral surfaces of the cells do not reflect their actual positions.

The epithelial cells are not only packed tightly, but they are also connected to each other and to the ECM underneath them. There are several types of connections between the cells, known as the cell-cell junctions, with different functions (Fig. 1C)[44]. Tight junctions form a transmembrane protein barrier against passive diffusion between the cells. Adherens junctions connect the actin cytoskeletons of the neighboring cells via transmembrane proteins bound across the lateral space. Desmosomes, like adherens junctions, form mechanical connections between cells, but they are connected to intermediate filaments instead of the actin cytoskeleton. On the other hand, gap junctions form an ionic and biochemical connection between the cells by creating small channels from one cell to another across the lateral space.

On their basal side, epithelial cells connect to the underlying ECM via focal adhesions and hemidesmosomes[44]. Both are multiprotein assemblies that connect the cytoskeleton to the various components of the basal lamina. The focal adhesions are connected to the actin cytoskeleton and the hemidesmosomes to the intermediate filaments.

2.2 Cell-cell junctions

Cell-cell junctions connect neighboring cells with various functions. Two of these junctions, the tight and the adherens junctions, are connected to the actin cytoskeleton and are essential to epithelial functions and their formation and regulation are closely related to each other. Here, I will outline the main components of these two cell-cell junction types. Since my thesis focuses on these junctions and actin cytoskeleton, I will not describe the structure and properties of the desmosomes and gap junctions in detail.

2.2.1 Tight junctions

Tight junctions are located on the lateral sides of the cells close to the apical surface, where they close the space between the cells. They are formed by two distinct parts: the bicellular junctions between two cells and the tricellular junctions at the intersections of three cells. In a cross-sectional image, the bicellular tight junctions manifest as sites where the membranes of the adjoining cells are in close contact. When viewed *en face* to the cell plasma membrane, these contact sites form a strand-like network that encircles the whole cell (see Fig. 2A and B). Close to the intersection of three cells, the strand network expands vertically and converge into a long tubular structure at the intersection itself. The bicellular strands are usually considered to compose of proteins; however, an important role of lipids has also been suggested[45,46]. Based on the protein model, these strands are formed by a complex system of transmembrane and intracellular proteins.

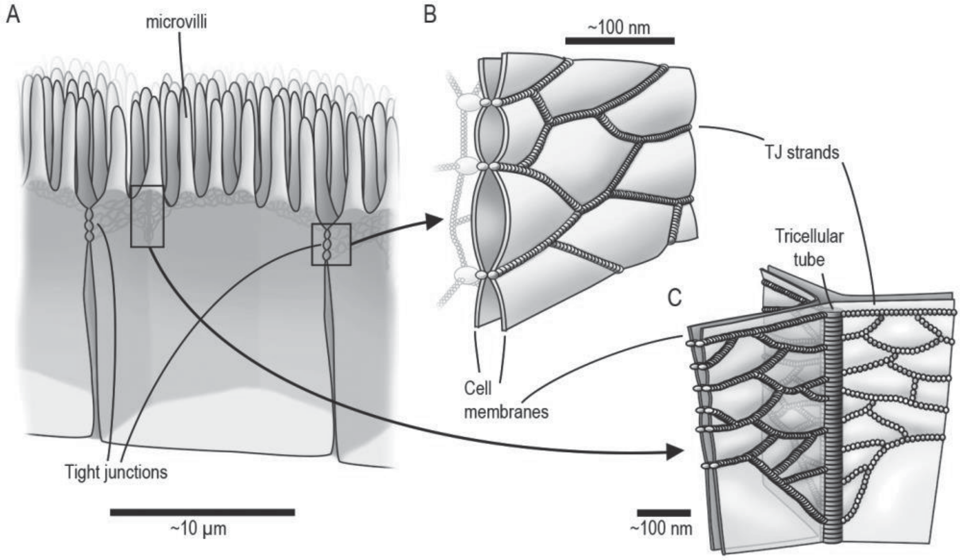

Figure 2. A) A schematic figure showing how the tight junctions encircle the apical end of the paracellular space between the epithelial cells and thus form the barrier. B) Close up of the bicellular strands that form a network dividing the space between the cells into small compartments. C) The tricellular tight junction central tube at the intersection of three cells. Figure adapted from Ref. 47.

The main structural transmembrane proteins in the bicellular strand network are claudins, a family of proteins with 27 members in mammals[48]. The extracellular parts of the claudins interact across the lateral space to form the diffusion barrier[14,49,50]. The prevalent model of the tight junction strands based on claudin crystal structures is that the claudins form a double row in each cell[50,51]. It is also well established that some claudins (e.g., claudin-2, -10a, -10b, and -17) form small extracellular channels to enable the movement of small solutes and water across the strands[52–57]. Other transmembrane proteins with more of a regulatory role are occludin and junctional adhesion molecule A (JAM-A). Occludin was the first transmembrane tight junction protein discovered[58] and has been shown to influence the tight junction barrier[59–61], especially the formation and stabilization of the intersections in the strands[62].

The cytoplasmic parts of the transmembrane proteins in the bicellular junctions interact with various scaffolding and regulatory proteins. The most well-known scaffolding proteins are of the zonula occludens (ZO) family, especially ZO-1, the first tight junction protein to be discovered[14,63]. Another cytoplasmic protein, cingulin, has a role in interactions between the tight junctions and microtubules as well as with recruiting small guanosine triphosphate (GTP)-binding proteins, also known as GTPases, to the junctions[14,64,65].

In contrast to the strand-like bicellular junctions, electron microscope images show the tricellular tight junctions as long tubes running between the three cells[28,66,67]. The research unraveling the composition of these structures is ongoing, and currently, the known main protein components are tricellulin and angulin[50]. Tricellulin, a member of the same protein family as occludin, can also be found in the strand-type junctions between two cells[28].

2.2.2 Adherens junctions

Adherens junctions connect the actin cytoskeleton of the neighboring cells. They also initialize the formation of cell-cell junctions and their stabilization[68]. The main transmembrane component of the adherens junctions are cadherins, more specifically E-cadherin in epithelia. The extracellular domains of two E-cadherins form a calcium-dependent bond between the cells[68]. The main interaction partners of the cytoplasmic tails of the E-cadherin are catenins: α-catenin, β-catenin, and p120-catenin. E-cadherin connects to actomyosin cytoskeleton by binding β-catenin, which subsequently binds to actin filaments via α-catenin[68]. α-catenin also interacts with various actin-associated proteins (e.g., vinculin and formin) and tight junction proteins (ZO-1)[69]. Adherens junctions are not only connected to actin but also interact with microtubules via p120-catenins and β-catenins[69]. In addition, to the cadherin-based junctions, adherens junctions also include another transmembrane protein, nectin, that connects to the actin cytoskeleton via adaptor afadin and has a role in the initial adherens junction formation[70].

The maturation and stability of tight junctions are tightly connected to the adherens junctions[70]: the latter form before the tight junctions, and interaction between ZO-1 and α-catenin or afadin is vital in this process[71]. Furthermore, the expression of ZO-1 affects the maturation of adherens junctions[72], indicating a complex interaction between the two types of cell-cell junctions.

2.3 Epithelial Barrier

The epithelial barrier can be divided into paracellular (between the cells) and transcellular (through the cells). The transfer of a solute, i.e., a molecule or an ion, through the paracellular barrier is passive: it diffuses only based on its (electro)chemical gradient. The main hindrance against their diffusion are the tight junctions that close the lateral space between the cells. On the other hand, in addition to the cell plasma membrane creating a formidable barrier against passive diffusion in the transcellular part, various active and facilitated passive transport processes occur through the cells.

2.3.1 Tight junction barrier

Tight junctions form a barrier against passive paracellular diffusion and thus define the baseline "tightness" of the epithelial barrier. Tight junctions have two main functions: "gate" and "fence"[13]. The gate refers to their role as a barrier against paracellular diffusion. The fence role describes the fact that tight junctions polarize the plasma membrane of the epithelial cells into two distinct domains: apical and basolateral. Therefore, they also restrict the lateral diffusion of membrane proteins and lipids between the two domains[13,73].

The tight junction barrier discriminates the solutes based on their size and charge to regulate their passage. In addition, the movement of molecules and ions are regulated differently[13,74–76]. Although the tight junctions usually form a seemingly impenetrable barrier against molecular permeation, relatively large macromolecules can still permeate through epithelia via the paracellular pathway. When Watson et al. and Van Itallie et al. studied the permeability of a range of sizes of polyethylene glycol (PEG) molecules, they found a biphasic permeability behavior, with an apparent cut-off size of around the molecular radius of 0.4 nm (see Fig. 3A)[16,77]. This led to the distinction of two routes across the barrier: the pore and the leak pathways. The pore pathway enables high-throughput diffusion of small solutes across tight junctions, compared to the low-permeability leak pathway, whose assumed size limit is over 6 nm[16,59,77,78].

The small pores in the channels formed by claudins enable solutes' size and charge-selective movement through the strands[17,52–57]. Since the claudin channels are thought to be the main pathway for ions, the claudin expression profile largely dictates an epithelium's ion permeability. The best-known example of the importance of this expression profile is the two strains of Madin-Darby canine kidney (MDCK) cells. MDCK I epithelia have over 30 times higher transepithelial electrical resistance (TER), a common measure of epithelial tightness, than MDCK II epithelia[79]. This difference has been shown to originate from the lack of expression of claudin-2, a well-known channel-forming claudin in "leaky" epithelia[80,81]. This high dependence of the TER on the claudin expression profile indicates that the pore pathway forms an important component in the ionic barrier of an epithelium. The dependence of the size-selectivity on the claudin-expression is not well understood, but the molecular radius limit of 0.4 nm seems to hold even if the expression varies[16,57]. Interestingly, it was recently shown that these channels could be gated similarly to some ion channels that pass through the cell plasma membrane[82], thus providing another possible means of barrier regulation.

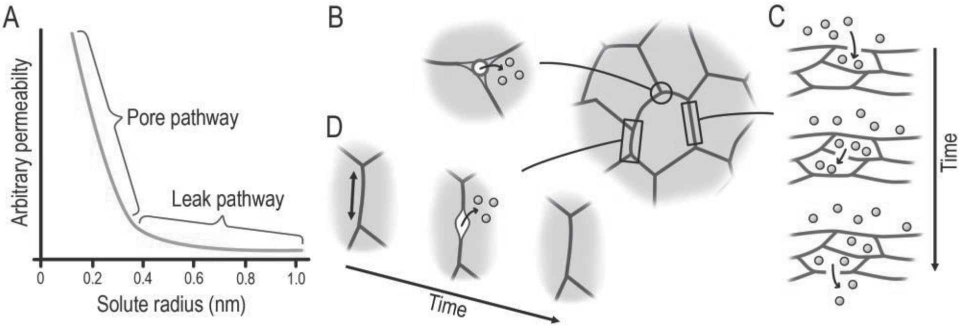

Figure 3. A) An adaptation of the polyethylene glycol (PEG) permeability results by Van Itallie et al.[16] shows biphasic permeability behavior and the cut-off radius at 0.4 nm. The pore pathway is the main pathway for solutes smaller than this radius and the leak pathway for the larger ones. The three candidates for the leak pathway are shown in B-D: B) The large pores in the tricellular junctions (top view); C) step-by-step permeation through the transient breaks in the strand network (*en face* to the plasma membrane); and D) transient local breaches of the bicellular strand following the elongation of the cell boundary.

Currently, the precise source of the leak pathway is under debate; the leading candidates are: 1) the large pores in the tricellular tight junctions, 2) transient breaks in the bicellular tight junction strands, and 3) transient local breaches of the bicellular tight junctions[16,27,33,57,59,83,84]. These candidates are depicted in Fig. 3B-D. Importantly, these candidates are not necessarily mutually exclusive[78].

Krug et al. observed that 3-kDa dextran macromolecules can permeate through the tricellular pores and that the expression of tricellulin affected the rate of permeation[28]. This indicated that the tricellular pores account for at least part of the leak pathway flux since the relative rarity of tricellular points in an epithelium would still lead to low permeability and little effect in ion conductance[28].

The second candidate, the transient breaks in the bicellular strands, is based on the observations that the strand network is a dynamic structure. In 2003, Sasaki et al.[83] imaged the strand networks between fibroblasts that were transfected with claudins and observed that these strands constantly move, break, and reseal in the time scale of seconds to minutes. Later, Van Itallie et al.[85] used a similar approach to show that the movement of the strands was constricted by the interactions between the claudins and ZO-1. Breaks in the strands have also been observed in freeze-fracture electron microscopy images of tight junctions[28,56,86,87]. Furthermore, the tight junction proteins move in the junctions at different rates. Shen et al.[88] showed that claudin-6 is primarily stably located in the tight junctions, whereas occludin diffuses rapidly in the junctions as well as between the junctions and intracellular occludin pools. Thus, the bicellular tight junctions are dynamic both at the strand and molecular levels. The theory of this dynamical structure forming the leak pathway is based on the idea of a step-by-step diffusion between strand-lined compartments through the strand breaks and finally through the whole strand network (Fig. 3C)[16,57,83,84,89]. This pathway has only been theorized due to the challenges of observing it experimentally.

The final and the newest candidate, the transient bicellular tight junction barrier breaches, was observed recently by Stephenson et al.[20]. Rapid elongation in the junctions, caused, e.g., by contracting cells close-by, led to a local leak (Fig. 3D). The leak was then fixed by an accumulation of actin and myosin II, leading to the re-establishment of the tight junction barrier. Thus, these rare transient leak events could explain the leak flux seen in the measurements.

2.3.2 Transcellular barrier and transport

In the transcellular barrier, the main obstacle is formed by the cell plasma membrane, which must be passed twice to transverse the whole cell. In contrast to the paracellular barrier, solutes can move across the plasma membrane either in an active or a passive manner. The active movement is enabled by the various transporters specific to certain molecules or ions. They use energy stored in either ATP, light, or the gradients of other solutes to transport the cargo against its (electro)chemical gradient[44]. In addition, solutes can also be transported across an epithelium by a process known as transcytosis, in which they are enclosed into a vesicle and moved from one side to another[44,90].

Transcellular transport can also occur by diffusion. Small uncharged molecules, such as oxygen, carbon dioxide, and ethanol, can diffuse straight through the lipid bilayer of the plasma membrane[44]. The membrane permeation of charged solutes, especially ions, and larger polar molecules is restricted due to the lipophilic center of the lipid bilayer. These solutes can pass the lipid bilayer by facilitated diffusion: by using ion channels or molecular transporters[44]. Ion channels discriminate ions based on their charge and size, and the transporter proteins are specific for their cargo. In addition, it has been theorized that small, lipophilic solutes can move through the epithelium by diffusion around the cell cytoplasm within the cell plasma membrane[91–93].

2.3.3 Examples of epithelial tissue barriers

While there are many covering epithelia with various functions in our bodies, they have one common task: protecting our bodies from the outside. For example, intestinal epithelium protects the body from the microbes and any adverse substances we consume, alveolar epithelium from respiratory viruses and air pollution, and skin from multiple external conditions, including ultraviolet light. The properties of all these barriers must be finetuned for their specific tasks. Here, I will present examples of different epithelial barriers. The TER values for these tissues and some cell lines are shown in Table 1 to compare their tightness.

The intestinal epithelium forms a selective barrier, whose function, in addition to being a barrier against adverse substances and microbes, is to absorb nutrients from the intestinal lumen[1]. Therefore, the regulation of permeability is of high importance. This barrier is formed by the intestinal epithelial monolayer and the mucus secreted by specialized intestinal epithelial cells[94]. The mucus hinders the solute movement near the epithelium, thus protecting the cells from large particles and microbes[94]. The intestinal surface area is maximized by folds and fingerlike villi[1]. Due to constant wear from absorption of nutrients and other substances from the lumen, the epithelial cells are continuously renewed: each cell is discarded by apoptosis after 4–5 days[95]. New cells are formed from pluripotent stem cells located in the crypts between the villi from where they migrate to the villus tips to replace the discarded cells[95]. The cell population is not uniform but includes, for example, absorptive enterocytes and mucus-secreting goblet cells[96]. A common cell line used to model intestinal epithelium *in vitro* is the enterocyte-like Caco-2, which originated from human colon carcinoma and has been used to study drug adsorption in the intestine[97–99]. Unfortunately, Caco-2 epithelia have been found to be very heterogeneous between different laboratories, which reduces comparability between results[100].

Table 1. Comparison between the transepithelial electrical resistance (TER) values for the example epithelia and common cell lines

Tissue/cell line	TER (Ω cm^2)	Source
Intestine		
Small intestine	50–100	101
Large intestine	300–400	101
Caco-2 cell line	250–4,000	102
Renal tubule		
Proximal tubule	6–10	103
Loop of Henle	350–700	103
Distal tubule	850	103
MDCK I cell line	>1,000	104
MDCK II cell line	~100	104
Skin epidermis	25,000	105
Alveolar epithelium (rat primary cells)	300–400	106,107
Retinal pigment epithelium		
Various species	100–350	108
Stem-cell derived	200–1500	108,109
ARPE-19 cell line	40	110,111

Renal tubules are a component of the kidney nephrons and receive the fluid filtered by the nephron glomerulus[1]. The tubules consist of three main segments: the proximal tubule, the loop of Henle, and the distal tubule. When the filtrate travels along the tubule, the cells of the renal epithelial monolayer reabsorb water and specific solutes (e.g., glucose and amino acids) from the filtrate into the blood circulation, as well as remove certain drugs and excess potassium from the blood and secrete it to the filtrate[1]. The epithelium itself becomes tighter farther along the tubule, as indicated by the TER values in Table 1. This increase in tightness can be attributed to the claudin expression profile in the epithelium[112]. For example, the expression of claudin-2, usually found in leaky epithelia, is only expressed in the proximal tubule and in the initial segments of the loop of Henle[113]. MDCK cell lines, originally from canine kidneys[114], are a commonly-used cell line to describe the properties of kidney epithelium and epithelium in general due to their clear polarization, formation of tight junctions, and rapid growth[104]. There are a variety of MDCK strains, of which the MDCK I and MDCK II are the most well-known[104].

The skin protects us against many outside threats, including chemical damage and microbes, but also prevents our tissues from drying out. The epithelial component of the skin is its outermost part, the epidermis. Unlike most other epithelia, the apical surface of the epidermis is facing the outside air, making it a dry epithelium[1]. In this stratified squamous epithelium, new cells are formed in the innermost layer from stem cells[1], from where they migrate outwards towards the skin surface. While moving away from the blood circulation, they are deprived of nutrients and, eventually, die. The dead cells form a tile-like barrier of dead cells in the outermost stratum corneum layer, from where they are shed over time. The barrier is mainly established by 20–30 layers of dead cells and granules full of lipids and keratin[1,115]. Notably, the lipids between the dead cells prevent the transfer of water or hydrophilic molecules through the skin. The keratin, a type of intermediate filament, gives the skin its strength, protecting the barrier from mechanical damage[115].

The oxygen uptake into the body occurs in pulmonary alveoli, where oxygen and carbon dioxide are transported into and out from the blood circulation, respectively, through the air-blood barrier[116]. This barrier also defends the body against bacteria, viruses, and allergens in the air[117]. The air-blood barrier is formed by three layers: the endothelial wall of the pulmonary capillaries, a basement membrane, and the alveolar epithelial type I cells[116]. The main barrier is formed by these epithelial cells, which are extremely thin and cover most of the surface of the alveoli[116,117].

Compared to the epithelia covered above, whose apical surfaces face either a lumen or the air, the RPE is a peculiar epithelium since its apical side is against a solid tissue[42]. The RPE resides in the rear of the eye, between the sensory retina and the vascularized choroid. Therefore, the apical surface is in direct contact with the photoreceptor outer segments. While the RPE has multiple essential functions related to our vision, it also forms the primary component of the outer blood-retinal barrier (BRB), separating the delicate outer neural retina from the blood circulation[118,119]. In addition to the RPE, the outer BRB includes two additional components: a thin layer of ECM directly below the RPE known as the Bruch's membrane and the fenestrated endothelial wall of the choroidal capillaries[118,119]. The Bruch's membrane composes mainly of laminin, collagen, proteoglycans, and elastin[120]. Typical cells used in studies include the ARPE-19 cell model, stem-cell-derived RPE cells, and rodent primary RPE cells[108,110,111,121,122].

2.4 Epithelial mechanics

Many normal processes of the epithelial tissue, including development, remodeling, and homeostasis, depend on their biomechanical environment and on mechanical forces either inside or between cells. For example, mechanical forces are present during cell division in anaphase, pulling the chromosomes apart and in cytokinesis to cleave the cell into two. Furthermore, extrusion of cells from the epithelium is a cooperative process in which neighboring cells push a cell out of the cell layer[123–125]. The cytoskeleton, focal adhesions, and adherens junctions enable cells to generate forces and sense and respond to the mechanical cues from their environment.

2.4.1 Cytoskeleton and focal adhesions

The cytoskeleton essentially gives cells their shape and broadly defines their mechanical properties. This intracellular scaffolding has various functions, including positioning cell organelles, functioning as a roadway for intracellular transport, and enabling cell movement[44]. The cytoskeleton consists of three main types of protein filaments: actin filaments, intermediate filaments, and microtubules. Each type is made of small subunits and has distinct functions and mechanical properties.

Actin filaments, or F-actin, are made of small G-actin monomers that form thin and polarized two-stranded helical filaments[44]. F-actin organizes into various structures with the help of different actin-binding proteins[126]. Actin nucleators such as the Arp2/3 and formins induce the polymerization of F-actin. Cross-linkers connect F-actin filaments to assemble a complex mesh that forms the cell cortex that gives the membrane mechanical support and strength (see Fig. 4). The filaments are also crosslinked into bundles to form so-called stress fibers that give cell contractile properties. The contractility of actin-based structures, not only in myofibrils in muscles but also in the stress fibers and the cell cortex in epithelia, is enabled by myosin II motor proteins[126,127]. The contractile system formed by F-actin and myosin II is usually referred to as the actomyosin cytoskeleton[128]. The F-actin structures are also connected to the cellular microenvironment: focal adhesions and adherens junctions connect the stress fibers and cell cortex to the ECM and to the neighboring cells, respectively (Fig. 4)[44]. This connection via the adherens junctions combines the individual contractile actomyosin cytoskeletons of the epithelial cells into a tissue-wide contractile system[129,130]. Actin also has a vital role in cell migration, intracellular transport, and forming the contractile ring to divide a cell into two in cytokinesis[44]. The organization and dynamics of the actin cytoskeleton, including the formation of cell cortex and stress fibers as well as their contractility, are mainly regulated by the Rho family of GTPases[131]. Members of this family, e.g., RhoA and Rac1, are activated in response to various signals and modify the actin filaments for example by activating myosin II via myosin light-chain kinase (MLCK) or actin-binding protein cofilin that severs the filaments[132].

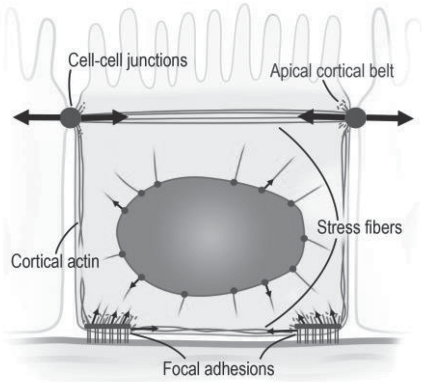

Figure 4. A schematic description of the positions of the cortical actin, the apical cortical belt, and the stress fibers, as well as the external connections at focal adhesions and cell-cell junctions.

Intermediate filaments are rope-like structures formed by long monomers and are organized into a network throughout a cell giving cell tensile strength[44]. Like F-actin, intermediate filaments are connected across cell boundaries by cell-cell junctions, in this instance the desmosomes, to share the mechanical stress between neighbors[44]. Furthermore, nuclear lamina, the main supporting structure of the nucleus, consists of intermediate filaments called lamins[133]. While the importance of intermediate filaments on cell mechanics has been well-established, the research has been largely overshadowed by that on actin[134].

Unlike the flexible actin and intermediate filaments, microtubules are stiff, hollow tubes formed by small tubulin monomers[44]. Their stiffness enables a cell to withstand compressive force from the environment or from the cell's own contractile actin structures[135]. Microtubules have multiple functions, including anchoring many cell organelles to their positions, functioning as roadways for intracellular transport by motor proteins such as dynein, and forming the mitotic spindle that separates the chromosomes during mitosis[44]. While microtubules are not connected to the environment like F-actin and intermediate filaments, they interact with focal adhesions[136] and cell-cell junctions[137].

Focal adhesions are large multiprotein structures that form at the periphery of cells and connect the actin cytoskeleton of the cell to the components of the ECM[138]. They have an essential role in cell adhesion, cell migration, and sensing the cell microenvironment[138,139]. The main transmembrane proteins in the focal adhesions are integrins, which form heterodimers that bind to specific components of the ECM on the outside.

The cytoplasmic tail of the integrin is associated with a plethora of proteins. The so-called integrin adhesome, i.e., the collection of proteins that localize and interact in the integrin-based structures, includes around 150 proteins[140]. Scaffolding proteins such as talin, α-actinin, and tensin interact with both integrins and actin, thus linking them together[138,140]. Many actin-associated proteins, including vinculin and vasodilator-stimulated phosphoprotein, interact with actin or other cytoplasmic components of the focal adhesions[138,140]. Further, there are many proteins that bind other proteins together as adaptors (e.g., zyxin) and signaling proteins (e.g., focal adhesion kinase) [138,140].

2.4.2 Mechanosensing in epithelium

While it has been known for a long time that mechanical forces actuate cellular processes based on biochemical signaling, as in the cell division, forces themselves can guide cellular behavior. Several proteins have been identified to be mechanosensitive, and new ones are constantly found. When these proteins are subjected to mechanical forces, their conformation changes may reveal so-called cryptic sites in the protein structure that can modulate its behavior or enable ligand binding[141]. There are also mechanically activated ion channels, whose ion conductivity changes as a response to mechanical forces[142]. For example, mechanosensitive Piezo channels allow auditory perception in the ear, where the fluid movement in the inner ear leads to forces applied on the channels and to a further neuronal response[143].

The advantage of mechanical signaling compared to biochemical signaling is speed. Whereas the biochemical signals are limited by the rate of diffusion or that of the motor proteins, mechanical signals are transmitted along filaments and can reach speeds of around six orders of magnitude faster than those of the biochemical signals[23]. In addition, the epithelial cells are in a prestressed state, which is produced by tension in the actomyosin and the cellular adhesions[23]. This increases the extend deformations can travel in the tissue approximately ten times compared to an unstressed solid material[23].

Processes in which mechanical forces are transformed into biochemical or bioelectrical signals are known as mechanotransduction. There is also a plethora of these mechanosensitive proteins in the epithelial tissues, enabling cellular signaling by forces. Most of the identified mechanosensitive proteins in epithelia are found in structures that transmit forces, i.e., focal adhesions, cell-cell junctions, and cytoskeleton. In the focal adhesions, tension applied to the talin rod domain leads to unfolding that reveals new binding sites for actin and vinculin[144]. This change recruits new adhesion molecules and thus mechanically reinforces the focal adhesions[144,145]. Focal adhesions can sample the ECM stiffness by dynamically fluctuating the traction force they pull the ECM with[146].

The mechanical connection between the cells in the cell-cell junctions, especially the adherens junctions, enables direct mechanical signaling between the cells. The mechanosensing in adherens junctions is related to various cellular processes in epithelia, including division, intercalation, migration, and energy metabolism[147,148]. Since the tension between the actomyosin cytoskeleton and the neighboring cells is transmitted via the cadherin-catenin complex, they play a major role in the adherens junction mechanosensitivity[147,149,150]. The binding of the cadherin extracellular domains between cells and between α-catenin and F-actin are so-called catch-bonds, which are strengthened by tension[151]. Like talin in the focal adhesions, vinculin binds to revealed cryptic sites in the α-catenin under tension, reinforcing and stabilizing the adherens junctions[147]. This reinforcement of the adherens junctions and cortical actomyosin cytoskeleton against tension protects the integrity of the tight junction barrier and epithelial integrity[152].

The adherens junctions are not the only mechanosensitive component in the cell-cell junctions. The actomyosin tension has been shown to influence the morphology and the barrier properties of the tight junctions[153–155]. While tight junctions are closely related to the adherens junctions, they also contain mechanosensitive elements[156]. Stretching ZO-1 reveals cryptic sites that recruit ZO-1-binding ligands[157] and might enable tensional regulation of epithelial barrier properties. Interestingly, it was recently observed that ZO-1 is under tension controlled by the ECM stiffness and JAM-A[158]. Therefore, since ZO-1 has a role in regulating the leak pathway permeability[89], tension seems to have the ability to control the tight junction barrier directly. In addition, double knockdown of ZO-1 and ZO-2 has been shown to increase cortical tension[21], further strengthening the connection between the properties of the tight junction barrier and the mechanical properties of the cells.

The mechanosensing is not limited to the connection points between the cell and its environment, but it also occurs inside the cell. Increased tension modifies the helical morphology of F-actin, which inhibits the binding of the F-actin-severing cofilin[159] and increases the binding affinity of myosin II, which leads to the formation of stress fibers[160,161]. Thus, this system enables the cell to respond to tension in a particular direction by reinforcing the actomyosin cytoskeleton to counter it. Moreover, the actomyosin cytoskeleton enables the transfer of tension from the environment directly to the nuclear envelope[23,162]. The forces are transmitted from the F-actin into the nucleoskeleton inside the nucleus. They can lead to the reorganization of the nuclear lamina, which can potentially affect chromatin organization and gene expression[163–168].

2.4.3 Epithelium as an active material

Cells both generate force with their molecular motors and are subject to many forces from their environment. The cells generate forces for various tasks, such as cell division, coordinated changes in shape during development, and neighbor extrusion[169,170]. External forces may originate from the neighboring cells, a wider tissue area, or outside the tissue. Active deformations of a single cell, for example, due to cell division or apoptosis, require the neighboring cells also to deform to maintain the connection between the cells and the integrity of the epithelial barrier. On the other hand, epithelial-scale events, such as embryogenesis or wound healing, or external forces, such as shear or tissue stretching, lead to epithelium-wide deformations[171–173].

Cells respond to forces viscoelastically (Fig. 5). The initial response is elastic, indicating that the cells return to their initial shape following a momentary force [169,174,175]. However, the cell deformations become irreversible under sustained stress as they dissipate the stress via various mechanisms, behaving like a viscous material[174–176]. The cells utilize their mechanosensitive machinery in the cell-cell junctions, focal adhesions, and cytoskeleton to initialize the stress dissipation. On a small scale, cells can remodel a junction between two cells by increasing or reducing its length to reduce stress. This may also lead to neighbor exchange, also known as intercalation, a process where a cell loses or gains a neighbor[169]. This happens by shrinking one bicellular junction into a four-cell junction, followed by a formation of a new junction perpendicular to the old one between two new neighbors[177]. These changes in the cell-cell junctions depend on the turnover of actomyosin cytoskeleton and junctional proteins and are guided by RhoA activity[175,178–180]. The time scale of the viscous behavior depends on the mechanisms that relax the strain and are in the range of tens of seconds to tens of minutes[171,174,175,181].

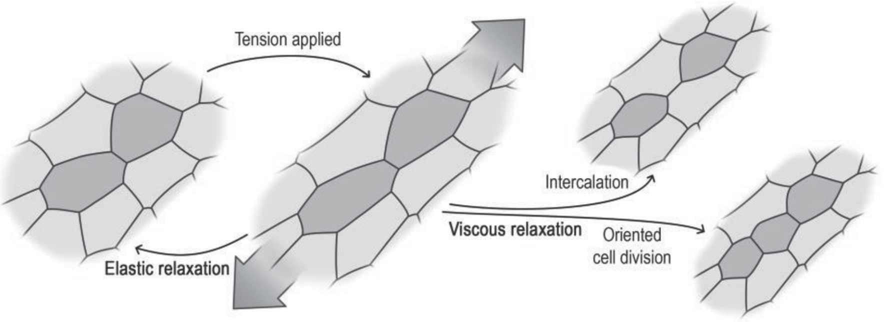

Figure 5. Cells respond viscoelastically to applied tension. After transient stress, the cells relax elastically and return to their initial shapes. Under sustained stress, the cells relax viscously by dissipating the stress by non-reversible shape changes or, for example, by intercalation (neighbor changes) or by oriented cell division.

Mechanical energy can also be dissipated via changes in cell numbers. When the epithelium is under stretch, it can relax by oriented cell division[169,182,183]. The cell divides perpendicular to its long axis based on the mechanical strain sensed at the tricellular junctions[184]. In addition, if an epithelium is too densely packed, the stress can be relaxed by cell extrusion to reduce cell crowding and, therefore, the mechanical pressure[185,186]. Amazingly, during these changes in the cell numbers, the epithelia can maintain the tight junction barrier. During cytokinesis, new junctions are formed by pulling the neighboring cells to the space between the dividing cells to maintain the barrier seal[187]. Also, while extruding a cell from the epithelium, the neighboring cells reform the junctions to seal the gap that the extruded cell would leave[188].

2.4.4 Effect of extracellular environment stiffness

The importance of the stiffness of the environment on many cellular processes has been well established. The stiffness of tissues – measured with Young's modulus, E (unit: pascal, Pa) – range from hundreds of pascals for neuronal and lung tissue to tens of kilopascals in cartilage and bone[25]. As a comparison, the stiffness of MDCK cells cultured on polydimethylsiloxane substrate was measured to be 1–3 kPa depending on the cell size[189]. The cells match their stiffness with the environment using their mechanosensitive machinery, a process known as mechanoreciprocity[25,190,191]. Talin has a prominent role in this process since it is positioned optimally to sense the mechanics of the ECM. Focal adhesions can sample the ECM stiffness by dynamically fluctuating the traction force they pull the ECM[146].

In addition to affecting the cell stiffness, the cells' environment influences many cellular functions. In a landmark study, Engler et al. showed that soft substrate under the mesenchymal stem cells induced neuron-like phenotype, whereas stiffer substrate led to cells with myogenic or osteogenic features[192]. Furthermore, when cultured on a substrate with a stiffness gradient, cells have been shown to migrate towards the increasing stiffness, a process known as durotaxis[193–196]. This directional migration has been found to be more efficient with cell communities than single cells due to long-range mechanical forces between the migrating cells[196].

In addition to communicating directly between themselves, cells have been shown to communicate mechanically over long distances via the ECM. Cells can sense strains in the substrate generated by another cell as far as 1,000 μm away via aligned collagen fibers[197,198]. Reinhart-King and coworkers found that the stiffness of the substrate markedly affects the range over which the cells can communicate via the substrate deformations[199]. Even though cells on stiff substrates exert more force on the substrate due to their higher contractility, the extent of the strain in the substrate was found to be smaller compared to soft substrates[199].

2.5 Epithelial pathologies

As the barrier between the body and the outside, epithelia are subjected to various adverse conditions and pathogens. Therefore, many diseases and conditions affect or originate from epithelial tissues, including IBD, celiac disease, diarrhea, chronic obstructive pulmonary disease, age-related macular degeneration (AMD), and microbial infections[118,200–202]. Mutations in tight junction claudins also lead to various conditions, such as deafness and familial hypomagnesemia with hypercalciuria and nephrocalcinosis[203,204]. Furthermore, carcinomas, or cancers of epithelial origin, are the most common type of cancer[7,205,206]. The changes in the epithelial barrier and mechanical properties are connected to IBD, to AMD, and to epithelial tumors.

2.5.1 Inflammatory bowel disease

IBD is a set of conditions that are characterized by chronic inflammation in the gastrointestinal tract. The main types of IBD are Crohn's disease and ulcerative colitis[2]. These diseases respectively affect the whole gastrointestinal tract and the colon, and manifest as episodes of inflammation, leading to, e.g., diarrhea and abdominal pain as well as disorders in the liver, joints, and skin[2,207–209]. The IBD has a significant effect on the patient's quality of life, and its prevalence has rapidly increased in industrialized countries throughout the last decades[5,210–212]. The pathogenesis of the IBD has been linked with genetic factors, intestinal microbes, environmental factors, and abnormalities in the immune response[2].

Epithelial barrier dysfunctions have an essential role in the IBD. The uncontrolled inflammation leads to the production of proinflammatory cytokines by cells of the immune system. These cytokines – including tumor necrosis factor alpha (TNF-α), interleukin-13, and interferon gamma – can cause drastic changes in the epithelial barrier, e.g., upregulation of claudin-2, apoptosis, endocytosis of occludin from the cell-cell junctions, and changes in the leak pathway[61,213–218]. Many of these changes in the barrier are intermediated by the MLCK that activates the myosin II in the actomyosin cytoskeleton[215,216,218,219]. The loss of the epithelial barrier leads to cation and water leakage, and thus to diarrhea[220,221].

In addition to causing the loss of barrier, the episodes of inflammation stiffen the epithelial cells by activating the contraction of the cortical actomyosin via MLCK[24]. Furthermore, the inflammation leads to fibrosis, accompanied by an increase in the ECM stiffness correlated with an increase in collagen production[222–226]. These increases in cell and ECM stiffness affect mechanotransduction in cells[227], influencing the mechanical signaling between a cell and its environment.

2.5.2 Age-related macular degeneration

AMD is the leading cause of legal blindness in western countries, affecting mainly the elderly[3,4]. There are two main types of AMD, the wet and dry forms, of which the former is rarer and more severe of the two[118]. AMD is a result of multiple factors, but it mainly originates in the outer BRB.

With age, small deposits of waste products and lipids, called drusens, form under the RPE cells in the Bruch's membrane[118,228]. In addition, the Bruch's membrane becomes thicker with age, further decreasing its permeability[118]. From here, AMD can progress into dry or wet forms[118]. In dry form, the RPE and the photoreceptors, deprived of nutrients and oxygen, degenerate, impairing the vision. Without oxygen, RPE becomes hypoxic and thus releases vascular endothelial growth factor, inducing growth of new capillaries from the choroid through the Bruch's membrane and the RPE itself, which is a hallmark of wet AMD. The loss of the BRB leaves the neural retina without a protective barrier, which eventually leads to loss of visual function in the macular part of the eye.

RPE is also subjected to oxidative stress by reactive oxygen species originating from high oxygen requirements of the neural retina, the phagocytosis of the photoreceptor outer segments, and being subjected to high-energy blue light[118,229,230]. This is accompanied by the reduction in the amount of antioxidants with age[118,231]. The oxidative stress has been shown to disrupt the RPE tight junctions, thus loosening the barrier[229,230]. AMD is also characterized by inflammation, and the accompanied cytokines affect the tight junctions of the RPE[232]. For example, TNF-α introduces changes in RPE claudin expression and tight junction morphology, as well as makes the junctions leakier and less selective for sodium and potassium[232].

2.5.3 Epithelial tumors

Epithelial tumors and tumor progression are characterized by disruption of the mechanical homeostasis. Both cellular tension and ECM stiffness have been shown to be increased in tumors[25,233–235]. In addition, the cells' mechanoreciprocity can be compromised[25,233]. Cells in tumors are also subjected to compressive forces from the expanding tumor due to the uncontrolled cell proliferation and the elevated interstitial fluid originating from the formation of new capillaries[25,26,236].

Increased cellular tension and cell-generated forces have been linked to increased cell growth, survival, and invasiveness[25,190]. ECM stiffening has been shown to induce epithelial-to-mesenchymal transition (EMT), a process in which epithelial cells become mesenchyme-like cells with higher invasive potential[205,237,238]. While EMT is a normal process during organogenesis, it has also been linked with cancer progression[237]. In addition, Stowers et al.[239] found that in mammary epithelium, the increased ECM stiffness affects the nuclear organization and chromatin accessibility to promote tumorigenic phenotype.

2.6 Biophysical measurements of epithelial properties

There are a plethora of experimental tools for studying both epithelial permeability and mechanics. While epithelial molecular and ionic barriers, in essence, describe the same phenomena – the resistance against solute movement through an epithelium – different methods are usually used to measure them. On the other hand, the methods for measuring epithelial mechanics have benefited from the techniques developed for material sciences that have found their uses in biomedical research.

2.6.1 Measuring the molecular permeability

Epithelial molecular permeability is usually studied by measuring the diffusion of tracer molecules from one aqueous compartment into another through the epithelium. Epithelial cell models such as MDCK and Caco-2 are traditionally cultured on permeable polymer supports for these measurements. The two chambers can be formed in a well-plate by the Transwell permeable supports[16,61,89,240,241]. The barrier properties of excised epithelial tissues are usually measured in a Ussing chamber type system, where the sample epithelium – which can also be a cell model on semipermeable support – is sandwiched between two chambers[27,74,217,242].

Various tracer molecules have been employed in these measurements. Molecules with different sizes have been used to study the size dependence of permeability. Molecules such as mannitol, fluorescein, or different sizes of PEG molecules have been employed to describe small molecule (< 1,000 Da) permeability[16,60,77,121,213,243,244]. On the other hand, for example, inulin, horseradish peroxidase, and different sizes of dextran are common tracers to describe larger molecules (> 1,000 Da)[28,60,244,245]. Especially PEGs and dextrans provide a convenient way of investigating the permeability of series of molecules with increasing size but with otherwise similar properties[16,28,77,245]. In addition, the effect of lipophilicity of the solute on the permeability has been studied, for example, using β-blockers[245]. These drug molecules are similar in size but have a large range of lipophilicities, ranging from lipophilic betaxolol to hydrophilic atenolol.

The tracer molecule of interest is placed into a compartment on one side, and samples are taken from the opposite side over time to measure the permeated amount. The sample concentration can be measured e.g. by fluorescence (fluorescein and fluorescein isothiocyanate tagged dextrans)[28,121,213,241,245], by high-performance liquid chromatography (PEGs)[16,246,247], or by scintillation counters (radioisotope tagged mannitol and inulin)[16,243,244,248]. The permeability coefficient can then be calculated from the slope of concentration as a function of time using equation

$$P = \frac{dC/dt}{C_0 A_{epi}}, \qquad 1$$

where dC/dt is the slope, C_0 is the initial concentration in the compartment where the tracer was placed, and A_{epi} is the area of the epithelium.

The described measurement method provides the bulk permeability coefficients for the whole epithelium. However, methods have been developed to study more local junctional permeability events. Richter et al.[249,250] used a novel system utilizing biotin-avidin binding and two different fluorophores in their respective compartments to indicate leak sites in the cell-cell junctions. Similarly, Stephenson et al.[20] presented a method where zinc ions and FluoZin3, a dye that emits fluorescence upon zinc binding, were placed on the two sides of the epithelium, making the junctional leak events detectable by the FluoZin3 signals with a high temporal resolution.

2.6.2 Measuring the electrical barrier

The electrical barrier properties of epithelia are measured by placing electrodes into the fluid compartments on either side of the tissues and by measuring the electrical resistance between them[102]. This is done by injecting a known current, measuring the resulting voltage across the epithelium, and using Ohm's law to obtain the resistance. Usually, 4-electrode systems are favored to separate the current injection and voltage measurement and reduce the effect of electrode impedance on the results[122,242]. The Ussing chamber is a common measurement system for the electrical properties, but epithelia on Transwell inserts can also easily be measured by so-called "chopstick" electrodes[102,248,251]. TER is a typical and easy measurement of epithelial health and maturation, and it is also used in tandem with molecular permeability to describe the epithelial barrier. On the other hand, the frequency-dependent transepithelial electrical impedance (TEZ) provides a more complete view of the electrical barrier since it enables the use of equivalent circuit models (discussed in section 2.7.1) to describe the properties of the different barrier components[121,122,252–254]. The TER and TEZ are normalized with the area of the measured epithelia to obtain comparable values between studies. Compared to the permeability measurements, which are usually conducted over many hours, the electrical measurements are almost instantaneous.

TER and TEZ provide information on the whole epithelia, and methods have been developed to obtain a higher resolution view of the resistive barrier properties. Conductivity scanning utilizes a small electrode that is used to scan the conductance near the epithelial surface[255,256]. This method is sensitive to the local conductance properties due to the electrode proximity to the epithelium compared to the typical measurements where the electrodes are far from the surface. In addition, Weber et al.[82] used the patch-clamp method, usually used for studying transmembrane ion channels, to measure the dynamic properties of claudin-2-based channels between two cells.

2.6.3 Measuring the biomechanics

Many methods have been used to study the mechanical properties of cells, including atomic force microscope, magnetic twisting cytometry, and optical tweezers[257–259]. For example, atomic force microscopy has been used to study the stiffness of MDCK epithelia[189]. Further, in the last years, fluorescence-based molecular force sensors have been developed to study forces inside cells[260,261]. These sensors, usually fusions of mechanosensitive proteins, change their fluorescent emission when subjected to forces, making them an ideal tool for studying forces between cells and their neighbors and environment.

Traction force microscopy has been used to study the forces that cells exert on the ECM[29,262–264]. This method is based on imaging the deformation of the material under the cells with known stiffness. The cells are cultured either on small microposts whose deflection can be imaged or on hydrogel with embedded fluorescent microbeads[29]. In these applications, polyacrylamide is a commonly used hydrogel since its stiffness can be easily modified to study its effect on epithelial mechanics[29]. This method has been used, for example, to study cell movement in homeostasis and migration[265–267].

In addition to observing the cells, they can be manipulated to provide more information on specific situations. Systems have been developed to stretch the material under the epithelia to study how epithelial cells behave under prolonged or transient stretch[176,268–271]. In addition, a method known as optogenetics can be used to activate specific processes inside cells by using light[272,273]. This method has been used in epithelial research to contract cells or parts of cells: For example, a system used to activate RhoA signaling, and therefore actomyosin cytoskeleton contraction, has been used to study adaptive properties of cell-cell junctions[174,175].

2.7 Computational modeling of biomedical systems

A model is an approximation of a real system. A system refers to a collection of interrelated objects[274], which can be, e.g., organisms, tissues, cells, or molecules. A model reduces the reality to the objects and properties relevant to the research questions to provide a new understanding of the system's behavior. The process of building a model is called modeling. This section will describe the general characteristics and purposes of computational biomedical models, the modeling process, common methods, and sources of error.

2.7.1 Characteristics and purposes of biomedical models

Models can take many forms, and those of biomedical systems are generally categorized into animal models, cell models, and computational models. Animal models, also called *in vivo* (lat. "within the living"), use various live animals to represent the human body. On the other hand, cell models use cell lines to describe the basic properties of human tissues. These are also called *in vitro* (lat. "within the glass") models to indicate that the cells are usually cultured on glass. Computational, or mathematical, models use mathematical formulations to describe the system of interest. The term *in silico* (lat. "in silicon") is sometimes used to relate the terminology with the *in vivo* and *in vitro* models, as the computations are done with computer cores made of silicon. Since the focus of this thesis is on computational models, the term "model" is used to refer to these models, if not stated otherwise.

Biomedical systems have unique characteristics when compared with systems built by humans, e.g., various machines. Tissues and cells are innately complex. This complexity arises from many things, including, but not limited to, multiple spatial and temporal scales, feedback mechanisms, nonlinearity, differences between individuals, interconnectivity, and adaptation[275]. Another major challenge is the fact that the system is rarely fully known. For example, there might always be unknown mechanisms at the cellular level that affect the system in question. Modeling these complex systems is more challenging than manufactured systems, whose properties are generally well defined and known.

Despite the challenges in modeling living systems, computational modeling forms a powerful tool in biomedical sciences. The description of the system and the problem with mathematical formulations enables the use of well-established theories of physics and chemistry to complement the experimental research. Models can test hypotheses, guide experiments, interpret experimental results, predict system behavior, and integrate knowledge[275,276]. As an example, computational modeling enables a convenient and inexpensive way of designing and testing new drugs.

2.7.2 Modeling process

Optimally, modeling is an iterative process in tandem with experimental work (Fig. 6). Results from experimental measurements are used to develop the model, which can then be used to interpret the results or make predictions of the system. This new knowledge from the modeling can be implemented into the experimental measurements and iteratively continue the process.

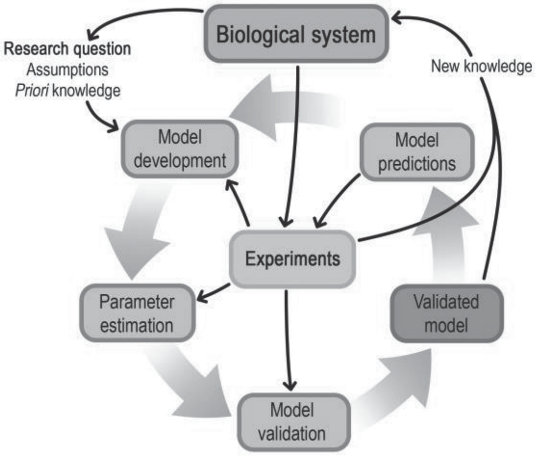

Figure 6. The iterative process between the experiments and computational modeling. Model is developed based on the research question and experiments. The choice of model type depends on the research question, *a priori* knowledge of the system, and the assumptions that can be made about the system. Experimental data is then used to obtain the model parameter values and to validate the model. The validated model can provide new knowledge on the biological system, be used to predict the system behavior, and thus guide the experimental work that can be used further to refine the model.

The model construction process is based on the experimental results and depends on the required capabilities of the model and the extent of *a priori* knowledge on the system[275,277]. A simple model that mathematically relates the system input to the output – e.g., the properties of solutes to their measured permeabilities – can be constructed with very little *a priori* knowledge on the system itself. In practice, curve fitting methods are usually used to derive this functional relationship. These simple models, known as phenomenological or black-box models, do not describe the events inside the system, which limits their usability[275]. While simple predictions on the system behavior based on a given input can be made with these models, their predictive power is limited by the data used to construct them.

More detailed and powerful models require more *a priori* knowledge to describe the processes and interactions that produce the system behavior. A model that describes the internal functions of the system is called the mechanistic or white-box model[275]. The first step of constructing a mechanistic model is the simplification of the real system. This is done by identifying the main components and features that govern the specific system function. These assumptions are guided by the purpose and the desired level of detail of the model. The simplified approximation of the real system is written in terms of mathematical formulations derived from general physical and chemical principles to describe the system. Next, the model parameters are estimated based on the experimental data, and the system is validated. The validated model can then be simulated to observe the model behavior and obtain new knowledge of the system. The model can also be used to create predictions of the system for further experiments that can be used to refine the model. In addition to being more robust for predictions, these models can explain the system and provide a more profound understanding. However, mechanistic models require a large amount of knowledge on the system and are thus not always feasible. In practice, models usually are between the full black and white-box models.

Validation is an essential step in the model-building process. The computational results should be compared with those from the real system to test the model's suitability to the required application[275,278,279]. Validation should already be conducted during the model construction to guide the modeling choices. The difference in the computational and experimental results indicates that the model is incomplete or that assumptions must be adjusted. In addition, since a model is constructed for a specific purpose, its validity for other applications must be verified since the same simplifications and assumptions may be unsuitable. However, a model that cannot be validated can have some value: it can provide simple hypotheses of the system and indicate what knowledge is missing.

2.7.3 Common modeling methods

Models that depend on time and/or space are generally described by differential equations, and solving them can be challenging. While some simple models can be solved analytically, this is not feasible for more complex problems. In these cases, the solution is usually obtained via numerical methods.

The principal idea of the numerical methods is the discretization of the differential equations and the system from the continuous system into discrete equations and a discrete system. Thus, the differential equations are solved only at specific time points and/or locations, and the obtained solution approximates the analytically correct solution. While there are numerical methods with different accuracies, the more accurate methods are computationally heavier to solve. The computational load is not only affected by the method but also by the resolution of the discretization: To obtain higher spatial resolution requires more positions at which to solve the model, therefore increasing the computational time. Thus, choosing the optimal numerical method and the fineness of the discretization for a model is an optimization between the required accuracy of the solution and computational time.

In modeling any system, a differential equation describes how the physical quantity to be solved, called the dependent variable, changes over time and/or space. Time (t) and spatial dimensions (x, y, and z) are called independent variables. The rate of this change is a function of these dependent and independent variables. Differential equations that depend on only one independent variable, such as time or a single spatial dimension, are ordinary differential equations (ODEs). Those that depend on two or more independent variables are called partial differential equations (PDEs). Different solution methods are required for these two types of equations. While in most biomedical models, the equations depend on time, there are also time-independent models, called steady-state models. Furthermore, if the model depends on neither time nor space, the system can be solved by straightforward calculations without differential equations.

Time-dependent ODEs are usually solved by so-called time marching methods. The basis of the methods is that the initial value of the dependent variable must be known, and therefore these models are usually called initial-value problems. The simplest way of discretizing ODEs is called the forward Euler method, which, unfortunately, is only accurate over small timesteps, which itself increases the computational time. Euler method is a member of a family of numerical methods called Runge-Kutta methods. The higher-order Runge-Kutta methods are computationally heavier than the Euler – the 1st order Runge-Kutta method – but enable longer time steps. These methods utilize intermediate time points to obtain a much more accurate solution. The most well-known is the 4th order Runge-Kutta method, which is considerably more accurate than the Euler method, even with longer steps. In addition to the Runge-Kutta methods, some methods utilize multiple steps in the past to increase the accuracy of the solution.

Solving PDEs requires their own numerical methods, most common of which are the finite difference method (FDM) and finite element method (FEM). In FDM, the geometrical domain of the model, be it in one, two, or three dimensions, is discretized uniformly in each dimension to form a uniform grid. The spatial derivatives are then described by finite differences. FDM also requires the definition of boundary conditions at the physical boundaries of the model domain, the two classes of which are Dirichlet and Neumann boundary conditions. The former defines the value of the dependent variable and the latter its derivative at a boundary. To summarize, in FDM, the equation, time, and space are discretized, and the solution is obtained in the discrete spatial points at discrete times.

FEM, a typical computational method used for engineering problems, solves the dependent variables everywhere in the geometrical domain of the model. Instead of a uniform grid, FEM uses complex meshes in which the geometry is discretized into triangular (2D) or tetrahedral (3D) elements. The equation to be solved is discretized into so-called element equations that are solved over each element. The discrete element equations are combined into a matrix to solve the model over all the elements. Like FDM, FEM also requires the definition of initial conditions for the variables and boundary conditions at the boundaries of the model domain.

Because models based on differential equations describe the system as a continuum, they cannot always properly describe systems consisting of small individual units, such as cells. The so-called individual-based models, also known as cellular automata or agent-based models, have been used to describe these kinds of systems. In these methods, the system is not governed by differential equations but by the behavior of individual units. These individual units – e.g., molecules, cells, or organisms – are described by predefined properties, rules that govern their behavior, and interactions with other units and their environment. These models are highly flexible, and the rules can depend on the properties of the unit and/or those of the other units and the environment. Relatively simple rules and unit properties can produce complex behavior compared to differential-equation-based methods.

Choosing the correct method is an essential step of the modeling process and is always dependent on the system and the purpose of the model. For example, depending on the model purpose, the epithelium can be described either as a continuum and solved using FEM or composed of individual cells and solved with individual-based methods.

2.7.4 Sources of errors

Modeling results always include an error originating from many sources when compared with the real system. First, because models are simplified representations of the real systems, they will innately differ from reality. While this error can be minimized by including more system components and features into the model, it cannot be fully removed. A model always approximates the real system and, therefore, cannot fully describe it. In addition, describing the system in more detail increases the model complexity and computational load.

The second source of errors is the numerical methods usually used to solve the models[278,279]. These methods depend on the discretization of the continuous equations, time, and space. In practice, this error can usually be minimized by having smaller temporal and spatial steps, with the downside of increasing the computational time.

Solving the discrete models creates the third source of model error[278,279]. Some complex methods, such as FEM, require the use of so-called iterative solution methods. These methods usually provide a solution close to the correct solution of the discrete model, but not exactly. In addition, round-off errors in calculations can produce minor errors.

In general, modeling is an optimization choice between model accuracy and computational time. Therefore, depending on the problem under investigation, a less accurate model might be desirable if it produces accurate enough results and can be solved quickly.

2.8 Computational modeling of epithelia

Computational modeling of epithelial properties is still a developing area of research, especially when compared with the well-established cardiac, neuronal, and bone modeling fields. While modeling of the epithelial barrier is commonly used in drug research due to its role as the gatekeeper of the body, these models are generally aiming to describe the permeability of drug molecules and do not provide a basic understanding of the structure and properties of the barrier itself. On the other hand, since epithelia are common systems used to study cellular and tissue mechanics due to their two-dimensional nature, models of epithelial mechanics are abundant, and their number is increasing.

2.8.1 Models of epithelial barrier properties

Properties of epithelial barriers have been modeled with varying levels of detail, ranging from the simplest model of describing the barrier only by a simple permeability coefficient to highly detailed models of tight junction structure. A permeability coefficient itself can be considered a model of the real system: It simplifies the complex barrier behavior into one number. While these numbers by themselves are quite a simplistic view of models, they can be used as a part of larger-scale models to describe the epithelial barrier. For example, many studies using an ocular drug delivery model of the whole eye simplify the outer BRB, mainly formed by the RPE, as a boundary with a defined permeability coefficient[280–284]. Some of these models are so-called multicompartmental models, in which well-mixed compartments represent body compartments (e.g., tissues or cells), and substances are transferred between them based on rate constants[280–282] according to the following equation:

$$\frac{dq_i}{dt} = \sum_j \left(k_{j,i}q_j - k_{i,j}q_i\right), \qquad 2$$

where q_i is the amount of substance in compartment i, $k_{j,i}$ is the rate constant from compartment j to i. Many multicompartmental models that include an epithelial barrier consider it only as a boundary between two compartments and thus represent the barrier properties only by a rate constant derived from a permeability coefficient. Multicompartmental models do not describe the geometry explicitly but only via compartment dimensions and boundary areas usually incorporated into the rate constants. However, some models include a description of the anatomic geometry and are thus solved with methods like FEM, and here the epithelium is usually described by a geometrical boundary between two domains[283]. In addition, there are some models of *in vitro* measurement systems in which a domain boundary similarly describes the epithelium with a given permeability coefficient[285].

In drug research, especially in the initial stages of designing a new drug, a modeling technique called quantitative structure property relationship is commonly used[286]. In this method, various physicochemical descriptors of the molecule, such as their molecular weight, octanol-water partition coefficient, polar surface area, and the number of hydrogen bond acceptors and donors, are related to their measured epithelial permeability by linear correlation[286–288]. Principal component analysis can then be used to find the descriptors that mainly dictate the permeability[286–288]. This method gives a convenient way to obtain a rapid prediction of the permeability of new drug molecules.

In addition to the models studying solute permeability, some describe the ionic barrier properties based on the description of the epithelium by an equivalent electrical circuit. In these circuits, the paracellular pathway is represented by resistive components and the transcellular pathway by a capacitive, sometimes combined with resistive components[252,253,289]. The capacitors correspond to the insulative properties of the plasma membrane[253]. Thus, in their simplest form, a frequency-dependent electrical epithelial barrier can be described by two variables: resistance and capacitance[121,122,252,253,289].

More detailed models of the barrier divide the epithelial tissue into components to better describe the properties of the separate pathways. Pak et al. constructed a multicompartmental model with separate compartments for the paracellular and transcellular permeability pathways to differentiate the behavior between them[290]. In a pulmonary epithelium model by Eriksson et al., the epithelium was reduced into two plasma membranes, giving a good approximation of this extremely thin epithelium with large cells[291]. The epithelium has also been described in even more detail, for example, for cornea, skin, lungs, or intestinal models[91,93,292–294]. These models usually define the permeabilities of various barrier components based on the solute's physicochemical properties and the structure of the barrier components. For example, plasma membrane permeability can be calculated based on the partition coefficient and the size of the solute[295]. On the other hand, the pores and the lateral space in the paracellular pathway are usually described by so-called Renkin-type functions, which relate the molecule size with the dimensions of a pore or a slit[296,297]. As analogs to electrical circuits, the permeabilities of these barrier components can be connected in series and in parallel to obtain the permeability of the whole barrier. This type of model can be defined without time-dependence, thus making them steady-state models[91,93].

Due to their importance as the barrier against the passive movement of ions and molecules across the epithelium, tight junctions have been the focus of some more detailed models. While many models describe these junctions only by a simple Renkin function with one pore size[30–32,93,298], more detailed models also exist. Guo et al.[33] represented the tight junctions with a combination of small static pores and slits to account for the pore and leak pathways, respectively. In addition, there are a few claudin-level models of the electrical barrier formed by the tight junctions. Yu et al. built an ion diffusion model through a claudin-2-based channel to understand the properties of these channels[54]. By combining experimental and computational methods, they indicated the source of the charge selectivity in these channels. Also, after the revelation of the temporal dynamics of these channels, Weber et al. constructed models of the channel opening/closing dynamics to understand the experimental measurements better when the strand compartmentalization was taken into account[34,299]. Models of the role of the larger-scale structural strand dynamics are mostly lacking, a random-resistor-network-based model by Washiyama et al.[35] being the sole model. This model did not explicitly describe the resistor network but relied upon percolation analysis to simplify the system.

2.8.2 Models of epithelial mechanics

Since epithelial tissue is a common system to study tissue mechanics and organogenesis, a plethora of modeling methods have been utilized to model epithelial mechanics. While the modeling of epithelial mechanics is not as well established as that of some other tissues, it is a considerably more active field of research than epithelial barrier modeling.

As the epithelia consist of similar cell units, the individual-based methods are generally the method of choice used to study the interactions and mechanics between the cells and the evolution of the epithelial tissues. However, a few studies have described these tissues as a continuum without defining discrete cells. For example, Conte et al.[300] and Allena & Aubry[301] used FEM to study the development of the embryonic epithelium in *Drosophila melanogaster*. Interestingly, there are also a few studies that utilize cell-level FEM models to study cellular organization in epithelia[302,303].

The individual-based methods used to model epithelia differ mainly on how the cells are described and how the system is solved while primarily being based on the same basic principle: minimization of the total system energy[304]. Due to the flat nature of the epithelial monolayer, a common simplification is to represent the cells in two dimensions. The total system energy is usually increased by the cell properties such as area and perimeter differing from their desired values and by interaction energy between cells[305,306]. While most of these methods are not restricted to any uniform lattice, one common method, the Cellular Potts model, utilizes a square lattice. In this method, each cell contains several connected square lattice locations, and the system evolves by lattice locations changing between cells to minimize the system energy[305–307]. The Cellular Potts model has, for example, been used to model epithelial morphogenesis and wound healing[308,309].

In the lattice-free methods, the cells or their parts are represented by vertices and interactions between these vertices. The evolution of the whole system as a function of time is a combination of each cell aiming to decrease its energy to minimize the total system energy. These models are generally evolved using an ODE of the form

$$\eta \frac{d\boldsymbol{r}_i}{dt} = \boldsymbol{F}_{tot,i}, \qquad 3$$

where η is a damping coefficient, $\boldsymbol{r}_i$ is the position of vertex i, t is the time, and $\boldsymbol{F}_{tot,i}$ is the total interaction force affecting vertex i, which can describe a cell or a part of a cell, depending on the method. The direction of the total force vector is towards the direction that reduces the system energy, i.e.

$$\boldsymbol{F}_{tot,i} = -\nabla E_{tot,i}, \qquad 4$$

where $E_{tot,i}$ is the total energy of vertex i and $\nabla = (\partial/\partial x, \partial/\partial y)$ in two dimensions.

In the simplest of these lattice-free models, the center-based model, cells are represented by a single vertex in the middle of the cell[305,306]. The interactions between the cells are described as forces between these vertices defined by various methods[310]. Center-based models have, for example, been used to study cell migration in intestinal crypts and epithelial curvature[311–313]. Vertex models, one of the most popular methods, represent the cells by their tricellular vertices and lines between these points to form the cell boundaries[305,306]. Like the Cellular Potts model, the vertex models are generally based on minimizing energy originating from changes in the cell area, perimeter, or the interactions between the adjacent cells[314,315]. Vertex models are a typical method for studying properties of epithelial tissues, and especially their morphogenesis and migration[39,314–322].

Some methods use a more accurate representation of the cells. The subcellular element method describes a cell as a collection of connected vertices[323,324]. The internal cell vertices function as cell cytoplasm, providing pressure against cell compression, whereas the connections between vertices of different cells describe the cell-cell junctions. The interaction forces between vertices in the same cells and those in the adjoining cells are calculated, and the cell movement is solved by Eq. 3. The subcellular element method has been used, e.g., to study mitotic rounding of dividing cells in epithelia[40]. Jamali et al.[41] used a slightly different approach in their sub-cellular viscoelastic model: they explicitly used vertices to describe the cell nucleus connected to the membrane vertices to provide internal pressure. Furthermore, a model by Tamulonis et al.[38] eliminated the internal vertices but used an approach similar to the vertex model, where the cell aims to retain its area by applying a pressure force normal to the cell boundary that depends on the cell area. Since the model describes a cell only by its boundary as a closed polygon, it has been termed a boundary-based method. This model has been used to study gastrulation during embryonic development in *Nematostella vectensis* and *Clytia hemisphaerica*[38,325].

The lattice-free models described thus far are solved using numerical methods such as the Euler or 4th order Runge-Kutta to provide the vertex locations in the next time point. However, a method called the immersed-boundary method takes a different approach to solving the system. In this method, a cell is described by closed polygons similar to the boundary-based method, but the system is solved by transferring the forces affecting the polygon vertices into an imaginary fluid, whose flow is solved, and the fluid movement is translated back to the movement of the vertices[326–329]. This method naturally maintains the cell area due to the fluid incompressibility but can also shrink or grow cells with fluid sinks or sources within the cells[328]. The immersed-boundary method has been used to model epithelial acinus and tube formation, tumorous growth, and cell organization[36,37,328,330–332].

Usually, the interactions between the vertices in these models are described by linear springs. The elastic behavior created by these springs gives a good approximation of biological tissues over short periods. However, it ceases to work for sustained deformations since tissues can dissipate stress in multiple methods. This dissipation can be modeled in many ways. For example, new vertices can be added for cells under stretch to divide stretched springs into two, or the rest length of the springs can be increased. Another approach is to use a dashpot in series with the spring to introduce the viscous behavior into the interactions.

Moreover, cells are not passive viscoelastic materials, but they actively move, reorganize, and divide. These active processes can be incorporated into the models as rules that govern the cell behavior. For example, to grow and divide a cell, the desired apical area can be doubled, and following the cell reaching this area, the cell is divided into two along a chosen division axis.

The ECM under the cells is not usually explicitly included in the models but can be considered to be taken into account in the damping coefficient to slow down the cell movements. In cross-sectional models of acini and ducts, the ECM has been modeled as a flexible boundary that the cells could link with[36,37,41]. In a vertex model by Schaumann et al.[321], the ECM was represented by a spring-connected network of points to which the cell vertices were connected by links describing the focal adhesions. The movement of this network of points can be solved using similar methods as the cell-based models, i.e., Eq. 3 and numerical methods.

3 AIMS OF THE STUDY

This thesis aimed to improve our understanding of the biophysical aspects of epithelial physiology by using computational modeling.

Specific study aims were

1. To indicate and parametrize the main passive barrier-forming components in epithelial tissue barriers (Studies I and II)

2. To study how the temporal dynamics of the tight junction barrier affect the measured barrier properties (Study II)

3. To improve experimental transepithelial electrical measurements (Study III)

4. To examine how the stiffness of the substrate affects the ability of epithelial cells to signal mechanically (Study IV)

4 MATERIALS AND METHODS

In this chapter, I will present the methods and models used in the studies of the thesis. These include the models of the BRB permeability, the tight junction barrier, the transepithelial electrical measurement system, and the epithelial biomechanics.

4.1 Summary of the models

The models created in each of the four studies in the thesis are summarized in Table 2, indicating the methods utilized and sources of experimental data used to build them.

Table 2. Summary of the models in the studies

	Methods	**Sources of data**
Study I	I built a steady-state model of the BRB permeability by combining the individual barrier component permeabilities in parallel and in series. The components were parameterized based on their geometry and the permeating molecules by size and lipophilicity.	The model parameters were either obtained directly from or estimated based on literature data.
Study II	I created a model to study the structural dynamics of the tight junction barrier that is composed of two components: molecular permeability and TER models. The permeability was modeled with a multi-compartmental approach with dynamic rate constants to describe the structural dynamics, whereas a network of dynamic resistors formed the electrical resistance model.	The parameters were obtained directly from the literature or were fitted based on experimental literature results.
Study III	I used a FEM-based model to describe a transepithelial resistance measurement system enabling the detailed description of the system and the positioning of the electrodes. The epithelium was represented by an equivalent resistor-capacitor system with known electrical properties. The model was used to calculate measurement sensitivity.	The model dimensions and the electrical properties of the epithelial tissue were based on manufacturer information and on the literature data.
Study IV	I developed an individual-based epithelial model to study the effect of the stiffness of the underlying substrate on the epithelial mechanics. The cells were described by closed polygons and the substrate by a hexagonal grid of points. The cell processes and structures were translated into forces that acted on the cell vertices and substrate points, and the system was evolved according to the total forces on each vertex and point. The model was used to grow an epithelium and investigate the effect of substrate stiffness on force transduction in the epithelial monolayer.	We conducted experiments with local mechanical stimuli to provide data to estimate the model parameters. Data from the literature was used for parts of the model.

4.2 Blood-retinal barrier permeability model (Study I)

In Study I, I developed a model to describe the permeability of the outer blood BRB as a function of the properties of the diffusion molecules to indicate the major components in this tissue barrier. The model described the interactions between the diffusing molecules and the various barrier components to provide separate permeabilities for each component. This model was based mainly on the work by Edwards & Prausnitz[93], who constructed a similar model for the corneal permeability barrier. While the model's approach was mechanistic, meaning that the aim was to describe the system as much in detail as possible, many of the equations used to describe the component permeabilities had been derived by fitting, i.e., a phenomenological approach. The model was created using Matlab (R2012a, Mathworks Inc, Natick, MA, USA).

4.2.1 Simplification of the blood-retinal barrier

The model was first divided into three components based on the three-part structure of the outer BRB: the RPE, the Bruch's membrane, and the choriocapillaris endothelium. The molecules were modeled to diffuse from the blood flow into the neural retina, first across the choriocapillaris endothelium, followed by the Bruch's membrane and the RPE. The schematic idea of the model is presented in Fig. 7.

The RPE was divided into two major permeation pathways: the paracellular and the transcellular. Following the model by Edwards & Prausnitz[93], the latter was further divided into two different permeation mechanisms, named transverse and lateral. The five-layered Bruch's membrane was simplified into a two-layered ECM with collagen and proteoglycan fibers. The choriocapillaris endothelium was reduced into circular fenestrations located in the endothelial wall.

Due to the serial order of these components, the total permeability could be calculated similarly to the serial connection of three conductivities, i.e.:

$$\frac{1}{P_{BRB}} = \frac{1}{P_{CE}} + \frac{1}{P_{BrM}} + \frac{1}{P_{RPE}}, \qquad 5$$

where P_{BRB} is the total BRB permeability, P_{CE} is the choriocapillaris endothelium permeability, P_{BrM} is the Bruch's membrane permeability, and P_{RPE} is the RPE permeability. Next, I will describe the individual components model in more detail.

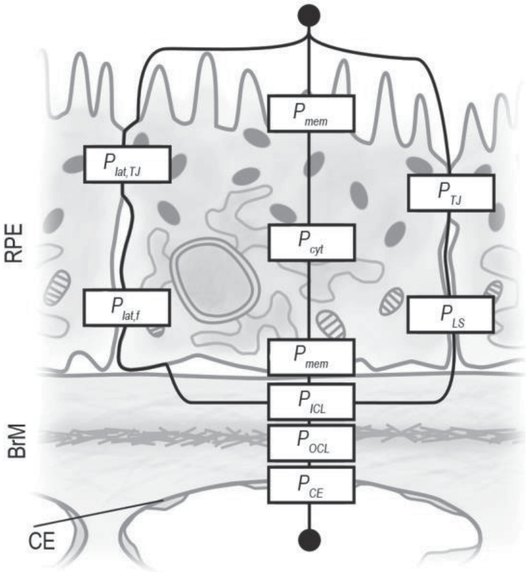

Figure 7. A schematic view of the main model components in the pathways in the outer BRB model. The paracellular pathway through the retinal pigment epithelium (RPE) consisted of the permeability of the lateral space (P_{LS}) and the tight junctions (P_{TJ}). The transverse transcellular pathway through the RPE included twice the permeability of the membrane (P_{mem}) and that of the cytosol (P_{cyt}). The final pathway through RPE, the lateral transcellular pathway, was described by a free component ($P_{lat,f}$) and tight junction component ($P_{lat,TJ}$) permeabilities. The Bruch's membrane (BrM) included the permeabilities of its inner and outer collagenous layers (P_{ICL} and P_{OCL}, respectively). The choriocapillaris endothelium (CE) was described by a single permeability component (P_{CE}). Reprinted with permission, Ref. 333 © Springer Nature.

4.2.2 Model of the retinal pigment epithelium

The RPE permeability was divided into three components: 1) The paracellular pathway of the RPE described the diffusion of the molecule in the paracellular space between the cells and through the tight junctions; 2) the transverse transcellular pathway modeled the movement of molecules through the cells by traversing the apical and basal plasma membrane and the cytoplasm; and 3) the lateral transcellular pathway considered the case in which a molecule would partition into the plasma membrane and diffuse within the membrane around the cell cytoplasm (see Fig. 7). The combined RPE permeability was calculated based on the parallel connection between the pathways:

$$P_{RPE} = P_{para} + P_{trans,tr} + P_{trans,lat}, \qquad 6$$

where P_{para} is the paracellular permeability, $P_{trans,tr}$ is the transverse transcellular permeability, and $P_{trans,lat}$ is the lateral transcellular permeability. The permeability of each pathway is calculated based on existing equations of diffusion through each kind of environment.

The paracellular space is described as a narrow slit, and the diffusion is hindered by the molecule's interactions with the slit walls by a Renkin-type equation. Unlike in the model by Edwards & Prausnitz[93], the tight junctions were divided into the pore and the leak pathways, the first of which was modeled as a series of circular pores through a number of horizontal strands and the latter as a slit narrower than the paracellular space. The circular pores were modeled similarly to the slits with a Renkin-type equation for circular holes. The paracellular model only depends on the size of the molecule.

The transverse transcellular permeation consisted of three phases: permeation through the basal plasma membrane, diffusion across the cytoplasm, and permeation through the apical plasma membrane. The membrane permeability was calculated as a combination of size- and lipophilicity-dependent equations, and the cytoplasmic diffusion was based on the observed hindered diffusion with an observed proportionality constant of 0.25 compared to free aqueous diffusion[334]. Two processes described the lateral transcellular permeability: partitioning of the solute into the membrane, followed by the diffusion in the membrane around the cell. The membrane diffusion is hindered at the tight junctions by their fence function. This pathway is highly dependent on both the size and lipophilicity of the molecule.

4.2.3 Models of the Bruch's membrane and the choriocapillaris endothelium

The two serially connected layers of the Bruch's membrane to be modeled were described to compose of tubular fibers in two different size scales: larger fibers for type-I collagen and smaller ones for proteoglycan. Since the molecules were assumed to diffuse in an aqueous environment, only their size affected their permeability.

The fenestrations in the choriocapillaris endothelium were described by their number and the diaphragm structure blocking part of the fenestration. Since they are actual holes through the endothelium, and thus there are no plasma membranes to be permeated, only the size of the molecule was considered to affect their permeability.

4.2.4 Parameters of the blood-retinal barrier model

The model parameters were obtained from various sources. For example, parameters such as the cell dimensions, height and number of horizontal strands in the tight junctions, the thickness of the Bruch's membrane, and the density of the choriocapillaris endothelium fenestrations were determined based on imaging data. Some parameters, however, had to be estimated. These included the fiber volume fractions in the layers of Bruch's membrane and, most importantly, a constant describing the relative amount of strand openness, i.e., the leak pathway. The magnitude of this leak parameter was obtained by fitting the model to the level of solute permeabilities in the experimental results. The values of all the parameters used in the model are presented in Study I.

4.3 Tight junction barrier model (Study II)

To better understand the role of one of the essential components in the epithelial barrier, the tight junctions, I built a model in Study II to describe how these dynamics structures govern the molecular permeability and the TER measurements. The dynamics were described as breaking and resealing of the bicellular strands. The model described the permeability and the TER measurements in separate models but using the same geometry and strand dynamics. The permeability model concentrated on the leak pathway, and the molecule chosen to describe this pathway was a 547-Da PEG, whereas the TER model included both the pore and leak components. The pore pathway was omitted from the permeability model since it has already been quite well established. The model was created using Matlab (R2015b).

4.3.1 Simplification and assumptions of the dynamic tight junction structure

In the model, the tight junctions were described by two components: the large pores at the tricellular junctions and the bicellular strand network in a two-dimensional plane between the cells. The natural strand network was reduced to a regular overlapping grid of rectangles (Fig. 8), and the strand breaking and resealing dynamics were incorporated on the strands, i.e., the boundaries between the rectangles. An intact strand, or a boundary, between two compartments could form a break with a probability of p_{break}, and a strand with a break could reseal with a probability of p_{seal}. The size of the cells was incorporated into the model as the density of tricellular points and the length of cell boundaries per area.

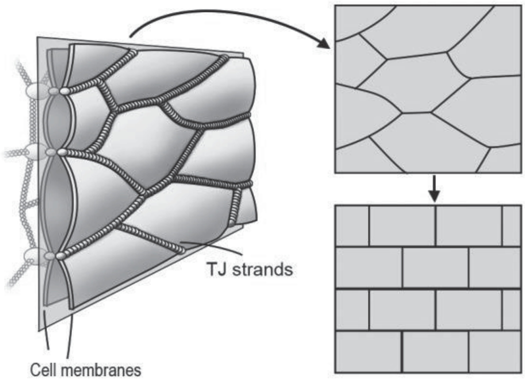

Figure 8. The strand network between the cells was simplified into a 2D plane, further reduced to the tiled rectangular compartment system lined by the tight junction strands used in the model. Figure adapted from Ref. 47.

4.3.2 Molecular permeability component of the tight junction model

The two components of the tight junctions in the molecular permeability model were simulated separately. The tricellular pores were modeled using a Renkin-type equation as a steady-state system and solved as a steady-state model.

The bicellular strand network permeability was calculated based on the multicompartmental modeling approach. The compartments in the model were lined by the tight junction strands in addition to the large apical and basal compartments above and below the strand network (see Fig. 9A). The system was solved based on the equation

$$\frac{dq_i}{dt} = \sum_j \left(k_{j,i}(t)q_j - k_{i,j}(t)q_i\right), \qquad 7$$

where $k_{i,j}(t)$ is the time-dependent rate constant between two compartments i and j. The strand breaking dynamics were incorporated into these rate constants. Their value is nonzero only when the strand between the compartments i and j has a break, and the strand state changes based on the probabilities p_{break} and p_{seal}. This allowed a stepwise solute diffusion through the strand network. The simulations were conducted with a known basal concentration, and the permeated concentration in the apical compartment was monitored. A system size of 50 small compartments wide was used in the simulations, and the simulations were run 512 times for each case to average the permeability over a larger area of the epithelium. Finally, based on the average amount of solute in the apical compartment, the permeability was calculated with Eq. 1.

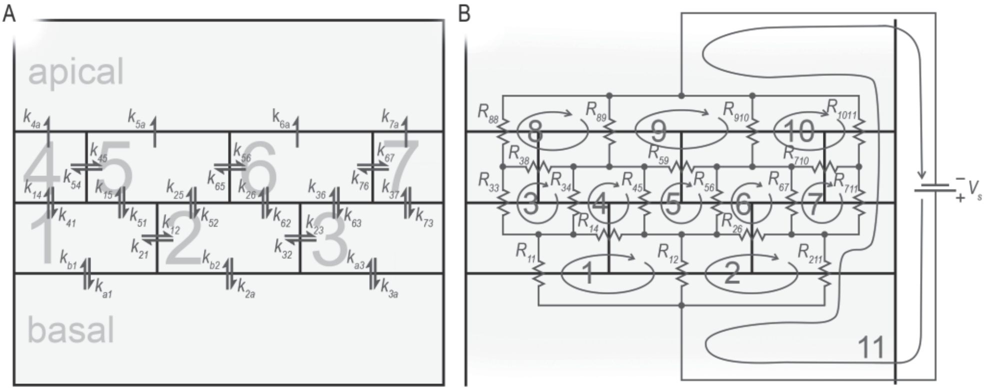

Figure 9. Schematic descriptions of the molecular permeability and the TER models. An example geometry of the system with three horizontal strands and three compartments in the bottom row. A) The strands line the space into small compartments (numbered 1–7), located between the large basal and apical compartments. Dynamic rate constants k_{ij} describe the rate of permeation from compartment i to j. Due to the assumed low concentration in the apical compartment, there was no diffusion back from the apical compartment. B) The TER model was built over the same geometry, but the model was described based on current loops that form into the strand network as shown (numbered 1–10). Dynamic resistances R_{ij} in the loops describe the resistance of a length of strand between two compartments and the voltage source (V_s) in the outer current loop (number 11). Reprinted from Ref. 47.

Due to the parallel connection between the tricellular and the bicellular pathways, the final permeability could be calculated with equation

$$P_{TJ} = P_{tTJ} + P_{bTJ}, \tag{8}$$

where P_{TJ} is the tight junction permeability, P_{tTJ} is tricellular pore permeability, and P_{bTJ} is the bicellular strand network permeability.

The molecular properties of the 547-Da PEG molecule needed in the model were the radius and free diffusion coefficient. Both were derived from its molecular mass based on fitted phenomenological equations.

4.3.3 Transepithelial electrical resistance component of the tight junction model

Like the molecular permeability model, the barrier components were simulated separately in the TER model. The tricellular pores were described by simple static resistors with known dimensions and resistivity.

The bicellular part of the model was constructed as a dynamic system of resistors to represent the dynamic strand resistance due to the strand breaking behavior. Since the system consists only of time-dependent resistors whose value changes instantly and thus the system of current loops (See Fig. 9B) can be described as a simple linear system with the equations of the form

$$\sum_j R_{i,j}(t)I_i - \sum_j R_{i,j}(t)I_j = \begin{cases} V_s, & \text{if the outer current loop} \\ 0, & \text{otherwise} \end{cases}, \qquad 9$$

where $R_{i,j}$ is the resistance of the section of a strand shared by current loops i and j, I_i is the current in the current loop i, and V_s is the outer current loop voltage.

The resistance of intact strands was assumed to be unchanging since the claudin channel dynamics are not visible in normal TER measurements, and they would not provide additional information on the epithelial level. While the TER measurement itself is almost instantaneous, the system was simulated for 10^6 seconds to describe the effect of the strand dynamics. Therefore, each time point can be thought of as a different section of junctions within the whole epithelium.

The total epithelial TER was then calculated based on the parallel connection between the two resistance components:

$$TER(t) = \left(\frac{1}{R_{tTJ}} + \frac{1}{R_{bTJ}(t)}\right)^{-1}, \qquad 10$$

where R_{tTJ} and R_{bTJ} are the tricellular and the bicellular resistances, respectively. Finally, an average over time was taken to obtain the total TER value.

4.3.4 Parameters of the tight junction model and model fitting

The models were fitted to data from the literature to quantify the properties of the tight junctions in chosen experimental measurements from the literature. The model parameters were mainly taken directly from the literature or estimated from figures. The values of the parameters directly related to each experimental measurement data, i.e., the density of the tricellular pores and the lengths of cell boundaries per area, the strand break forming probability, p_{break}, and the resistance of the intact strand, R_{strand}, were defined based on the provided experimental imaging, permeability and TER data for each measurement. The values of the parameters used in the tight junction model are described in Study II.

The density of the tricellular pores and the lengths of cell boundaries per area were defined from images of epithelia with their boundaries shown by immunofluorescence using ImageJ Fiji[335]. The break forming probability was obtained by iteratively fitting the molecular permeability model to the experimental permeability data, followed by fitting the TER model to the measured TER values by varying the strand resistance parameter.

4.4 Transepithelial electrical measurement system model (Study III)

In Study III, I described a model of TEZ measurement of epithelial tissue in a well plate insert using a 4-electrode setup. It was used to describe the measurement system's sensitivity of different electrode placements in relation to the epithelium. I created the model using the finite element method with COMSOL Multiphysics® (v5.2a, www.comsol.com, COMSOL AB, Stockholm, Sweden).

4.4.1 Definition of the measurement system model

The model geometry is composed of two aqueous chambers described by two end-to-end cylinders and the epithelial tissue as the boundary between the cylinders. The four electrodes were represented by smaller cylinders, two on each chamber, whose surface boundaries were used for the voltage measurement or the current injection. The geometry is shown in Fig. 10.

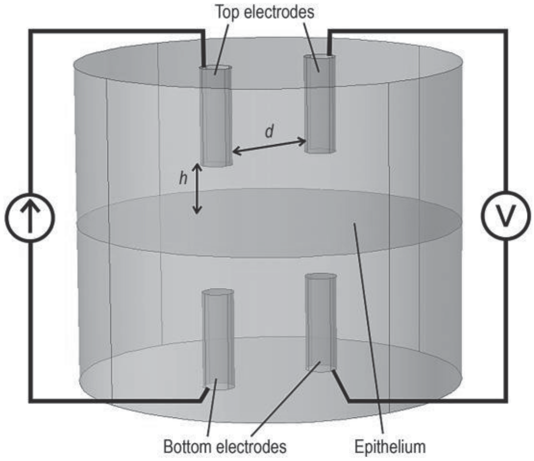

Figure 10. The geometry of the electrical measurement system model. The geometry consisted of end-to-end cylinders describing the measurement system's two compartments with the epithelium in between. The two pairs of electrodes for current injection and voltage measurement are shown above and below the epithelium. Parameters *h* and *d* describe the electrode distance from the epithelium and the electrode-to-electrode distance, respectively. Reprinted with permission, Ref. 336 © Springer Nature.

The governing equation in the model was Laplace's equation, i.e.:

$$(\sigma + i\omega\varepsilon_0\varepsilon_r)\nabla^2 V = 0, \tag{11}$$

where σ is the medium conductivity, ω is the angular frequency, ε_0 is the vacuum permittivity, ε_r is the relative permittivity, and V is the electrical potential. The epithelial electrical barrier properties were described by an equivalent circuit with resistor and capacitor in series whose values were obtained from the literature[122]. The electrode boundaries were described using Neumann boundary conditions with a unit current for the current injection electrode and Dirichlet boundary condition with 0 V for the ground electrode. The surface probes were used on the measurement electrodes to measure the potential difference across the epithelium. The outside boundaries of the model were fully insulated. To model impedance, the frequency of the injected current was varied.

4.4.2 Calculation of the sensitivity distribution

To calculate the measurement sensitivity distribution of electrode placement, the current – or so-called lead – field of both the current injection and voltage measurement electrode pairs were first defined by injecting a unit current through each pair separately. Then, the dot product of these two lead fields was calculated as the epithelial boundary to obtain the sensitivity distribution:

$$S = J_{LI} \cdot J_{LE}, \tag{12}$$

where S is the sensitivity, J_{LI} is the lead field produced by the current injection electrodes, and J_{LE} is that of the voltage measurement electrodes[337].

4.4.3 Parameters of the measurement system model

The main material parameters needed in this model were the resistive and capacitive properties of the epithelium as well as the resistivity and the relative permittivity of the fluid on either side of the epithelium. The values of these parameters were based on the literature, and I used values measured from the human embryonic stem cell derived RPE[122] for the tissue properties. Values such as the input current were arbitrary since they did not affect the results. The parameter values are described in Study III.

4.5 Epithelial mechanics model (Study IV)

In Study IV, I developed an individual-based model to study the effects of the ECM stiffness on the transduction of forces in the epithelial monolayer. The model development was conducted in tandem with experimental work with MDCK II epithelia. The model was used to simulate the effect of a pointlike movement of a single cell on the cell displacement and deformation in the epithelia. A natural-looking epithelium was virtually grown from a single cell using random cell areas and times between divisions to provide variability between the epithelia. Data from our micromanipulation measurement with MDCK II cells and the literature was used to obtain the model parameters. The model was created using Matlab (R2021a), together with a graphical user interface (GUI) for the simulations and analysis of the results. The experimental methods are described only briefly since my role was model development and simulations.

4.5.1 Experimental methods to study local epithelial deformation

The MDCK II cells were transfected with mEmerald-occludin to enable the fluorescent imaging of the cell boundaries. The epithelia were cultured on collage-coated polyacrylamide hydrogels, which could be made with different stiffnesses. Furthermore, the hydrogels were embedded with fluorescent microbeads whose movement could be imaged concurrently with the occluding-Emerald.

To study the pointlike micromanipulation, a sharp pipette attached to a programmable micromanipulator was used to penetrate the apical surface of a single cell to a level below the junctions. Next, the micromanipulator was used to move the penetrated cell a given distance (Fig. 11A). The deformation of both the cells and the hydrogel was live imaged during the measurement.

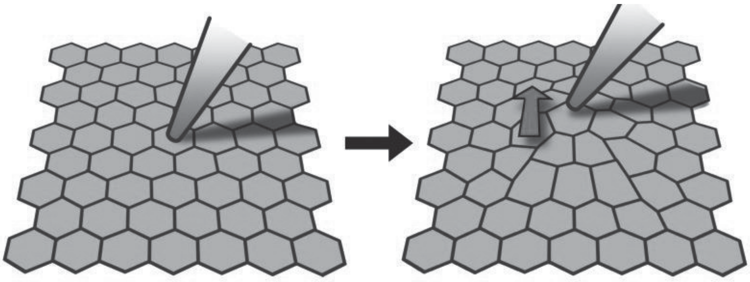

Figure 11. A pipette was used to move a cell a given distance to produce a local mechanical change in the epithelium.

The cell image data was segmented with the Trainable Weka segmentation plugin in ImageJ Fiji[335]. The deformation of the segmented cells was analyzed with a custom Matlab script. The hydrogel deformation was analyzed using the particle image velocimetry analysis tool in Fiji.

4.5.2 Description of the epithelial mechanics model

The model was based on the existing cell-level boundary-based model by Tamulonis et al.[38] and also borrowed aspects from the vertex models[315,316]. In the model, the cells are represented by their cell membranes as closed two-dimensional polygons. While the model by Tamulonis et al. [38] described the cells in two dimensions from their side showing the apicobasal axis, our model used the more common point of view of the apical surface used in the two-dimensional vertex models (Fig. 12A). However, the cell membrane was discretized with finer resolution than in the vertex model, and cells were connected via intercellular interactions, unlike in the vertex model.

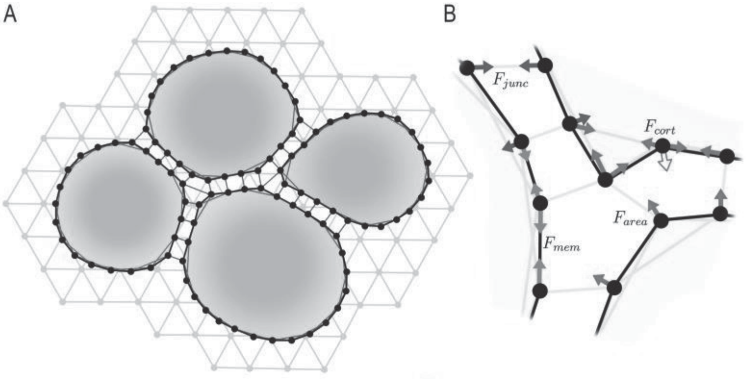

Figure 12. A) Description of the epithelial mechanics model. The cells were described by closed polygons to represent the cell membrane. The cellular structures and processes are described by interactions between the polygon vertices, of which the actomyosin cortex (red lines) and cell-cell junctions (blue lines) are shown. The underlying substrate is modeled as a triangular grid, and the mechanical properties are incorporated into the interactions between the grid points. The cell polygons and the substrate are connected via focal adhesion interactions (not depicted here). B) Example of forces that determine the movement of the cell vertices: cell-cell junction forces (F_{junc}), cortical forces (F_{cort}), membrane forces (F_{mem}), and intracellular pressure or area force (F_{area}). Note that the forces are presented only for some vertices for simplicity. All forces, including those that are not shown here, affect the appropriate vertices.

The model evolves by incorporating the cell structures, processes, and movement into forces acting on the polygon vertices. The underlying substrate, natural or synthetic, is simplified into a two-dimensional triangular grid (Fig. 12B), to which the vertices of the cell polygons are attached to describe the focal adhesions. The mechanical properties of the substrate are incorporated into the interactions between the grid points.

The model is evolved by moving the cell polygon vertices and substrate grid points based on the total force originating from the various interactions by solving the dampened equations of motion:

$$\eta \frac{d\boldsymbol{r}_i}{dt} = \boldsymbol{F}_{i,tot}, \quad 13$$

$$\eta \frac{d\boldsymbol{s}_m}{dt} = \boldsymbol{F}_{m,tot}, \quad 14$$

where η is the damping coefficient, $\boldsymbol{r}_i$ and $\boldsymbol{s}_m$ are the positions of the cell vertex i and substrate point m, respectively, and $\boldsymbol{F}_{i,tot}$ and $\boldsymbol{F}_{m,tot}$ are the corresponding total forces affecting the vertex i and the point m. The system of equations of motion was solved by using 2nd or 4th order Runge-Kutta solution methods with variable time steps.

The forces included in the $\boldsymbol{F}_{i,tot}$ depend on the type of the simulations and can include forces describing cell cortical tension, intracellular pressure, cell-cell junctions, focal adhesions, cell membrane elasticity, cell division, and contact between cells. Some of these forces are depicted in Fig. 12B. The total substrate forces $\boldsymbol{F}_{m,tot}$ include the elasticity of the material and the focal adhesions. The forces are mainly calculated by describing the structures and interactions by elastic spring. Unlike in the model by Tamulonis et al., the number of cell vertices is not constant, but they can be added or removed when required. Similarly, the cell-cell junctions are dynamic, enabling cells to change their neighbors and thus move among the other cells.

4.5.3 Parameter fitting and simulations of the epithelial mechanics model

The parameters related to the initial growth and division were estimated mainly based on the time scales of the different phases of the cell cycle. The cell apical area distribution in the virtual epithelium was defined based on the experimental MDCK II data. To remove any residual stresses in the grown epithelia, they were relaxed before the mechanical simulations with a smaller damping coefficient.

In the micromanipulation simulations, a single cell was moved by a virtual micromanipulator the same distance as in the experiments. These simulations were run with substrates having the stiffnesses used in the experiments, and the simulation results were compared to the experimental data to fit many of the model parameters. The fitted model was then used to study micromanipulation on substrates with stiffness interfaces to study their effect on the propagation of intercellular forces.

The parameter values for cells and those related to each of the different simulation cases are presented in Study IV.

5 RESULTS

The results are presented based on the aims of the thesis. First, the main components of the epithelial tissue barriers are presented, followed by the results regarding the effects of tight junction structural dynamics on the measured barrier properties. Next, I go through the main results of the impact of electrode positioning on transepithelial electrical measurements. Finally, I will present the results showing the effect of substrate stiffness on the propagation of forces in the epithelium.

5.1 Governing components of tissue barriers (Studies I and II)

I will first present the results of the main barrier components regarding the outer BRB, followed by the analysis of the main components of the leak pathway in the tight junctions.

5.1.1 Permeability components of the outer blood-retinal barrier (Study I)

To study the governing barrier components against transepithelial molecular permeation, I used the model described in section 4.1 for the outer BRB. Since all the three components of the outer BRB were connected in series, the one with the lowest permeability governed the total permeability. As expected, the results indicated that the epithelial component of the outer BRB, the RPE, formed the main barrier against molecular permeability from blood circulation to the retina through the back of the eye within the range of the simulated molecular properties (Fig. 13A and B). The second most important component was the Bruch's membrane, with the final component, the choriocapillaris endothelium, having a negligible impact on the combined permeability. The permeability of RPE remained approximately three orders of magnitude lower for large and hydrophilic molecules, whereas the difference was approximately only one order of magnitude for small hydrophilic molecules.

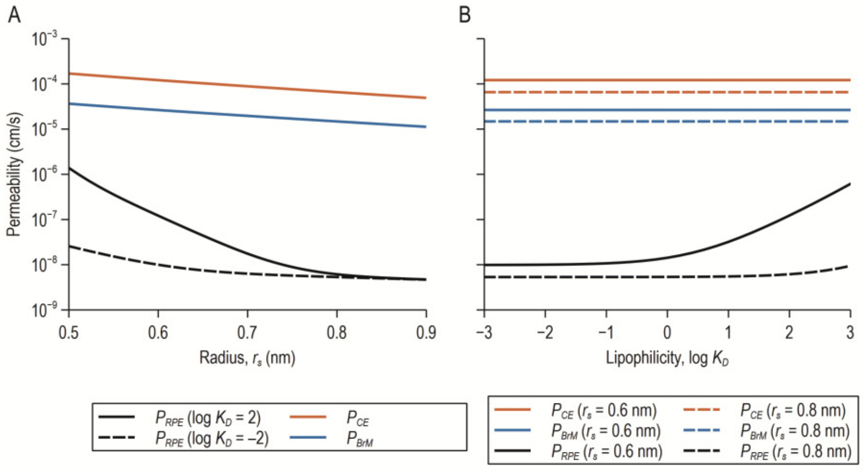

Figure 13. The permeabilities of the components of the outer BRB as a function of solute properties. A) The permeabilities as a function of solute radius for two lipophilicity values (2 and –2), and B) as a function of solute lipophilicity for two solute radii (6 and 8 nm). P_{RPE}, retinal pigment epithelium permeability; P_{BrM}, Bruch's membrane permeability, P_{CE}, choriocapillaris endothelium permeability.

Within the RPE, the permeability was divided into paracellular, transcellular transverse, and transcellular lateral components, as described in section 4.1.2. Since these components are connected in parallel, the most permeable component mainly defines the total RPE, and therefore the outer BRB, permeability. The relative importance of these components was highly dependent on the molecular radius (r_s) and the lipophilicity (log K_D), as shown in Fig. 14A and B. The paracellular pathway was dominant for most simulated molecules, excluding small lipophilic molecules (high log K_D). In this pathway, the main component was the tight junctions, which therefore form the governing barrier against passive diffusion not only across the RPE but the whole outer BRB. The lateral transcellular pathway was more prominent of the two transcellular pathways for the range of molecular properties studied. The transverse pathway had higher permeability only for the smallest and most lipophilic molecules (r_s = 0.5 nm and log K_D = 3).

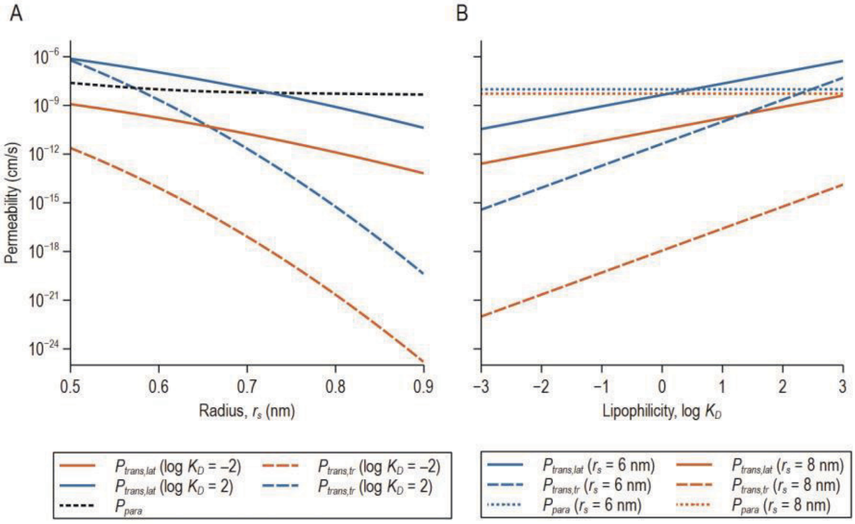

Figure 14. The permeabilities of the three RPE pathways, paracellular pathway (P_{para}), transcellular transverse pathway ($P_{trans,tr}$), and transcellular lateral pathway ($P_{trans,lat}$), as a function of solute properties. A) The permeabilities as a function of solute radius (r_s) for two lipophilicity (log K_D) values (2 and –2) and B) as a function of solute lipophilicity for two solute radii (6 and 8 nm).

Next, I studied the importance of model components by conducting a parameter sensitivity analysis on the most relevant parameters in the model. The parameters chosen for the analysis were predicted to be important based on the simulation results, i.e., the parameters describing the tight junctions or whose values were uncertain. The analysis indicated that the parameters that affect the RPE permeability the most were the radius of claudin-formed channels and the constant describing the relative amount of broken strands in the tight junctions, i.e., leak pathway.

5.1.2 The components of the tight junctions (Study II)

Based on the findings with the model of the outer BRB, a model to study the structure and properties of the tight junctions in more detail was constructed (see section 4.2 for more information). While the tight junction permeability has been shown to compose of the pore and leak pathways, this model concentrated on the latter since it is more poorly understood. In addition, the TER was included to complement the molecular permeability to fully describe the epithelial barrier measurements.

As described in section 4.2, I assumed that the leak pathway is formed by both the large tricellular pores and the bicellular strand dynamics. The model was fitted to experimental data on the cell size, molecular permeability, and TER from the literature. Our results indicated that these two components form the leak pathway with a varying degree for different epithelia. In addition, the role of these two components for the molecular permeability and TER was also different.

The tricellular tubes were found to be the source of 100 %, 40 %, and 33 % of the total leak permeability for MDCK C7, MDCK II, and Caco-2, respectively. On the other hand, the bicellular strand opening probabilities for the same epithelia were found to be 0.005, 0.036, and 0.47 μm^{-1} s^{-1}, thus indicating a correlation between the bicellular strand dynamics and their role in the total paracellular permeability. I also found considerable variability in the relative contributions of the tricellular tubes for the MDCK II from the four considered studies, ranging from 15 to 66 %. The obtained strand break probabilities, however, were found to be similar.

Next, I studied the role of tricellular and bicellular components in governing the TER measurement for the same epithelia. The tricellular tubes formed 52, 2.0, and 42 % of the total measured TER respectively for MDCK C7, MDCK II, and Caco-2. Here, the lower value indicates higher relative resistance of the tricellular tubes compared to the bicellular strands. The strand resistance values obtained from the model fitting were 10.62, 0.36, and 7.65 GΩ µm for the respective epithelia, showing a good correspondence between the relative role of the bicellular resistance and the strand resistance.

Thus, our model indicates that MDCK C7 has a low level of bicellular strand dynamics and high strand resistance, leading to both a tight barrier as measured both by molecular permeability or by TER. MDCK II is the opposite, having very dynamic strands and low strand resistance, leading to a leaky barrier based on both measurements. However, interestingly, Caco-2 exhibits both high strand dynamics and strand resistance, leading to an epithelium that seems leaky based on molecular permeability measurements but tight based on TER.

5.2 Effect of the strand dynamics on the barrier measurements (Study II)

The strand dynamics affect the molecular permeability and TER differently since the first is measured over hours and the latter in under a second. This difference was well indicated in the parameter sensitivity analysis of the parameters describing the bicellular strand dynamics. For MDCK II, with its higher-level strand dynamics, the changes in the break opening and closing probabilities led to considerably larger changes in the molecular permeability than in the resistance. Changes in the resistance of the strands led to an approximately same level of effect on the resistance as the changes in the break probabilities. This indicated that the resistance of the strands, i.e., the movement of ions through the claudin-formed channels, was as important as the strand dynamics for the resulting resistance. On the other hand, with already a low-level strand dynamics of MDCK C7, changes in the break probabilities did not affect the TER, whose bicellular component was entirely defined by the resistance of the strands.

The fact that the strand dynamics have a different effect on the molecular permeability compared to the TER became more evident at low levels of strand dynamics and when the number of strands was high. In the opposite situation – with high values of break probability or at low strand numbers – the continuous open paths through the strand network were very common. This is visualized for the TER in Fig. 15A, showing the coefficient of variation in the TER values as a function of time or – by assuming that each time point corresponds to a different section of bicellular junction within the epithelium – as a function of location. The high variability in the MDCK II results with low strand numbers was a direct outcome of the highly probable continuous paths through the strand network. However, as the break opening probability decreased and/or the number of strands increased, these paths became less likely, as indicated by the decreasing variability. The continuous paths were also somewhat common with two strands and the level of strand dynamics corresponding to MDCK C7, as shown by the higher variability compared to the higher strand numbers (Fig. 15A). However, while being extremely rate, these paths were also observed with the strand number of 3. Thus, with a low level of dynamics and high strand numbers, the bicellular resistance was defined mainly by the strand resistance since the horizontal strands in practice formed a series of resistors with a little effect from the strand dynamics.

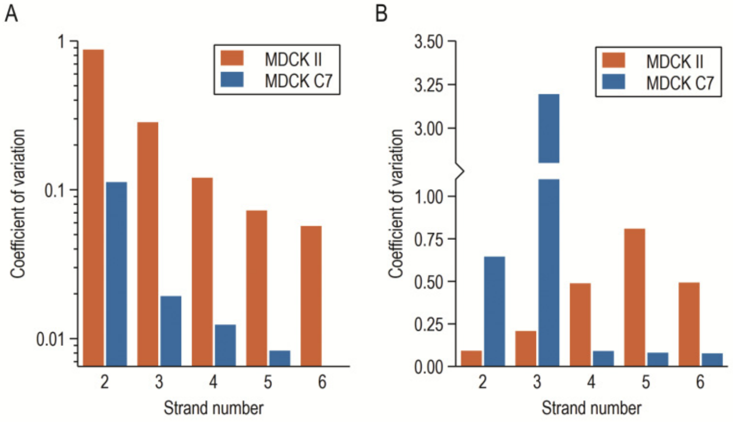

Figure 15. The coefficient of variation A) in the simulation data on the bicellular resistance components and B) between the individual permeabilities of the bicellular strand network for horizontal strand numbers 2 to 6 in MDCK II and MDCK C7. Note the broken y-axis in B.

The strand dynamics led to two distinct modes of permeability across the bicellular junctions as the breaks became rarer and/or as the strand number increased. This was highlighted by the variability between permeability simulations, as indicated in Fig. 15B by the coefficients of variation for the MDCK II and C7 levels of break probabilities and for strand numbers between 2 and 6. The common continuous open paths through the network, especially at high break opening probabilities and low strand numbers, led to a low variance between individual simulations due to one dominating permeation pathway. However, as the break probability decreased and the strand number increased, these open paths became rarer, and the step-by-step diffusion through the compartments became the dominant way of permeation. Thus, with these conditions, the variability between the individual simulations was low due to a single dominating permeability mechanism. Between these two extremes with low variance, there was a state in which both of these permeability methods contributed, leading to a high variance between the simulations, which can be explained by the large difference in the rate of permeation between the open path and the step-by-step methods. As shown in Fig. 15B, the highest variance for the high and low levels of the strand breaking dynamics, represented by the MDCK II and C7, occurred at strand numbers 3 and 5, respectively. Interestingly, the open paths with MDCK C7 with 3 strands were not visible in the variance of the TER in the same conditions.

To study the frequency and duration of the open paths through the strand network in detail, I calculated these values based on the bicellular resistance simulation data (Fig. 16). While the duration of a single break is determined by the static break resealing probability, the duration of the open path formed by a combination of breaks is more complex. With the strand number of 2, the open path durations were similar between the MDCK II and C7 and showed values in a similar range to those of a single break (Fig. 16A). It is important to note that the open paths were so common with the MDCK II with 2 strands that, most likely, the duration data has overlap between different open paths since they cannot be differentiated from the data. The average duration and the number of the open paths in the MDCK C7 dropped rapidly as the strand number is increased, and at strand number 4, there was only a single open path during the whole 10^6-second simulation (Fig. 16A). With MDCK II, the average duration plateaus around 3 seconds.

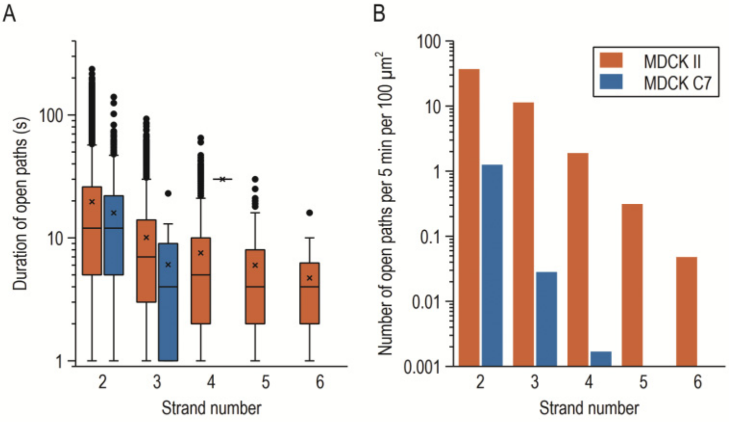

Figure 16. A) The duration of the open paths through the strand network for MDCK II and C7 as a function of the strand number. Please note that the minimum duration is 1 second due to the time stepping in the simulations. B) The number of the open path events during a period of 5 minutes in an area of 100 µm² for the MDCK II and C7 for the strand numbers 2–6.

A reduction in their number accompanied the decrease in the duration of the open paths. Taking the number of these paths during the simulations, the length of the simulated section of junctions, and the average MDCK junction length per area, I calculated the number of the open path events in an area of 10 × 10 µm² during the period of 5 minutes. This number is related approximately logarithmically to the strand number for both cell types (Fig 16B). Based on the standard strand number of 4, one would expect to observe around 2 of these events in this area during 5 minutes for MDCK II. With the same strand number, a single event would be observed on average every 52 hours with MDCK C7.

5.3 Effect of electrode positioning on transepithelial electrical measurements (Study III)

The finite element model of the TEZ measurement system was used to study how the positioning of the electrodes affects the measured impedance as well as the sensitivity distribution of the measurement, i.e., the section of the planar epithelium that affects the measured results the most (see section 4.4 for details). The changes in the electrode positions in our simulations did not affect the resulting TEZ values. We also studied if local defects would be visible in the simulated measurements. The simulated defects at different locations in relation to the electrodes produced identical TEZ values, indicating that the regular 4-electrode measurement system with electrodes millimeters away from the surfaces is not a viable option for studying local defects or variations in the epithelial barrier.

Interestingly, both the placement of the electrodes and the measurement frequency had a drastic effect on the measurement sensitivity distribution. The farther away the electrodes were from the epithelium, the more uniform the sensitivity was. In addition, there were areas with negative sensitivity values at low frequencies, indicating that small changes in the electrical properties in these areas would have the opposite effect on the measurement.

To better visualize the difference in the sensitivity distribution, a 2-electrode system, otherwise identical to the 4-electrode one, was simulated at different electrode heights. In this system, the two electrodes were located in the middle of the system, and they are used both for current injection and voltage measurements. Electrode impedance was not considered.

Results from these simulations for electrode heights of 1 and 4 mm are shown in Fig. 16. The sensitivity field concentrates near the electrode position when the electrodes are close to the epithelial surface (Fig. 17A). However, whereas at high frequencies, the spot of high sensitivity is directly below the electrode, at lower frequencies, the high sensitivity forms a ring around the center with a radius of around 1 mm. This ring results from the current density spreading to a larger area when the impedance of the epithelium is higher at low frequencies. At high frequencies, as the impedance decreases, the current density concentrates directly between the electrodes. When the electrodes are farther away at 4 mm from the epithelium (Fig. 17B), there is only a minor difference in sensitivity between the measurement frequencies and a function of the distance from the center point.

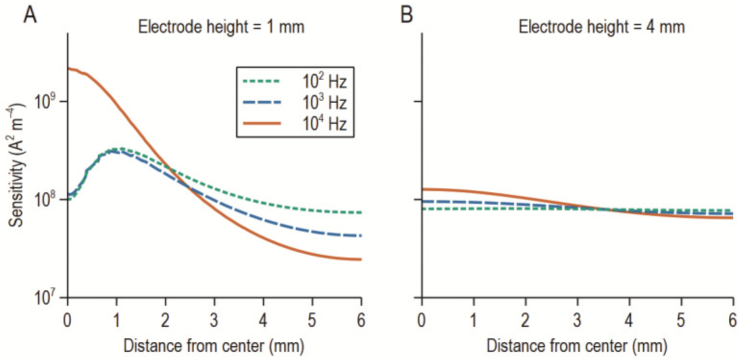

Figure 17. The sensitivity of a 2-electrode measurement setup on the epithelium as a function of distance from the center of the electrode and measurement frequency. The results are shown for two-electrode distances from the epithelium, A) 1mm and B) 4 mm.

5.4 Effect of substrate stiffness on force propagation in the epithelia (Study IV)

I constructed the model platform described in section 4.5 to study the propagation of forces in epithelial monolayers on the substrates with different stiffnesses. When moving a single cell, we observed that the displacement of the other cells in the monolayer was more restricted on the substrates with higher stiffnesses. This was reflected in the increases in the forces that described the cortical tension of the cells, the cell-cell interactions, and the cell-substrate interactions. While the maximum cell displacements were similar between the substrate stiffnesses, there were large differences in the maximum forces. When comparing the maximum forces between the softest 1.1-kPa substrate with those of the stiffest 11-kPa substrate, we observed 1.8, 2.1, and 1.3-fold increases in the cortical, junction, and focal adhesion forces, respectively. Even though the cell displacement was reduced at a long distance with the stiffer substrates, there were no apparent differences in the cortical or junction forces between the substrate stiffnesses at these distances. There was, however, a clear difference in the focal adhesion forces, which was higher on the stiff substrates.

We also investigated the effect of local increases and decreases in substrate stiffness on the propagation of forces between the cells. When there was an increasing stiffness gradient close by, the cortical and junction forces for the cells in the soft area between the mechanical stimulus and the gradient were increased. On the other hand, the focal adhesion forces remained low until close to the gradient, where their magnitude was 3.5 to 5-fold compared to normal values at this distance from the mechanical stimulus. Opposite effects were seen when the manipulated cell was on a stiff substrate: the cortical and junction forces were reduced until the interface, and the focal adhesion forces were relatively reduced around the interface itself.

We observed large differences in the cell and substrate displacements at similar locations in the simulations. This can be explained by the fact that the cells in the model describe their apical surface, and the substrate-binding focal adhesions were located on the basal side of the cell. Therefore, the substrate displacement approximately corresponded to that of the basal side of the cells, and the difference between the displacements implied the deformation of the cells in the apico-basal direction. The focal adhesion forces that described the connection of the apical cell vertices to the substrate points thus included both the mechanical properties of the focal adhesions and those of the cell in the apico-basal axis.

To study the relationship between the cell and substrate displacement in detail, I plotted the maximum cell and substrate displacements with different substrate stiffnesses against each other and calculated how their ratio changes as a function of cell displacement, as shown in Fig. 18. The substrate displacements were initially small compared to those of the cells, owing to the apico-basal deformation of the cells. Thus, minor displacements of the apical surface were not enough to visibly deform the substrate since the tension in the focal adhesions and in the apico-basal axis of the cells created a buffer between the two. With the softest 1.1-kPa substrate, the relative displacement increased with the increasing cell displacement and began to saturate at above 0.6. On the other end, the 11-kPa substrate saturated faster to a relative displacement of around 0.23, after which there was an apparent decrease in the relative displacement, indicating the cell detachment from the substrate. A similar reduction signifying the detachment could also be seen with the 4.5-kPa substrate, but only later. The cell detachment from the substrate was defined based on a limit focal adhesion force in the model. Here, it is seen that this limit force was reached at different amounts of cell-substrate displacement difference depending on the substrate stiffness. For the 4.5 and 11-kPa substrates, the maximum cell and substrate displacements differed by 9.1 and 7.9 μm near the point of detachment, respectively. This suggests that the cells on the softer substrates can deform more in the apico-basal axis before detaching from the substrate.

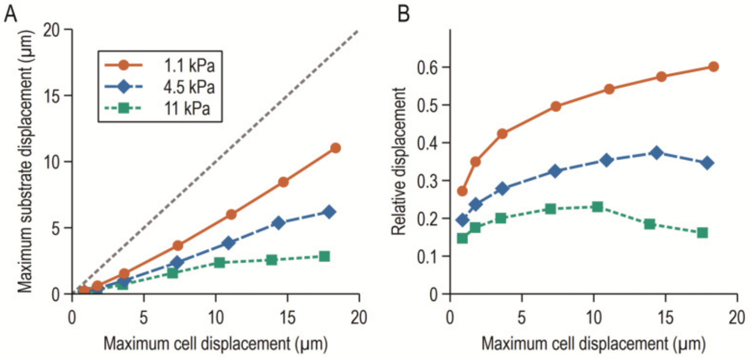

Figure 18. A) Maximum substrate displacement as a function of the corresponding maximum cell displacement for the substrates with stiffnesses 1.1, 4.5, and 11 kPa. The dashed line visualizes the 1-to-1 relationship. B) Relative displacement (maximum substrate displacement / maximum cell displacement) as a function of the corresponding cell displacement.

The developed epithelial mechanics modeling platform can be run from the Matlab command line using user-defined configuration files. However, I designed and programmed a GUI to make the platform easily approachable for less command-line-oriented users with a lesser programming background (see Fig. 19). The GUI was divided into two main parts: The simulation tab (Fig. 19A) and the results plotting and analysis tab (Fig. 19B).

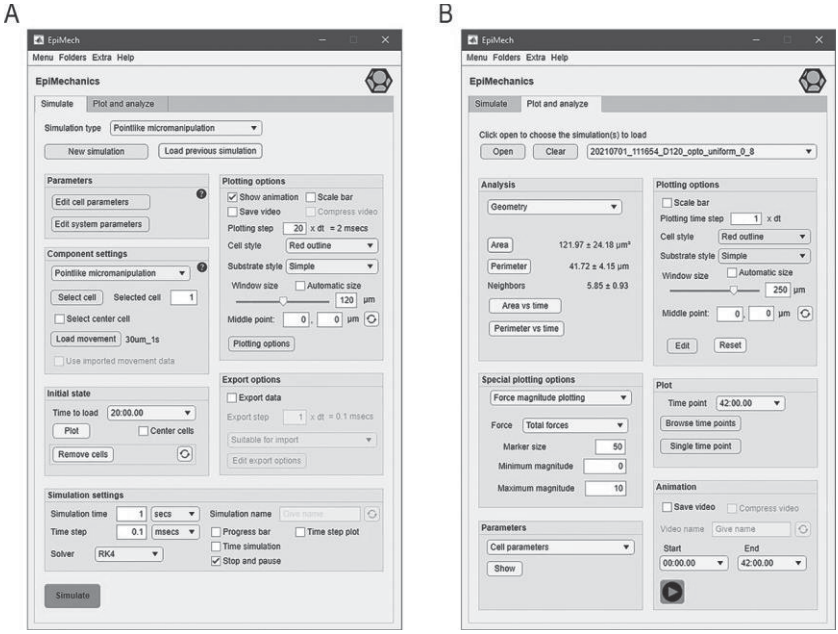

Simulation type: Pointlike micromanipulation
Component settings: Pointlike micromanipulation
Selected cell: 1
☐ Select center cell
Load movement: 30um_1s
☐ Use imported movement data
☑ Show animation ☐ Scale bar
☐ Save video ☐ Compress video
Plotting step: 20 x dt = 2 msecs
Cell style: Red outline
Substrate style: Simple
Window size: ☐ Automatic size 120 µm
Middle point: 0, 0 µm
☐ Export data
Export step: 1 x dt = 0.1 msecs
Suitable for import
Time to load: 20:00.00
☐ Center cells
Simulation time: 1 secs
Time step: 0.1 msecs
Solver: RK4
Simulation name: Give name
☐ Progress bar ☐ Time step plot
☐ Time simulation
☑ Stop and pause

20210701_111654_D120_opto_uniform_0_8
Analysis: Geometry
Area 121.97 ± 24.18 µm²
Perimeter 41.72 ± 4.15 µm
Neighbors 5.85 ± 0.93
☐ Scale bar
Plotting time step: 1 x dt
Cell style: Red outline
Substrate style: Simple
Window size: ☐ Automatic size 250 µm
Middle point: 0, 0 µm
Special plotting options: Force magnitude plotting
Force: Total forces
Marker size: 50
Minimum magnitude: 0
Maximum magnitude: 10
Time point: 42:00.00
Parameters: Cell parameters
☐ Save video ☐ Compress video
Video name: Give name
Start: 00:00.00
End: 42:00.00

Figure 19. The graphical user interface (GUI) of the epithelial mechanics model. The GUI is divided into two main components: the simulation tab (A) and the results plotting and analysis tab (B).

In the simulation tab, the user can edit model parameters and define settings related to the plotting and data export during a simulation. The user can begin a simulation from a single cell or load previous simulation data as the initial state for a new simulation. In addition, the loaded epithelium can be edited by removing cells, for example, if only a smaller epithelial area is needed.

In the plotting and analysis tab, the user can load previously simulated data for analysis. The GUI enables the visualization and animation of the cells and the substrate in various ways, as well as specific plotting options to visualize cell shapes using different shape descriptors, such as circularity and aspect ratio. In addition, the magnitude of each force affecting the cell vertices and the displacement of the cells and the substrate between two time points can be plotted.

6 DISCUSSION

This thesis aimed to better our understanding of the epithelial barrier properties and mechanobiology by creating new computational tools that provide platforms to complement and quantify experimental research. The models in Studies I and II concentrated on the identification of the main components in the epithelial barrier, whereas the model presented in Study III aimed to optimize electrical barrier measurement of epithelial tissues. Finally, the model created in Study IV investigated the relationship between the substrate stiffness and the propagation of forces between the cells.

6.1 Governing components in tissue barriers

The simulation results of the permeability barrier properties of the outer BRB indicated that the epithelial component in the barrier, the RPE, is the governing component in the three-part outer BRB. This was expected since this had already been shown in experimental studies when comparing the permeabilities of small molecules (radius < 1 nm) through isolated choroid-RPE and choroid-Bruch's membrane. However, the Bruch's membrane becomes a more relevant component against passive diffusion with age as it gains more thickness and its composition changes[118]. Together with the formation of the drusen, these changes have been linked to the limited availability of oxygen and nutrients in the RPE and the retina. These changes could decrease the BrM permeability to similar levels as that of the RPE since there is at a minimum only approximately one and a half order of magnitude difference between the two.

It was clear from the results that the choriocapillaris endothelium provides a little hindrance for diffusion from the blood circulation into the retina, which can be explained by the fenestrations through the endothelial cells. However, there are tissue barriers that include an epithelium and endothelium where the latter has a more essential role. In their theoretical study, Edwards & Prausnitz[93] found that the endothelium in the corneal barrier had a permeability of only around magnitude higher than the stratified corneal epithelium. This is in stark contrast to our results, which showed that the choriocapillaris endothelium is between two and four orders of magnitude more permeable than the RPE, depending on the molecular properties of the solute. Likewise, it has been shown that the gut endothelial cells in the intestine form a second line of defense for the intestinal epithelium by regulating the passive permeability of large macromolecules and preventing the invasion of microorganisms[338–340]. Furthermore, the role of the alveolar endothelium in the lung alveoli has been shown to have a barrier role comparable to the alveolar epithelium[341,342]. The role of the corneal, intestinal, and alveolar barriers differs from that of the outer BRB since they protect our bodies from the outside, whereas the outer BRB protects the neural retina from the threats already in the blood circulation. In addition, the high nutrient and oxygen requirements of the RPE and the neural retina could be impeded by the tighter barrier formed by the choriocapillaris endothelium.

Within the RPE, the results show that the paracellular pathway sets the rate-limiting component for most molecules. This was also reflected by the importance of the parameters describing the tight junction structure in the sensitivity analysis. Especially the parameter describing the leak pathway affected the permeabilities of all the test molecules similarly, indicating that it sets the base level for the permeability. This finding made us concentrate more on the barrier formed by the tight junctions, especially the leak pathway.

6.2 Source of the leak pathway

The source of the leak pathway has eluded researchers for many years. While the large pores in the tricellular junctions have been shown to contribute to the leak permeability of large macromolecules[28], this does not seem to be the sole pathway for smaller molecules that are still unable to pass through the claudin-formed pores. The results from the tight junction model showed that the permeability of the tricellular pores is not enough to explain the leak pathway permeability other than in the tighter epithelium. The results show that the stepwise diffusion through the strand openings can explain the missing permeability component for the epithelia with leakier junctions. While this pathway has been theorized[16,33,57,78,84], observing it experimentally is challenging due to the small size of the junctions and their location between the cells. Recently, Saito et al.[62] studied the effect of the knockout of tricellulin and occludin on the morphology of the tight junction strand network and on the permeability of dextrans. To relate these two experimental measurements, they utilized the model presented in Study II. They showed that tricellulin and occludin regulate the strand network morphology, which affects the macromolecule permeability, indicating the importance of this component on the leak pathway.

While the leak pathway concept was initially derived based on the observed molecular permeability, it is still worth discussing how these various candidates for the leak pathway affect the TER measurements. Krug et al. have calculated the relative contribution of the large tricellular pores to the paracellular resistance to be at the level of 1 % for the MDCK II cells, whereas for Caco-2, this value was as high as 25 %[28,343]. The corresponding contributions in our results were 2 % and 42 %. While the Caco-2 is higher than the one calculated by Krug, the results show agreement with the idea that the tricellular pore contributions differ between epithelia, and this role largely depends on the resistance of the bicellular strands. Since the strand dynamics were found to have only a minor effect on the TER, the bicellular strand seemed to form almost a series system of resistors.

Unfortunately, the last theorized candidate for the leak pathway, the transient bicellular tight junction barrier breaches observed by Stephenson et al.[20], was too recent to be included in the model presented in Study II. These breaches seem to form an additional pathway through the junctions, especially for the epithelia with low strand break opening probabilities.

In summary, the findings indicate that multiple components form the leak pathway. The relative roles of the suggested candidates differ between epithelia. In general, the tighter the bicellular junctions – be that lower level of strand dynamics or higher strand resistance – the more the tricellular pores contribute to the barrier properties. In addition, the results also show that the contributions of these suggested pathways are not directly connected between the molecular permeability and the TER, and thus both are needed to better describe the epithelial barrier in the most detail.

6.3 Tight junction strand dynamics and the barrier properties

The breaking and resealing dynamics of the tight junction bicellular strand network dynamics lead to two distinct methods of passage for the molecules and current. The time-dependence of the molecular permeability measurement enables the step-by-step method of diffusion between the strand-lined compartments over a long period. This method is highly dependent on the level of strand breaking dynamics and the horizontal strand number. These two properties are also tightly linked to the second permeation method, the continuous open paths through the strand network, since they define the probability of having these paths.

The open paths also form one conduction path for the electric current through the bicellular tight junctions. The other main path comes from the claudin-formed pores that enable the movement of specific ions where the current can flow directly through the strands. In addition, in reality, the ions can pass through the strand network using the step-by-step method utilized by molecules, but the instantaneous TER measurement cannot observe this.

The results show that the open paths have a considerable impact on molecular permeability. The rate difference between the permeability methods was large, indicating that if there is a reasonable probability of these paths occurring, there is a considerable difference in permeability rate compared to the situation with no open paths. With TER, the open paths must be extremely common to impact the bicellular resistance. This indicates that the current flow through the strands is mostly the dominating current path through the bicellular junctions, basically leading to a system with a series of resistors defined by the horizontal strands.

The rate of permeation through the strand network via the step-by-step method – and the probability of the open paths – is also highly dependent on the morphology of the network. While this was not considered in Study II, wider compartments would lead to a higher probability of having a break in a longer section of the strand, meaning that there would be, on average, fewer steps to be taken through the network. Saito et al.[62] used our model to study the effect of the compartment width on the TER and the permeability of 4 and 10-kDa dextrans. They observed large differences in both values. For example, doubling the width of the compartments led approximately to a 180 % increase in the permeability of the 4-kDa dextrans and a 27 % decrease in the TER. In addition, omitting the horizontal compartmentalization led to a 1,480 % increase in the permeability of the 4-kDa dextrans and a 91 % decrease in the TER compared to the morphology used in Study II. These large changes were caused by the higher probability of continuous open path formation. Therefore, the complex interplay between the strand dynamics and the strand network morphology produces a complex and highly nonlinear relationship between the permeability and TER and provides the cells a means of regulating different aspects of the barrier.

An interesting question related to the continuous open paths is that could these events be observed in the measurements? The traditional permeability averages the results over the whole epithelium and over time, making it impossible to see small local events. However, the newly developed methods can indicate local permeability leaks in the junctions[20,249,250]. The simulated length of junctions of 5 μm for each simulation is roughly the equivalent of the length of junctions between two cells. Therefore, based on our results, these events should be visible with the typical strand number of 4 for epithelia similar to MDCK II. With their biotin-avidin-based methods, Richter and coworkers could indicate dextran leaks both in the tricellular and bicellular junctions[249,250]. Later, Stephenson et al.[20] showed bicellular transient leaks with their approach and related them to morphological changes at the cellular level. The duration of these events was in the range of hundred seconds, making them on average longer than what was observed for the open paths for typical strand numbers in our results. Thus, it is unclear if these events are related to the strand-level dynamics and hence the tightness of the junctions or if they are entirely separate phenomena.

As with the permeability, the traditional TER measurement averages the current flow throughout the epithelium and thus hides any local leak events. Bringing the electrodes closer to the junction enables more local resistance measurement. The conductance scanning experiments have shown that they can differentiate between the local conductivities of the cell centers and the junction area[255,256]. However, to the best of my knowledge, these methods have not been used to study the local junction conductivity over long time periods. On the other hand, the patch-clamp method used by Weber et al.[82] showed the conductance of the junctions in a submicrometer section over the duration of tens of seconds to minutes. They did not observe any large changes in the conductivity that would indicate an open path. However, the patch-clamp pipette could restrict the strand dynamics, and more importantly, based on our results, these events would be rare in the used measurement area and duration.

6.4 Electrode positioning and transepithelial electrical measurements

In our simulations of the electrode positioning, we observed no differences in the virtually measured TEZ values with either epithelium with homogeneous properties or between defects of similar size but different locations. The only thing that seemed to matter is the amount of defective area. Therefore, positioning is not an issue when studying or monitoring the maturation of the epithelia. These results also indicate that this kind of system, with electrodes on the scale of millimeters, cannot localize any defects in the epithelial barrier or any possible current leaks caused by the tight junction strand dynamics. The sensitivity distributions show that bringing electrodes closer to the epithelium makes the measured area more concentrated. However, the closest distance considered in the simulations was 1 mm. No closer distances were simulated since the electrodes themselves are in this size scale and thus would most likely not be able to make the measured area more concentrated. The scanning electrode studies were able to differentiate between the cell centers and cell-cell junctions using specialized pipette electrodes with a distance of 0.2–13 μm between the electrode tip and the epithelial surface[255,256]. However, it is not clear what size of an electrode or distance is required at minimum to observe the local conductivity differences.

The results related to the measurement sensitivity distributions were double-edged. On the one hand, the electrode positioning and the measurement frequency had an apparent effect on the distribution and thus the area of the epithelium that is mainly measured. On the other hand, large changes in the epithelial barrier properties in these areas would also change the sensitivity distribution itself, thus changing the measured area. While minor changes in the barrier would not lead to visible changes in the sensitivity distribution, their location would not be revealed with a measurement system similar to the one simulated in Study III. It would be interesting to simulate the sensitivity distributions of the electrode scanning measurement systems since, in this size scale, defects in the cell-cell junctions would be prominent in relation to the size of the electrodes themselves.

6.5 Effect of substrate stiffness on the transmission of forces in epithelial monolayers

We found that the mechanical system composing the cell monolayer and substrates of different stiffnesses responded differently to the external force produced by the micromanipulation of the single cell. Based on our results on the propagation of cell displacement and forces, it was clear that an external force affects the cells in the monolayer in two ways: they moved the cells or deformed the cell shape.

The ability of the cells to be moved by force depended on the substrate's stiffness, the cell's ability to deform on its apico-basal axis, and the movability of the neighboring cells. A large cell movement required deformation of the substrate, which was more difficult when the substrate was stiff. The apico-basal deformation allowed small displacement of the apical surface but restricted the larger movements. In the model, the deformability of the apico-basal axis was incorporated into the focal adhesion strength, which was found to be higher for the cells on stiff substrates. Another part of the cell deformation was that of the apical plane. The external force can change the area and perimeter of the cell's apical surface. The amount that a cell deformed apically depended on its ability to move and on the subsequent cells in the monolayer to move or deform. If the next cell could be easily moved, the apical deformation was small. However, the cell deformed more in the opposite case since it could not pull the neighboring cells as much.

From the perspective of transmission of forces between the cells, the more efficient transmission occurred when the apical deformation was low. As discussed, this can be achieved by increasing the cells' ability to be moved by force, e.g., by having a softer substrate or reduced substrate-binding strength. Goodwin et al.[344] studied cell displacement in the developing *Drosophila* embryos and found an inverse correlation between the strength of the basal cell-ECM adhesions and the apical displacement. They suggested that reduced basal binding, which resulted in more pronounced apical displacement, would lead to more efficient apical force transmission, thus agreeing with our results. However, the force transmission can also be improved by making the apical surface more difficult to deform since the subsequent cells are forced to move more. Based on this hypothesis, increasing the values of the force constants that directly affect the deformability of the apical surface would also enhance the transmission of forces over longer distances. This is what we observed during the model fitting since fitting the model to the experimental decay of the cell displacement required changing the parameters describing the stiffness of the cortical actomyosin ring. Using higher values led to increased cell displacement over longer distances. The tension in the cytoskeleton has been shown to enable mechanical communication over longer distances within cells compared to heterogeneous solids[23,345,346], and the same seems true for epithelial monolayers.

To summarize, on stiff substrates, the movement of the cells is impaired by the higher forces required to deform the substrate and the high focal adhesion strengths. Therefore, especially close to the micromanipulated cell, they deform both in the apical plane – as indicated by the increased cortical force – and in the apico-basal axis – as shown by the increased focal adhesion force. In contrast, the cells move more easily on soft substrates due to the more deformable substrate and the lower focal adhesion strength. Therefore, the cells do not deform as much in the apical plane. Taken together, while the cells are subjected to similar levels of junction forces further away from the manipulated cells, these forces affect the cells differently: on stiff substrates, the cells deform in the apical plane, and on soft substrates, they are displaced.

Also, we found that a gradient in the substrate stiffness affected both the propagation of displacement and forces farther away from the gradient. With an increasing gradient, the cortical forces increased and the cell displacement decreased in the soft region between the gradient and the manipulated cell compared to the case with a uniform soft substrate. This can be explained by the larger forces needed to displace the cells on the stiffer side of the interface. This reduces the capabilities of the cells on the soft region to move, and thus they deform in the apical surface more than normal. The opposite occurs when there is a decreasing gradient: the easier-to-move cells on the soft side of the gradient do not limit the movement of the cells on the stiff region as much compared to the case with a uniform stiff substrate. This leads to higher cell displacement and lower cortical forces, indicating a smaller amount of apical deformation.

The stiffness of the substrate is known to strengthen the focal adhesions and increase the stiffness of the cell itself[25,146,190,191]. This was replicated by our model's fitted focal adhesion strength parameter values, whose magnitude increased with substrate stiffness. Also, the analysis of the difference between the cell and substrate deformations showed that according to our model, the ability of the cells to deform in the apico-basal axis is highly dependent on the substrate stiffness. On stiffer substrates, the cells were thus stiffer in the apico-basal direction compared to the soft substrates. Since the model has only one parameter describing both of these phenomena, it is impossible to estimate the contribution of each component.

Overall, the stiffness was found to affect the cell-cell junctions, focal adhesions, and cortical actomyosin forces. Therefore, by passively affecting the cells' ability to move and deform following an external force, the substrate has the ability to influence the forces sensed by mechanosensitive proteins at these locations. Also, changes in stiffness at a distance can affect the magnitude of the sensed forces.

6.6 Model limitations

The models developed in this thesis all have their limitations. The permeability of the outer BRB (Study I) was limited in two main ways. First, proper validation of the model data was challenging due to the limited amount of experimental data. At the time of the publication, there were only three studies with data on the permeability of the RPE related to the effect of the molecular properties. Unfortunately, one of these studies was retracted after Study I was published[347]. Therefore, more experimental studies of RPE permeability as a function of molecular properties are needed to validate the model properly. Nevertheless, even without rigorous validation, the model still indicated the relevant parameters in the barrier and the currently missing experimental knowledge. Another limiting factor in this model was the challenge of describing the permeability properties of the cell plasma membrane. It is challenging to describe the complex interactions related to transmembrane molecular permeation with simple generalized equations. Thus, the usability of the model to investigate the effect of lipophilicity on the RPE permeability in more detail is limited.

The tight junction model of Study II had assumptions that may limit its usability. A large portion of the model was based on hypotheses and assumptions of the tight junction structure, which meant that a lot of the parameter values were estimated based on a little experimental data. Also, simplifying the bicellular tight junction strand morphology into a regular grid of rectangles did not do justice to the variety of morphologies observed in experiments[34862,348–350]. Saito et al.[62] used the model to study the effect of strand morphology and found that it significantly affected the obtained permeability values, indicating that the rigorous analysis of the strand dynamics required information on the morphology. We also assumed that the resistance of the tight junctions could be equated to that of the whole epithelium, i.e., the TER. Krug et al.[27] developed a method to separate the transcellular and paracellular components from the TER and found that, depending on the epithelium, the paracellular resistance can considerably impact the TER. Therefore, our assumption seems not the be true, especially in epithelia with higher resistance tight junctions.

While the electrical measurement system model describes the system in detail, its main limitation relates to its ability to describe measurement in finer scale and better resolution. To adequately describe measurements in the cellular scale, the cells would have to be described as individual units instead of a homogeneous layer, thus complicating the model geometry significantly. In addition, the model is missing the description of the electrode impedance, which is known to affect measurements.

At its current state, the epithelial mechanics model of Study IV is limited mainly to studying the elastic properties of the epithelial monolayer. While the model contains some remodeling of the cellular structures, the cortical tension remodeling would have to be implemented to fully describe viscous properties in the tissues. In addition, the substrate model only describes linear materials, such as polyacrylamide, and thus cannot be used as such to study the role of natural, heterogeneous, and fibrous ECM. Furthermore, based on the low variance observed in the cell displacement compared to those in the experimental data, the mechanical properties of real epithelia are heterogeneous rather than uniform, as assumed in the model.

6.7 Future aspects

The tight junction model presented in this thesis could be improved in the future to study the structural dynamics of the tight junctions in more detail by cooperation between the experimental and computational fields. Data on the strand morphology and strand dynamics would enable a more rigorous analysis of the tight junction barrier. Furthermore, the data obtained from the tight junction model could be used to design and optimize a measurement system that could detect the effect of the strand dynamics on the measured resistances, such as the conductance scanning experiments[255,256].

Also, the model on the epithelial mechanics creates a good platform for adding new features, cell components, and mechanical stimuli to further the understanding of the force transmission in the epithelial monolayer. For example, the description of nuclei within the cells would enable studying their role in the mechanical system and the forces transmitted to them. Furthermore, it would be interesting to study the effect of fibrous ECM on force transmission.

Finally, since the connection between the properties of the barrier and epithelial cell mechanics through ZO-1 has been shown[21,155,157,158], the models could be used to study the relationship between these two properties of the epithelial tissues. This would create a platform that would support the investigation and data analysis of the effect of various mechanical stimuli on the mechanical state of the cell and then further to the barrier properties.

7 CONCLUSIONS

This thesis aimed to develop computational models to improve our understanding of epithelial barrier properties and mechanics. It resulted in novel modeling platforms that can create new mechanistic knowledge on these epithelial functions. The following list details the conclusions for each aim stated in chapter 3.

1. My computational model of the BRB (Study I) indicated that the main permeability-limiting component for most molecules in epithelial tissue barriers is the paracellular pathway between the epithelial cells, and especially the tight junctions. Furthermore, the developed tight junction model (Study II) suggested that the leak pathway is formed both by the structural strand dynamics and the large pores in the tricellular junctions with different relative magnitudes depending on the epithelium. The role of these two pathways was also different for the molecular permeability and TER.

2. The tight junction model (Study II) suggested that the strand dynamics in the bicellular tight junctions have a different effect on the measured values of molecular permeability and TER. The observed open paths were found to have a more important role in the permeability of molecules compared to the resistance.

3. My model of the transepithelial electrical measurements (Study III) revealed that the placement of the electrodes in relation to the epithelium, together with the measurement frequency, has a profound effect on the region of the epithelium whose properties were primarily measured but not on the measured values.

4. The model of epithelial mechanics (Study IV) showed that substrate stiffness has a clear impact on the propagation of forces between cells in the epithelial monolayer. The cells were found to transmit information on the local heterogeneities in the stiffness over long distances based on their ability to resist deformations.

The models developed here help the experimental research by creating platforms to test hypotheses, analyze results, and produce new hypotheses. Computational modeling, combined with experimental work, provides a valuable tool to improve our understanding of the properties and relationship of the epithelial barrier and mechanics.

8 REFERENCES

1. Marieb, E. N. *Essentials of Human Anatomy & Physiology*. (Pearson Education Inc., 2009).

2. Guan, Q. A Comprehensive Review and Update on the Pathogenesis of Inflammatory Bowel Disease. *J. Immunol. Res.* **2019**, (2019).

3. Wong, W. L. *et al.* Global prevalence of age-related macular degeneration and disease burden projection for 2020 and 2040: A systematic review and meta-analysis. *Lancet Glob. Heal.* **2**, e106–e116 (2014).

4. Colijn, J. M. *et al.* Prevalence of Age-Related Macular Degeneration in Europe. *Ophthalmology* **124**, 1753–1763 (2017).

5. Burisch, J., Jess, T., Martinato, M. & Lakatos, P. L. The burden of inflammatory bowel disease in Europe. *J. Crohn's Colitis* **7**, 322–337 (2013).

6. Ylisaukko-Oja, T. *et al.* Healthcare resource utilization and treatment costs of Finnish chronic inflammatory bowel disease patients treated with infliximab*. *Scand. J. Gastroenterol.* **54**, 726–732 (2019).

7. Bray, F. *et al.* Global cancer statistics 2018: GLOBOCAN estimates of incidence and mortality worldwide for 36 cancers in 185 countries. *CA. Cancer J. Clin.* **68**, 394–424 (2018).

8. Hinck, L. & Näthke, I. Changes in cell and tissue organization in cancer of the breast and colon. *Curr. Opin. Cell Biol.* **26**, 87–95 (2014).

9. Cozzitorto, C. & Spagnoli, F. M. Pancreas organogenesis: The interplay between surrounding microenvironment(s) and epithelium-intrinsic factors. in *Current Topics in Developmental Biology* vol. 132 221–256 (Elsevier Inc., 2019).

10. Scheibner, K. *et al.* Epithelial cell plasticity drives endoderm formation during gastrulation. *Nat. Cell Biol.* **23**, 692–703 (2021).

11. Lang, C., Conrad, L. & Iber, D. Organ-Specific Branching Morphogenesis. *Front. Cell Dev. Biol.* **9**, (2021).

12. Merkel, M. & Manning, M. L. Using cell deformation and motion to predict forces and collective behavior in morphogenesis. *Semin. Cell Dev. Biol.* **67**, 161–169 (2017).

13. Zihni, C., Mills, C., Matter, K. & Balda, M. S. Tight junctions: From simple barriers to multifunctional molecular gates. *Nat. Rev. Mol. Cell Biol.* **17**, 564–580 (2016).

14. Van Itallie, C. M. & Anderson, J. M. Architecture of tight junctions and principles of molecular composition. *Semin. Cell Dev. Biol.* **36**, 157–165 (2014).

15. Graham, W. V., Marchiando, A. M., Shen, L. & Turner, J. R. No static at all: A new perspective on molecular architecture of the tight junction. *Ann. N. Y. Acad. Sci.* **1165**, 314–322 (2009).

16. van Itallie, C. M. *et al.* The density of small tight junction pores varies among cell types and is increased by expression of claudin-2. *J. Cell Sci.* **121**, 298–305 (2008).

17. Krug, S. M. *et al.* Charge-selective claudin channels. *Ann. N. Y. Acad. Sci.* **1257**, 20–28 (2012).

18. Guillot, C. & Lecuit, T. Mechanics of Epithelial Tissue Homeostasis and Morphogenesis. *Science (80-.).* **340**, 1185–1189 (2013).

19. Bazellières, E. *et al.* Control of cell–cell forces and collective cell dynamics by the intercellular adhesome. *Nat. Cell Biol.* **17**, 409–420 (2015).

20. Stephenson, R. E. *et al.* Rho Flares Repair Local Tight Junction Leaks. *Dev. Cell* **48**, 445-459.e5 (2019).

21. Cartagena-Rivera, A. X., Van Itallie, C. M., Anderson, J. M. & Chadwick, R. S. Apical surface supracellular mechanical properties in polarized epithelium using noninvasive acoustic force spectroscopy. *Nat. Commun.* **8**, 1030 (2017).

22. Paluch, E. K. *et al.* Mechanotransduction: Use the force(s). *BMC Biol.* **13**,

1–14 (2015).

23. Wang, N., Tytell, J. D. & Ingber, D. E. Mechanotransduction at a distance: mechanically coupling the extracellular matrix with the nucleus. *Nat. Rev. Mol. Cell Biol.* **10**, 75–82 (2009).

24. Cunningham, K. E. & Turner, J. R. Myosin light chain kinase: Pulling the strings of epithelial tight junction function. *Ann. N. Y. Acad. Sci.* **1258**, 34–42 (2012).

25. Butcher, D. T., Alliston, T. & Weaver, V. M. A tense situation: forcing tumour progression. *Nat. Rev. Cancer* **9**, 108–122 (2009).

26. Broders-Bondon, F., Ho-Bouldoires, T. H. N., Fernandez-Sanchez, M. E. & Farge, E. Mechanotransduction in tumor progression: The dark side of the force. *J. Cell Biol.* **217**, 1571–1587 (2018).

27. Krug, S. M., Fromm, M. & Günzel, D. Two-path impedance spectroscopy for measuring paracellular and transcellular epithelial resistance. *Biophys. J.* **97**, 2202–2211 (2009).

28. Krug, S. M. *et al.* Tricellulin forms a barrier to macromolecules in tricellular tight junctions without affecting ion permeability. *Mol. Biol. Cell* **20**, 3713–24 (2009).

29. Ribeiro, A. J. S., Denisin, A. K., Wilson, R. E. & Pruitt, B. L. For whom the cells pull: Hydrogel and micropost devices for measuring traction forces. *Methods* **94**, 51–64 (2016).

30. Saitoh, R. *et al.* Correction of permeability with pore radius of tight junctions in Caco-2 monolayers improves the prediction of the dose fraction of hydrophilic drugs absorbed by humans. *Pharm. Res.* **21**, 749–55 (2004).

31. Avdeef, A. Leakiness and size exclusion of paracellular channels in cultured epithelial cell monolayers-interlaboratory comparison. *Pharm. Res.* **27**, 480–489 (2010).

32. Diecke, F. P. *et al.* Comparative permeabilities of the paracellular and transcellular pathways of corneal endothelial layers. *J. Membr. Biol.* **242**, 41–51 (2011).

33. Guo, P., Weinstein, A. M. & Weinbaum, S. A dual-pathway ultrastructural model for the tight junction of rat proximal tubule epithelium. *Am. J. Physiol. - Ren. Physiol.* **285**, (2003).

34. Weber, C. R. & Turner, J. R. Dynamic modeling of the tight junction pore pathway. *Ann. N. Y. Acad. Sci.* **1397**, 209–218 (2017).

35. Washiyama, M. *et al.* Percolation analysis in electrical conductivity of madin-darby canine kidney and Caco-2 cells by permeation-enhancing agents. *Biol. Pharm. Bull.* **36**, 384–389 (2013).

36. Rejniak, K. A. & Dillon, R. H. A single cell-based model of the ductal tumour microarchitecture. *Comput. Math. Methods Med.* **8**, 51–69 (2007).

37. Rejniak, K. A. & Anderson, A. R. A. A Computational Study of the Development of Epithelial Acini: I. Sufficient Conditions for the Formation of a Hollow Structure. *Bull. Math. Biol.* **70**, 677–712 (2008).

38. Tamulonis, C. *et al.* A cell-based model of Nematostella vectensis gastrulation including bottle cell formation, invagination and zippering. *Dev. Biol.* **351**, 217–228 (2011).

39. Fletcher, A. G., Osterfield, M., Baker, R. E. & Shvartsman, S. Y. Vertex Models of Epithelial Morphogenesis. *Biophys. J.* **106**, 2291–2304 (2014).

40. Nematbakhsh, A. *et al.* Multi-scale computational study of the mechanical regulation of cell mitotic rounding in epithelia. *PLoS Comput. Biol.* **13**, 1–22 (2017).

41. Jamali, Y., Azimi, M. & Mofrad, M. R. K. A sub-cellular viscoelastic model for cell population mechanics. *PLoS One* **5**, (2010).

42. Strauss, O. The Retinal Pigment Epithelium in Visual Function. *Physiol. Rev.* **85**, 845–881 (2005).

43. Campanale, J. P., Sun, T. Y. & Montell, D. J. Development and dynamics of cell polarity at a glance. *J. Cell Sci.* **130**, 1201–1207 (2017).

44. Alberts, B. *et al. Molecular biology of the cell.* (Garland Science, 2008).

45. Grebenkämper, K. & Galla, H. J. Translational diffusion measurements

of a fluorescent phospholipid between MDCK-I cells support the lipid model of the tight junctions. *Chem. Phys. Lipids* **71**, 133–143 (1994).

46. Lingaraju, A., Long, T. M., Wang, Y., Austin, J. R. & Turner, J. R. Conceptual barriers to understanding physical barriers. *Semin. Cell Dev. Biol.* **42**, 13–21 (2015).

47. Tervonen, A., Ihalainen, T. O., Nymark, S. & Hyttinen, J. Structural dynamics of tight junctions modulate the properties of the epithelial barrier. *PLoS One* **14**, 1–26 (2019).

48. Tsukita, S., Tanaka, H. & Tamura, A. The Claudins: From Tight Junctions to Biological Systems. *Trends Biochem. Sci.* **44**, 141–152 (2019).

49. Krause, G., Protze, J. & Piontek, J. Assembly and function of claudins: Structure-function relationships based on homology models and crystal structures. *Semin. Cell Dev. Biol.* **42**, 3–12 (2015).

50. Piontek, J., Krug, S. M., Protze, J., Krause, G. & Fromm, M. Molecular architecture and assembly of the tight junction backbone. *Biochim. Biophys. Acta - Biomembr.* **1862**, 183279 (2020).

51. Suzuki, H., Tani, K., Tamura, A., Tsukita, S. & Fujiyoshi, Y. Model for the architecture of claudin-based paracellular ion channels through tight junctions. *J. Mol. Biol.* **427**, 291–297 (2015).

52. Hou, J., Renigunta, A., Yang, J. & Waldegger, S. Claudin-4 forms paracellular chloride channel in the kidney and requires claudin-8 for tight junction localization. *Proc. Natl. Acad. Sci. U. S. A.* **107**, 18010–18015 (2010).

53. Conrad, M. P., Piontek, J., Günzel, D., Fromm, M. & Krug, S. M. Molecular basis of claudin-17 anion selectivity. *Cell. Mol. Life Sci.* **73**, 185–200 (2016).

54. Yu, A. S. L. *et al.* Molecular basis for cation selectivity in claudin-2-based paracellular pores: Identifi cation of an electrostatic interaction site. *J. Gen. Physiol.* **133**, 111–127 (2009).

55. Rosenthal, R. *et al.* Claudin-15 forms a water channel through the tight junction with distinct function compared to claudin-2. *Acta Physiol.* **228**,

1–15 (2019).

56. Rosenthal, R. *et al.* Claudin-2-mediated cation and water transport share a common pore. *Acta Physiol.* **219**, 521–536 (2017).

57. Günzel, D. & Yu, A. S. L. *Claudins and the modulation of tight junction permeability. Physiological Reviews* vol. 93 (2013).

58. Furuse, M. *et al.* Occludin: A novel integral membrane protein localizing at tight junctions. *J. Cell Biol.* **123**, 1777–1788 (1993).

59. Buschmann, M. M. *et al.* Occludin OCEL-domain interactions are required for maintenance and regulation of the tight junction barrier to macromolecular flux. *Mol. Biol. Cell* **24**, 3056–3068 (2013).

60. Al-Sadi, R. *et al.* Occludin regulates macromolecule flux across the intestinal epithelial tight junction barrier. *Am. J. Physiol. - Gastrointest. Liver Physiol.* **300**, 1054–1064 (2011).

61. Van Itallie, C. M., Fanning, A. S., Holmes, J. & Anderson, J. M. Occludin is required for cytokine-induced regulation of tight junction barriers. *J. Cell Sci.* **123**, 2844–2852 (2010).

62. Saito, A. C. *et al.* Occludin and tricellulin facilitate formation of anastomosing tight-junction strand network to improve barrier function. *Mol. Biol. Cell* **32**, 722–738 (2021).

63. Itoh, M. *et al.* The 220-kD protein colocalizing with cadherins in non-epithelial cells is identical to ZO-1, a tight junction-associated protein in epithelial cells: cDNA cloning and immunoelectron microscopy. *J. Cell Biol.* **121**, 491–502 (1993).

64. Yano, T., Matsui, T., Tamura, A., Uji, M. & Tsukita, S. The association of microtubules with tight junctions is promoted by cingulin phosphorylation by AMPK. *J. Cell Biol.* **203**, 605–614 (2013).

65. Aijaz, S., D'Atri, F., Citi, S., Balda, M. S. & Matter, K. Binding of GEF-H1 to the tight junction-associated adaptor cingulin results in inhibition of Rho signaling and G1/S phase transition. *Dev. Cell* **8**, 777–786 (2005).

66. Staehelin L.A. Further observations on the fine structure of freeze-cleaved

tight junctions. *J. Cell Sci.* **13**, 763–786 (1973).

67. Ikenouchi, J. *et al.* Tricellulin constitutes a novel barrier at tricellular contacts of epithelial cells. *J. Cell Biol.* **171**, 939–945 (2005).

68. Hartsock, A. & Nelson, W. J. Adherens and tight junctions: Structure, function and connections to the actin cytoskeleton. *Biochim. Biophys. Acta - Biomembr.* **1778**, 660–669 (2008).

69. Harris, T. J. C. & Tepass, U. Adherens junctions: From molecules to morphogenesis. *Nat. Rev. Mol. Cell Biol.* **11**, 502–514 (2010).

70. Campbell, H. K., Maiers, J. L. & DeMali, K. A. Interplay between tight junctions & adherens junctions. *Exp. Cell Res.* **358**, 39–44 (2017).

71. Maiers, J. L., Peng, X., Fanning, A. S. & DeMali, K. A. ZO-1 recruitment to α-catenin -a novel mechanism for coupling the assembly of tight junctions to adherens junctions. *J. Cell Sci.* **126**, 3904–3915 (2013).

72. Ikenouchi, J., Umeda, K., Tsukita, S., Furuse, M. & Tsukita, S. Requirement of ZO-1 for the formation of belt-like adherens junctions during epithelial cell polarization. *J. Cell Biol.* **176**, 779–786 (2007).

73. van Meer, G. & Simons, K. The function of tight junctions in maintaining differences in lipid composition between the apical and the basolateral cell surface domains of MDCK cells. *EMBO J.* **5**, 1455–1464 (1986).

74. Krug, S. M. *et al.* Tricellulin is regulated via interleukin-13-receptor α2, affects macromolecule uptake, and is decreased in ulcerative colitis. *Mucosal Immunol.* **11**, 345–356 (2018).

75. Balda, M. S. *et al.* Functional dissociation of paracellular permeability and transepithelial electrical resistance and disruption of the apical-basolateral intramembrane diffusion barrier by expression of a mutant tight junction membrane protein. *J. Cell Biol.* **134**, 1031–1049 (1996).

76. Steed, E., Balda, M. S. & Matter, K. Dynamics and functions of tight junctions. *Trends Cell Biol.* **20**, 142–149 (2010).

77. Watson, C. J., Rowland, M. & Warhurst, G. Functional modeling of tight junctions in intestinal cell monolayers using polyethylene glycol oligomers.

Am. J. Physiol. - Cell Physiol. **281**, (2001).

78. Liang, G. H. & Weber, C. R. Molecular aspects of tight junction barrier function. *Curr. Opin. Pharmacol.* **19**, 84–89 (2014).

79. Stevenson, B. R., Anderson, J. M., Goodenough, D. A. & Mooseker, M. S. Tight junction structure and ZO-1 content are identical in two strains of Madin-Darby canine kidney cells which differ in transepithelial resistance. *J. Cell Biol.* **107**, 2401–2408 (1988).

80. Furuse, M., Furuse, K., Sasaki, H. & Tsukita, S. Conversion of zonulae occludentes from tight to leaky strand type by introducing claudin-2 into Madin-Darby canine kidney I cells. *J. Cell Biol.* **153**, 263–272 (2001).

81. Tokuda, S. & Furuse, M. Claudin-2 knockout by TALEN-mediated gene targeting in MDCK cells: Claudin-2 independently determines the leaky property of tight junctions in MDCK cells. *PLoS One* **10**, 1–22 (2015).

82. Weber, C. R. *et al.* Claudin-2-dependent paracellular channels are dynamically gated. *Elife* **4**, 1–20 (2015).

83. Sasaki, H. *et al.* Dynamic behavior of paired claudin strands within apposing plasma membranes. *Proc. Natl. Acad. Sci. U. S. A.* **100**, 3971–3976 (2003).

84. Anderson, J. M., Van Itallie, C. M. & Fanning, A. S. Setting up a selective barrier at the apical junction complex. *Curr. Opin. Cell Biol.* **16**, 140–145 (2004).

85. Van Itallie, C. M., Tietgens, A. J. & Anderson, J. M. Visualizing the dynamic coupling of claudin strands to the actin cytoskeleton through ZO-1. *Mol. Biol. Cell* **28**, 524–534 (2017).

86. Zeissig, S. *et al.* Changes in expression and distribution of claudin 2, 5 and 8 lead to discontinuous tight junctions and barrier dysfunction in active Crohn's disease. *Gut* **56**, 61–72 (2007).

87. Rosenthal, R. *et al.* Claudin-2, a component of the tight junction, forms a paracellular water channel. *J. Cell Sci.* **123**, 1913–1921 (2010).

88. Shen, L., Weber, C. R. & Turner, J. R. The tight junction protein complex

undergoes rapid and continuous molecular remodeling at steady state. *J. Cell Biol.* **181**, 683–695 (2008).

89. Van Itallie, C. M., Fanning, A. S., Bridges, A. & Anderson, J. M. ZO-1 stabilizes the tight junction solute barrier through coupling to the perijunctional cytoskeleton. *Mol. Biol. Cell* **20**, 3930–40 (2009).

90. Fung, K. Y. Y., Fairn, G. D. & Lee, W. L. Transcellular vesicular transport in epithelial and endothelial cells: Challenges and opportunities. *Traffic* **19**, 5–18 (2018).

91. Mitragotri, S. Modeling skin permeability to hydrophilic and hydrophobic solutes based on four permeation pathways. *J. Control. Release* **86**, 69–92 (2003).

92. Johnson, M. E., Blankschtein, D. & Langer, R. Evaluation of Solute Permeation through the Stratum Corneum: Lateral Bilayer Diffusion as the Primary Transport Mechanism. *J. Pharm. Sci.* **86**, 1162–1172 (1997).

93. Edwards, A. & Prausnitz, M. R. Predicted permeability of the cornea to topical drugs. *Pharm. Res.* **18**, 1497–508 (2001).

94. Turner, J. R. Intestinal mucosal barrier function in health and disease. *Nat. Rev. Immunol.* **9**, 799–809 (2009).

95. Beumer, J. & Clevers, H. Regulation and plasticity of intestinal stem cells during homeostasis and regeneration. *Dev.* **143**, 3639–3649 (2016).

96. Noah, T. K., Donahue, B. & Shroyer, N. F. Intestinal development and differentiation. *Exp. Cell Res.* **317**, 2702–2710 (2011).

97. Pinto, M. *et al.* Enterocyte-like differentiation and polarization of the human colon carcinoma cell line Caco-2 in culture. *Biol.Cell* **47**, 323–330 (1983).

98. Artursson, P., Palm, K. & Luthman, K. Caco-2 monolayers in experimental and theoretical predictions of drug transport. *Adv. Drug Deliv. Rev.* **64**, 280–289 (2012).

99. Shah, P., Jogani, V., Bagchi, T. & Misra, A. Role of Caco-2 cell monolayers in prediction of intestinal drug absorption. *Biotechnol. Prog.* **22**, 186–198

(2006).

100. Hayeshi, R. *et al.* Comparison of drug transporter gene expression and functionality in Caco-2 cells from 10 different laboratories. *Eur. J. Pharm. Sci.* **35**, 383–396 (2008).

101. Fleischer, D. Biological Transport Phenomena in the Gastrointestinal Tract: Cellular Mechanisms. in *Transport Processes in Pharmaceutical Systems* (eds. Amigon, G., Lee, P. & Topp, E.) (Marcel Dekker, Inc., 2000).

102. Srinivasan, B. *et al.* TEER Measurement Techniques for In Vitro Barrier Model Systems. *J. Lab. Autom.* **20**, 107–126 (2015).

103. Denker, B. M. & Sabath, E. The biology of epithelial cell tight junctions in the kidney. *J. Am. Soc. Nephrol.* **22**, 622–625 (2011).

104. Dukes, J. D., Whitley, P. & Chalmers, A. D. The MDCK variety pack: Choosing the right strain. *BMC Cell Biol.* **12**, 2–5 (2011).

105. Davies, D. J., Ward, R. J. & Heylings, J. R. Multi-species assessment of electrical resistance as a skin integrity marker for in vitro percutaneous absorption studies. *Toxicol. Vitr.* **18**, 351–358 (2004).

106. Geys, J., De Vos, R., Nemery, B. & Hoet, P. H. M. In vitro translocation of quantum dots and influence of oxidative stress. *Am. J. Physiol. - Lung Cell. Mol. Physiol.* **297**, (2009).

107. Mitchell, L. A., Overgaard, C. E., Ward, C., Margulies, S. S. & Koval, M. Differential effects of claudin-3 and claudin-4 on alveolar epithelial barrier function. *Am. J. Physiol. - Lung Cell. Mol. Physiol.* **301**, 40–49 (2011).

108. Rizzolo, L. J. Barrier properties of cultured retinal pigment epithelium. *Exp. Eye Res.* **126**, 16–26 (2014).

109. Gong, J. *et al.* Stem cell-derived retinal pigment epithelium from patients with age-related macular degeneration exhibit reduced metabolism and matrix interactions. *Stem Cells Transl. Med.* **9**, 364–376 (2020).

110. Ablonczy, Z. *et al.* Human retinal pigment epithelium cells as functional models for the RPE in vivo. *Investig. Ophthalmol. Vis. Sci.* **52**, 8614–8620 (2011).

111. Lynn, S. A. *et al.* Ex-vivo models of the Retinal Pigment Epithelium (RPE) in long-term culture faithfully recapitulate key structural and physiological features of native RPE. *Tissue Cell* **49**, 447–460 (2017).

112. Yu, A. S. L. Claudins and the kidney. *J. Am. Soc. Nephrol.* **26**, 11–19 (2015).

113. Kiuchi-Saishin, Y. *et al.* Differential expression patterns of claudins, tight junction membrane proteins, in mouse nephron segments. *J. Am. Soc. Nephrol.* **13**, 875–886 (2002).

114. Gaush, C. R., Hard, W. L., Smith, T. F. & Read, W. O. Characterization of an Established Line of Canine Kidney Cells (MDCK). *Proc. Soc. Exp. Biol. Med.* **122**, 931–935 (1966).

115. Wickett, R. R. & Visscher, M. O. Structure and function of the epidermal barrier. *Am. J. Infect. Control* **34**, 98–110 (2006).

116. Chang, M. M.-J., Shih, L. & Wu, R. Pulmonary Epithelium: Cell Types and Functions. in *The Pulmonary Epithelium in Health and Disease* (ed. Proud, D.) 1–26 (John Wiley & Sons, Ltd, 2008).

117. Guillot, L. *et al.* Alveolar epithelial cells: Master regulators of lung homeostasis. *Int. J. Biochem. Cell Biol.* **45**, 2568–2573 (2013).

118. Bhutto, I. & Lutty, G. Understanding age-related macular degeneration (AMD): Relationships between the photoreceptor/retinal pigment epithelium/Bruch's membrane/choriocapillaris complex. *Mol. Aspects Med.* **33**, 295–317 (2012).

119. Campbell, M. & Humphries, P. The blood-retina barrier tight junctions and barrier modulation. in *Biology and Regulation of Blood-Tissue Barriers* (ed. Yan Cheng, C.) 70–84 (Springer, New York, NY, 2013).

120. Booij, J. C., Baas, D. C., Beisekeeva, J., Gorgels, T. G. M. F. & Bergen, A. A. B. The dynamic nature of Bruch's membrane. *Prog. Retin. Eye Res.* **29**, 1–18 (2010).

121. Savolainen, V. *et al.* Impedance spectroscopy in monitoring the maturation of stem cell-derived retinal pigment epithelium. *Ann. Biomed. Eng.* **39**, 3055–3069 (2011).

122. Onnela, N. *et al.* Electric impedance of human embryonic stem cell-derived retinal pigment epithelium. *Med. Biol. Eng. Comput.* **50**, 107–116 (2012).

123. Gudipaty, S. A. & Rosenblatt, J. Epithelial cell extrusion: Pathways and pathologies. *Semin. Cell Dev. Biol.* **67**, 132–140 (2017).

124. Ladoux, B. & Mège, R. M. Mechanobiology of collective cell behaviours. *Nat. Rev. Mol. Cell Biol.* **18**, 743–757 (2017).

125. Ohsawa, S., Vaughen, J. & Igaki, T. Cell Extrusion: A Stress-Responsive Force for Good or Evil in Epithelial Homeostasis. *Dev. Cell* **44**, 284–296 (2018).

126. Blanchoin, L., Boujemaa-Paterski, R., Sykes, C. & Plastino, J. Actin dynamics, architecture, and mechanics in cell motility. *Physiol. Rev.* **94**, 235–263 (2014).

127. Ivanov, A. I. *et al.* Myosin II regulates the shape of three-dimensional intestinal epithelial cysts. *J. Cell Sci.* **121**, 1803–1814 (2008).

128. Murrell, M., Oakes, P. W., Lenz, M. & Gardel, M. L. Forcing cells into shape: The mechanics of actomyosin contractility. *Nat. Rev. Mol. Cell Biol.* **16**, 486–498 (2015).

129. Chanet, S. *et al.* Actomyosin meshwork mechanosensing enables tissue shape to orient cell force. *Nat. Commun.* **8**, 1–13 (2017).

130. Heer, N. C. *et al.* Actomyosin-based tissue folding requires a multicellular myosin gradient. *J. Cell Sci.* **130**, 1876–1886 (2017).

131. Hall, A. Rho GTPases and the actin cytoskeleton. *Science (80-.).* **279**, 509–514 (1998).

132. Sit, S. T. & Manser, E. Rho GTPases and their role in organizing the actin cytoskeleton. *J. Cell Sci.* **124**, 679–683 (2011).

133. de Leeuw, R., Gruenbaum, Y. & Medalia, O. Nuclear Lamins: Thin Filaments with Major Functions. *Trends Cell Biol.* **28**, 34–45 (2018).

134. Sanghvi-Shah, R. & Weber, G. F. Intermediate Filaments at the Junction

of Mechanotransduction, Migration, and Development. *Front. Cell Dev. Biol.* **5**, 1–19 (2017).

135. Brangwynne, C. P. *et al.* Microtubules can bear enhanced compressive loads in living cells because of lateral reinforcement. *J. Cell Biol.* **173**, 733–741 (2006).

136. Seetharaman, S. & Etienne-Manneville, S. Microtubules at focal adhesions - a double-edged sword. *J. Cell Sci.* **132**, 1–11 (2019).

137. Vasileva, E. & Citi, S. The role of microtubules in the regulation of epithelial junctions. *Tissue Barriers* **6**, 1–20 (2018).

138. Geiger, B., Bershadsky, A., Pankov, R. & Yamada, K. M. Transmembrane extracellular matrix-cytoskeleton crosstalk. *Nat. Rev. Mol. Cell Biol.* **2**, 793–805 (2001).

139. Wehrle-Haller, B. Structure and function of focal adhesions. *Curr. Opin. Cell Biol.* **24**, 116–124 (2012).

140. Winograd-Katz, S. E., Fässler, R., Geiger, B. & Legate, K. R. The integrin adhesome: From genes and proteins to human disease. *Nat. Rev. Mol. Cell Biol.* **15**, 273–288 (2014).

141. Vajda, S., Beglov, D., Wakefield, A. E., Egbert, M. & Whitty, A. Cryptic binding sites on proteins: definition, detection, and druggability. *Curr. Opin. Chem. Biol.* **44**, 1–8 (2018).

142. Haswell, E. S., Phillips, R. & Rees, D. C. Mechanosensitive channels: What can they do and how do they do it? *Structure* **19**, 1356–1369 (2011).

143. Qiu, X. & Müller, U. Mechanically gated ion channels in mammalian hair cells. *Front. Cell. Neurosci.* **12**, 1–10 (2018).

144. del Rio, A. *et al.* Stretching Single Talin Rod Molecules Activates Vinculin Binding. *Science (80-.).* **323**, 638–641 (2009).

145. Giannone, G., Jiang, G., Sutton, D. H., Critchley, D. R. & Sheetz, M. P. Talin1 is critical for force-dependent reinforcement of initial integrin-cytoskeleton bonds but not tyrosine kinase activation. *J. Cell Biol.* **163**, 409–419 (2003).

146. Plotnikov, S. V., Pasapera, A. M., Sabass, B. & Waterman, C. M. Force fluctuations within focal adhesions mediate ECM-rigidity sensing to guide directed cell migration. *Cell* **151**, 1513–1527 (2012).

147. Pinheiro, D. & Bellaïche, Y. Mechanical Force-Driven Adherens Junction Remodeling and Epithelial Dynamics. *Dev. Cell* **47**, 3–19 (2018).

148. Salvi, A. M. & DeMali, K. A. Mechanisms linking mechanotransduction and cell metabolism. *Curr. Opin. Cell Biol.* **54**, 114–120 (2018).

149. Charras, G. & Yap, A. S. Tensile Forces and Mechanotransduction at Cell–Cell Junctions. *Curr. Biol.* **28**, R445–R457 (2018).

150. Angulo-Urarte, A., van der Wal, T. & Huveneers, S. Cell-cell junctions as sensors and transducers of mechanical forces. *Biochim. Biophys. Acta - Biomembr.* **1862**, 183316 (2020).

151. Buckley, C. D. *et al.* The minimal cadherin-catenin complex binds to actin filaments under force. *Science (80-.).* **346**, 1254211 (2014).

152. Acharya, B. R. *et al.* A Mechanosensitive RhoA Pathway that Protects Epithelia against Acute Tensile Stress. *Dev. Cell* **47**, 439-452.e6 (2018).

153. Turner, J. R. *et al.* Physiological regulation of epithelial tight junctions is associated with myosin light-chain phosphorylation. *Am. J. Physiol. - Cell Physiol.* **273**, (1997).

154. Yu, D. *et al.* MLCK-dependent exchange and actin binding region-dependent anchoring of ZO-1 regulate tight junction barrier function. *Proc. Natl. Acad. Sci. U. S. A.* **107**, 8237–8241 (2010).

155. He, W. Q. *et al.* Contributions of myosin light chain kinase to regulation of epithelial paracellular permeability and mucosal homeostasis. *Int. J. Mol. Sci.* **21**, (2020).

156. Citi, S. The mechanobiology of tight junctions. *Biophys. Rev.* **11**, 783–793 (2019).

157. Spadaro, D. *et al.* Tension-Dependent Stretching Activates ZO-1 to Control the Junctional Localization of Its Interactors. *Curr. Biol.* **27**, 3783-3795.e8 (2017).

158. Haas, A. J. *et al.* Interplay between Extracellular Matrix Stiffness and JAM-A Regulates Mechanical Load on ZO-1 and Tight Junction Assembly. *Cell Rep.* **32**, 107924 (2020).

159. Hayakawa, K., Tatsumi, H. & Sokabe, M. Actin filaments function as a tension sensor by tension-dependent binding of cofilin to the filament. *J. Cell Biol.* **195**, 721–727 (2011).

160. Uyeda, T. Q. P., Iwadate, Y., Umeki, N., Nagasaki, A. & Yumura, S. Stretching actin filaments within cells enhances their affinity for the myosin ii motor domain. *PLoS One* **6**, (2011).

161. Ohashi, K., Fujiwara, S. & Mizuno, K. Roles of the cytoskeleton, cell adhesion and rho signalling in mechanosensing and mechanotransduction. *J. Biochem.* **161**, 245–254 (2017).

162. Stewart, R. M. *et al.* Nuclear-cytoskeletal linkages facilitate cross talk between the nucleus and intercellular adhesions. *J. Cell Biol.* **209**, 403–418 (2015).

163. Aureille, J., Belaadi, N. & Guilluy, C. Mechanotransduction via the nuclear envelope: a distant reflection of the cell surface. *Curr. Opin. Cell Biol.* **44**, 59–67 (2017).

164. Le, H. Q. *et al.* Mechanical regulation of transcription controls Polycomb-mediated gene silencing during lineage commitment. *Nat. Cell Biol.* **18**, 864–875 (2016).

165. Ihalainen, T. O. *et al.* Differential basal-to-apical accessibility of lamin A/C epitopes in the nuclear lamina regulated by changes in cytoskeletal tension. *Nat. Mater.* **14**, 1252–1261 (2015).

166. Uhler, C. & Shivashankar, G. V. Regulation of genome organization and gene expression by nuclear mechanotransduction. *Nat. Rev. Mol. Cell Biol.* **18**, 717–727 (2017).

167. Lammerding, J. & Kirby, T. J. Emerging views of the nucleus as a cellular mechanosensor. *Nat. Cell Biol.* **20**, 373–381 (2018).

168. Serrano Cardona, L. & Muñoz Mata, E. Paraninfo Digital. *Early Hum. Dev.* **83**, 1–11 (2013).

169. Mao, Y. & Baum, B. Tug of war–The influence of opposing physical forces on epithelial cell morphology. *Dev. Biol.* **401**, 92–102 (2015).

170. Wolfenson, H., Yang, B. & Sheetz, M. P. Steps in Mechanotransduction Pathways that Control Cell Morphology. *Annu. Rev. Physiol.* **81**, 585–605 (2019).

171. Bonnet, I. *et al.* Mechanical state, material properties and continuous description of an epithelial tissue. *J. R. Soc. Interface* **9**, 2614–2623 (2012).

172. Sadeghipour, E., Garcia, M. A., Nelson, W. J. & Pruitt, B. L. Shear-induced damped oscillations in an epithelium depend on actomyosin contraction and E-cadherin cell adhesion. *Elife* **7**, 1–16 (2018).

173. Brugués, A. *et al.* Forces driving epithelial wound healing. *Nat. Phys.* **10**, 683–690 (2014).

174. Staddon, M. F., Cavanaugh, K. E., Munro, E. M., Gardel, M. L. & Banerjee, S. Mechanosensitive Junction Remodeling Promotes Robust Epithelial Morphogenesis. *Biophys. J.* **117**, 1739–1750 (2019).

175. Cavanaugh, K. E., Staddon, M. F., Munro, E., Banerjee, S. & Gardel, M. L. RhoA Mediates Epithelial Cell Shape Changes via Mechanosensitive Endocytosis. *Dev. Cell* **52**, 152-166.e5 (2020).

176. Khalilgharibi, N. *et al.* Stress relaxation in epithelial monolayers is controlled by the actomyosin cortex. *Nat. Phys.* **15**, 839–847 (2019).

177. Tetley, R. J. & Mao, Y. The same but different: Cell intercalation as a driver of tissue deformation and fluidity. *Philos. Trans. R. Soc. B Biol. Sci.* **373**, 20170328 (2018).

178. Kim, T., Gardel, M. L. & Munro, E. D. Determinants of fluidlike behavior and effective viscosity in cross-linked actin networks. *Biophys. J.* **106**, 526–534 (2014).

179. McFadden, W. M., McCall, P. M., Gardel, M. L. & Munro, E. M. Filament turnover tunes both force generation and dissipation to control long-range flows in a model actomyosin cortex. *PLoS Comput. Biol.* **13**, 1–27 (2017).

180. Iyer, K. V., Piscitello-Gómez, R., Paijmans, J., Jülicher, F. & Eaton, S. Epithelial Viscoelasticity Is Regulated by Mechanosensitive E-cadherin Turnover. *Curr. Biol.* **29**, 578-591.e5 (2019).

181. Clément, R., Dehapiot, B., Collinet, C., Lecuit, T. & Lenne, P. F. Viscoelastic Dissipation Stabilizes Cell Shape Changes during Tissue Morphogenesis. *Curr. Biol.* **27**, 3132-3142.e4 (2017).

182. Wyatt, T. P. J. *et al.* Emergence of homeostatic epithelial packing and stress dissipation through divisions oriented along the long cell axis. *Proc. Natl. Acad. Sci. U. S. A.* **112**, 5726–5731 (2015).

183. Campinho, P. *et al.* Tension-oriented cell divisions limit anisotropic tissue tension in epithelial spreading during zebrafish epiboly. *Nat. Cell Biol.* **15**, 1405–1414 (2013).

184. Bosveld, F. *et al.* Epithelial tricellular junctions act as interphase cell shape sensors to orient mitosis. *Nature* **530**, 495–498 (2016).

185. Marinari, E. *et al.* Live-cell delamination counterbalances epithelial growth to limit tissue overcrowding. *Nature* **484**, 542–545 (2012).

186. Franco, J. J., Atieh, Y., Bryan, C. D., Kwan, K. M. & Eisenhoffer, G. T. Cellular crowding influences extrusion and proliferation to facilitate epithelial tissue repair. *Mol. Biol. Cell* **30**, 1890–1899 (2019).

187. Higashi, T., Arnold, T. R., Stephenson, R. E., Dinshaw, K. M. & Miller, A. L. Maintenance of the Epithelial Barrier and Remodeling of Cell-Cell Junctions during Cytokinesis. *Curr. Biol.* **26**, 1829–1842 (2016).

188. Gudipaty, S. A. & Rosenblatt, J. Epithelial cell extrusion: Pathways and pathologies. *Semin. Cell Dev. Biol.* **67**, 132–140 (2017).

189. Nehls, S., Nöding, H., Karsch, S., Ries, F. & Janshoff, A. Stiffness of MDCK II Cells Depends on Confluency and Cell Size. *Biophys. J.* **116**, 2204–2211 (2019).

190. Paszek, M. J. *et al.* Tensional homeostasis and the malignant phenotype. *Cancer Cell* **8**, 241–254 (2005).

191. Solon, J., Levental, I., Sengupta, K., Georges, P. C. & Janmey, P. A.

Fibroblast adaptation and stiffness matching to soft elastic substrates. *Biophys. J.* **93**, 4453–4461 (2007).

192. Engler, A. J., Sen, S., Sweeney, H. L. & Discher, D. E. Matrix Elasticity Directs Stem Cell Lineage Specification. *Cell* **126**, 677–689 (2006).

193. Lo, C. M., Wang, H. B., Dembo, M. & Wang, Y. L. Cell movement is guided by the rigidity of the substrate. *Biophys. J.* **79**, 144–152 (2000).

194. Vincent, L. G., Choi, Y. S., Alonso-Latorre, B., del Álamo, J. C. & Engler, A. J. Mesenchymal stem cell durotaxis depends on substrate stiffness gradient strength. *Biotechnol. J.* **8**, 472–484 (2013).

195. Wong, J. Y., Velasco, A., Rajagopalan, P. & Pham, Q. Directed movement of vascular smooth muscle cells on gradient-compliant hydrogels. *Langmuir* **19**, 1908–1913 (2003).

196. Sunyer, R. *et al.* Collective cell durotaxis emerges from long-range intercellular force transmission. *Science (80-.).* **353**, 1157–1161 (2016).

197. Miron-Mendoza, M., Seemann, J. & Grinnell, F. Collagen fibril flow and tissue translocation coupled to fibroblast migration in 3D collagen matrices. *Mol. Biol. Cell* **19**, 2051–8 (2008).

198. Ma, X. *et al.* Fibers in the extracellular matrix enable long-range stress transmission between cells. *Biophys. J.* **104**, 1410–1418 (2013).

199. Reinhart-King, C. A., Dembo, M. & Hammer, D. A. Cell-cell mechanical communication through compliant substrates. *Biophys. J.* **95**, 6044–6051 (2008).

200. Mullin, J. M., Agostino, N., Rendon-Huerta, E. & Thornton, J. J. Keynote review: Epithelial and endothelial barriers in human disease. *Drug Discov. Today* **10**, 395–408 (2005).

201. Sawada, N. *et al.* Tight junctions and human diseases. *Med. Electron Microsc.* **36**, 147–156 (2003).

202. Gohy, S. *et al.* Altered generation of ciliated cells in chronic obstructive pulmonary disease. *Sci. Rep.* **9**, 1–12 (2019).

203. Kitano, T., Kitajiri, S. I., Nishio, S. Y. & Usami, S. I. Detailed clinical features of deafness caused by a claudin-14 variant. *Int. J. Mol. Sci.* **20**, 1–12 (2019).

204. Claverie-Martin, F. Familial hypomagnesaemia with hypercalciuria and nephrocalcinosis: Clinical and molecular characteristics. *Clin. Kidney J.* **8**, 656–664 (2015).

205. Ribatti, D., Tamma, R. & Annese, T. Epithelial-Mesenchymal Transition in Cancer: A Historical Overview. *Transl. Oncol.* **13**, 100773 (2020).

206. Dongre, A. & Weinberg, R. A. New insights into the mechanisms of epithelial–mesenchymal transition and implications for cancer. *Nat. Rev. Mol. Cell Biol.* **20**, 69–84 (2019).

207. Uko, V., Thangada, S. & Radhakrishnan, K. Liver disorders in inflammatory bowel disease. *Gastroenterol. Res. Pract.* **2012**, (2012).

208. Sarbu, M. I. & Sarbu, N. Musculoskeletal clinical and imaging manifestations in inflammatory bowel diseases. *Open Med.* **14**, 75–84 (2019).

209. Huang, B. L., Chandra, S. & Shih, D. Q. Skin manifestations of inflammatory bowel disease. *Front. Physiol.* **3 FEB**, 1–13 (2012).

210. Jussila, A. *et al.* High and increasing prevalence of inflammatory bowel disease in Finland with a clear North-South difference. *J. Crohn's Colitis* **7**, e256–e262 (2013).

211. Kappelman, M. D., Moore, K. R., Allen, J. K. & Cook, S. F. Recent trends in the prevalence of Crohn's disease and ulcerative colitis in a commercially insured US population. *Dig. Dis. Sci.* **58**, 519–525 (2013).

212. Okabayashi, S., Kobayashi, T. & Hibi, T. Inflammatory Bowel Disease in Japan-Is It Similar to or Different from Westerns?-. *J. Anus, Rectum Colon* **4**, 1–13 (2020).

213. Mankertz, J. *et al.* TNFα up-regulates claudin-2 expression in epithelial HT-29/B6 cells via phosphatidylinositol-3-kinase signaling. *Cell Tissue Res.* **336**, 67–77 (2009).

214. Gitter, A. H., Bendfeldt, K., Schulzke, J. D. & Fromm, M. Leaks in the epithelial barrier caused by spontaneous and TNF-α-induced single-cell apoptosis. *FASEB J.* **14**, 1749–1753 (2000).

215. Marchiando, A. M. *et al.* Caveolin-1-dependent occludin endocytosis is required for TNF-induced tight junction regulation in vivo. *J. Cell Biol.* **189**, 111–126 (2010).

216. Shen, L. Tight junctions on the move: Molecular mechanisms for epithelial barrier regulation. *Ann. N. Y. Acad. Sci.* **1258**, 9–18 (2012).

217. Watson, C. J., Hoare, C. J., Garrod, D. R., Carlson, G. L. & Warhurst, G. Interferon-γ selectively increases epithelial permeability to large molecules by activating different populations of paracellular pores. *J. Cell Sci.* **118**, 5221–5230 (2005).

218. Weber, C. R. *et al.* Epithelial myosin light chain kinase activation induces mucosal interleukin-13 expression to alter tight junction ion selectivity. *J. Biol. Chem.* **285**, 12037–12046 (2010).

219. Clayburgh, D. R. *et al.* Epithelial myosin light chain kinase-dependent barrier dysfunction mediates T cell activation-induced diarrhea in vivo. *J. Clin. Invest.* **115**, 2702–2715 (2005).

220. Sandle, G. I. Pathogenesis of diarrhea in ulcerative colitis: New views on on old problem. *J. Clin. Gastroenterol.* **39**, 49–52 (2005).

221. Martini, E., Krug, S. M., Siegmund, B., Neurath, M. F. & Becker, C. Mend Your Fences: The Epithelial Barrier and its Relationship With Mucosal Immunity in Inflammatory Bowel Disease. *Cmgh* **4**, 33–46 (2017).

222. Stallmach, A., Schuppan, D., Riese, H. H., Matthes, H. & Riecken, E. O. Increased collagen type III synthesis by fibroblasts isolated from strictures of patients with Crohn's disease. *Gastroenterology* **102**, 1920–1929 (1992).

223. Shimshoni, E., Yablecovitch, D., Baram, L., Dotan, I. & Sagi, I. ECM remodelling in IBD: Innocent bystander or partner in crime? The emerging role of extracellular molecular events in sustaining intestinal inflammation. *Gut* **64**, 367–372 (2015).

224. Stewart, D. C. *et al.* Quantitative assessment of intestinal stiffness and

associations with fibrosis in human inflammatory bowel disease. *PLoS One* **13**, 1–16 (2018).

225. Johnson, L. A. *et al.* Matrix stiffness corresponding to strictured bowel induces a fibrogenic response in human colonic fibroblasts. *Inflamm. Bowel Dis.* **19**, 891–903 (2013).

226. Rieder, F. & Fiocchi, C. Intestinal fibrosis in IBD - A dynamic, multifactorial process. *Nat. Rev. Gastroenterol. Hepatol.* **6**, 228–235 (2009).

227. Petrey, A. C. & De La Motte, C. A. The extracellular matrix in IBD: A dynamic mediator of inflammation. *Curr. Opin. Gastroenterol.* **33**, 234–238 (2017).

228. Abdelsalam, A., Del Priore, L. & Zarbin, M. A. Drusen in age-related macular degeneration: Pathogenesis, natural course, and laser photocoagulation-induced regression. *Surv. Ophthalmol.* **44**, 1–29 (1999).

229. Bailey, T. A. *et al.* Oxidative Stress Affects the Junctional Integrity of Retinal Pigment Epithelial Cells. *Investig. Ophthalmol. Vis. Sci.* **45**, 675–684 (2004).

230. Ozkaya, E. K., Anderson, G., Dhillon, B. & Bagnaninchi, P. O. Blue-light induced breakdown of barrier function on human retinal epithelial cells is mediated by PKC-ζ over-activation and oxidative stress. *Exp. Eye Res.* **189**, 107817 (2019).

231. Chen, M. & Xu, H. Parainflammation, chronic inflammation, and age-related macular degeneration. *J. Leukoc. Biol.* **98**, 713–725 (2015).

232. Peng, S., Gan, G., Rao, V. S., Adelman, R. A. & Rizzolo, L. J. Effects of proinflammatory cytokines on the claudin-19 rich tight junctions of human retinal pigment epithelium. *Investig. Ophthalmol. Vis. Sci.* **53**, 5016–5028 (2012).

233. Chin, L. K., Xia, Y., Discher, D. E. & Janmey, P. A. Mechanotransduction in cancer. *Curr. Opin. Chem. Eng.* **11**, 77–84 (2016).

234. Ondeck, M. G. *et al.* Dynamically stiffened matrix promotes malignant transformation of mammary epithelial cells via collective mechanical signaling. *Proc. Natl. Acad. Sci. U. S. A.* **116**, 3502–3507 (2019).

235. Northcott, J. M., Dean, I. S., Mouw, J. K. & Weaver, V. M. Feeling stress: The mechanics of cancer progression and aggression. *Front. Cell Dev. Biol.* **6**, 1–12 (2018).

236. Tokuda, S. *et al.* Effects of hydrostatic pressure on carcinogenic properties of epithelia. *PLoS One* **10**, 1–25 (2015).

237. Nisticò, P., Bissell, M. J. & Radisky, D. C. Epithelial-mesenchymal transition: General principles and pathological relevance with special emphasis on the role of matrix metalloproteinases. *Cold Spring Harb. Perspect. Biol.* **4**, 1–10 (2012).

238. Dong, Y. *et al.* Higher matrix stiffness as an independent initiator triggers epithelial-mesenchymal transition and facilitates HCC metastasis. *J. Hematol. Oncol.* **12**, 1–15 (2019).

239. Stowers, R. S. *et al.* Matrix stiffness induces a tumorigenic phenotype in mammary epithelium through changes in chromatin accessibility. *Nat. Biomed. Eng.* **3**, 1009–1019 (2019).

240. Fanning, A. S. & Anderson, J. M. Zonula occludens-1 and -2 are cytosolic scaffolds that regulate the assembly of cellular junctions. *Ann. N. Y. Acad. Sci.* **1165**, 113–120 (2009).

241. Richter, J. F. *et al.* Occludin knockdown is not sufficient to induce transepithelial macromolecule passage. *Tissue Barriers* **7**, 1–14 (2019).

242. Clarke, L. L. A guide to Ussing chamber studies of mouse intestine. *Am. J. Physiol. - Gastrointest. Liver Physiol.* **296**, (2009).

243. Amasheh, S. *et al.* Claudin-2 expression induces cation-selective channels in tight junctions of epithelial cells. *J. Cell Sci.* **115**, 4969–4976 (2002).

244. Shen, L. *et al.* Myosin light chain phosphorylation regulates barrier function by remodeling tight junction structure. *J. Cell Sci.* **119**, 2095–2106 (2006).

245. Pitkänen, L., Ranta, V. P., Moilanen, H. & Urtti, A. Permeability of retinal pigment epithelium: Effects of permeant molecular weight and lipophilicity. *Investig. Ophthalmol. Vis. Sci.* **46**, 641–646 (2005).

246. Mari Hämäläinen, K., Kontturi, K., Auriola, S., Lasse Murtomäki & Urtti, A. Estimation of pore size and pore density of biomembranes from permeability measurements of polyethylene glycols using an effusion-like approach. *J. Control. Release* **49**, 97–104 (1997).

247. Van Itallie, C. M. & Anderson, J. M. Measuring size-dependent permeability of the tight junction using PEG profiling. *Methods Mol. Biol.* **762**, 1–11 (2011).

248. Pongkorpsakol, P., Turner, J. R. & Zuo, L. Culture of Intestinal Epithelial Cell Monolayers and Their Use in Multiplex Macromolecular Permeability Assays for In Vitro Analysis of Tight Junction Size Selectivity. *Curr. Protoc. Immunol.* **131**, 1–24 (2020).

249. Richter, J. F., Schmauder, R., Krug, S. M., Gebert, A. & Schumann, M. A novel method for imaging sites of paracellular passage of macromolecules in epithelial sheets. *J. Control. Release* **229**, 70–79 (2016).

250. Reiche, J., Schumann, M. & Richter, J. F. The Sandwich Assay: A Method for Subcellular Visualization of Paracellular Macromolecule Passage in Epithelial Sheets. *Curr. Protoc. Cell Biol.* **78**, 20.10.1-20.10.13 (2018).

251. Li, H., Sheppard, D. N. & Hug, M. J. Transepithelial electrical measurements with the Ussing chamber. *J. Cyst. Fibros.* **3**, 123–126 (2004).

252. Günzel, D. *et al.* From TER to trans- and paracellular resistance: Lessons from impedance spectroscopy. *Ann. N. Y. Acad. Sci.* **1257**, 142–151 (2012).

253. Gerasimenko, T. *et al.* Impedance Spectroscopy as a Tool for Monitoring Performance in 3D Models of Epithelial Tissues. *Front. Bioeng. Biotechnol.* **7**, (2020).

254. Benson, K., Cramer, S. & Galla, H. J. Impedance-based cell monitoring: Barrier properties and beyond. *Fluids Barriers CNS* **10**, 1–11 (2013).

255. Gitter, A. H., Bertog, M., Schulzke, J. D. & Fromm, M. Measurement of paracellular epithelial conductivity by conductance scanning. *Pflugers Arch. Eur. J. Physiol.* **434**, 830–840 (1997).

256. Chen, C. C., Zhou, Y., Morris, C. A., Hou, J. & Baker, L. A. Scanning ion conductance microscopy measurement of paracellular channel

conductance in tight junctions. *Anal. Chem.* **85**, 3621–3628 (2013).

257. Sugimura, K., Lenne, P. F. & Graner, F. Measuring forces and stresses in situ in living tissues. *Dev.* **143**, 186–196 (2016).

258. Unal, M. *et al.* Micro and Nano-Scale Technologies for Cell Mechanics. *Nanobiomedicine* **1**, 1–29 (2014).

259. Roca-Cusachs, P., Conte, V. & Trepat, X. Quantifying forces in cell biology. *Nat. Cell Biol.* **19**, 742–751 (2017).

260. Yang, C. *et al.* Mechanical dynamics in live cells and fluorescence-based force/tension sensors. *Biochim. Biophys. Acta - Mol. Cell Res.* **1853**, 1889–1904 (2015).

261. Jurchenko, C. & Salaita, K. S. Lighting Up the Force: Investigating Mechanisms of Mechanotransduction Using Fluorescent Tension Probes. *Mol. Cell. Biol.* **35**, 2570–2582 (2015).

262. Trepat, X. *et al.* Physical forces during collective cell migration. *Nat. Phys.* **5**, 426–430 (2009).

263. Onochie, O. E., Zollinger, A., Rich, C. B., Smith, M. & Trinkaus-Randall, V. Epithelial cells exert differential traction stress in response to substrate stiffness. *Exp. Eye Res.* **181**, 25–37 (2019).

264. Malinverno, C. *et al.* Endocytic reawakening of motility in jammed epithelia. *Nat. Mater.* **16**, 587–596 (2017).

265. Ambrosi, D., Duperray, A., Peschetola, V. & Verdier, C. Traction patterns of tumor cells. *J. Math. Biol.* **58**, 163–181 (2009).

266. Tambe, D. T. *et al.* Collective cell guidance by cooperative intercellular forces. *Nat. Mater.* **10**, 469–475 (2011).

267. Molladavoodi, S., Kwon, H. J., Medley, J. & Gorbet, M. Human corneal epithelial cell response to substrate stiffness. *Acta Biomater.* **11**, 324–332 (2015).

268. Trepat, X. *et al.* Effect of stretch on structural integrity and micromechanics of human alveolar epithelial cell monolayers exposed to

thrombin. *Am. J. Physiol. - Lung Cell. Mol. Physiol.* **290**, 1104–1110 (2006).

269. Gudipaty, S. A. *et al.* Mechanical stretch triggers rapid epithelial cell division through Piezo1. *Nature* **543**, 118–121 (2017).

270. Rentzsch, I. *et al.* Variable stretch reduces the pro-inflammatory response of alveolar epithelial cells. *PLoS One* **12**, 1–16 (2017).

271. Harris, A. R. *et al.* Characterizing the mechanics of cultured cell monolayers. *Proc. Natl. Acad. Sci. U. S. A.* **109**, 16449–16454 (2012).

272. Oakes, P. W. *et al.* Optogenetic control of RhoA reveals zyxin-mediated elasticity of stress fibres. *Nat. Commun.* **8**, (2017).

273. Valon, L., Marín-Llauradó, A., Wyatt, T., Charras, G. & Trepat, X. Optogenetic control of cellular forces and mechanotransduction. *Nat. Commun.* **8**, 14396 (2017).

274. Motta, S. & Pappalardo, F. Mathematical modeling of biological systems. *Brief. Bioinform.* **14**, 411–422 (2013).

275. Cobelli, C. & Carson, E. *Introduction to Modeling in Physiology and Medicine. Introduction to Modeling in Physiology and Medicine* (Academic Press, 2008). doi:10.1016/B978-0-12-160240-6.X5001-7.

276. Brodland, G. W. How computational models can help unlock biological systems. *Semin. Cell Dev. Biol.* **47–48**, 62–73 (2015).

277. Glynn, P., Unudurthi, S. D. & Hund, T. J. Mathematical modeling of physiological systems: An essential tool for discovery. *Life Sci.* **111**, 1–5 (2014).

278. Viceconti, M. *et al.* In silico trials: Verification, validation and uncertainty quantification of predictive models used in the regulatory evaluation of biomedical products. *Methods* **185**, 120–127 (2021).

279. Henninger, H. B., Reese, S. P., Anderson, A. E. & Weiss, J. A. Validation of computational models in biomechanics. *Proc. Inst. Mech. Eng. Part H J. Eng. Med.* **224**, 801–812 (2010).

280. Mac Gabhann, F. *et al.* Protein transport to choroid and retina following

periocular injection: Theoretical and experimental study. *Ann. Biomed. Eng.* **35**, 615–630 (2007).

281. Amrite, A. C., Edelhauser, H. F. & Kompella, U. B. Modeling of corneal and retinal pharmacokinetics after periocular drug administration. *Investig. Ophthalmol. Vis. Sci.* **49**, 320–332 (2008).

282. Ranta, V. P. *et al.* Barrier analysis of periocular drug delivery to the posterior segment. *J. Control. Release* **148**, 42–48 (2010).

283. Balachandran, R. K. & Barocas, V. H. Computer modeling of drug delivery to the posterior eye: Effect of active transport and loss to choroidal blood flow. *Pharm. Res.* **25**, 2685–2696 (2008).

284. Jooybar, E., Abdekhodaie, M. J., Farhadi, F. & Cheng, Y. L. Computational modeling of drug distribution in the posterior segment of the eye: Effects of device variables and positions. *Math. Biosci.* **255**, 11–20 (2014).

285. Davies, A. E., Williams, R. L., Lugano, G., Pop, S. R. & Kearns, V. R. In vitro and computational modelling of drug delivery across the outer blood–retinal barrier. *Interface Focus* **10**, (2020).

286. Pecoraro, B. *et al.* Predicting Skin Permeability by Means of Computational Approaches: Reliability and Caveats in Pharmaceutical Studies. *J. Chem. Inf. Model.* **59**, 1759–1771 (2019).

287. Kidron, H., Vellonen, K. S., Del Amo, E. M., Tissari, A. & Urtti, A. Prediction of the corneal permeability of drug-like compounds. *Pharm. Res.* **27**, 1398–1407 (2010).

288. Subramanian, G. & Kitchen, D. B. Computational approaches for modeling human intestinal absorption and permeability. *J. Mol. Model.* **12**, 577–589 (2006).

289. Schmid, T., Bogdan, M. & Günzel, D. Discerning Apical and Basolateral Properties of HT-29/B6 and IPEC-J2 Cell Layers by Impedance Spectroscopy, Mathematical Modeling and Machine Learning. *PLoS One* **8**, 1–12 (2013).

290. Pak, J. *et al.* Computational modeling of drug transport across the in vitro

cornea. *Comput. Biol. Med.* **92**, 139–146 (2018).

291. Eriksson, J. *et al.* Pulmonary absorption – estimation of effective pulmonary permeability and tissue retention of ten drugs using an ex vivo rat model and computational analysis. *Eur. J. Pharm. Biopharm.* **124**, 1–12 (2018).

292. Naegel, A., Heisig, M. & Wittum, G. Detailed modeling of skin penetration-An overview. *Adv. Drug Deliv. Rev.* **65**, 191–207 (2013).

293. Yu, J. Y. & Rosania, G. R. Cell-based multiscale computational modeling of small molecule absorption and retention in the lungs. *Pharm. Res.* **27**, 457–467 (2010).

294. Lanevskij, K. & Didziapetris, R. Physicochemical QSAR Analysis of Passive Permeability Across Caco-2 Monolayers. *J. Pharm. Sci.* **108**, 78–86 (2019).

295. Lieb, W. R. & Stein, W. D. Non-stokesian nature of transverse diffusion within human red cell membranes. *J. Membr. Biol.* **92**, 111–119 (1986).

296. RENKIN, E. M. Filtration, diffusion, and molecular sieving through porous cellulose membranes. *J. Gen. Physiol.* **38**, 225–243 (1954).

297. Dechadilok, P. & Deen, W. M. Hindrance factors for diffusion and convection in pores. *Ind. Eng. Chem. Res.* **45**, 6953–6959 (2006).

298. Adson, A. *et al.* Quantitative approaches to delineate paracellular diffusion in cultured epithelial cell monolayers. *J. Pharm. Sci.* **83**, 1529–1536 (1994).

299. Weber, C. R. Dynamic properties of the tight junction barrier. *Ann. N. Y. Acad. Sci.* **1257**, 77–84 (2012).

300. Conte, V., Muñoz, J. J. & Miodownik, M. A 3D finite element model of ventral furrow invagination in the Drosophila melanogaster embryo. *J. Mech. Behav. Biomed. Mater.* **1**, 188–198 (2008).

301. Allena, R. & Aubry, D. An extensive numerical simulation of the cephalic furrow formation in Drosophila embryo. *Comput. Methods Biomech. Biomed. Engin.* **15**, 445–455 (2012).

302. Chen, H. H. & Brodland, G. W. Cell-level finite element studies of viscous cells in planar aggregates. *J. Biomech. Eng.* **122**, 394–401 (2000).

303. Brodland, G. W., Viens, D. & Veldhuis, J. H. A new cell-based FE model for the mechanics of embryonic epithelia. *Comput. Methods Biomech. Biomed. Engin.* **10**, 121–128 (2007).

304. Brodland, G. W. Computational modeling of cell sorting, tissue engulfment, and related phenomena: A review. *Appl. Mech. Rev.* **57**, 47–76 (2004).

305. Osborne, J. M., Fletcher, A. G., Pitt-Francis, J. M., Maini, P. K. & Gavaghan, D. J. Comparing individual-based approaches to modelling the self-organization of multicellular tissues. *PLOS Comput. Biol.* **13**, e1005387 (2017).

306. Van Liedekerke, P., Palm, M. M., Jagiella, N. & Drasdo, D. Simulating tissue mechanics with agent-based models: concepts, perspectives and some novel results. *Comput. Part. Mech.* **2**, 401–444 (2015).

307. Alert, R. & Trepat, X. Physical Models of Collective Cell Migration. *Annu. Rev. Condens. Matter Phys.* **11**, 77–101 (2020).

308. Hirashima, T., Rens, E. G. & Merks, R. M. H. Cellular Potts modeling of complex multicellular behaviors in tissue morphogenesis. *Dev. Growth Differ.* **59**, 329–339 (2017).

309. Noppé, A. R. Simulating the collective behaviour of a monolayer of epithelial cells using a cellular Potts model. (The University of Queensland, 2018).

310. Pathmanathan, P. *et al.* A computational study of discrete mechanical tissue models. *Phys. Biol.* **6**, 036001 (2009).

311. Meineke, F. A., Potten, C. S. & Loeffler, M. Cell migration and organization in the intestinal crypt using a lattice-free model. *Cell Prolif.* **34**, 253–266 (2001).

312. Mosaffa, P., Asadipour, N., Millán, D., Rodríguez-Ferran, A. & J Muñoz, J. Cell-centred model for the simulation of curved cellular monolayers. *Comput. Part. Mech.* **2**, 359–370 (2015).

313. Van Leeuwen, I. M. M. *et al.* An integrative computational model for intestinal tissue renewal. *Cell Prolif.* **42**, 617–636 (2009).

314. Nagai, T. & Honda, H. A dynamic cell model for the formation of epithelial tissues. *Philos. Mag. B Phys. Condens. Matter; Stat. Mech. Electron. Opt. Magn. Prop.* **81**, 699–719 (2001).

315. Fletcher, A. G., Osborne, J. M., Maini, P. K. & Gavaghan, D. J. Implementing vertex dynamics models of cell populations in biology within a consistent computational framework. *Prog. Biophys. Mol. Biol.* **113**, 299–326 (2013).

316. Alt, S., Ganguly, P. & Salbreux, G. Vertex models: from cell mechanics to tissue morphogenesis. *Philos. Trans. R. Soc. B Biol. Sci.* **372**, 20150520 (2017).

317. Barton, D. L., Henkes, S., Weijer, C. J. & Sknepnek, R. Active Vertex Model for cell-resolution description of epithelial tissue mechanics. *PLoS Comput. Biol.* **13**, 1–34 (2017).

318. Lin, S. Z., Li, B. & Feng, X. Q. A dynamic cellular vertex model of growing epithelial tissues. *Acta Mech. Sin. Xuebao* **33**, 250–259 (2017).

319. Merzouki, A., Malaspinas, O. & Chopard, B. The mechanical properties of a cell-based numerical model of epithelium. *Soft Matter* **12**, 4745–4754 (2016).

320. Aegerter-Wilmsen, T. *et al.* Exploring the effects of mechanical feedback on epithelial topology. *Development* **137**, 499–506 (2010).

321. Schaumann, E. N., Staddon, M. F., Gardel, M. L. & Banerjee, S. Force localization modes in dynamic epithelial colonies. *Mol. Biol. Cell* **29**, 2835–2847 (2018).

322. Koride, S., Loza, A. J. & Sun, S. X. Epithelial vertex models with active biochemical regulation of contractility can explain organized collective cell motility. *APL Bioeng.* **2**, 031906 (2018).

323. TJ, N. Modeling multicellular systems using subcellular elements. *Math Biosci Eng* **2**, 613–24 (2005).

324. Sandersius, S. A., Weijer, C. J. & Newman, T. J. Emergent cell and tissue dynamics from subcellular modeling of active biomechanical processes. *Phys. Biol.* **8**, (2011).

325. van der Sande, M., Kraus, Y., Houliston, E. & Kaandorp, J. A cell-based boundary model of gastrulation by unipolar ingression in the hydrozoan cnidarian Clytia hemisphaerica. *Dev. Biol.* **460**, 176–186 (2020).

326. Tanaka, S., Sichau, D. & Iber, D. LBIBCell: A cell-based simulation environment for morphogenetic problems. *Bioinformatics* **31**, 2340–2347 (2015).

327. Battista, N. A., Strickland, W. C. & Miller, L. A. IB2d : a Python and MATLAB implementation of the immersed boundary method. *Bioinspir. Biomim.* **12**, 036003 (2017).

328. Rejniak, K. A. An immersed boundary framework for modelling the growth of individual cells: An application to the early tumour development. *J. Theor. Biol.* **247**, 186–204 (2007).

329. Peskin, C. S. Flow patterns around heart valves: A numerical method. *J. Comput. Phys.* **10**, 252–271 (1972).

330. Stopka, A., Kokic, M. & Iber, D. Cell-based simulations of biased epithelial lung growth. *Phys. Biol.* **17**, 016006 (2020).

331. Vetter, R. *et al.* Aboave-Weaire's law in epithelia results from an angle constraint in contiguous polygonal lattices. *bioRxiv* 591461 (2019) doi:10.1101/591461.

332. Kokic, M., Iannini, A., Villa-Fombuena, G., Casares, F. & Iber, D. Minimisation of surface energy drives apical epithelial organisation and gives rise to Lewis' law. *bioRxiv* 590729 (2019) doi:10.1101/590729.

333. Tervonen, A., Vainio, I., Nymark, S. & Hyttinen, J. Prediction of passive drug permeability across the blood-retinal barrier. *Pharm. Res.* **31**, 2297–2311 (2014).

334. Verkman, A. S. Solute and macromolecule diffusion in cellular aqueous compartments. *Trends Biochem. Sci.* **27**, 27–33 (2002).

335. Schindelin, J. *et al.* Fiji: An open-source platform for biological-image analysis. *Nat. Methods* **9**, 676–682 (2012).

336. Tervonen, A. & Hyttinen, J. Sensitivity distribution of electrical impedance epithelial measurement systems. in *IFMBE Proceedings* vol. 65 (2018).

337. Malmivuo, J. & Plonsey, R. *Bioelectromagnetism Principles and Applications of Bioelectric. Oxford University Press* (1995).

338. Spadoni, I. *et al.* A gut-vascular barrier controls the systemic dissemination of bacteria. *Science (80-.).* **350**, 830–834 (2015).

339. Liu, S. *et al.* The concept revolution of gut barrier: from epithelium to endothelium. *Int. Rev. Immunol.* **40**, 401–408 (2021).

340. Dicks, L. M. T., Dreyer, L., Smith, C. & van Staden, A. D. A review: The fate of bacteriocins in the human gastro-intestinal tract: Do they cross the gut–blood barrier? *Front. Microbiol.* **9**, 1–14 (2018).

341. Bhattacharya, J. & Matthay, M. A. Regulation and repair of the alveolar-capillary barrier in acute lung injury. *Annu. Rev. Physiol.* **75**, 593–615 (2013).

342. Herold, S., Gabrielli, N. M. & Vadász, I. Novel concepts of acute lung injury and alveolar-capillary barrier dysfunction. *Am. J. Physiol. - Lung Cell. Mol. Physiol.* **305**, (2013).

343. Krug, S. M. Contribution of the tricellular tight junction to paracellular permeability in leaky and tight epithelia. *Ann. N. Y. Acad. Sci.* **1397**, 219–230 (2017).

344. Goodwin, K. *et al.* Basal Cell-Extracellular Matrix Adhesion Regulates Force Transmission during Tissue Morphogenesis. *Dev. Cell* **39**, 611–625 (2016).

345. Na, S. *et al.* Rapid signal transduction in living cells is a unique feature of mechanotransduction. *Proc. Natl. Acad. Sci. U. S. A.* **105**, 6626–6631 (2008).

346. Hu, S., Chen, J., Butler, J. P. & Wang, N. Prestress mediates force propagation into the nucleus. *Biochem. Biophys. Res. Commun.* **329**, 423–428

(2005).

347. Beebe, D. C. Retraction: Sclera-choroid-RPE transport of eight b-blockers in human, bovine, porcine, rabbit, and rat models. *Investig. Ophthalmol. Vis. Sci.* **56**, 1678 (2015).

348. Gong, Y. *et al.* Biochemical and biophysical analyses of tight junction permeability made of claudin-16 and claudin-19 dimerization. *Mol. Biol. Cell* **26**, 4333–4346 (2015).

349. Sonoda, N. *et al.* Clostridium perfringens enterotoxin fragment removes specific claudins from tight junction strands: Evidence for direct involvement of claudins in tight junction barrier. *J. Cell Biol.* **147**, 195–204 (1999).

350. Capaldo, C. T. *et al.* Proinflammatory cytokine-induced tight junction remodeling through dynamic self-assembly of claudins. *Mol. Biol. Cell* **25**, 2710–2719 (2014).

PUBLICATIONS

PUBLICATION
I

Prediction of passive drug permeability across the blood-retinal barrier

Tervonen, A., Vainio, I., Nymark, S. & Hyttinen, J.

Pharmaceutical Research (2014), 31(9): 2297–2311

https://doi.org/10.1007/s11095-014-1325-3

Prediction of Passive Drug Permeability across the Blood-Retinal Barrier

Aapo Tervonen[1,2], Iina Vainio[1,2], Soile Nymark[1,2] & Jari Hyttinen[1,2]

1 BioMediTech, Tampere University of Technology, Tampere, Finland
2 Department of Electronics and Communications Engineering, Tampere University of Technology, Tampere, Finland

RUNNING HEAD: Permeability across the Blood-Retinal Barrier

CORRESPONDING AUTHOR:
Aapo Tervonen
Address: Tampere University of Technology, Box 692, 33101 Tampere, Finland
Email: aapo.tervonen@tut.fi

ABSTRACT

Purpose: The purpose of this study is to develop a computational model of the physical barrier function of the outer blood-retinal barrier (BRB), which are vital for normal retinal function. To our best knowledge no comprehensive models of BRB has been reported.

Methods: The model construction is based on the three-layered structure of the BRB: retinal pigment epithelium (RPE), Bruch's membrane and choriocapillaris endothelium. Their permeabilities we calculated based on the physical theories and experimental material and permeability studies in the literature, which were used to describe diffusional hindrance in specific environments.

Results: Our compartmental BRB model predicts permeabilities with magnitudes similar to the experimental values in the literature. However, due to the small number and varying experimental conditions there is large variability of the available experimental data, rendering validation of the model difficult. The model suggests that the paracellular pathway of the RPE largely defines the total BRB permeability.

Conclusions: Our model is the first BRB model of its level and combines the present knowledge of the BRB barrier function. Furthermore, the model forms a platform for the future model development to be used for the design of new drugs and drug administration systems.

KEYWORDS
Blood-retinal barrier, permeability, structure-based model, compartmental model, lipophilicity

Abbreviations

AMD, age-related macular degeneration; BRB, outer blood-retinal barrier; BrM, Bruch's membrane; CE, choriocapillaris endothelium; Da, Dalton (1 Da = 1.66×10^{-23} kg); ICL, inner collagenous layer; OCL, outer collagenous layer; RPE, retinal pigment epithelium; TJ, tight junctions; Å Ångstrom (1 Å = 1×10^{-10} m)

Notation

D_0 free diffusion coefficient ($m^2\ s^{-1}$); k_B Boltzmann's constant (1.38×10^{-23} J K^{-1}); K_D octanol-water distribution coefficient; M_s solute's molecular mass (Da); P_{BRB} BRB permeability coefficient (m s^{-1}); r_s solute particle's radius (m); T absolute temperature (K); η dynamic viscosity (Pa s)

Retinal pigment epithelium

D_{lat} lateral diffusion coefficient within the membrane ($m^2\ s^{-1}$); $d_{lat,i}$ diffusion distance of ith part of the lateral diffusion pathway (m s^{-1}); d_{RPE} RPE cell flat-to-flat diameter (m); d_{TJp} TJ pore separation (m); h_{LS} lateral space height (m); $H_p(\lambda_p)$ pore hindrance factor; h_{pore} pore height (m); h_{RPE} RPE cell height (m); $H_s(\lambda_s)$ slit hindrance factor; h_{slit} slit height (m); h_{TJ} TJ region height (m); h_{TJs} TJ strand height (m); h_{TJss} TJ strand separation (m); K_{mem} membrane distribution coefficient; l_{cb} cell boundary length per unit area (m m^{-2}); m membrane volume selectivity (Da^{-1}); n_{TJs} TJ strand number; P_{cyt} cytoplasm permeability coefficient (m s^{-1}); P_{lat} lateral diffusion transcellular permeability coefficient (m s^{-1}); $P_{lat,i}$ permeability coefficient of ith part of the lateral diffusion pathway (m s^{-1}); P_{LS} lateral space permeability coefficient (m s^{-1}); P_{mem} membrane permeability coefficient (m s^{-1}); P^0_{mem} membrane permeability coefficient of a theoretical, infinitely small molecule (m s^{-1}); P_{para} paracellular permeability coefficient (m s^{-1}); P_{pore} pore permeability coefficient (m s^{-1}); P_{RPE} RPE permeability coefficient (m s^{-1}); P_{slit} slit permeability coefficient (m s^{-1}); P_{TJ} TJ permeability coefficient (m s^{-1})

P_{TJl} TJ leak pathway permeability coefficient (m s^{-1}); P_{TJp} TJ pore pathway permeability coefficient (m s^{-1}); P_{TJs} TJ strand permeability coefficient (m s^{-1}); P_{TJss} permeability coefficient of the space between TJ strands (m s^{-1}); P_{tr} transverse transcellular permeability coefficient (m s^{-1}); P_{trans} transcellular permeability coefficient (m s^{-1}); r_{pore} pore radius (m); r^*_{RPE} average RPE cell radius (m)

r_{TJp} TJ pore radius (m); W_{LS} lateral space half-width (m); W_s slit half-width (m); α_{leak} TJ leak parameter; $\epsilon_{lat,i}$ hindrance factor of ith part of the lateral diffusion pathway (m s^{-1}); ϵ_{LS} relative surface area of the lateral space; ϵ_{pore} relative surface area of the pores; ϵ_{slit} relative surface area of the slit

ϵ_{TJp} relative surface area of the TJ pores; τ_{RPE} RPE lateral space tortuosity

Bruch's membrane

$D_{eff,m}$ effective diffusion coefficient within the matrix m ($m^2\ s^{-1}$); D_{ICL} effective diffusion coefficient within ICL ($m^2\ s^{-1}$); d_{ICL} ICL thickness (m); D_{OCL} effective diffusion coefficient within OCL ($m^2\ s^{-1}$)

d_{OCL} OCL thickness (m); D_m diffusion coefficient within the matrix m ($m^2\ s^{-1}$); f adjusted fiber volume fraction; F_m hydrodynamic interactions in matrix m; P_{BrM} BrM permeability coefficient (m s^{-1}); P_{ICL} ICL permeability coefficient (m s^{-1}); P_{OCL} OCL permeability coefficient (m s^{-1}); r_{CF} collagen fibril radius (m); r_f fiber radius (m); r_{PG} proteoglycan radius (m); S_m steric interactions in matrix m; $\varphi_{CF,ICL}$ collagen volume fraction in ICL; $\varphi_{CF,OCL}$ collagen volume fraction in OCL; Φ_m partition coefficient between the matrix m and solvent; φ_f fiber volume fraction; $\varphi_{PG,ICL}$ proteoglycan volume fraction in ICL; $\varphi_{PG,OCL}$ proteoglycan volume fraction in OCL

Choriocapillaris endothelium

h_{fen} fenestration height (m); P_{CE} CE permeability coefficient (m s^{-1}); r_{dia} diaphragm pore radius (m); ϵ_{dia} relative surface area of the diaphragm pores

Introduction

An important part of the blood-ocular barrier is the outer blood-retinal barrier (BRB), which is a three-layered structure in the eye, between the retina and choroid. It has many important roles in normal retinal function. It forms the barrier between the systemic blood circulation and the delicate retinal environment. In addition, the BRB is the primary location for many retinal diseases, most notably age-related macular degeneration (AMD), which causes visual impairment or even loss of vision (1,2). In this article, we describe a computational, structure-based model of passive diffusion across the BRB for the prediction of molecular permeability.

The BRB forms a challenge for drug administration against the retinal diseases because it retards the passive drug permeation from the systemic circulation. Moreover, also the anterior administration pathways that avoid the BRB, such as eye drops or intraocular injections, have their disadvantages (3). Nowadays, an emerging administration pathway is through the sclera, which is more permeable than the cornea and closer to the retina. Transscleral drug delivery is more targeted than systemic administration or eye drops, and less risky than intraocular injections. However, with this type of administration as well the BRB forms a barrier against the drug permeation (3). In order to improve transscleral drug delivery systems, detailed model of the BRB barrier properties is well warranted.

The BRB consists of three components: retinal pigment epithelium (RPE), Bruch's membrane (BrM) and choriocapillaris endothelium (CE). RPE is formed by a monolayer of pigment RPE cells, and it is the tightest component, largely because of the tight junctions (TJ) between the cells (2). RPE lies on the BrM, which is a thin extracellular matrix layer and forms a passive barrier against the diffusion (4). CE is a fenestrated endothelium and it is the most permeable component in the BRB (2). Permeability of a molecule through these layers is determined by its physicochemical properties, such as size and lipophilicity (5), which further define interactions between the molecule and the BRB components.

Computational models based on the properties of the diffusing molecule and the tissue material properties and structure as well as physical laws may provide an easy and inexpensive method to better understand the components and behavior of BRB barrier properties. In addition, a validated model of BRB could be used to design and validate *in vitro* BRB models for drug development and delivery systems. At the moment, there are no such models available. There is only few computational diffusion models that include the BRB, most of which are pharmacokinetic models (6–8) with phenomenological characteristics. Many of the existing models describe the BRB with a single permeability coefficient (6,7,9) and one model uses three coefficients for different molecule types (8). The model by Haghjou et al. (10) took a step further relating the physicochemical properties of the molecule to the permeability across the retina, choroid and sclera. In all of these models, the BRB plays only a small role, because all the layers of the eye (6–8) or even the whole eye (9,10) are included in the models. However, for some other tissues there are more detailed and structure-based models of other anatomical barriers, such as cornea (11,12) and skin (13), which are based on the properties of both the molecule and the tissue material and structure of the barrier. This kind of models can connect the permeability of a molecule to its interactions with the barrier and provide information about the actual diffusion pathway and rate-limiting components.

In the present study, we introduce a structure-based, compartmental computational model based on the physical laws of passive diffusion across human BRB. To our knowledge, such model has not been published earlier. Our model, reflecting the corneal model of Edwards & Prausnitz (12), aims to relate the properties of the molecule, such as the lipophilicity and radius, to the permeability of the material and to the tissue diffusion pathways. Also, we introduce a TJ model structure for epithelial model. We gather the present knowledge regarding the structural components of the BRB by providing the structural parameters of the model. These were extracted either directly from the literature or were approximated based on available data. Furthermore, we provide parameter sensitivity analysis indicating the importance of given parameters in BRB modeling. In addition, we summarize and discuss the characteristics of the presently available experimental data of BRB permeability. Altogether, the model combines our present knowledge of the BRB passive diffusion-based barrier properties.

Methods

The main function of the model is to product permeability coefficients for each component and pathway of the diffusion across the BRB based on the given molecular property inputs. The RPE and BrM models largely based on the computational framework established for corneal diffusion model by Edwards & Prausnitz (11,12). The two barriers are similar in many ways: they both consist of an pithelium, an extracellular matrix layer and an endothelium. There are some major differences, such as the thickness of the extracellular matrix layer and the number of the cell layers (2,12). The main differences between their and our models result from these tissue characteristics as well as from some refined equations used in the present model. Equations used or based on the equation by them are 2, 4, 11–13, 17, 20, 21 and 24. All the calculations were performed with MATLAB (version R2012a, The MathWorks, Inc., Natick, Massachusetts, United States).

The diffusion pathways and the geometry of the model

The three components of the BRB and the way they are divided into the main pathways and permeability subcomponents are shown in Fig. 1. RPE is divided into two main pathways: the paracellular pathway between the cells and transcellular pathway through the cells. The latter is further divided into two: transverse diffusion across the cell membranes and cytoplasm and lateral diffusion along the cell membrane. The geometrical basis of the compartmental RPE model is presented in Fig. 2. The hexagonal RPE cells are presented with perfect hexagonal cylinders, ignoring the more detailed surface characteristics (Fig. 2a). Small space is left between the neighboring cells to represent the lateral space, which is closed near the apical membrane by TJs (Fig. 2c). The web-like structure of the TJs (14) is modeled with parallel strands that encircle the cells (Fig 2b). Two pathways are modeled for the TJs: small molecules can pass through small pores formed between so-called 10-nm particles in the strands and larger molecules through the breaks in the strands, caused by their dynamic nature (14). A similar dual pathway model was introduced by Guo et al. (15) as they determined the structure of the TJs in renal tubules.

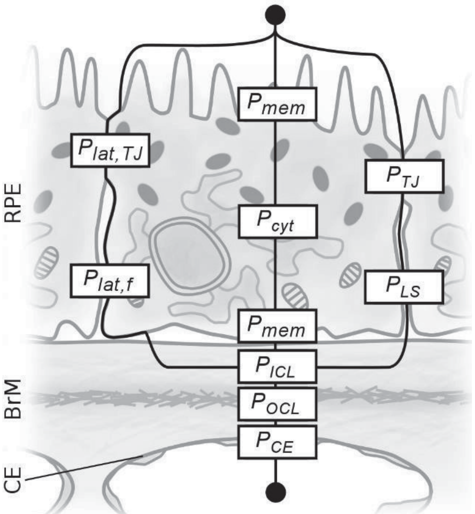

Figure 1. The pathways and their subcomponents across the BRB (RPE, retinal pigment epithelium; BrM, Bruch's membrane; CE, Choriocapillaris endothelium; $P_{lat,TJ}$, permeability of the lateral pathway TJ component; $P_{lat,f}$, permeability of the lateral pathway free component; P_{mem}, membrane permeability; P_{cyt}, cytosol permeability; P_{TJ}, TJ permeability; P_{LS}, lateral space permeability; P_{ICL}, inner collagenous layer permeability; P_{OCL}, outer collagenous layer permeability; P_{CE}, choriocapillaris endothelium permeability)

BrM is modeled with two collagenous layers – the inner (ICL) and outer collagenous layers (OCL) – which form the bulk of it. Both layers are represented with randomly oriented collagen fibrils and ground substance consisting of proteoglycans, which more or less corresponds to the real BrM structure (4). The main differences between the layers are that ICL is more tightly interwoven and has twice the thickness of the OCL (16).

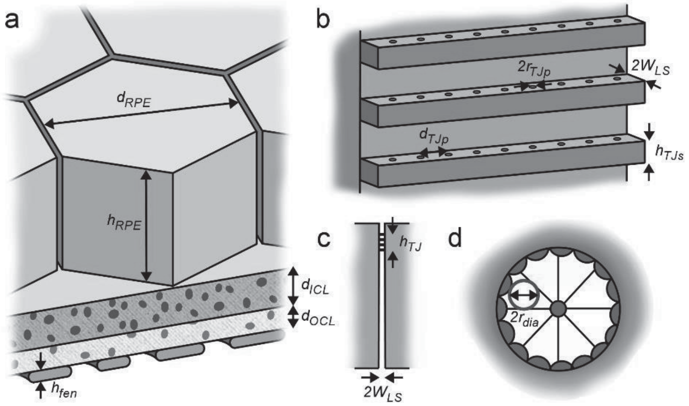

Figure 2. The geometrical idea of the model. a) The three layers of BRB: retinal pigment epithelium RPE, Bruch's membrane and choriocapillaris endothelium (d_{RPE}, RPE flat-to-flat diameter; h_{RPE}, RPE cell height; d_{ICL}, ICL thickness; d_{OCL}, OCL thickness; h_{fen}, fenestration height). b) The geometrical illustration of the TJ model, showing the strands and pores (r_{TJp}, TJ pore radius; WLS, lateral space half-width; d_{TJp}, TJ pore separation; h_{TJs}, TJ strand height). c) The lateral space between the RPE cells, closed off by the TJs on the apical end (h_{TJ}, TJ region height). d) A CE fenestration showing the radial fibrils and the circular pore used to model the openings (r_{fen}, fenestration pore radius)

Because the fenestrations are permeable to even macromolecules, other diffusion pathways are ignored in the CE model. The fenestrations have diaphragms spanning over them, consisting of eight radial fibrils that leave triangular pores between them (Fig. 2d) (17).

Diffusion across the retinal pigment epithelium

In the present work, RPE is modeled by connecting the paracellular and transcellular diffusion pathways in parallel, as described by equation

$$P_{RPE} = P_{para} + P_{trans}, \tag{1}$$

where P_{RPE}, P_{para} and P_{trans} are the permeability coefficients (unit m s^{-1}) of the RPE, paracellular pathway and transcellular pathway, respectively. The main assumption in the model is that a solute cannot change pathway when permeating across the RPE.

Paracellular pathway

The paracellular pathway is modeled with the lateral space and TJs connected in series. A so-called slit model (18) is used to model the lateral space. The permeability coefficient for a solute molecule with a radius of r_s (m) in a slit with a width of $2W_{slit}$ (m) is given as

$$P_{slit} = \frac{\varepsilon_{slit} D_0 H_s (r_s / W_{slit})}{h_{slit}}, \tag{2}$$

where ε_{slit} is the relative surface area of the slit, D_0 is the solute's free diffusion coefficient (m^2 s^{-1}), H_s is the slit hindrance factor as a function of r_s/W_{slit} and h_{slit} is the slit height (m). The slit hindrance factor H_s includes the effects of solute partitioning into the slit as well as the hydrodynamic and steric interactions with its walls. Hydrodynamic interactions are interactions between the solute and the wall mediated by the solvent (19). A function for H_s was determined by Dechadilok & Deen (20) as

$$H_s(\lambda_s) = 1 + \frac{9}{16}\lambda_s \ln\lambda_s - 1.19358\lambda_s + 0.4285\lambda_s{}^3 - 0.3192\lambda_s{}^4 + 0.08428\lambda_s{}^5, \tag{3}$$

where $\lambda_s = r_s/W_{slit}$. The lateral space height is calculated as $h_{LS} = \tau_{RPE}\,(h_{RPE} - h_{TJ})$ (m), where τ_{RPE} is the lateral space tortuosity, h_{RPE} and h_{TJ} are the RPE cell height (m) and TJ region height (m), respectively. For lateral space, the relative surface area can be calculated as

$$\varepsilon_{LS} = 2W_{LS} l_{cb} = 2W_{LS}\left[\left(\frac{2}{\sqrt{3}d_{RPE}^2}\right)\left(\frac{12}{\sqrt{3}}\frac{d_{RPE}}{2}\right)\frac{1}{2}\right], \tag{4}$$

where W_{LS} is the lateral space half-width (m), l_{cb} is the cell boundary length per unit area (m m^{-2}) and d_{RPE} is the hexagonal RPE cell flat-to-flat diameter (m). The part in square brackets is the cell density times the circumference of one cell divided by two to encounter the fact that cell boundaries are calculated twice.

The TJ pore pathway is modeled by connecting n_{TJs} number of parallel strands and ($n_{TJs} - 1$) number of spaces between the strands in series. Each TJ strand is modeled as a barrier having equally spaced pores through it, and the strand permeability is calculated using a so-called pore model (18). The permeability of a solute through pores with a radius of r_{pore} (m) is given by

$$P_{pore} = \frac{\varepsilon_{pore} D_0 H_p (r_s / r_{pore})}{h_{pore}}, \tag{5}$$

where ε_{pore} is the relative surface area of the pores, H_p is the pore hindrance factor as a function of r_s/r_{pore} and h_{pore} is the pore height (m). H_p is analogous to the slit hindrance factor, and its function was determined by Dechadilok & Deen (20) as

$$H_p(\lambda_p) = 1 + \frac{9}{8}\lambda_p \ln \lambda_p - 1.56034\lambda_p + 0.528155\lambda_p{}^2 + 1.91521\lambda_p{}^3 - 2.81903\lambda_p{}^4 + 0.270788\lambda_p{}^5 + 1.10115\lambda_p{}^6 - 0.435933\lambda_p{}^7, \tag{6}$$

where $\lambda_p = r_s/r_{pore}$. The relative surface area of the TJ pores can be calculated as

$$\varepsilon_{TJp} = \pi r_{TJp}^2 \frac{l_{cb}}{d_{TJp}}, \tag{7}$$

where r_{TJp} is the TJ pore radius (m), l_{cb} is calculated as shown in Eq. 4 and d_{TJp} is the TJ pore separation (m). The spaces between strands are modeled with the slit model (Eq. 2), using the same values for ε_{slit} and W_{slit} as with the lateral space but with height $h_{TJss} = (h_{TJ} - n_{TJs}h_{TJs})/(n_{TJs} - 1)$, where h_{TJs} (m) is the TJ strand height. The total TJ pore pathway permeability is calculated as

$$P_{TJp} = \left(\frac{n_{TJs}}{P_{TJs}} + \frac{n_{TJs} - 1}{P_{TJss}} \right)^{-1}, \tag{8}$$

where P_{TJs} is the TJ strand permeability and P_{TJss} is the permeability of the space between the strands.

The TJ leak pathway model does not take into account the TJ strand structure, but this pathway is modeled using the slit model (Eq. 2) and multiplying it with parameter α_{leak}, which describes the amount of strand breaks and the effect of the TJ network structure on the leak pathway permeability. The slit height used in the model is h_{TJ}.

The total TJ permeability can be calculated from equation

$$P_{TJ} = P_{TJp} + P_{TJl}, \tag{9}$$

where P_{TJl} is the TJ leak pathway permeability, and the total paracellular permeability is given by equation

$$P_{para} = \left(\frac{1}{P_{LS}} + \frac{1}{P_{TJ}} \right)^{-1}, \tag{10}$$

where P_{LS} is the lateral space permeability.

Transcellular pathway

In the transcellular pathway, the transverse and lateral diffusion pathways are connected in parallel, similarly to Edwards & Prausnitz (12). The transverse pathway consists of the solute 1) permeating the basolateral cell membrane, 2) diffusing across the cell cytoplasm and 3) permeating the apical cell membrane. The lateral diffusion pathway consists of the solute partitioning into the basolateral cell membrane, diffusing within the cell membrane around the cytoplasm and partitioning out from the membrane in the apical side

The cell membrane permeation model by Edwards & Prausnitz utilized data by Lieb & Stein (21). The present model uses the same data, but the equation parameters (*m*, *A* and *B*) are parameterized based on the molecular mass rather than van der Waals volume used by Lieb & Stein. The cell membrane permeability is given as

$$P_{mem} = P_{mem}^0 10^{-mM_s}, \tag{11}$$

where P^0_{mem} is the membrane permeability of a theoretical, infinitely small molecule, m is the membrane size selectivity (1.355 Da^{-1}) and M_s is the solute's molecular mass (Da). P^0_{mem} as a function of lipophilicity is given by equation

$$\log P^0_{mem} = A \log K_D + B\,, \tag{12}$$

where A and B are fitted parameters with values 1.355 and –3.655, respectively, and K_D is the solute molecule's octanol/water distribution coefficient at pH 7.4. When diffusing through the cytoplasm, the intracellular structures such as mitochondria and endoplasmic reticulum hinder the diffusion rate. The diffusion rate within the cytoplasm is approximately 25 % that of in free solution (22). Thus, the cytoplasm permeability coefficient is

$$P_{cyt} = \frac{0.25 D_0}{h_{RPE}}\,. \tag{13}$$

The lateral diffusion pathway is modeled similarly to Edwards & Prausnitz (12). However, in the present model the pathway is divided into two components, one consisting of the free diffusion in the membrane and the other of the diffusion across the TJs. These two parts are connected in series, as solute partitions into the membrane at the basolateral membrane and diffuses freely until the restricting TJs which hinder the diffusion more, similarly to the paracellular pathway. The permeability of both the free and TJ parts is calculated with equation

$$P_{lat,i} = \frac{\varepsilon_{lat,i} K_{mem} D_{lat}}{d_{lat,i}}\,, \tag{14}$$

where $\varepsilon_{lat,i}$ is a hindrance factor describing the reduction in diffusion rate due to the membrane proteins, K_{mem} is the membrane distribution coefficient, D_{lat} is the lateral diffusion coefficient within the membrane, $d_{lat,i}$ is the diffusion distance and the subscript i is either f or TJ. By assuming that the TJs form a similar barrier against membrane diffusion as with paracellular pathway, it is reasonable to assume that parameter $\varepsilon_{lat,TJ}$ equals α_{leak}. The relation between K_{mem} and K_D was determined by Mitragotri (23) to be

$$K_{mem} = K_D^{0.7}\,. \tag{15}$$

Mitragotri (23) also modeled the diffusion within lipid bilayer and derived equation

$$D_{mem} = 2 \times 10^{-9} \exp\left[-0.46\left(\frac{r_s}{1.62}\right)^2\right], \tag{16}$$

where r_s has the unit of Å. The division of r_s by 1.62 is added to the equation in the present model to account for the different methods the molecular radius is calculated. This is based on the validation and good fit of the Mitragotri's model with measured values (23). Edwards & Prausnitz (12) calculated the total diffusion distance for a cylindrical cell and it can be adapted for RPE as

$$d_{mem,total} = \tau_{RPE} h_{RPE} + \frac{1}{3} r^*_{RPE}\,, \tag{17}$$

where r^*_{RPE} is the average radius of the hexagonal RPE cell, which is given as 1.05 r_{RPE}, with r_{RPE} being the center-to-flat cell radius. The lateral TJ diffusion distance is equal to h_{TJ} and the lateral free diffusion distance is calculated as $d_{mem,f} = d_{mem,total} - h_{TJ}$.

The total transcellular permeability is given as

$$P_{trans} = P_{tr} + P_{lat} = \left(\frac{2}{P_{mem}} + \frac{1}{P_{cyt}} \right)^{-1} + \left(\frac{1}{P_{lat,TJ}} + \frac{1}{P_{lat,free}} \right)^{-1}, \tag{18}$$

and the total RPE permeability is calculated as shown in Eq. 1.

Diffusion across the Bruch's membrane

A model known as fiber matrix model (12) is used for the BrM model, because it describes interactions between the diffusing solute and stationary fibers. The model is constructed in two scales, including larger collagen fibrils and smaller proteoglycan molecules. Both scales and both layers are modeled as randomly oriented fiber matrices.

Effective diffusion coefficient in a fiber matrix is given by equation

$$D_{eff,m} = \Phi_m D_m, \tag{19}$$

where Φ_m is the matrix partition coefficient and D_m is the diffusion coefficient within the matrix (24). The subscript m denotes collagen or proteoglycan matrix in either the ICL or OCL. A common form for Φ_m in randomly oriented fiber matrices was derived by Ogston (25) as

$$\Phi_m = \exp(-f), \tag{20}$$

where

$$f = \phi_f \left(1 + \frac{r_s}{r_f} \right)^2, \tag{21}$$

and ϕ_f is the fiber volume fraction and r_f is the fiber radius (m).

The diffusion coefficient within the matrix includes the hydrodynamic and steric interactions between the fibers and the solute. These two interactions can be separated into separate factors as shown in equation

$$D_m = F_m S_m D_0, \tag{22}$$

where F_m denotes the hydrodynamic and S_m the steric interactions (26). There are several approaches to calculate each of these factors. For hydrodynamic interactions, a form introduced by Clague & Phillips (27) is used in the present model and is given as

$$F_m = \exp\left(-a\phi_f^b\right), \tag{23}$$

where a and b are fitted parameters that depend on r_s and r_f. A fit proposed by Amsden (28) is used with parameter values $a = \pi$ and $b = 0.174 \ln(59.6\, r_f / r_s)$. Steric interactions are modeled with a commonly used equation derived by Johansson & Löfroth (19):

$$S_f = \exp\left(-0.84 f^{1.09}\right). \tag{24}$$

To define the effective diffusion coefficients within the ICL or OCL, first the effective proteoglycan matrix diffusion coefficients are calculated. This is followed by the calculation of the effective collagen matrix diffusion coefficients, while using the effective proteoglycan matrix diffusion coefficients instead of D_0 as the base diffusion coefficient in Eq. 22. The BrM permeability coefficient is calculated with equation

$$P_{BrM} = \left(\frac{1}{P_{ICL}} + \frac{1}{P_{OCL}} \right)^{-1} = \left(\frac{d_{ICL}}{D_{ICL}} + \frac{d_{OCL}}{D_{OCL}} \right)^{-1}, \tag{25}$$

where d_{ICL} and d_{OCL} are the ICL and OCL thicknesses (m), respectively. The diffusion coefficient within each layer equals to the corresponding effective collagen matrix diffusion coefficient.

Diffusion across the choriocapillaris endothelium

The diaphragms of the CE fenestrations span over the fenestration leaving triangular openings between the fibers. These openings are modeled with circular openings which fit inside these sectors, as presented in Fig. 2d. Because of the circular openings, the fenestrations can be modeled using the pore model already used for the TJ pores (Eq. 5). The relative surface area of the pores is the product of the relative surface area of the attenuated region, the fenestrations in an attenuated region and the diaphragm pores in a fenestration.

Properties of the solute molecules

The molecular properties needed to predict the permeability are free diffusion coefficient, molecular size and lipophilicity. Free diffusion coefficient can be calculated from empirical relationship between the molecular mass and diffusion coefficient derived by Avdeef (29) at 37 °C as

$$D_0 = 9.9 \times 10^{-9} M_s^{-0.453}. \tag{26}$$

This equation was fitted using 147 molecules with molecular mass ranging between 30–1,200 Da and with $R^2 = 0.94$ (29).

A commonly used expression relating diffusion coefficient to molecular radius is Stokes-Einstein equation, which does not work for molecules with a radius of under five times that of the solvents. Due to this, a form of this equation derived by Sutherland (30) is used instead, and it is given as

$$r_s = \frac{k_B T}{4\pi\eta D_0}, \tag{27}$$

where k_B is Boltzmann constant (1.38×10^{-23} J K^{-1}), T is the absolute temperature (K), η is the solvents dynamic viscosity (Pa s). This equation assumes that the solvent molecules can slip past the surface of the solute molecules, contrary to Stokes-Einstein equation. Also, Sutherland equation corresponds well to the average of maximum and minimum molecular projection radii calculated with Marvin Calculator Plugins (MarvinSketch 5.10.1, 2012, ChemAxon, http://www.chemaxon.com) (data not shown). A normal body temperature of 310 K and dynamic viscosity of 0.00069 Pa s are used. The model is mainly limited to molecules with molecular mass of under 1,000 Da. The lipophilicity is represented with distribution coefficients at pH 7.4 and the values are calculated with Marvin Calculator Plugins.

Parameter values

Parameters for RPE

All the parameter values are shown in Table I. The parameters needed for the RPE are the RPE cell and lateral space dimensions, the parameters defining TJs as well as the membrane diffusion hindrance factors. The values of TJ strand height and pore separation are defined by the 10-nm particle structure (14). The TJ region height was measured from images of porcine RPE (31).

Table I The model parameter values

Description	Parameter	Value	Reference
Parameters of the RPE			
RPE cell flat-to-flat diameter	d_{RPE}	10 μm	(36)
RPE cell height	h_{RPE}	12 μm	(36)
Lateral space half-width	W_{LS}	20 nm	(36)
Lateral space tortuosity	τ_{RPE}	1.1	(36)
TJ region height	h_{TJ}	0.4 μm	(31)
TJ strand height	h_{TJs}	10 nm	(14)
TJ strand number	n_{TJs}	4	(37)
TJ pore radius	r_{TJp}	0.82 nm	See text
TJ pore separation	d_{TJp}	10 nm	(14)
TJ leak parameter	α_{leak}	0.0005	See text
Free membrane hindrance factor	$\varepsilon_{lat,f}$	0.42	(38)
Parameters for the BrM			
ICL thickness	d_{ICL}	2 μm	See text
OCL thickness	d_{OCL}	1 μm	See text
Proteoglycan radius	r_{PG}	0.5 nm	(39)
Collagen fibril radius	r_{CF}	30 nm	(4)
Proteoglycan volume fraction in ICL	$\phi_{PG,ICL}$	0.07	See text
Proteoglycan volume fraction in OCL	$\phi_{PG,OCL}$	0.04	See text
Collagen volume fraction in ICL	$\phi_{CF,ICL}$	0.40	See text
Collagen volume fraction in OCL	$\phi_{CF,OCL}$	0.30	See text
Parameters for the CE			
Fenestration height	h_{fen}	20 nm	(31)
Diaphragm pore radius	r_{dia}	3.3 nm	See text
Relative surface area of the diaphragm pores	ε_{dia}	0.0075	See text

The TJ pore radius of 0.44 nm measured by Watson et al. (32) was determined by calculating the Stokes-Einstein radius of the PEG oligomer that barely made it through the TJ pores. By combining the data measured by Watson et al. and the hindrance factor used in our model, the TJ pore radius is calculated to be 0.48 nm. This radius is transformed first into a molecular mass with the method used by Watson, and then a radius comparable to the solutes in this model is calculated with Eq. 26 and 27. The value of the TJ leak parameter is approximated based on the results by Watson et al. (32) from Caco-2 cells and the magnitude scale of the measured choroid-RPE permeabilities discussed later. Also, the approximated value of α_{leak} is close to the calculated value for renal tubules (15). The free membrane diffusion hindrance factor is assumed to be the same as for the lipid molecules.

Parameter for BrM

The parameters needed for the modeling of the BrM are the ICL and OCL thicknesses, as well as the radii and fiber volume fractions of the proteoglycan and collagen fibrils in both the ICL and OCL. The ICL and OCL thicknesses are calculated from the total BrM thickness of 3 μm (2) and the relative thicknesses of the two layers. The proteoglycans are approximated only by the glycosaminoglycan side chains, neglecting the core proteins. Thus the proteoglycan radius is equal to the glycosaminoglycan radius.

There are no data about the fiber volume fraction in the literature, so they were approximated. The collagen volume fraction in the corneal stroma determined from figures in Ref. (33) is approximately 0.27. Based on the differences in images from the corneal stroma (33) and BrM (16), the values for the BrM are estimated to be higher than those of corneal stroma. Parameters $\varphi_{PG,ICL}$ and $\varphi_{PG,OCL}$ are the volume fractions when collagen fibrils are ignored, as they only describe the proteoglycan ground substance (11).

Parameters for CE

The fenestration height, diaphragm pore size and relative surface are of the diaphragm pores are the parameters required for the CE. The diaphragm pore radius is calculated by using the sector angle of 45 degrees and sector radius of 12 nm (34). Federman (35) measured the relative fenestrated area to be 0.60. The surface area of the fenestrations inside the regions is calculated from figures in Ref. (34), resulting in value of 0.25. The relative area of the eight diaphragm pores in a fenestration is calculated by assuming the fenestration radius of 40 nm (34), giving a value of 0.05.

Calculations and experimental permeability data review

The functionality of the BRB model is evaluated by calculating how the permeability of BRB and its components behave as a function of the solute radius and lipophilicity. Value ranges of r_s = 5−9 Å (corresponding to M_s = 163−598 Da) and log K_D = −3…3 are used, as most of the drug molecules for which there are data fit within these limits.

A sensitivity analysis is conducted to study the importance of certain model parameters by increasing and decreasing the value of these parameters one at a time by 25 % and calculating the absolute change in the permeability of the respective BRB component. The parameters chosen for the RPE are n_{TJs}, r_{TJp}, d_{TJp}, α_{leak} and $\varepsilon_{mem,f}$. The first four parameters largely define the TJ model and parameters α_{leak} and $\varepsilon_{mem,f}$ dictate the permeability of the transcellular pathway. The chosen parameters affect both the paracellular and transcellular pathways, so four solutes with different sizes and lipophilicities are used (r_s = 6 and 8 nm and log K_D = −2 and 2) to estimate the effect on permeability. For the BrM, parameters $\phi_{PG,ICL}$, $\phi_{PG,OCL}$, $\phi_{CF,ICL}$ and $\phi_{CF,OCL}$ are chosen, because the fiber volume fractions are the uncertain values in the BrM model. As only the solute size affects diffusion in the BrM, two sizes of solutes are used (r_s = 6 and 8 nm).

A literature review of the available experimental permeability data from BRB and its components is carried out to compare the measured and experimental results from excised animal eyes. Because of the differences in study methods and tissue sources, only studies with multiple solute molecules are included to show the behavior of the permeability. Furthermore, only molecules with the molecular mass of under 1000 Da are included. Also, if there are multiple values within a study measured e.g. with different concentrations or permeation directions, the coefficient most fitting for passive steady-state diffusion is chosen fitting into our model principles. E.g. if there are permeability coefficients for both diffusion directions, the smaller is chosen as the larger value may include the effects of active transport (5). Most permeability studies include choroid, so choroid-RPE system is considered to correspond to BRB and choroid-BrM to BrM. The behavior of choroid-RPE permeability is analyzed only as a function of lipophilicity and, for choroid-BrM permeability, only molecular radius is used. The molecular radius and lipophilicity for the solutes are calculated as described.

Results

Model behavior

RPE, BrM and CE models

The behavior of the RPE transcellular (P_{trans}) and paracellular permeabilities (P_{para}) as a function of solute molecular radius and lipophilicity are presented in Fig. 3a and 3b, respectively. In Fig. 3a, P_{para} decreases logarithmically as the radius increases, but begins to even out with high radii. With all the shown values of log K_D, P_{trans} decreases exponentially with the increasing radius. The change in P_{trans} ranges over four orders of magnitude within the given radius range, compared to the less than one magnitude change in P_{para}. The behaviors of the P_{trans} curves as a function of the radius are similar. As shown in Fig. 3b, lipophilicity has no effect on P_{para}. All three curves for P_{trans} with different radii increase exponentially over four orders of magnitude within the shown lipophilicity range. The transcellular pathway becomes more significant than the paracellular pathway at log $K_D \geq 0$ for small molecules ($r_s < 6$ Å) and, as the lipophilicity increases, it becomes significant also for medium sized molecules ($r_s = 6$–8 Å). For large solutes ($r_s > 8$ Å), the paracellular pathway is the main diffusion pathway independent of lipophilicity within the given value range.

The behavior of BrM (P_{BrM}) and CE permeabilities (P_{CE}) as a function of the solute radius is shown in Fig. 3c. Both P_{BrM} and P_{CE} decrease exponentially as the radius increases. This decrease is, however, slower than the modeled decrease with transcellular permeability, being less than one order of magnitude within the given range of the increasing radius for both P_{BrM} and P_{CE}.

The BRB components are from the tightest to the leakiest: RPE, BrM and CE. RPE is 600 to 3000 times less permeable than BrM for solutes with log $K_D = 0$. For very hydrophilic solutes (log $K_D = -3$) the difference is similar, but for very lipophilic (log $K_D = 3$) and small solutes, the difference is only around 2.7-fold. Also for the given radius range, BrM is on average 4.5 times less permeable than CE.

BRB model

The rate-limiting components for the total BRB permeability in respect to the molecular properties are depicted in Fig. 3d. The paracellular pathway of the RPE is the dominating component for most solutes, as the transcellular pathway mainly sets the permeability for small and lipophilic solutes. The behavior of the total BRB permeabilities as a function of solute radius and lipophilicity is shown in Fig. 3e and 3f, respectively. For hydrophilic solutes, the radius is the main rate-determining property, but with lipophilic solutes both the radius and lipophilicity are important. The differences in permeability caused by the solute properties become more prominent with small and lipophilic molecules.

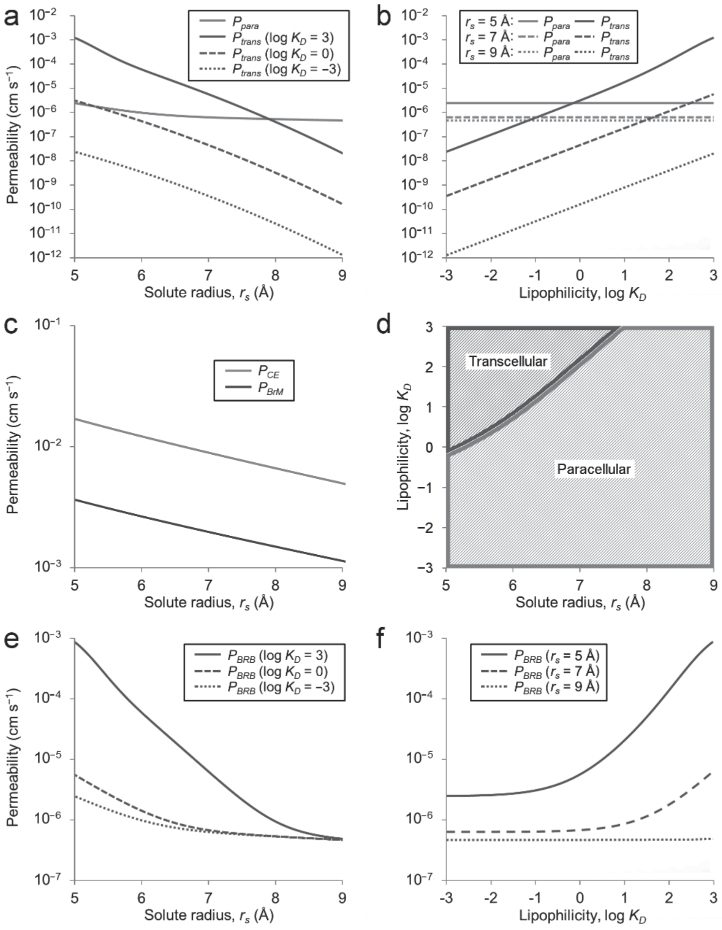

Figure 3. Results of the model behavior. a) paracellular (P_{para}) and transcellular permeabilities (P_{trans}) with three lipophilicities as a function solute radius, b) paracellular and transcellular permeabilities with three radii as a function solute lipophilicity, c) Bruch's membrane (P_{BrM}) and choriocapillaris endothelium permeabilities (P_{CE}) as a function of solute radius, d) the rate-limiting pathway of BRB permeability as a function of solute radius and lipophilicity, and total BRB permeability (P_{BRB}) as a function of e) solute radius with three lipophilicities and f) lipophilicity with three radii

Sensitivity analysis

For RPE, the chosen parameters for the sensitivity analysis were the TJ strand number (n_{TJs}), TJ pore radius (r_{TJp}), TJ pore separation (d_{TJp}), leak parameter (α_{leak}) and free membrane hindrance factor ($\varepsilon_{mem,f}$). The results of this analysis are shown in Fig. 4a. The effect of r_{TJp} on RPE permeability is significant, especially when increasing its value and with small molecules (r_s = 6 Å). For small hydrophilic solutes the increase of r_{TJp} by 25 %, leads to 2.3-fold change in the RPE permeability (P_{RPE}). The changes of α_{leak} values to both direction lead to around 18−25 % change in P_{RPE} for all the solutes, the impact being smaller with small solutes. The effects of both n_{TJs} and d_{TJp} on P_{RPE} are the largest but not significant with small hydrophilic solutes. Finally, there are no notable effects caused by the changes in $\varepsilon_{mem,f}$.

For BrM, the parameters for sensitivity analysis included the proteoglycan and collagen volume fractions in the ICL and OCL ($\phi_{PG,ICL}$, $\phi_{PG,OCL}$, $\phi_{CF,ICL}$ and $\phi_{CF,OCL}$). The results are shown in Fig. 4b. The ICL volume fractions, i.e. $\phi_{PG,ICL}$ and $\phi_{CF,ICL}$, appear to be the most significant, as changes in them lead to respective changes of 15−23 % and 35−47 % in BrM permeability (P_{BrM}). The difference between the two sizes of solutes (r_s = 6 and 8 Å) is generally small, excluding $\phi_{PG,ICL}$ for which there is 4−6 % difference. The changes in both the OCL volume fractions are insignificant.

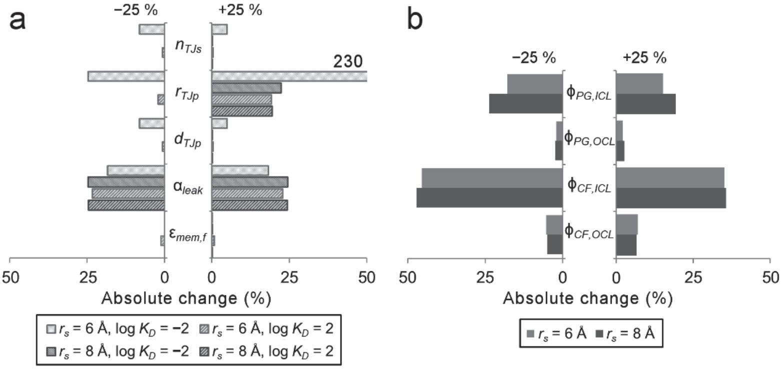

Figure 4. Results of the sensitivity analysis, showing the absolute changes on a) P_{RPE} and b) P_{BrM} when parameter values are changed ± 25 %. The parameters for the RPE: n_{TJs}, TJ strand number; r_{TJp}, TJ pore radius; d_{TJp}, TJ pore separation; α_{leak}, leak parameter; $\varepsilon_{mem,f}$, free membrane hindrance factor), and for the BrM : proteoglycan and collagen volume fractions in the ICL and OCL, $\phi_{PG,ICL}$, $\phi_{PG,OCL}$, $\phi_{CF,ICL}$ and $\phi_{CF,OCL}$)

Review of experimental permeability data

The literature review revealed that the available experimental permeability data is insufficient for the validation of the BRB model. With the given preconditions, 32 independent permeability values were found for choroid-RPE tissue and 23 for choroid-BrM. The choroid-RPE values are from bovine (5,40), porcine (40,41) and rabbit (40) with a lipophilicity range of –2.12…2.79, and those of choroid-BrM from bovine (42), porcine (42,43) and human (44) with a radius range of 3.51–8.10 Å (corresponding to M_s = 75−474 Da). The measured choroid-RPE permeability coefficients as a function of lipophilicity presented so far in the literature are shown in Fig. 5a, excluding the rabbit data as it has similar behavior as the other species in that study (40) and thus does not provide new information. Permeability data of choroid-BrM as a function of molecular radius in presented in Fig. 5b.

As can be seen, there is no clear behavior in the choroid-RPE permeability results as a whole. Two of the studies concluded that the permeability increases as the lipophilicity increases (5,41) while the third one (40) concluded the opposite. There is no systematic difference between the animals. For choroid-BrM, the permeability decreases as a function of the molecular size. However, between two studies (42,43), there are differences of over three orders of magnitude in choroid-BrM permeability for large molecules.

When comparing the results of our model (Fig. 3f) and the measured permeability values (Fig. 5a) for the whole BRB, there is no clear agreement of the behavior as a function of lipophilicity but the magnitudes between the two are in similar scale. Between the predicted and measured values for the BrM, there is a difference of at least one order of magnitude depending on which of the two experimental studies is used and the behavior is similar.

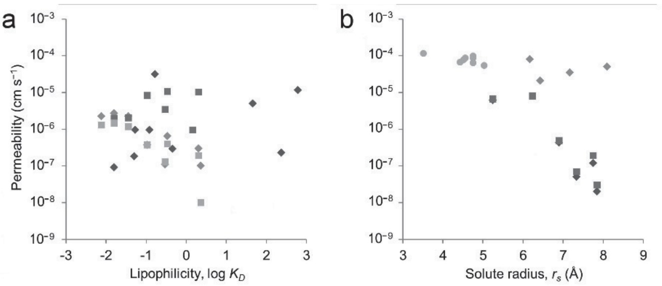

Figure 5. Results for the permeability literature review. a) Choroid-RPE permeability as a function of lipophilicity in porcine (blue diamonds (41) and purple diamonds (40)) and bovine eyes (red squares (5) and green squares (40)) and b) choroid-BrM permeability as a function of solute radius in porcine (blue diamonds (42) and purple diamonds (43)), bovine (red squares (42)) and human eyes (green dots (44))

Discussion

We constructed a model of passive diffusion across the outer blood-retinal barrier (BRB). To our best knowledge, this is the first model for BRB that is based on the physicochemical properties of both the BRB and the diffusion solute molecule, defining the interactions between the two during diffusion. This makes the model suitable for the studies of drug permeation through the BRB, for molecule-specific pharmacokinetic models as well as to help construct *in vitro* BRB models.

The model consists of the three layered structure of the BRB – the retinal pigment epithelium (RPE), Bruch's membrane (BrM) and choriocapillaris endothelium (CE). Although the model is created to represent *in vivo* systemic drug administration, suitable model components can be utilized as needed for other models, such as those for transscleral delivery routes. This three-layer structure is more accurate representation of the BRB than any of the preceding models that include passive diffusion across the BRB. In addition, compared with the corneal model (12) used as a framework for our model, the TJ and treatment of molecular properties model presented here is more detailed in structure.

Our TJ model represents the static biological TJ structure (14) fairly accurately. However, the TJ are a dynamic structure with many factors regulating their function. For example, the physical interactions between the RPE cells and the retinal photoreceptors, chemical secreted factor, pharmacological methods as well as ions like potassium can regulate the permeability of the tight junctions (45,37). In addition to the regulatory factors, the accuracy of our static TJ model could be further enhanced by including the web-like strand structure. Furthermore, including the TJ pore charge selectivity and non-uniform pore sizes and spacing (14) could improve the model but would simultaneously make it more complex.

Model behavior

The present work investigates the permeability behavior of BRB and its parts in relation to the solute radius and lipophilicity. RPE is divided into paracellular and transcellular pathways, which are structurally very different. In the transcellular pathway, the diffusion of the solute dependents on the diffusion of the lipids (13), whereas in the paracellular pathway a route for permeation already exists. Furthermore, the independence of the paracellular pathway of the solute's lipophilicity makes it a general rate-limiting pathway for the solute permeation, because the transcellular permeability decreases rapidly with the decreasing lipophilicity.

When examining the transcellular pathway in more detail, it is notable that that the transverse transcellular pathway is insignificant in comparison with the lateral diffusion transcellular pathway. For instance, for a solute with log $K_D = 2$ and $r_s = 6$ Å, the lateral diffusion pathway is around 50 times more permeable than the transverse pathway. One reason for this may be that the solutes lipophilic enough to partition into a cell membrane tend to remain inside it rather than partition into the aqueous cytosol. The difference between the transverse and lateral diffusion pathways was also noted by Edwards & Prausnitz (12) in their corneal model, and they reasoned it to result from the data used to derive the cell membrane permeation model. The main difference in permeability behavior between our model and the corneal model (12) is that in our model the lateral diffusion pathway depends on the solute size. This can be seen with large solutes ($r_s = 9$ Å) as the permeability does not depend on lipophilicity in our model, unlike in the corneal model with the corresponding solutes (12).

According to our model, the effect of BrM or CE on the total BRB permeability is small due to their higher permeabilities. The simplification of only including the fenestrations in the CE model was justified, as its permeability exceeds both those of RPE and BrM and thus has no effect on the total BRB permeability.

Model parameters

The sensitivity and importance of certain parameters from both the RPE and BrM models was studied by changing their value by 25 % to both directions and calculating the change in the permeability of the respective component. According to our results in the paracellular TJ pathway, the most important parameter is the TJ pore radius (r_{TJp}), which defines the solute size limit for the TJ pore pathway. On the other hand, the uniform changes in permeability of all the four solutes caused by changes in the leak parameter (α_{leak}) indicate that it sets the magnitude for the whole RPE permeability. As the paracellular pathway is generally the rate-limiting one, it is obvious that r_{TJp} and α_{leak} together define the RPE permeability. Neither of these parameters was used in the model by Edwards & Prausnitz (12). Based on the sensitivity analysis on their corneal model, they found the parameters of the lateral diffusion pathway – lateral diffusion coefficient and pathway length – to be the most important parameters for corneal epithelium (12). This indicates relative unimportance of the TJs in their model compared to ours.

With BrM, the main interest is in the approximated proteoglycan and collagen fibril volume fractions. The volume fractions in the ICL ($\phi_{PG,ICL}$ and $\phi_{CF,ICL}$) are significantly more important than those in the OCL ($\phi_{PG,OCL}$ and $\phi_{CF,OCL}$), because of their larger values as well as the difference of thicknesses between the two BrM layers. Furthermore, due to the large amount of collagen, its effects are larger in both layers. The differences between solute sizes are generally miniscule. For collagen this results from the large size difference between the solutes ($r_s < 1$ nm) and fibrils ($r_{CF} = 30$ nm). The solute size difference is more noticeable with $\phi_{PG,ICL}$, because of the similar radius of the solutes and proteoglycans. Edwards & Prausnitz (12) also found that the volume fractions mostly define the permeability of the corneal stroma.

The RPE permeability dominates the total BRB permeability in our model. Therefore it is clear that they are both largely defined by two parameters: the TJ pore radius and the leak parameter. Their importance reflects the mutual significance of both the paracellular and lateral diffusion pathways, as already seen with the model behavior. There was not much data to base the approximations of the important parameters, mainly the leak parameter and the collagen volume fraction in the ICL. As the leak parameter largely defines the magnitude of the total BRB permeability in our model and magnitude is similar between the predictions and the experimental results, it seems the approximation was good. In a very recent study (46), the packing density of collagen fibrils in the ICL, which can be thought to correspond to $\phi_{CF,ICL}$, was calculated to be 0.48. Our approximation ($\phi_{CF,ICL} = 0.40$) is relatively close. The sensitivity analysis shows, that the corresponding 20 % increase of $\phi_{CF,ICL}$ is not enough to make the BrM permeability a significant component in the whole BRB permeability.

Available experimental BRB permeability data

Unfortunately very limited number of studies has been conducted to obtain experimental data of BRB permeability. There are only three studies providing the permeability coefficients of the entire BRB (5,40,41). Steuer et al. (41) used only one measurement time point (30 minutes) to calculate the permeability, which may cause issues due to the longer lag times of lipophilic molecules compared with the hydrophilic ones to reach equilibrium (5). Further, there was conflicting results. The reason for the conflict in behavior between the results by Pitkänen et al. (5) and Kadam et al. (40) may be that the latter calculated the choroid-RPE permeability by subtracting the permeability of the sclera from the permeability of the sclera-choroid-RPE. This may affect the comparability of the permeabilities of solutes with different lipophilicities due to tissue binding in sclera. Moreover, Pitkänen et al. (5) measured only the permeability of the choroid-RPE and because of this, the behavior measured by them can be considered more suitable in relation to the present model. However, it is noteworthy that the magnitudes of the permeabilities of the hydrophilic molecules are similar between Pitkänen et al. (5) and Kadam et al. (40), which indicates that the conflict in behavior is more prominent with lipophilic solutes. Pitkänen et al. (5) also measured the effect of molecular size on the BRB permeability and showed that the permeability decreases as molecular size increases. Their test molecules were beyond the size limit of the present model, but they indicate similar behavior. Furthermore, a factor that may affect the comparability of the experimental permeability results are the regulatory mechanisms that affect the TJ permeability discussed earlier. Due to the very limited amount of the experimental work in the literature, it is practically impossible to validate our BRB model with the available data. However, we can conclude that the model produces permeability coefficients with similar magnitudes and behavior as a function of the molecular properties in comparison with the experimental measurements.

The challenge in measuring the BrM permeability is that it is a very thin tissue layer and thus difficult to extract intact. Thus, all the experimental studies include the choroid in the measurement sample (42–44). Based on the literature review, the BrM permeability decreases as a function of molecular size, but the absolute values for just the BrM permeability are unknown because of the choroid. The magnitude difference between the permeability results by Cheruvu & Kompella (42) and Pescina et al. (43) might be a consequence of the higher solute concentration used by the latter, because high concentrations saturate the tissue with the bound solutes and thus lead to higher permeabilities. Anyhow, our model predicts a permeability coefficient of at least one magnitude higher than the measured permeability values, which may indicate the effect of the choroid on the measured values as well as an issue in the model. This issue may arise from the unsuitability of the fiber matrix model for the BrM, the approximations of the unknown parameter values or the simplifications done in the model.

For 4 kDa FITC-dextrans, there is around 70 to 170-fold difference between the permeabilities across choroid-RPE and choroid-BrM (5). For small molecules, the difference between the two depends on what experimental results are compared. For example, if the values by Kadam et al. (40) and Cheruvu & Kompella (42) – measured with similar setups – are compared, there is no significant difference between them. This may point out a large effect of the choroid and the inaccuracy it causes in the results. Based on the existing data, it is impossible to estimate the real difference between the RPE and BrM permeabilities.

Comparison with other models

The present model includes a structurally more detailed description of the BRB than any of the preceding pharmacokinetic models (6–10). Also, when compared with the corneal model by Edwards & Prausnitz (12), which was used as a framework for our model, there are certain biological differences and model improvements. Firstly, the baseline permeability of the corneal endothelium, which is modeled similarly to the RPE as they are both monolayers, is around one order of magnitude higher than that of the RPE. This permeability is set by the paracellular pathway, and the TJs are tighter in the present RPE model, which corresponds well to the difference in the measured permeabilities from the BRB and cornea (5,12). The TJ geometry is completely different between our model and the corneal model (12). The earlier model used only a narrowed slit to represent TJs and our model used a two-pathway model with more accurate geometry. The TJ structure in our model is similar to the TJ model of the renal tubules by Guo et al. (15), but the motive for the models is different: our model tries to predict the permeabilities, whereas the model of the renal tubules studied the structure of the TJs. The other major difference is the significance of molecular size with lipophilic solutes as discussed before.

The phenomenological descriptive model by Haghjou et al. (10) related certain molecular properties to the permeability across RPE-choroid-sclera in a rabbit eye by using multiple linear regression. The best fit for hydrophilic molecules (log $K_D < 0$) depended on lipophilicity and protein binding. Molecular size was also quite significant factor, but did not contribute to the accuracy of the model. Lipophilicity did not greatly affect the permeability of hydrophilic solutes in the present model, as they generally do not pass any lipophilic barriers. For lipophilic molecules (log $K_D > 0$), Haghjou et al. (10) did not find a good fit with the permeability data, which may partly explain the variability in the choroid-RPE permeability data discussed earlier and the challenge of modeling the transcellular pathway.

Model challenges and limitations

The main challenge in modeling the BRB is the lack of biological experimental data of some of the structural parameters of the BRB and its components. This was compensated by approximating some of their values, such as the leak parameter or the BrM volume fractions, mainly based on obtained from other tissues. The approximation of some important parameters creates uncertainty in the model. Furthermore, as already discussed, the lack of suitable and consistent permeability data prevents proper validation.

As our model is of passive diffusion only, the specific effects of active transport on the permeability are ignored. Active transport processes are specific for each molecule, and thus not suitable for a model based solely on basic molecular descriptors, and there is very little comprehensive data to model them. Although the experimental data may include active transport processes, which reduce the feasibility of comparison between the model and the experimental results, it is at the moment the closest suitable data for the evaluation of the BRB models functionality. Likewise, the model does not take into account the solute binding into extra- or intracellular structures, such as the melanin pigment within the RPE cells. Melanin binding is a specific process and has been shown to affect the permeability (40,43). The dynamic binding is difficult to incorporate into a steady-state model, although a method proposed to include the matrix binding (42) could be used here: diffusion constant (D_{cyt}) is divided by $1 + K$, where K is an association constant specific for each solute, for which there is no extensive experimental data. In addition, this would have only affected the already-insignificant transverse diffusion pathway and our model represents a steady-state situation, where time- and concentration-dependent phenomena are neglected. Also, some refinements for our TJ model were discussed earlier.

For BrM, the accuracy and number of the layers and biomolecules could be increased. In addition to proteoglycans and collagen, BrM contains other biomolecules, such as lipids which accumulate from the RPE and affect the permeability (4). However, the lack of data of all the layers and biomolecules prevents further improvements at this time. Furthermore, as shown by Pescina et al. (43), permeability across choroid-BrM does depend on lipophilicity because by the specific melanin binding in the tissue. However, the choroid is much thicker than the BrM which most probably affects the results significantly, thus making any approximations of its effect solely on BrM difficult. Electrostatic interactions between the fibers and solutes are ignored as well although they could be incorporated into the model (47).

The main simplification with the solute molecules was the assumed spherical shape. Most molecules are irregularly shaped, so for example the orientation of a molecule trying to diffuse through a TJ pore becomes significant. However, the slit, pore and fiber-matrix models also assume this geometry, and it would need statistical or random Markov type models to take into account the individual shape of each molecule.

Conclusions

In this study, a computational, structure-based model of passive diffusion across the BRB was constructed generally based on the corneal model by Edwards & Prausnitz (12). Our model shows rather good correspondence in magnitude with the experimental results. Accurate validation, however, is not feasible due to the lack of consistency in the reported experimental data indicating great variation in the permeability behavior between the studies. Our model indicates that the paracellular pathway of the RPE largely defines the permeability of the whole BRB, the transcellular pathway having some effect with small and lipophilic solutes. The parameter sensitivity analysis shows that many of the parameters we were forced to approximate are important and further studies are needed to define more accurate values for many structural properties of the RPE and BRB as a whole. Despite the lack of data, the model presented here is the most accurate model of passive diffusion through BRB and our TJ model is more accurate than those in the other structure-based models for other barriers. The model gathers the knowledge of the BRB permeability. Thus the model presented her can be used as a base for future BRB models utilizing coming experimental data as well as for testing the hypotheses of BRB permeability for drug molecules. Hence, this type of models has a potential to reduce the need of animal experiments as well as save resources.

Acknowledgments

The study was financially supported by the Academy of Finland (grant numbers 252225 and 260375) and TEKES – the Finnish Funding Agency for Technology and Innovation (grant number 718/31/2011).

References

1. Strauss O. The retinal pigment epithelium in visual function. Physiol Rev. 2005;85(3):845–81.

2. Bhutto I, Lutty G. Understanding age-related macular degeneration (AMD): relationships between the photoreceptor/retinal pigment epithelium/Bruch's membrane/choriocapillaris complex. Mol Aspects Med. 2012;33(4):295–317.

3. Del Amo EM, Urtti A. Current and future ophthalmic drug delivery systems. A shift to the posterior segment. Drug Discov Today. 2008;13(3-4):135–43.

4. Booij JC, Baas DC, Beisekeeva J, Gorgels TGMF, Bergen AAB. The dynamic nature of Bruch's membrane. Prog Retin Eye Res. 2010;29(1):1–18.

5. Pitkänen L, Ranta V-P, Moilanen H, Urtti A. Permeability of retinal pigment epithelium: effects of permeant molecular weight and lipophilicity. Invest Ophthalmol Vis Sci. 2005;46(2):641–6.

6. Mac Gabhann F, Demetriades AM, Deering T, Packer JD, Shah SM, Duh E, et al. Protein transport to choroid and retina following periocular injection: theoretical and experimental study. Ann Biomed Eng. 2007;35(4):615–30.

7. Amrite AC, Edelhauser HF, Kompella UB. Modeling of corneal and retinal pharmacokinetics after periocular drug administration. Invest Ophthalmol Vis Sci. 2008;49(1):320–32.

8. Ranta V-P, Mannermaa E, Lummepuro K, Subrizi A, Laukkanen A, Antopolsky M, et al. Barrier analysis of periocular drug delivery to the posterior segment. J Control Release. 2010;148(1):42–8.

9. Balachandran RK, Barocas VH. Computer modeling of drug delivery to the posterior eye: effect of active transport and loss to choroidal blood flow. Pharm Res. 2008;25(11):2685–96.

10. Haghjou N, Abdekhodaie MJ, Cheng Y-L. Retina-choroid-sclera permeability for ophthalmic drugs in the vitreous to blood direction: quantitative assessment. Pharm Res. 2013;30(1):41–59.

11. Edwards A, Prausnitz MR. Fiber matrix model of sclera and corneal stroma for drug delivery to the eye. AIChE J. 1998;44(1):214–25.

12. Edwards A, Prausnitz MR. Predicted permeability of the cornea to topical drugs. Pharm Res. 2001;18(11):1497–508.

13. Mitragotri S. Modeling skin permeability to hydrophilic and hydrophobic solutes based on four permeation pathways. J Control Release. 2003;86(1):69–92.

14. Anderson JM, Van Itallie CM. Physiology and function of the tight junction. Cold Spring Harb Perspect Biol. 2009;1(2):1–16.

15. Guo P, Weinstein AM, Weinbaum S. A dual-pathway ultrastructural model for the tight junction of rat proximal tubule epithelium. Am J Physiol Renal Physiol. 2003;285(2):F241–57.

16. Goldbaum MH, Madden K. A new perspective on Bruch's membrane and the retinal pigment epithelium. Br J Ophthalmol. 1982 1;66(1):17–25.

17. Bearer EL, Orci L. Endothelial fenestral diaphragms: a quick-freeze, deep-etch study. J Cell Biol. 1985;100(2):418–28.

18. Ho NFH, Raub TJ, Burton PS, Barsuhn CL, Audus KL, Borchardt RT. Quantitative Approaches to Delineate Passive Transport Mechanisms in Cell Culture Monolayers. In: Amidon GL, Lee PI, Topp EM, editors. Transport Processes in Pharmaceutical Systems. New York: Marcel Dekker, Inc; 2000. p. 219–316.

19. Johansson L, Löfroth J-E. Diffusion and interaction in gels and solutions. 4. Hard sphere Brownian dynamics simulations. J Chem Phys. 1993;98(9):7471–9.

20. Dechadilok P, Deen WM. Hindrance Factors for Diffusion and Convection in Pores. Ind Eng Chem Res. 2006;45(21):6953–9.

21. Lieb WR, Stein WD. Non-Stokesian nature of transverse diffusion within human red cell membranes. J Membr Biol. 1986;92(2):111–9.

22. Verkman AS. Solute and macromolecule diffusion in cellular aqueous compartments. Trends Biochem Sci. 2002;27(1):27–33.

23. Mitragotri S. A theoretical analysis of permeation of small hydrophobic solutes across the stratum corneum based on Scaled Particle Theory. J Pharm Sci. 2002;91(3):744–52.

24. Johnson EM, Berk DA, Jain RK, Deen WM. Diffusion and partitioning of proteins in charged agarose gels. Biophys J. Elsevier; 1995;68(4):1561–8.

25. Ogston AG. The spaces in a uniform random suspension of fibres. Trans Faraday Soc. 1958;54(1):1754–7.

26. Phillips RJ. A hydrodynamic model for hindered diffusion of proteins and micelles in hydrogels. Biophys J. 2000;79(6):3350–3.

27. Clague DS, Phillips RJ. Hindered diffusion of spherical macromolecules through dilute fibrous media. Phys Fluids. 1996;8(7):1720–31.

28. Amsden B. Solute Diffusion within Hydrogels. Mechanisms and Models. Macromolecules. 1998;31(23):8382–95.

29. Avdeef A. Leakiness and size exclusion of paracellular channels in cultured epithelial cell monolayers-interlaboratory comparison. Pharm Res. 2010;27(3):480–9.

30. Sutherland W. LXXV. A dynamical theory of diffusion for non-electrolytes and the molecular mass of albumin. Philos Mag. 1905;9(54):781–5.

31. Prünte C, Kain HL. Enzymatic digestion increases permeability of the outer blood-retinal barrier for high-molecular-weight substances. Graefe's Arch Clin Exp Ophthalmol. 1995;233(2):101–11.

32. Watson CJ, Rowland M, Warhurst G. Functional modeling of tight junctions in intestinal cell monolayers using polyethylene glycol oligomers. Am J Physiol Cell Physiol. 2001;281(2):C388–97.

33. Hirsch M, Prenant G, Renard G. Three-dimensional supramolecular organization of the extracellular matrix in human and rabbit corneal stroma, as revealed by ultrarapid-freezing and deep-etching methods. Exp Eye Res. 2001;72(2):123–35.

34. Melamed S, Ben-Sira I, Ben-Shaul Y. Ultrastructure of fenestrations in endothelial choriocapillaries of the rabbit—a freeze-fracturing study. Br J Ophthalmol. 1980;64(7):537–43.

35. Federman JL. The fenestrations of the choriocapillaris in the presence of choroidal melanoma. Trans Am Ophthalmol Soc. 1982;80:498–516.

36. Garron LK. The Ultrastructure of the Retinal Pigment Epithelium with Observations on the Choriocapillaris and Bruch's Membrane. Trans Am Ophthalmol Soc. 1963;61:545–88.

37. Rajasekaran SA, Hu J, Gopal J, Gallemore R, Ryazantsev S, Bok D, et al. Na,K-ATPase inhibition alters tight junction structure and permeability in human retinal pigment epithelial cells. Am J Physiol Cell Physiol. 2003;284(6):C1497–507.

38. O'Leary TJ. Lateral diffusion of lipids in complex biological membranes. Proc Natl Acad Sci U S A. 1987;84(2):429–33.

39. Ogston AG, Preston BN, Wells JD. On the Transport of Compact Particles Through Solutions of Chain-Polymers. Proc R Soc A Math Phys Eng Sci. 1973 May;333(1594):297–316.

40. Kadam RS, Cheruvu NPS, Edelhauser HF, Kompella UB. Sclera-choroid-RPE transport of eight β-blockers in human, bovine, porcine, rabbit, and rat models. Invest Ophthalmol Vis Sci. 2011;52(8):5387–99.

41. Steuer H, Jaworski A, Elger B, Kaussmann M, Keldenich J, Schneider H, et al. Functional characterization and comparison of the outer blood-retina barrier and the blood-brain barrier. Invest Ophthalmol Vis Sci. 2005;46(3):1047–53.

42. Cheruvu NPS, Kompella UB. Bovine and porcine transscleral solute transport: influence of lipophilicity and the Choroid-Bruch's layer. Invest Ophthalmol Vis Sci. 2006;47(10):4513–22.

43. Pescina S, Santi P, Ferrari G, Padula C, Cavallini P, Govoni P, et al. Ex vivo models to evaluate the role of ocular melanin in trans-scleral drug delivery. Eur J Pharm Sci. 2012;46(5):475–83.

44. Hussain A, Rowe L, Marshall J. Age-related alterations in the diffusional transport of amino acids across the human Bruch's-choroid complex. J Opt Soc Am A. 2002;19(1):166.

45. Peng S, Rahner C, Rizzolo LJ. Apical and basal regulation of the permeability of the retinal pigment epithelium. Invest Ophthalmol Vis Sci. 2003;44(2):808–17.

46. Warnke PH, Alamein M, Skabo S, Stephens S, Bourke R, Heiner P, et al. Primordium of an artificial Bruch's membrane made of nanofibers for engineering of retinal pigment epithelium cell monolayers. Acta Biomater. 2013; http://dx.doi.org/10.1016/j.actbio.2013.07.029

47. Johnson EM, Deen WM. Electrostatic Effects on the Equilibrium Partitioning of Spherical Colloids in Random Fibrous Media. J Colloid Interface Sci. 1996;178(2):749–56.

PUBLICATION
II

Structural dynamics of tight junctions modulate the properties of the epithelial barrier

Tervonen, A., Ihalainen, T.O., Nymark, S. & Hyttinen, J.

PLOS ONE (2019), 14(4): e0214876
https://doi.org/10.1371/journal.pone.0214876

RESEARCH ARTICLE

Structural dynamics of tight junctions modulate the properties of the epithelial barrier

Aapo Tervonen*, **Teemu O. Ihalainen**, **Soile Nymark**, **Jari Hyttinen**

Faculty of Medicine and Health Technology and BioMediTech Institute, Tampere University, Tampere, Finland

* aapo.tervonen@tuni.fi

OPEN ACCESS

Citation: Tervonen A, Ihalainen TO, Nymark S, Hyttinen J (2019) Structural dynamics of tight junctions modulate the properties of the epithelial barrier. PLoS ONE 14(4): e0214876. https://doi.org/10.1371/journal.pone.0214876

Editor: Michael Koval, Emory University School of Medicine, UNITED STATES

Received: December 13, 2018

Accepted: March 21, 2019

Published: April 9, 2019

Data Availability Statement: All relevant data are within the manuscript and its Supporting Information files.

Funding: The study was funded by: Rector's Graduate School of Tampere University of Technology (AT); Academy of Finland (www.aka.fi/en) projects (grant numbers 252225 (AT, JH), 298638 (AT, JH), 287287 (SN), and 294054 (SN)), Academy of Finland postdoctoral (grant number 267471) (TOI) and research fellow funding (grant number 308315) (TOI); and the Emil Aaltonen Foundation (emilaaltonen.fi/apurahat/in-english/)

Abstract

Tight junctions are dynamic structures that are crucial in establishing the diffusion and electrical barrier of epithelial monolayers. Dysfunctions in the tight junctions can impede this barrier function and lead to many pathological conditions. Unfortunately, detailed understanding of the non-specific permeation pathway through the tight junctions, the so-called leak pathway, is lacking. We created computational models of the leak pathway to describe the two main barrier measures, molecular permeability and transepithelial electric resistance while using common structural dynamics. Our results showed that the proposed alternatives for the leak pathway, the bicellular strand opening dynamics and the tricellular pores, contribute together with distinct degrees, depending on the epithelium. The models can also capture changes in the tight junction barrier caused by changes in tight junction protein composition. In addition, we observed that the molecular permeability was markedly more sensitive to changes in the tight junction structure and strand dynamics compared with transepithelial electric resistance. The results highlight that our model creates a good methodological framework to integrate knowledge on the tight junction structure as well as to provide insights and tools to advance tight junction research.

Introduction

Epithelial cell monolayers cover body surfaces and line different organs. These tissues separate the underlying organs from their surroundings by creating tight barriers, and cell-cell junctions play a crucial role in this process. The most significant components for the barrier function are the tight junctions (TJs). These dynamic structures bring the membranes of adjacent cells into close contact, and thus seal the paracellular space between them. Due to their important role in the epithelial function, it is not surprising that there are several diseases, such as inflammatory bowel disease and celiac disease, which are linked to dysfunctions in TJ proteins or in the TJ complexes themselves [1, 2]. In these pathological conditions, the epithelium usually becomes leaky [3], and thus rendering it unfit for its task. In the present work, we

(SN). The funders had no role in study design, data collection and analysis, decision to publish, or preparation of the manuscript.

Competing interests: The authors have declared that no competing interests exist.

investigate the dynamic properties of the epithelial barrier by developing a computational model of TJ structure.

In epithelia, TJs encircle the cells near the apical side, as shown in Fig 1A, and they are categorized into bicellular and tricellular junctions [4]. Bicellular TJs (bTJs) appear as a network of anastamosing strands on the cell membranes between two cells [5, 6] and tricellular TJs (tTJs) form at the intersections of three cells [7] (Fig 1B). Generally, the bTJ strands are considered to be composed of different proteins; however, it has been proposed that lipids might have an important role in TJ formation [8–12]. According to the protein model, the strands comprise transmembrane proteins that bind to the respective proteins in the neighboring cells [13, 14]. The main transmembrane proteins in the strands are claudins, of which there are several types, and occludin [13, 15]. These proteins are connected to the actomyosin cytoskeleton via scaffolding proteins, such as ZO-1 [13]. Near the tTJs, the bTJ strand network extends vertically and converges near a 10-nm-diameter central tube [4, 7, 16]. It is not completely understood how these proteins form the strands or how the lipids might fit into this ensemble [11–13]. However, progress has been made as structural bTJ strand models were recently proposed [14, 17] based on the claudin crystal structure [18, 19].

TJ tightness varies between epithelial tissues and tasks [20]. These differences arise, for example, from the number of strands [21] and the bTJs' protein composition, which has a large impact on the ion permeability of the strands [22]. Additionally, TJ barrier is not a static structure, since it is regulated by changes in the TJ protein composition and through the actomyosin cytoskeleton [23, 24].

The properties of the epithelial barrier are usually characterized by how ions and small molecules permeate through the epithelium [25]. Transepithelial electrical resistance (TER) is the most straightforward measurement of the ion permeability since it simply measures the instantaneous electrical resistance of the tissue [26]. In low-TER epithelia, the TJs define the total epithelial resistance due to the considerably higher resistance of the transcellular pathway formed by the cell bodies [27–30]. However, the transcellular component becomes more significant as

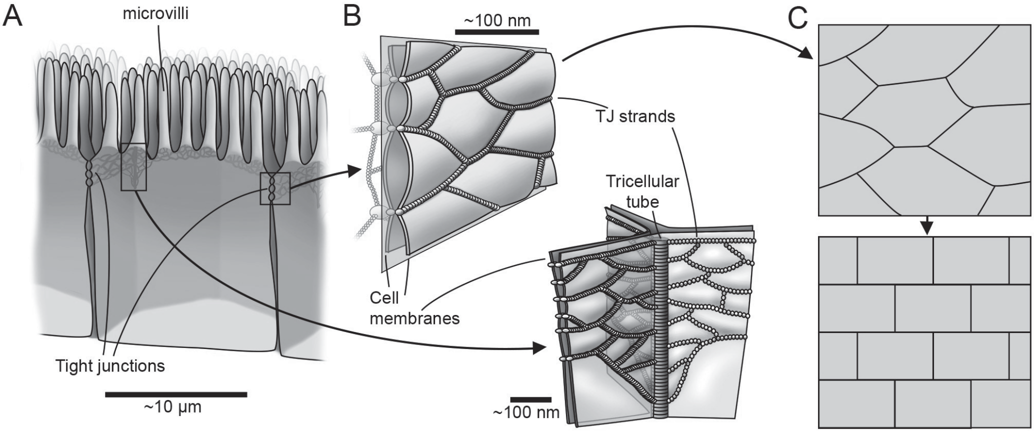

Fig 1. Tight junction structure and model simplification. (A) A schematic figure showing how the tight junctions (TJs) encircle the apical end of the paracellular space between the epithelial cells, and thus form the barrier. (B) Close up of the bTJ strands (top) that form a network dividing the space between the cells into compartments and the tTJ central tube at the intersection of three cells (bottom). (C) A 2D depiction of the TJ strands and the compartment ultrastructure, based on the cutting plane shown in b. This structure is further simplified to form the 2D TJ strand network used in the model.

https://doi.org/10.1371/journal.pone.0214876.g001

the TER increases. The permeability of noncharged molecules has been approached by studying how small tracer molecules, such as polyethylene glycols (PEGs) [31–36], dextrans [16, 37, 38], and mannitol [33, 39], traverse the epithelial barrier. Especially different sizes of PEGs have been an invaluable tool when studying how molecular size (<1 kDa) affects the TJ permeation [31–36], since they have been shown to permeate paracellularly [40, 41].

Molecules and ions are hypothesized to permeate through the TJs via two routes: pore and leak pathways [31, 33, 42, 43]. Although these pathways were defined based on the permeability of noncharged molecules [31, 33], they can be extended to the context of the TER. The pore pathway is a high-throughput pathway for molecules with a radius smaller than 0.4 nm through pores formed by some claudins [31–33]. The ion permeability of these pores depends on the ion-specificity of the claudins forming them [44]. The leak pathway is a nonspecific, low-throughput pathway with an assumed size limit of over 6 nm [20, 31, 33, 45]. The origin of this pathway is debated, the two main candidates being 1) the pores in the tTJ central tubes and 2) transient bTJ strand breaks [16, 20, 22, 33, 45–48]. The tTJ pores have been shown to enable macromolecule diffusion: Krug et al. [16] showed that 3-kDa dextran passes through the epithelium via the tTJ pores and suggested that they could form the leak pathway. They further showed that changes in the expression of tricellulin, a TJ protein found especially in the tTJs, affected the permeability of macromolecules, but only minor changes in the permeability of small (<1 kDa) molecules or in TER were seen [16].

The bTJ strands have been shown to remodel constantly at the protein-level [43, 49] as well as at the strand-level in transfected fibroblasts by constant strand breaking and sealing events [46, 50]. The bTJ strand breaks have also been observed in freeze fracture electron microscope images [16, 51–53]. Furthermore, Van Itallie and coworkers recently showed that the connection between ZO-1 and claudins stabilizes the movement of the strands while, interestingly, not affecting the break frequency [50]. In addition, ZO-1 knockdown and double ZO-1/2 knockdown have been demonstrated to increase the leak pathway permeability while only slightly affecting the TER [34, 54]. Based on these findings, it has been suggested that structural dynamics in the strands could enable a step-by-step passage for molecules too large to pass through claudin pores. However, the slow dynamics in the strand structure would not be visible in the almost-instantaneous TER measurement [22, 33, 34, 46, 48]. Moreover, Liang & Weber [20] suggested that these two pathways are not mutually exclusive.

In recent years, experimental research on the TJ structure and function has been abundant and many important advances have been made [14, 18, 55–58]. However, the small size of the TJs and the molecules passing through them, together with the fast time scales of the events, make TJs and especially their structural dynamics challenging to study experimentally. Computational models complement experimental work and provide an excellent tool to investigate the characteristics of the TJ barrier in more detail. Most of the previous computational models of the TJ barrier [47, 59–64] describe a simplified and static TJ structure and do not include any level of structural dynamics. Weber and coworkers have constructed models describing the transient opening behavior of the claudin pores without the strand-level dynamics [65, 66]. To the best of our knowledge, the only computational model to include the strand dynamics is a percolation analysis model of the TJ strands as a random resistor network by Washiyama et al. [67]. However, a model that describes the structural TJ dynamics in relation to both the molecular permeability and the TER seems to be lacking.

In this work, we developed computational models for both the molecular permeability and the TER with common structural dynamics to investigate the origin of the leak pathway. We fitted the models to experimental data from two strains of MDCK monolayers and Caco-2 monolayer to parametrize the TJ structure. This, in addition to studying the leak pathway, enabled us to investigate how the different properties of this dynamic system affect the molecular permeability and the TER. With our models, we aim to fill the gap in knowledge between the structural and the functional properties of the TJs.

Model description

Modeling framework

The computational models of the dynamic TJ structure for both the molecular permeability and TER use common geometry and dynamic parameters. Both models are divided into the bTJ and the tTJ components. The bTJ geometry is constructed as a two-dimensional structure with a uniformed depth based on the vertical model plane cutting through the TJs in the thin lateral space between the cells as shown in Fig 1B. The real TJ strand network structure is further simplified to an overlapping tile-like ordered network (Figs 1C and 2). Only a section of the strand network is modeled, but the models are averaged for the whole epithelium by long simulation times and by running them multiple times. The main assumptions of the models are as follows:

- TJs form the governing barrier against ionic and permeation of noncharged molecules in the epithelium
- Leak pathway is formed by both the static tricellular pores and by the bicellular strand dynamics, as suggested by Liang & Weber [20]
- tTJ pores are assumed to be similar between epithelia
- bTJ strands are impermeable to molecules too large to pass through claudin pores but not to ions
- bTJ strands undergo stochastic breaking and resealing events in the scale of seconds to tens of seconds

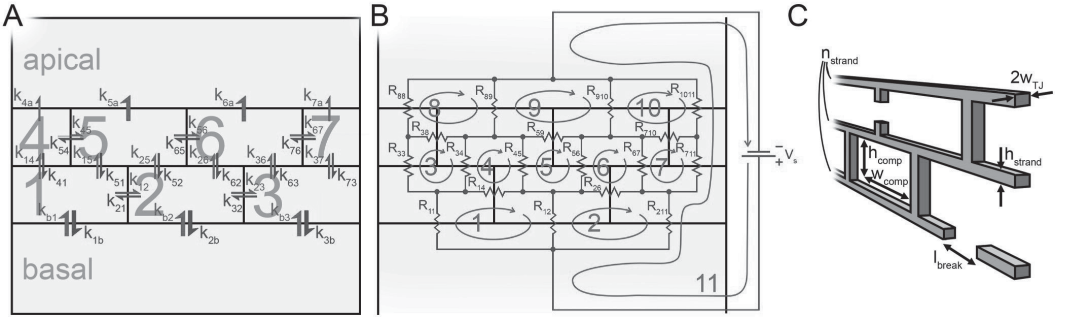

Fig 2. Schematic description of the molecular permeability and TER models. Schematic descriptions of the molecular permeability and the TER models as well as the geometrical parameters. An example of the geometrical idea of the models with three strands and the width of three compartments. (A) The molecular permeability model comprises bTJ compartments (numbered 1–7) lined by the TJ strands and the basal and apical compartments below and above the TJs, respectively. Rate constants k_{ij} describe the rate of permeation from compartment i to j. We assume low concentration in the apical compartment, and thus omit the backflow into the small compartments. To describe the strand breaks, the rate constant values are varied based on given probabilities that depend on length of strand between the compartments. (B) The TER model consists of a similar geometry, but instead of compartments the basic model units are the current loops (numbered 1–10). The outer current loop (number 11) has a voltage source (V_s) to enable the computation of the total resistance. Resistance R_{ij} is the resistance of the strand shared by current loops i and j, except for those with $i = j$, when the resistor is not shared by other loops. Again, the resistances vary based on given probabilities that depend on the length of strand between the compartments. (C) Illustration of the geometrical parameters that describe the bTJ strands. n_{strand}, strand number; h_{comp}, small compartment height; w_{comp}, small compartment width; w_{TJ} TJ half-width; h_{strand}, height of single bTJ strand; l_{break}, size of the break in the bTJ strand.

https://doi.org/10.1371/journal.pone.0214876.g002

- bTJ strands have homogeneous properties throughout the network
- In the time scale of the model, molecular diffusion rate and fluid resistance inside the compartments have no effect on permeability and TER, respectively.

The bTJ molecular permeability model is based on a multi-compartmental approach. Thus, the strand dynamics and the geometry presented as an example structure in Fig 2A are incorporated into rate constants that describe the permeation between the compartments lined by the bTJ strands. The rate constants depend on a stochastic component that describes the strand state as either intact or broken, and whose value changes based on given probabilities. The amount of substance in the basal compartment below the strand network remains constant and the amount of substance in the apical compartment above the strand network is used to calculate the molecular permeability. The model is simulated using a PEG molecule with the mass of 547 Da (calculated radius of 0.51 nm), since it is unable to permeate through the claudin pores and has been used in many experimental permeability studies. The static tTJ pore pathway is combined with the bTJ results afterwards.

The bTJ resistance model uses the same geometry and dynamics as the molecular permeability model. However, the system is solved using nodal analysis and Kirchhoff's circuit laws. An example resistor network system is shown in Fig 2B. Current loops form in the resistor network as depicted, and Kirchhoff's loop rule is used for each loop, combined into an equation group, and solved. The dynamics and the geometry shown in Fig 2B are incorporated into the resistances between the compartments. In a similar way to the permeability model, the tTJ resistance is calculated separately and summed with the bTJ simulation results.

Molecular permeability model

The permeabilities of the bTJ and the tTJ components are calculated separately and then combined in the end based on the parallel connection. The bTJ molecular permeability model is constructed using a multi-compartmental approach. The amount of substance in the small bTJ compartments as a function of time is described by an equation of the form

$$\frac{\mathrm{d}q_i(t)}{\mathrm{d}t} = \sum_{j\neq i}^{n}(k_{ji}(t)q_j(t) - k_{ij}(t)q_i(t)), \tag{1}$$

where $q_i(t)$ is the amount of substance in compartment i at time t and $k_{ji}(t)$ is the time-dependent rate constant for permeation from compartment j to i (s^{-1}). Because the model is in 2D, the unit of q_i is m^{-1} instead of unity. This is taken into account when the results are calculated with Eq 8.

Since we consider the apical compartment to be considerably larger than the small bTJ compartments, we assume that the concentration in it remains very low. Thus, we can ignore the backflow of molecules from the apical compartment into the bTJ compartments, as shown in Fig 2A. The amount of substance in the basal compartment is assumed to remain constant ($\mathrm{d}q_{basal}(t)/\mathrm{d}t = 0$).

Because we assume no molecular permeation through an intact strand, the rate constants for the permeation between the compartments depends only on the strand break permeability coefficient:

$$k_{ij}(t) = \frac{l_{break}r_{ij}(t)}{A_i}P_{break}, \tag{2}$$

where l_{break} is the size of the break in the strand, as indicated in Fig 2C (m), $r_{ij}(t)$ is a function describing the state of the strand between compartments i and j, A_i is the area of compartment

i (m^2), and P_{break} is the permeability coefficient of the strand break of indefinite length (m s^{-1}). In a 3D model, break area and compartment volume would be used instead of the break size and compartment area, respectively [68].

Function $r_{ij}(t)$ can have a value of either 0 or 1, describing intact and broken states, respectively. The value of $r_{ij}(t)$ can change with given probabilities: If the strand is intact, a break will form with the probability p_{break} (m^{-1}s^{-1}), and if the strand is broken, it will seal with the probability p_{seal} (s^{-1}). To obtain the break forming probability for a section of strand between two compartments, p_{break} must be multiplied by the length of that section. This means that longer sections of strand have higher value of p_{break}. Based on the time scale of the dynamics, the possible changes in the strand states were chosen to happen every second.

The initial state of the strands can be either intact or broken. The probability of them being in either state is calculated with Markov chain after infinite time:

$$\begin{bmatrix} p_{ij,intact} & p_{ij,broken} \end{bmatrix} = \begin{bmatrix} \frac{1}{2} & \frac{1}{2} \end{bmatrix} \begin{bmatrix} 1 - p_{break} l_{ij} & p_{break} l_{ij} \\ p_{seal} & 1 - p_{seal} \end{bmatrix}^{\infty}, \tag{3}$$

where $p_{ij,intact}$ and $p_{ij,broken}$ are the probabilities of the strand section between compartments i and j being in intact or broken states initially, respectively, and l_{ij} is the length of the strand section between those compartments (m).

Since the break size is taken into account in Eq 2, P_{break} is calculated relative to the amount of TJs in the entire epithelium, and thus making it dependent on the cell boundary length per area of epithelium:

$$P_{break} = \frac{\epsilon_{TJ} D_0 H_s(r_m/w_{TJ})}{h_{strand}}, \tag{4}$$

where ϵ_{TJ} is the relative area of the TJs in the epithelium, D_0 is the aqueous diffusion coefficient of the permeating molecule (m^2 s^{-1}), $H_s(r_m/w_{TJ})$ is the break slit hindrance factor that depends on the molecular radius r_m (m) and on the TJ half-width w_{TJ} (m), and h_{strand} is the bTJ strand height (m) (See Fig 2C for an illustration of the geometrical parameters) [69]. Parameter ϵ_{TJ} is calculated as

$$\epsilon_{TJ} = 2 w_{TJ} l_{cb}, \tag{5}$$

where l_{cb} is the cell boundary length per area of epithelium (m^{-1}). Function H_s describes how the break walls affect the diffusion of a molecule of a given size and was derived by Dechadilok & Deen [70] by fitting a polynomial to computational results as

$$H_s(\lambda) = 1 + \frac{9}{16}\lambda \ln(\lambda) - 1.19358\lambda + 0.4285\lambda^3 - 0.3192\lambda^4 + 0.08428\lambda^5, \tag{6}$$

where $\lambda = r_m/w_{TJ}$.

With zero initial conditions for the bTJ compartments, there is a so-called lag phase in the beginning of a simulation, especially with systems having more horizontal strands and lower value of p_{break}. During this phase, the increase in the amount of substance in the apical compartment (q_{apical}) is nonlinear. Since the permeability is calculated from the linear phase in q_{apical}, the simulation is made to enter straight into this phase by setting the initial values of the amount of substance in each of the small bTJ compartments to the equilibrium state during the linear phase. This is done by simulating the permeability model multiple times and for a long time with zero initial conditions to obtain the equilibrium values for each compartment row.

The constant amount of substance for the basal compartment is set to

$$q_{basal} = c_{basal} N_A A_{basal}, \tag{7}$$

where c_{basal} is the basal compartment concentration (M), N_A is Avogadro's constant (6.022×10^{23} mol^{-1}), and A_{basal} is the area of the basal compartment, replacing the volume since the model is in 2D (m^2).

The system of differential equations described by Eq 1 is solved using Matlab's (Release 2015b, The MathWorks, Inc., Natick, Massachusetts, United States) ode23 ordinary differential equation solver. This solver uses second and third order Runge-Kutta formulas, and we found that it gives the same results as the more robust fourth and fifth order Runge-Kutta solver (ode45), while being considerably faster. The simulation is run multiple times and the linear phase of the average q_{apical} curve is used to calculate the bTJ permeability coefficient:

$$P_{bTJ} = \frac{\mathrm{d}q_{apical}(t)}{\mathrm{d}t} \frac{1}{w_{model} c_{basal}}, \tag{8}$$

where w_{model} is the width of the model system (m), which replaces the area in this 2D model. Next, a first degree polynomial is fitted to the linear phase of the average q_{apical} to obtain the slope. Since the relative area of the junctions in the epithelium is considered in Eq 4, P_{bTJ} is already scaled for the bTJs in the whole epithelium.

The tTJ central tubes are modeled as static pores, and an equation similar to Eq 4 is used:

$$P_{tTJ} = \frac{\epsilon_{tTJ} D_0 H_p(r_m/r_{tTJ})}{h_{tTJ}}, \tag{9}$$

where ϵ_{tTJ} is the relative area of the tricellular pores in the epithelium, $H_p(r_m/r_{tTJ})$ is pore hindrance factor, r_{tTJ} is the tricellular pore radius (m), and h_{tTJ} is the tricellular pore height (m) [69]. The relative area of the pores is calculated as

$$\epsilon_{tTJ} = \pi r_{tTJ}^2 \rho_{tTJ}, \tag{10}$$

where ρ_{tTJ} is the density of the tricellular junctions in an epithelium (m^{-2}). The equation for H_p was also derived by Dechadilok & Deen [70] by fitting a polynomial to computational results as

$$\begin{aligned} H_p(\lambda) = \quad & 1 + \frac{9}{8}\lambda \ln(\lambda) - 1.56034\lambda + 0.528155\lambda^2 + 1.91521\lambda^3 - 2.81903\lambda^4 \\ & + 0.270788\lambda^5 + 1.10115\lambda^6 - 0.435933\lambda^7 \end{aligned}, \tag{11}$$

where $\lambda = r_m/r_{tTJ}$. This equation is more accurate than the much-used Renkin equation when λ is close to unity [70].

The total epithelial TJ permeability is finally calculated based on the parallel connection between the two pathways as

$$P_{TJ} = P_{bTJ} + P_{tTJ}. \tag{12}$$

The required properties of the permeating molecule for this model are the molecular radius and the aqueous diffusion coefficient. Since we use a PEG oligomer with a mass of 547 Da, an equation relating the mass of a PEG oligomer to its size is used [71]:

$$r_m = 0.29 M_m^{0.454}, \tag{13}$$

where r_m is in Å (0.1 nm) and M_m is the molecular mass (Da). The aqueous diffusion coefficient is calculated with an empirical relationship derived by Avdeef [61]:

$$D_0 = 9.9 \times 10^{-9} M_m^{-0.453}. \tag{14}$$

The default simulation time for the bTJ model is two hours and the stochastic behavior is further averaged by running the simulations 512 times. We found that the results were not affected by further averaging. The simulations were run using the Finnish IT Center for Science's (CSC) Taito supercluster using parallel computing (nodes with two 12-core Intel Haswell E5-2690v3 processors running at 2.6 GHz and 128 GB of DRR4 memory operating at 2133 MHz). A Matlab implementation of the permeability model is given in S1 File.

TER model

In the TER model, the bTJ and tTJ components are again calculated separately and connected in parallel in the end. The bTJ resistance model is constructed as a network of dynamic resistors (Fig 2B). Since we are interested in the resistance, the strand capacitance is ignored. For each current loop i (Fig 2B), the equation is of the form

$$\sum_{j}^{n} R_{ij}(t) I_i - \sum_{i \neq j}^{n} R_{ij}(t) I_j = \begin{cases} V_s, & \text{for the outer current loop} \\ 0, & \text{otherwise} \end{cases}, \tag{15}$$

where $R_{ij}(t)$ is the time-dependent resistance of the section of strand that is shared by current loops i and j (Ω), I_i is the current in loop i (A), and V_s is the voltage applied by the external source in the outer loop (V).

The strand dynamics are incorporated into the resistances $R_{ij}(t)$, making them analogous to the rate constants in the bTJ permeability model. Because ions can also pass through the intact strands, $R_{ij}(t)$ depends on both the intact strand and break resistances:

$$R_{ij}(t) = \left(\frac{(l_{ij} - l_{break}) r_{ij}(t)}{R_{strand}} + \frac{r_{ij}(t)}{R_{break}} \right)^{-1}, \tag{16}$$

where l_{ij}, l_{break}, and $r_{ij}(t)$ have been described in the bTJ permeability model, R_{strand} is the intact strand resistance per strand length (Ωm), and R_{break} is the resistance of a break (Ω).

The break resistance is calculated with the equation

$$R_{break} = \frac{\rho_{em} h_{strand}}{A_{break}}, \tag{17}$$

where ρ_{em} is the resistivity of the extracellular medium (Ωm) and A_{break} is the area of the break in the strand (m^2), calculated as $2 w_{TJ}\, l_{break}$.

Although the TER measurement is basically instantaneous, the bTJ resistance model is simulated for a long time to average the results. The current flowing in the outer loop I_{outer} (A) is used to calculate the bTJ resistance at each time point with Ohm's law:

$$R_{bTJ}(t) = \frac{V_s}{I_{outer}(t)} \frac{w_{model}}{l_{cb}}, \tag{18}$$

where the factor w_{model}/l_{cb} scales the results for the whole epithelium. To solve the bTJ model, the linear system defined by Eq 15 is transformed to matrix form and solved using Matlab.

The pores in the tTJ tubes are modeled as a static and their resistance is calculated as

$$R_{tTJ} = \frac{\rho_{em} h_{tTJ}}{\pi {r_{tTJ}}^2 \rho_{tTJ}}. \tag{19}$$

For each simulation time point of the bTJ resistance model, the total TER is calculated based on the parallel connection as

$$TER(t) = \left(\frac{1}{R_{bTJ}(t)} + \frac{1}{R_{tTJ}} \right)^{-1}. \tag{20}$$

Finally, to obtain the average TER for the simulation, the time average is taken from the results. The simulation time is 10^6 seconds and the simulations were run using the CSC's Taito supercluster with serial computing. A Matlab implementation of the TER model is given in S2 File.

Parameter values

Here we describe the default values of the model parameters. The TJ structure in our model is described by bTJ compartment dimensions, strand number (n_{strand}), strand height (h_{strand}), TJ half-width (w_{TJ}), tricellular pore radius (r_{tTJ}), and tricellular pore height (h_{tTJ}). The TJ dynamics are described by break forming and sealing probabilities (p_{break} and p_{seal}, respectively), and break size (l_{break}).

Although there is a lot a variety in the TJ strand morphology [5, 72–75], we used one strand morphology since the main focus is the break dynamics. The chosen bTJ compartment width (w_{comp}) and height (h_{comp}) were both 100 nm. These values are in the range of the bTJ compartment sizes found in the freeze-fracture replicas [5, 72–75] as well as by Kaufmann et al. using super-resolution microscopy [76]. The horizontal number of the compartments in the simulated systems was set to 50 and the heights of the apical and basal compartments in the molecular permeability model were both set to 200 nm. Based on the strand numbers in MDCK monolayers (3–5 strands) [52, 53, 74, 77], Caco-2 monolayers (4–5 strands) [78], and retinal pigment epithelium (4 strands) [39], the default strand number was set to $n_{strand} = 4$.

The value of $h_{strand} = 6$ nm was based on the electron microscopy of TJ freeze-fracture replicas and the TJ strand architecture model by Suzuki et al. [14]. TJ half-width was chosen as $w_{TJ} = 4$ nm, estimated based on the architecture model by Suzuki et al. [14] and transmission electron microscope images [54, 79, 80]. The dimensions of the tricellular pores, $r_{tTJ} = 5$ nm and $h_{tTJ} = 1$ μm, were taken from the measured values from freeze-fracture replicas [7, 16].

The dynamic parameters of the strand dynamics were more uncertain due to the lack of experimental data. The strand breaks were assumed to remain open on average around 30 seconds based on the time scale of the dynamics in the transfected fibroblasts [46, 50]. This led to the break sealing probability of $p_{seal} = 0.033$ s^{-1}. The break size was approximated based on the figures and videos by Sasaki et al. [46] and by Van Itallie et al. [50], leading to a value of $l_{break} =$ 20 nm. This value was also used to quantify breaks by Rosenthal and coworkers [52, 53]. The break forming probability (p_{break}) is fitted in the Results section based on the literature data. Due to the time scale of the dynamics and computational limitations, we restricted the possible state changes in the strands to occur every second.

The basal compartment concentration and the voltage of the external source used to measure the resistance are scaling parameters and do not affect the results. The chosen values were $c_{basal} = 1$ mM and $V_s = 1$ V, respectively. Also, the resistive properties of the breaks and the strands are needed. The resistivity of the extracellular medium required for the breaks was $\rho_{em} = 0.537$ Ωm [16]. The value of the strand resistance (R_{strand}) depends on the epithelium, and is fitted in the Results section.

Table 1. Model parameters.

Description	Parameter	Value	Reference
bTJ compartment width	w_{comp}	100 nm	[a]
bTJ compartment height	h_{comp}	100 nm	[a]
bTJ strand number	n_{strand}	4	[39, 52, 53, 77, 78]
Single bTJ strand height	h_{strand}	6 nm	[14]
TJ half-width	w_{TJ}	4 nm	[a]
tTJ pore radius	r_{tTJ}	5 nm	[7]
tTJ pore height	h_{tTJ}	1 μm	[7, 16]
Break sealing probability	p_{seal}	0.033 s^{-1}	[a]
Break size	l_{break}	20 nm	[a]
Basal compartment concentration	c_{basal}	1 mM	[a]
Voltage source in the external loop	V_s	1 V	[a]
Extracellular medium resistivity	ρ_{em}	0.537 Ω m	[16]

[a] See text for explanation.

https://doi.org/10.1371/journal.pone.0214876.t001

The cell boundary length per epithelial area (l_{cb}) and tTJ pore density (ρ_{tTJ}) are also highly dependent on the epithelium. They were determined using ImageJ Fiji [81, 82] from the immunofluorescence microscopy images illustrating the cell-cell junctions in the studies our models were fitted for, and the values are described in the Results section. The only unknown parameters values were p_{break} (both permeability and TER models) and R_{strand} (TER model). These values are found by iteratively fitting the models to the experimental data. The model parameters described here are summarized in Table 1.

Results

Model fitting and the origin of the leak pathway

The models were used to study the roles of tricellular junctions and bicellular strand dynamics in the leak pathway for the epithelial molecular permeability and TER. The models were fitted to the experimental data by varying the values of the break forming probability (p_{break}) and the TJ strand resistance (R_{strand}). Since the cell boundary length (l_{cb}) and tTJ density (ρ_{tTJ}) had a strong impact on the simulation results (see Parameter sensitivity analysis), we only used experimental data that included immunofluorescence microscopy images showing the cell-cell junctions. Therefore, unfortunately, the PEG profiling studies by Watson et al. [31, 32], Van Itallie et al. [35], and Linnankoski et al. [36] had to be excluded from our model fitting.

First, the permeability model was fitted to the experimental data of 547-Da PEG oligomer permeation, since this molecule utilizes the leak pathway and it was used in the suitable studies [33, 34, 54, 83]. The fitting was done by iteratively changing the value of p_{break} (with the accuracy of 0.001 μm^{-1} s^{-1}) and comparing the simulation result with the experimental result. The value of p_{break} for MDCK C7 was calculated rather than fitted since the tTJ pores were enough to form the leak pathway for this epithelium, and thus making the fitting impossible. The value was iteratively calculated with Eq 3 using the chosen break sealing probability and the average amount of breaks per strand length for high-TER MDCK [52, 53]. Next, the TER model was fitted using the obtained values of p_{break} to iteratively find the values of R_{strand} (with the accuracy of 0.01 GΩ μm). The experimental data used to fit the model, the values of experimental permeability and TER, the values of l_{cb} and ρ_{tTJ}, as well as the fitting results are shown in Table 2.

Table 2. Values of the model parameters used to fit the molecular permeability and the TER model.

Epithelia	P_{exp}	TER_{exp}	l_{cb}	ρ_{tTJ}	p_{break}	R_{strand}
	(nm s^{-1})	(Ω cm^2)	(μm^{-1})	(μm^{-2})	(μm^{-1} s^{-1})	(GΩ μm)
Caco-2 [33]	10.0	220	0.525	0.130	0.047	7.65
MDCK C7 [33]	1.0	460	0.424	0.078	0.005*	10.62
MDCK IIa [33]	4.3	28	0.484	0.106	0.032	0.46
MDCK IIb [34]	0.8	54	0.185	0.014	0.029	0.32
MDCK IIc [83]	2.9	41	0.311	0.035	0.038	0.45
MDCK IId [54]	2.3	30	0.179	0.014	0.044	0.20
MDCK IIb ZO-1 KD [34]	3.1	62	0.189	0.015	0.047	0.45
MDCK IId ZO-1/2 dKD [54]	26.0	26	0.200	0.019	0.084	0.34

P_{exp}, experimental permeability of 547-Da PEG; TER_{exp}, experimental TER; l_{cb}, cell boundary length per area; ρ_{tTJ}, tricellular TJ pore density; p_{break}, break forming probability; R_{strand}, strand resistance.

* calculated.

https://doi.org/10.1371/journal.pone.0214876.t002

The cell sizes in MDCK II monolayers, as indicated by the cell boundary length per area (l_{cb}) and and the tricellular pore density (ρ_{tTJ}) in Table 2, varied greatly between the measurements. However, they were on average the largest of the fitted epithelia. The cells in Caco-2 monolayer were the smallest and in MDCK C7 monolayer between the two extremes. Surprisingly, the experimental permeability of high-resistance MDCK C7 was higher than that of the low-resistance MDCK IIb, which is most likely explained by the difference in cell size.

Although there was some variation in the values of p_{break} for MDCK II, they are similar to each other having a mean (±SD) of 0.036 (±0.007). This is especially interesting when considering the great variability in the cell size. As for the TER, the variation was higher, with a mean (±SD) of 0.36 (±0.12) GΩ μm. The values of both p_{break} and R_{strand} were found to differ significantly for MDCK C7. Its values of p_{break} and R_{strand} were 7.2 times lower and over 30 times larger, respectively, compared with those of the average MDCK II. The properties of Caco-2 were a combination of the two MDCK strains: While the value of p_{break} was similar to that of the MDCK II, R_{strand} was closer to the value of MDCK C7. The resistance of a single 20-nm break in the strands was R_{break} = 0.2 GΩ. The resistances of the same length of strand for average MDCK II, MDCK C7, and Caco-2 were 18 GΩ, 531 GΩ, and 383 GΩ, respectively. Thus, the strands had 90 to 2670 times higher resistance compared with the breaks.

To further check the validity of our results, we used the MDCK C7 p_{break} and R_{strand} values to simulate the TER for the original MDCK C7 epithelia (measured TER 5650 Ω cm^2) [84] by changing the cell size. Unlike with the other results considered here, the figures in [84] did not allow rigorous determination of the cell size properties, and therefore the cell radius was estimated to be between 15 and 20 μm (Fig 1A in [84]). Assuming perfect hexagonal cell array, we calculated the values of l_{cb} and ρ_{tTJ} to be between 0.050–0.067 μm^{-1} and 0.001–0.003 μm^{-2}, respectively. The obtained TER values for these cell radii of 15 and 20 μm were 4820 and 7310 Ω cm^2, respectively. This indicated that the difference in cell size explains the difference in TER between the two experimental MDCK C7 results.

Fig 3 shows the relative contributions of the two assumed leak pathway components—the tTJ pores and the bTJ strand dynamics—to the total leak pathway. MDCK C7 was the only epithelia considered here whose permeability was dominated by the tTJ pathway. Since the leak pathway was originally defined by the permeability, it can be said that the MDCK C7 leak pathway was fully formed by the tTJ pores. The role of bTJ dynamics was more prevalent, but variable, for the MDCK II permeability, having a mean (±SD) of 60.1 (±21.7)%. The bTJ

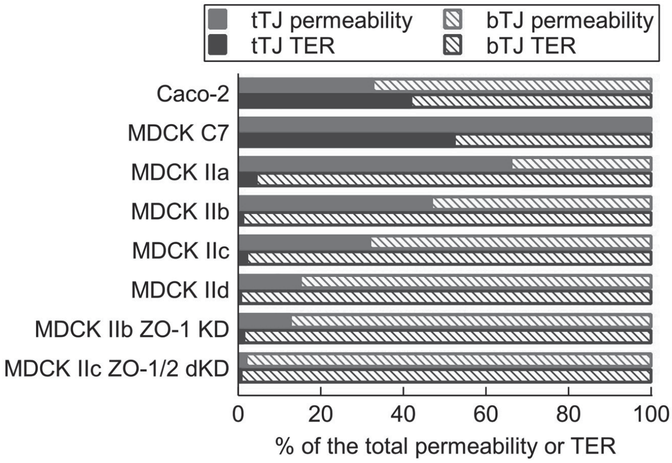

Fig 3. Relative roles of the tricellular and bicellular pathways. The relative roles of tTJ (solid) and bTJ (dashed) on both the molecular permeability (red) and TER (blue) for all the simulated epithelia (Caco-2 [33], MDCK C7 [33], MDCK IIa [33], MDCK IIb [34], MDCK IIc [83], MDCK IId [54], MDCK IIb ZO-1 KD [34], and MDCK IIc ZO-1/2 dKD MDCK IId [54]).

https://doi.org/10.1371/journal.pone.0214876.g003

dynamics was also the main pathway for the Caco-2 permeability. As for the TER, the role of the tTJ pores was insignificant for the MDCK II with a mean (±SD) relative role of 2.0 (±1.7)% between the four measurements. In both MDCK C7 and Caco-2, the tTJ pathway formed approximately half of the resistance of the epithelium.

Simulating experimentally-induced changes in the TJs

Next, we investigated how the developed models can recapitulate disturbances or changes in the TJ proteins, based on the studies of ZO-1 knockdown in MDCK II by Van Itallie et al. [34] and double ZO-1/2 knockdown in MDCK II by Fanning et al. [54]. Since both suggested that the observed changes in the barrier properties caused by these knockdowns were a result of decreased strand stability, we fitted our models to these results by varying the break forming probability p_{break}. The TER model also required fitting of R_{strand}. The results of the fitting are shown in Table 2 and the relative pathway roles in Fig 3 before (MDCK IIb and MDCK IIc) and after (MDCK IIb ZO-1 KD and MDCK IIc ZO-1/2 dKD) the knockdowns.

According to our results, the knockdown of ZO-1 led to a 62% increase in p_{break} and to a 41% increase in R_{strand}. In addition, the decreased bTJ tightness resulted in a 65% increase in the relative role of the bTJ pathway. The effect of the ZO-1/2 double knockdown was larger; it caused a 121% increase in p_{break} and a 70% increase in R_{strand}. The increase in the relative role of bTJ caused by the double knockdown (44%) was smaller than that of the ZO-1 knockdown due to the higher original contribution of bTJ in MDCK IIc. The changes in the relative roles of the pathways in TER were insignificant for both the single and double knockdown.

The effect of strand number on permeability and TER

Next, we studied the effect of the number of strands on the barrier properties by changing the strand number (n_{strand}) for the average MDCK II and MDCK C7 epithelia. These monolayers were chosen to illustrate the effect of n_{strand} for different levels of strand dynamics and strand resistances. Although these epithelia do not necessarily manifest varying numbers of strands, they provide two systems with different properties to base our simulations on. We simulated the model with $n_{strand} = [2, 6]$ for both permeability and TER, and the results for these simulations are shown in Fig 4A and 4B, respectively. To remove the impact of the cell size from the comparison, the simulations were run with the mean values of cell boundary length per area ($l_{cb} = 0.282\ \mu\text{m}^{-1}$) and tricellular TJ pore density ($\rho_{tTJ} = 0.049\ \mu\text{m}^{-2}$) of all the MDCK data included here (2 and C7).

Naturally, the permeability decreased as n_{strand} increased (Fig 4A). In addition, the increase in n_{strand} also led to an increase in the relative role of the tTJ pathway of the total permeability. This growing importance of the tTJ pathway led to saturation of the permeability at approximately 6 and 3 strands for MDCK II and C7, respectively. In contrast, TER grew when n_{strand} increased (Fig 4B). However, similarly to permeability, the significance of the tTJ pores increased with n_{strand}. TER also showed the saturation behavior, but the saturation occurred past the simulated strand numbers for both of the MDCK strains. Moreover, the scale of the changes caused by the varying n_{strand} were considerable larger for MDCK II in both permeability and TER. Also, the largest difference in permeability relative to the 4-strand standard system was almost two orders of magnitude compared with the under one order of magnitude for TER.

The raw, unaveraged simulation data indicating the time course of the simulations (Fig 4C and 4D) showed the different behavior in the MDCK II and C7 monolayers for both permeability and TER. Full opening events, in which there was an open pathway through the strand network via the breaks, are indicated in the TER results by the sharp downward spikes. The spikes disappeared altogether at 6 strands for MDCK II and at 3 strands for MDCK C7. These events were not always clear in the permeability results, since the sharp steps in q_{apical} may be a result of molecules stored into the small compartments released into the apical compartment. For example, as indicated by the TER results of 2-strand MDCK II, there was at least one full opening present around half of the time. However, no sharp steps were seen in q_{apical} in any of the simulations shown. In contrast, there were multiple, minuscule scale steps in q_{apical} e.g. for 6-strand MDCK II.

As n_{strand} increased, the slopes for the bulk of the permeability simulations decreased for both MDCK II and C7 (Fig 4C and 4D). However, the increase in n_{strand} in MDCK II led to more variable simulation results as well as to an increase in the number of the visibly different q_{apical} curves with full openings. Interestingly, the behavior of MDCK C7 was different; generally, when n_{strand} increased, the variability in the results decreased. This was most likely due to the lack of full opening events. Furthermore, the clearly distinct q_{apical} curves in the 3-strand MDCK C7 differed considerably more from the bulk of the simulations compared with other simulated systems.

Thus, the simulation raw data showed a biphasic behavior for bTJ permeability as a function of TJ tightness, defined by both the strand number and the level of strand dynamics. With low strand numbers and high values of break forming probability, the bulk of permeability through the strand network passed via the full opening events. This resulted in low variance between the individual simulations, as shown, e.g., by the 2-strand MDCK II (Fig 4C). With high strand numbers and low values of levels of strand dynamics, however, the bulk of the permeability occurred via the step-by-step diffusion through the compartment network. Again, this resulted in low variance between the individual simulations, as shown, e.g., by the 5- and 6-strand MDCK C7 (Fig 4C). Between these two extremes, there was a transition zone where the variance between the simulations was higher.

The permeability model was simulated with the equilibrium state of the system as the initial condition. These states for each of the compartment rows were found by running the models

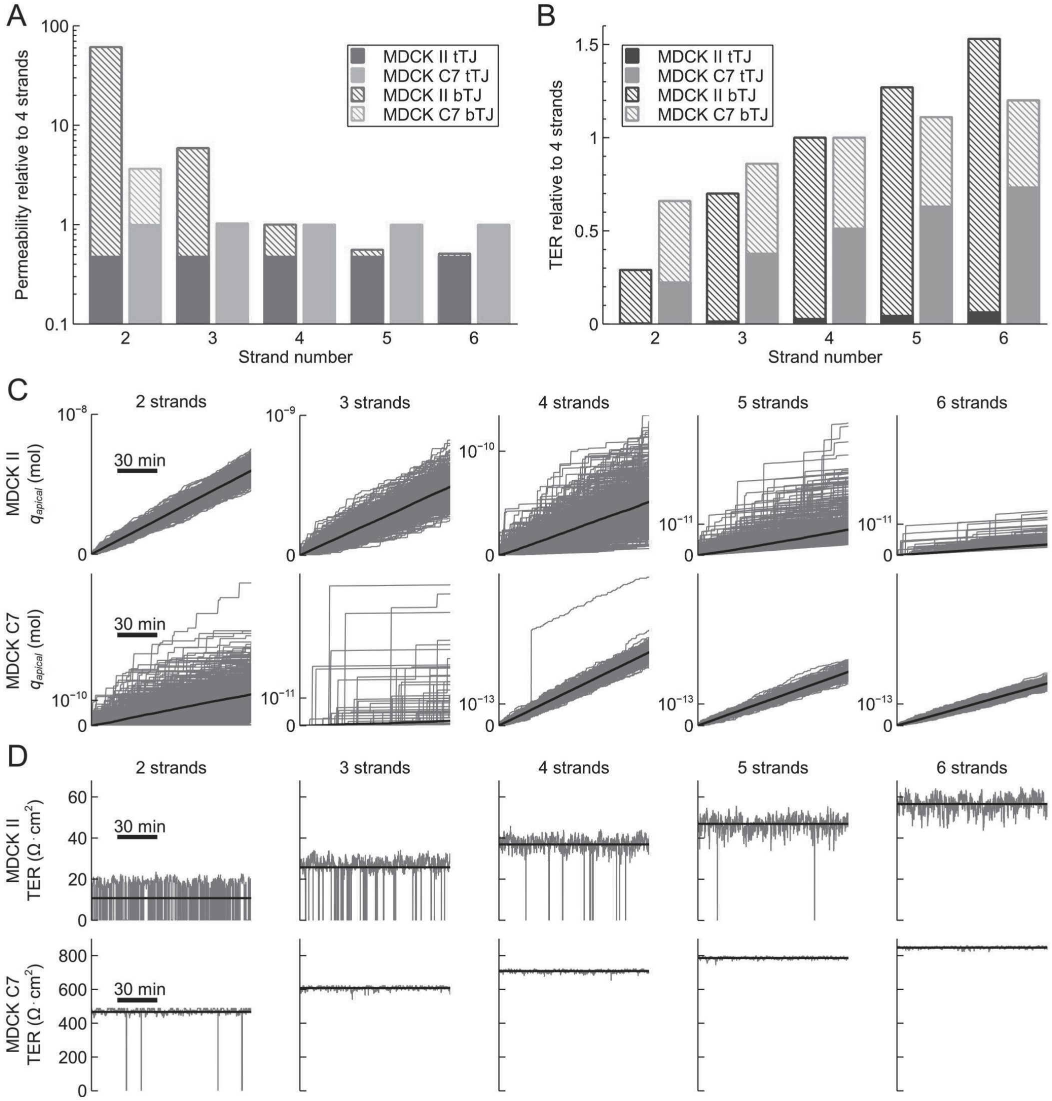

Fig 4. Effect of strand number on permeability and TER. The effect of strand number (n_{strand} = [2, 6]) on (A) molecular permeability and (B) TER in average MDCK II (red and blue) and MDCK C7 (orange and cyan), shown relative to the system with 4 strands. The relative roles of tTJ (solid) and bTJ (dashed) pathways are also illustrated relative to the 4-strand total values. (C) Raw simulation data of the 512 simulations of the apical amount of substance (q_{apical}) as a function of time for average MDCK II (top) and MDCK C7 (bottom) for systems with the strand number from 2 to 6. The average values of the 512 for each time point are shown with the black lines. (D) TER as a function of time for average MDCK II (top) and MDCK C7 (bottom) during a 2-hour section of the simulation for systems with the strand number from 2 to 6. The average values for the whole simulation are shown with the black lines.

https://doi.org/10.1371/journal.pone.0214876.g004

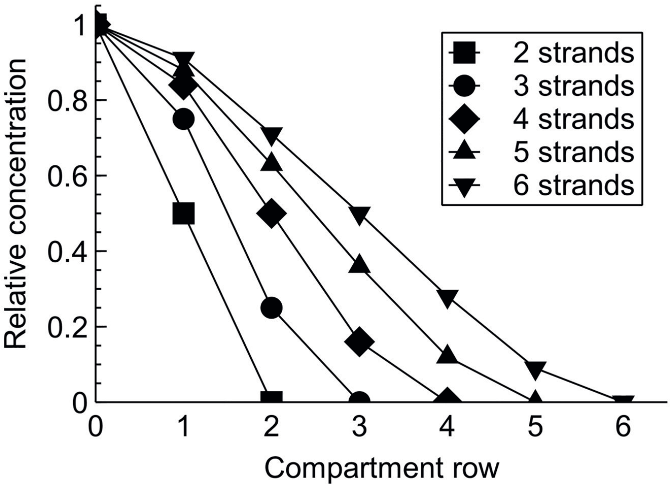

Fig 5. Relative equilibrium concentrations in the equilibrium state. The relative equilibrium concentrations are shown in relation to the concentration in the basal compartment (compartment row 0) for the 2–6 strand TJ systems. The compartment row with relative concentration of 0 refers to the apical compartment for that system, since its concentrations was assumed to remain very low during the simulations.

https://doi.org/10.1371/journal.pone.0214876.g005

with zero initial conditions for a long time. The relative equilibrium concentrations compared to the basal compartment are shown in Fig 5 for systems with 2–6 strands. The parameters affecting the rate constants or the magnitude of p_{break} had no effect on these values; they only defined how fast the linear phase was reached. Interestingly, while the differences between the small TJ compartments were approximately linear, the equilibrium concentration change between the basal compartment and the bottom small compartment row as well as the top small compartment row and the apical compartment showed nonlinear discontinuities.

In addition, although the lag phase was not included in the simulations, we calculated the length of this phase for each of the bTJ permeability simulations to describe the time it takes for the permeating molecules to pass through the TJs. This was done by running the simulation with zero initial values for the small bTJ compartments and by extrapolating the linear phase of q_{apical} backwards to determine its intersection with the time axis. Longer than normal simulation times were used in some cases to obtain a linear phase of sufficient length. The lag times for both of the MDCK strains are shown in Table 3. As expected, the lag time grew as the strand number increased and as the break forming probability decreased. Interestingly, the lag

Table 3. The lag times in minutes for MDCK II and MDCK C7 with the different strand numbers.

n_{strand}	MDCK II	MDCK C7
2	0.04	4.82
3	0.64	14.24
4	2.81	83.10
5	4.38	156.99
6	11.54	251.90

n_{strand}, strand number.

https://doi.org/10.1371/journal.pone.0214876.t003

time for 5-strand MDCK II and 2-strand MDCK C7 were close to each other, although having a large difference in the actual permeability coefficients. The same biphasic behavior can be seen in the lag times when the barrier became tighter. The lag times grew slowly for MDCK II as n_{strand} was increased. However, with the higher strand numbers for MDCK II and for all the results for MDCK C7, the increase in n_{strand} led to considerably larger changes in the lag times.

Comparison with steady-state models

To test if the results produced by the dynamic bTJ models presented here could be reached with simpler methods, we created steady-state (SS) bTJ models that assumed a static system with an average number of breaks per strand for both barrier properties. In the SS bTJ permeability model, the compartment rows were reduced into a single large compartment between the strands, since the compartments in the same row could be assumed to be in equilibrium. The SS bTJ resistance model similarly assumed to only contain horizontal strands, and thus simplifying the model to a series connection of identical strands. The number of static open breaks for both SS models was defined from Eq 3. For comparison, we ran the simulations for the varying strand number for both MDCK II and C7 presented in the previous section, and the results of the comparison are shown in Fig 6.

It can be clearly seen that the SS models were not able to produce comparable results for bTJ permeability nor for bTJ resistance. The permeabilities predicted by the SS model were well above those produced by our dynamic model (Fig 6A). Moreover, the SS permeabilities showed very little change overall when the strand number was increased from 2 to 6. As for the bTJ resistance, the values produced by the SS model were approximately one and two orders of magnitude lower, respectively, than those from our dynamic model for MDCK II and C7 (Fig 6B).

Parameter sensitivity analysis

Finally, we performed a sensitivity analysis on certain model parameters by individually altering their values ±25%. The chosen parameters for both models were break forming and sealing probabilities (p_{break} and p_{seal}, respectively), break size (l_{break}), cell boundary length per area (l_{cb}), and tTJ pore density (ρ_{tTJ}). Strand resistance (R_{strand}) was additionally included for the

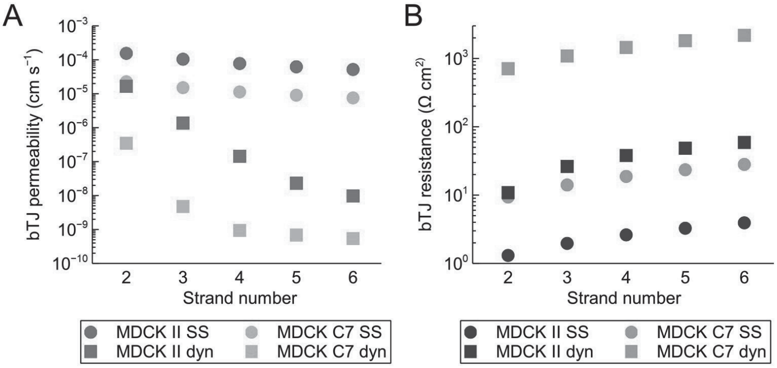

Fig 6. Comparison between the dynamic and steady-state models. Comparison between the bTJ results of our dynamic (dyn) model (squares) and a simple steady-state (SS) model (circles) for (A) permeability and (B) resistance. The simulations were run both for MDCK II (red and blue) and C7 (orange and cyan).

https://doi.org/10.1371/journal.pone.0214876.g006

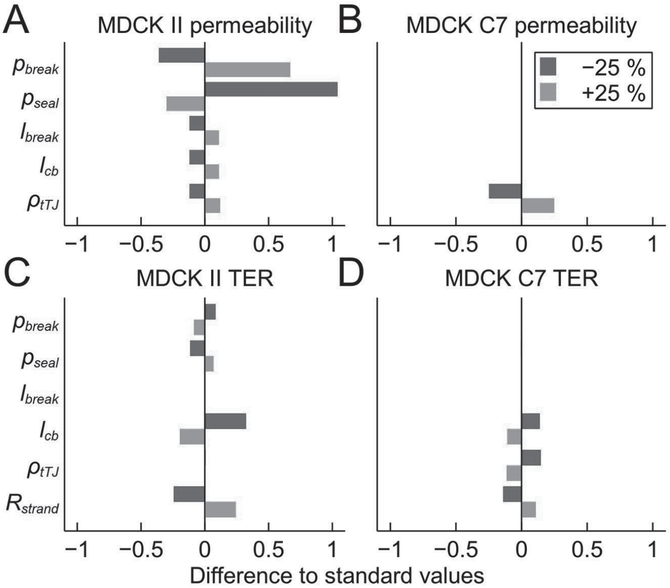

Fig 7. Parameter sensitivity analysis. Results of the parameter sensitivity analysis. We varied the values of the chosen parameters by ±25% and both the permeability and TER simulation results were compared with the normal system. The analysis was conducted for average MDCK II permeability (A) and TER (C) as well as MDCK C7 permeability (B) and TER (D). p_{break}, break forming probability; p_{seal}, break sealing probability; l_{break}, break size; l_{cb}, strand length per area; ρ_{tTJ}, tricellular TJ pore density; R_{strand}, strand resistance.

https://doi.org/10.1371/journal.pone.0214876.g007

TER model. Parameters l_{cb} and ρ_{tTJ} both depend on the cell size, and thus are not independent from each other. However, by changing them individually we could observe the relative roles of these parameters. We ran the analysis for both the average MDCK II and the MDCK C7 using the same default values of l_{cb} (0.282 μm^{-1}) and ρ_{tTJ} (0.049 μm^{-2}) as with the strand number simulations. The results comparing the sensitivity simulations with the standard simulations are shown in Fig 7.

The permeability of MDCK II was very sensitive to the changes in the strand dynamics, since alterations in the break probabilities led to large changes in the permeability. The variance of these parameters had a significantly smaller effect on the MDCK II TER. While the alterations in l_{break} affected the MDCK II permeability, they had no effect on TER. Alterations in the values of l_{cb} and ρ_{tTJ} had similar levels of influence on the MDCK II permeability. The MDCK II TER was unchanged by the variance of ρ_{tTJ}. However, it was affected more by the variance of l_{cb} than the permeability. Finally, the changes in TER were equal to the alterations in R_{strand} for MDCK II, indicating direct proportionality.

The results were extremely different for MDCK C7. Due to the lower level of strand dynamics, the alterations in the parameters describing the breaks (p_{break}, p_{seal}, and l_{break}) had no effect on either permeability or TER. This was also the case with l_{cb} for permeability. On the other hand, the results indicate direct dependence of permeability on ρ_{tTJ} for MDCK C7. The impacts of both l_{cb} and ρ_{tTJ} were similar for TER, but smaller than the parameter value variations. Finally, the influence of R_{strand} for MDCK C7 was smaller than for MDCK II.

Discussion

Tight junctions (TJs) are an indispensable part of the epithelia that form the barriers between many of the body's compartments, and yet not enough is known about their structure or structural dynamics. In this work, we have developed a computational model of the dynamic TJ structure to study the origin and the properties of the leak pathway—the nonspecific permeation pathway through the TJs. This was done by simulating the epithelial molecular permeability of a PEG oligomer and transepithelial electrical resistance (TER) with the same structural strand dynamics for different epithelial monolayers and scenarios. The model combines the current knowledge and theory of the dynamic TJ structure into a computational framework.

There are experimental findings that attest to both candidates for the leak pathway: the tricellular junction pores and the bicellular strand dynamics. Krug et al. [16] observed that 3-kDa dextran mainly diffuses through the tTJ pores, and through the bTJs to a lesser extent. While our model did not extend to macromolecule permeation, the limited size of the strand breaks would result in the tTJ pores being the main pathway for the molecules of this size. Krug et al. also calculated the role of the tTJ pores to be minuscule for ion permeation due to their rarity [16]. At the moment, there is no direct evidence of the dynamic bTJ strand breaking and sealing events forming the leak pathway, but it has been theorized [20, 22, 33, 47, 48]. Although dynamic strand breaks have been observed in transfected fibroblasts [46, 50] and static breaks in freeze-fracture images [16, 51–53], no strand breaks were detected by Weber et al. in their bTJ patch clamp measurements [56]. They discussed multiple reasons for this, including that the breaks may not be distinguishable from the patch seal break [56]. It is, however, also possible that the strong electrode seal between the pipette and the junctional membrane might stabilize the strands mechanically and therefore prevent the strand level dynamics.

While one of the assumptions in our models was that the leak pathway is formed by both the bTJ strand dynamics and tTJ pores, interestingly, the permeability leak pathway of the MDCK C7 was formed solely by the tTJ pores. Whereas the relative roles of two pathways in permeability varied greatly between our four MDCK II fitting results, they all showed that the tTJ pores by themselves were incapable of producing the measured permeability values. A possible cause for the variation between the MDCK II results is the cell culture times in the experiments. The reported respective culturing periods for the MDCK IIa, IIb, and IId were from 4 to 8 days, from 7 to 10 days, and 10 days [33, 34, 54]. There was no culture time directly reported for MDCK IIc [83]. This indicates that longer culturing periods might have led to a higher significance of the bTJ pathway and to a higher level of strand dynamics. However, since the amount of the data is limited, this might be a coincidence. Similar to MDCK II, approximately half of the permeability leak pathway was formed by the bTJ dynamics for Caco-2. As for the TER, the MDCK II was dominated by the bTJ pathway, as was also calculated by Krug et al. [16]. On the contrary, the impact of tTJ pores on the Caco-2 and the MDCK C7 was significant, due to the higher strand resistance.

Thus, as theorized by Liang & Weber [20], our model suggests that the tTJ pores and the bTJ strand dynamics may both contribute to the leak pathway with varying degrees. Moreover, the significance of these two alternatives was different for permeability and TER. The tTJ pores were the prominent permeation pathway only for epithelia with more stable strands, since the extremely rare breaks did not enable fast step-by-step permeation. The strand dynamics had a lesser role in determining the bTJ resistance, as the strand resistance, and thus their molecular composition was the dominating factor. The tTJ pores became more important only with the higher strand resistances. This two-component leak pathway is further supported by how changes in the expression of occludin and tricellulin, effect the macromolecular permeation.

Although it is not completely understood how, the expression of levels of occludin, mainly located in the bTJ strands, have been shown to regulate the leak pathway permeability [45, 83, 85, 86]. On the other hand, Krug et al. [16, 87] have shown that increased expression of tricellulin leads to a decreased permeability of >4-kDa dextrans and vice versa.

Although there was diversity in the cell sizes, the main differences between the epithelial barriers rose from the distinct levels of the bTJ strand dynamics and strand resistances. Of the epithelia considered here, Caco-2 was found to have the most dynamic strands. The obtained break forming probabilities for the MDCK II results were quite similar to each other, while MDCK C7 had extremely limited strand dynamics. Surprisingly, while the strands of Caco-2 were the most dynamic, its strand resistance was comparable to that of the MDCK C7. In addition, the large difference in measured TER between MDCK II and C7 was also observed in the obtained strand resistances, which is in line with the current understanding that the TER is mainly defined by the conductive properties of the claudins, especially claudin-2, found in the strands [33, 74, 88]. The strand resistances of every epithelia were significantly higher than the strand break resistance. However, due to the rarity of the breaks, especially full openings, the strand resistances largely defined the overall TER, as shown by the sensitivity analysis. The MDCK C7 TER measured by Van Itallie et al. [33] was considerably smaller than the originally measured values (460 vs. 5650 Ω cm^2) [84]. Our simulations show that this difference is explained by the cell size, since the C7 cells of Van Itallie et al. [33] are distinctly smaller than those of Gekle et al. [84], which leads to smaller length of bTJs and number of tTJ per area and thus higher TER. Further, although the claudin-2 dynamics model by Weber et al. [66] used a 3-strand model instead of the 4-strand used here and their description of the leak pathway differed from ours, there are surprising similarities. The calculated steady-state strand resistance defined for their claudin-2-transfected high-resistance MDCK I model equals to approximately 0.32 GΩ μm, which is close to our claudin-2-containing MDCK II values.

Our models showed what kind of changes in the dynamic structure could lead to the observed experimental changes in the TJ barrier properties. Van Itallie et al. [34] found that ZO-1 stabilizes the TJ barrier, and therefore we described the decrease in stability caused by the ZO-1 knockdown by an increase in the strand break forming probability. The permeability results of the double ZO-1/2 knockdown study by Fanning et al. [54] were similarly replicated by changing this parameter. The higher change in the break forming probability in the double knockdown is in line with the observations that the two ZOs have redundant roles [54, 89], and thus knocking out both of them should decrease the strand stability even more. The decreased stability caused by the lack of binding between claudin-2 and ZO-1 was recently visualized in fibroblasts by Van Itallie et al. [50]. Interestingly, they found no difference in the number of breaks with or without this binding. However, this result might have been caused by the nonepithelial model system. On the other hand, we did not consider possible changes in the bTJ strand number or morphology due to the knockdowns. Umeda et al. [89] showed that ZO-1 knockout/ZO-2 knockdown completely eliminated the bTJ strands, accompanied by extremely low TER compared with the control. However, we expected that the strand number was not greatly affected by the ZO-1 and double ZO-1/2 knockdowns, since only a minor change in TER was reported [34, 54]. In addition, since we also had to increase the strand resistances to fit the TER model to these data, our results indicate that these knockdowns might also affect the strand resistance in a presently unknown manner.

The understanding regarding the role of the bTJ strand number in the properties of the epithelial barrier has changed over time. TER was originally found to depend exponentially on bTJ strand number [21]. This was hypothesized to arise from transient pores in the compartmentalized bTJ strand network [21, 90]. However, this idea has been refuted since TER is now known to mainly depend on the TJ claudin composition [5, 74, 88]. Our results agree that the dependence of TER on the strand number is not straightforward and show a complex dependence on strand resistance that is defined by the protein composition, the strand number, as well as the level of structural dynamics. The saturation towards higher strand numbers comes from the increasing relative role of the static tTJ pathway. Moreover, the results of TER as a function of time show the immensely varying behavior of the resistance in the epithelia with different levels of strand dynamics and numbers.

To the best of our knowledge, there have been no experimental studies that directly investigate the effect of strand number on molecular permeability. Colegio et al. [75] showed that an increase in strand number caused by the increased claudin-2 and -4 expression had no effect on the permeability of mannitol that diffuses via the leak pathway. However, based on their freeze-fracture images [75], the strand numbers were in the range of the permeability saturation shown in our simulations, and thus mannitol permeability should remain unchanged, indicating agreement with our results. The saturation in our results was caused by the tTJ pores, as the permeability of the bTJ pathway become lower than that of the tTJ pathway. The unaveraged permeability simulation raw data revealed vastly different permeability behavior depending on the strand numbers and levels of breaking dynamics. The observed biphasic behavior in the permeability simulations is most likely a property of the dynamic network system. In the high-permeability side of this behavior, the change in the number of the full opening events in the strand network caused by alterations in the strand number or level of dynamics led to large changes in permeability. However, since the low-permeability end of this behavior depends on the step-by-step diffusion between the compartments, the alterations in the strand number or dynamics have a lesser effect on the permeability.

Overall, our results concerning the effect of strand number, the ZO knockdowns, as well as the sensitivity analysis showed that changes in the bTJ structure or dynamics lead to considerably larger changes in the molecular permeability compared with the TER. Thus, measuring only the TER might hide important unseen changes in molecular permeability and in the barrier properties. The TER is a good indicator of epithelial condition and is straightforward to measure, but it contains a lot of uncertainty due to the differences in measurement setup and conditions. Our results strengthen the idea that both the molecular permeability and the TER are needed to properly define the TJ as a barrier [91, 92].

Our comparison with the steady-state models showed that they are not able to reproduce the same behavior as our dynamic models. Since there were constant breaks in the steady-state model, the changes in the strand number or the number of breaks had only a minor effect on the permeability and the TER. Nevertheless, our models had their limitations concerning both the chosen parameter values and the geometry. Because of the lack of rigorous experimental data, we were forced to estimate and fit the probabilities of the strand dynamics and build the model partially with assumptions and hypotheses available in the literature. Moreover, the TJ strand morphology is very diverse and heterogeneous, the number of strands varies within an epithelium [39, 55, 77, 78, 93], and the strands typically become tighter towards the apical direction [13]. Also, the expression of tricellulin differs between the epithelia, but the effects of its expression level on the TER and the permeability of molecules with similar size to 547-Da PEG were minor [16]. Further, many molecules permeate the epithelia through the cells using active transport processes, which are difficult to model due to their specificity. However, the PEG oligomers are hydrophilic [40], indicating that they mainly diffuse via the TJs. Thus, our model reflects the PEG-based permeability measurements. In addition, our model lacks the claudin-2 pore dynamics that have previously been observed [56, 66]. However, we opted to exclude these dynamics, since their effect has not been characterized for noncharged molecules. Finally, although there is evidence that the TJs form the main conduction pathway [27, 28], Günzel et al. [26] calculated that for many epithelia the transcellular resistance affects the overall TER or is even lower than the paracellular resistance. This indicates that our assumption that TJs define the TER will not work for every epithelium and condition.

We demonstrated that our dynamic structure models can reproduce the basic TJ barrier behavior. With the simplified structure and dynamics, the models enable the comparison between the molecular permeability and the TER under the same dynamic context at the level of the TJs. We showed that the TJ strand breaking dynamics can drastically alter both of these barrier properties independently of each other, highlighting the importance of both measures for characterizing the epithelial barrier. Furthermore, our results indicated that the leak pathway may be formed both by the tTJ pores and the bTJ strand dynamics with varying degrees, but differently for the permeability and the TER. Our models create a good methodological framework that can be used to integrate knowledge on TJ structure, parametrize experimental measurements, and produce hypotheses that can be studied experimentally. Refined versions of the models could include a more realistic strand network as well as inhomogeneities in the strands. This would provide tools to study how diseases that affect the TJ structure alter the properties of the epithelial barrier.

Supporting information

S1 File. Tight junctions permeability model. A Matlab model file of the tight junctions molecular permeability model.
(ZIP)

S2 File. Tight junctions TER model. A Matlab model file of the tight junctions transepithelial electric resistance model.
(ZIP)

Acknowledgments

We thank Daniel García León, Dr. Michelangelo Paci, Julia Johansson, Jussi Koivumäki, and Peter Heath for helpful comments and the Finnish IT Center for Science (CSC) for computational resources.

Author Contributions

Conceptualization: Aapo Tervonen, Teemu O. Ihalainen, Soile Nymark, Jari Hyttinen.

Data curation: Aapo Tervonen.

Formal analysis: Aapo Tervonen.

Funding acquisition: Aapo Tervonen, Jari Hyttinen.

Investigation: Aapo Tervonen.

Methodology: Aapo Tervonen.

Project administration: Aapo Tervonen, Jari Hyttinen.

Resources: Aapo Tervonen.

Software: Aapo Tervonen.

Supervision: Aapo Tervonen, Teemu O. Ihalainen, Jari Hyttinen.

Validation: Aapo Tervonen, Soile Nymark.

Visualization: Aapo Tervonen.

Writing – original draft: Aapo Tervonen.

Writing – review & editing: Aapo Tervonen, Teemu O. Ihalainen, Soile Nymark, Jari Hyttinen.

References

1. Shen L, Su L, Turner JR. Mechanisms and functional implications of intestinal barrier defects. Digest Dis. 2009; 27:443–9. https://doi.org/10.1159/000233282
2. Barmeyer C, Schulzke JD, Fromm M. Claudin-related intestinal diseases. Semin Cell Dev Biol. 2015; 42:30–8. https://doi.org/10.1016/j.semcdb.2015.05.006 PMID: 25999319
3. Mullin JM, Agostino N, Rendon-Huerta E, Thornton JJ. Keynote review: Epithelial and endothelial barriers in human disease. Drug Discov Today. 2005; 10:359–408. https://doi.org/10.1016/S1359-6446(05)03379-9
4. Ikenouchi J, Furuse M, Furuse K, Sasaki H, Tsukita S, Tsukita S. Tricellulin constitutes a novel barrier at tricellular contacts of epithelial cells. J Cell Biol. 2005; 171:939–45. https://doi.org/10.1083/jcb.200510043 PMID: 16365161
5. Stevenson BR, Anderson JM, Goodenough DA, Mooseker MS. Tight junction structure and ZO-1 content are identical in two strains of Madin-Darby canine kidney cells which differ in transepithelial resistance. J Cell Biol. 1988; 107:2401–8. https://doi.org/10.1083/jcb.107.6.2401 PMID: 3058723
6. Rahner C, Fukuhara M, Peng S, Kojima S, Rizzolo LJ. The apical and basal environments of the retinal pigment epithelium regulate the maturation of tight junctions during development. J Cell Sci. 2004; 117:3307–18. https://doi.org/10.1242/jcs.01181 PMID: 15226402
7. Staehelin LA. Further Observations on the Fine Structure of Freeze-Cleaved Tight Junctions. J Cell Sci. 1973; 13:763–86. PMID: 4203962
8. Hein M, Post A, Galla HJ. Implications of a non-lamellar lipid phase for the tight junction stability. Part I: Influence of basic amino acids, pH and protamine on the bilayer-hexagonal II phase behaviour of PS-containing PE membranes. Chemistry and physics of lipids. 1992; 63(3):213–221. https://doi.org/10.1016/0009-3084(92)90037-P PMID: 1493615
9. Hein M, Madefessel C, Haag B, Teichmann K, Post A, Galla HJ. Implications of a non-lamellar lipid phase for the tight junction stability: Part II: Reversible modulation of transepithelial resistance in high and low resistance MDCK-cells by basic amino acids, Ca2+, protamine and protons. Chem Phys Lipids. 1992; 63(3):223–233. https://doi.org/10.1016/0009-3084(92)90038-Q PMID: 1337316
10. Grebenkämper K, Galla HJ. Translational diffusion measurements of a fluorescent phospholipid between MDCK-I cells support the lipid model of the tight junctions. Chem Phys Lipids. 1994; 71(2):133–143. https://doi.org/10.1016/0009-3084(94)90066-3 PMID: 8076400
11. Lingaraju A, Long TM, Wang Y, Austin JR, Turner JR. Conceptual barriers to understanding physical barriers. Semin Cell Dev Biol. 2015; 42:13–21. https://doi.org/10.1016/j.semcdb.2015.04.008 PMID: 26003050
12. Zihni C, Mills C, Matter K, Balda MS. Tight junctions: from simple barriers to multifunctional molecular gates. Nat Rev Mol Cell Bio. 2016; 17:564–80. https://doi.org/10.1038/nrm.2016.80
13. Van Itallie CM, Anderson JM. Architecture of tight junctions and principles of molecular composition. Semin Cell Dev Biol. 2014; 36:157–65. https://doi.org/10.1016/j.semcdb.2014.08.011 PMID: 25171873
14. Suzuki H, Tani K, Tamura A, Tsukita S, Fujiyoshi Y. Model for the Architecture of Claudin-Based Paracellular Ion Channels through Tight Junctions. J Mol Biol. 2015; 427:291–7. https://doi.org/10.1016/j.jmb.2014.10.020 PMID: 25451028
15. Hewitt KJ, Agarwal R, Morin PJ. The claudin gene family: expression in normal and neoplastic tissues. BMC Cancer. 2006; 6:186. https://doi.org/10.1186/1471-2407-6-186 PMID: 16836752
16. Krug SM, Amasheh S, Richter JF, Milatz S, Günzel D, Westphal JK, et al. Tricellulin forms a barrier to macromolecules in tricellular tight junctions without affecting ion permeability. Mol Biol Cell. 2009; 20:3713–24. https://doi.org/10.1091/mbc.E09-01-0080 PMID: 19535456
17. Irudayanathan FJ, Trasatti JP, Karande P, Nangia S. Molecular Architecture of the Blood Brain Barrier Tight Junction Proteins–A Synergistic Computational and In Vitro Approach. J Phys Chem B. 2015; 120:77–88. https://doi.org/10.1021/acs.jpcb.5b09977 PMID: 26654362
18. Suzuki H, Nishizawa T, Tani K, Yamazaki Y, Tamura A, Ishitani R, et al. Crystal structure of a claudin provides insight into the architecture of tight junctions. Science. 2014; 344:304–7. https://doi.org/10.1126/science.1248571 PMID: 24744376
19. Saitoh Y, Suzuki H, Tani K, Nishikawa K, Irie K, Ogura Y, et al. Tight junctions. Structural insight into tight junction disassembly by Clostridium perfringens enterotoxin. Science. 2015; 347:775–8. PMID: 25678664

20. Liang GH, Weber CR. Molecular aspects of tight junction barrier function. Curr Opin Pharmacol. 2014; 19:84–9. https://doi.org/10.1016/j.coph.2014.07.017 PMID: 25128899
21. Claude P. Morphological Factors Influencing Transepithelial Permeability: a Model for the Resistance of the Zonula Occludens. J Membrane Biol. 1978; 39:219–32. https://doi.org/10.1007/BF01870332
22. Günzel D, Yu ASL. Claudins and the modulation of tight junction permeability. Physiol Rev. 2013; 93:525–69. https://doi.org/10.1152/physrev.00019.2012 PMID: 23589827
23. Turner J. 'Putting the squeeze' on the tight junction: understanding cytoskeletal regulation. Semin Cell Dev Biol. 2000; 11:301–8. https://doi.org/10.1006/scdb.2000.0180 PMID: 10966864
24. Rodgers LS, Fanning AS. Regulation of epithelial permeability by the actin cytoskeleton. Cytoskeleton. 2011; 68:653–60. https://doi.org/10.1002/cm.20547 PMID: 22083950
25. Van Itallie CM, Anderson JM. The molecular physiology of tight junction pores. Physiology. 2004; 19:331–8. https://doi.org/10.1152/physiol.00027.2004 PMID: 15546850
26. Günzel D, Zakrzewski SS, Schmid T, Pangalos M, Wiedenhoeft J, Blasse C, et al. From TER to trans- and paracellular resistance: lessons from impedance spectroscopy. Ann NY Acad Sci. 2012; 1257:142–51. https://doi.org/10.1111/j.1749-6632.2012.06540.x PMID: 22671600
27. Gitter AH, Bertog M, Schulzke JD, Fromm M. Measurement of paracellular epithelial conductivity by conductance scanning. Pflug Arch Eur J Phy. 1997; 434:830–40. https://doi.org/10.1007/s004240050472
28. Zhou Y, Chen CC, Weber AE, Zhou L, Baker LA, Hou J. Potentiometric-scanning ion conductance microscopy for measurement at tight junctions. Tissue Barriers. 2013; 1:e25585. https://doi.org/10.4161/tisb.25585 PMID: 24533255
29. Benson K, Cramer S, Galla HJ. Impedance-based cell monitoring: barrier properties and beyond. Fluids and Barriers of the CNS. 2013; 10:5. https://doi.org/10.1186/2045-8118-10-5 PMID: 23305242
30. Srinivasan B, Kolli AR, Esch MB, Abaci HE, Shuler ML, Hickman JJ. TEER Measurement Techniques for In Vitro Barrier Model Systems. J Lab Autom. 2015; 20(2):107–126. https://doi.org/10.1177/2211068214561025 PMID: 25586998
31. Watson CJ, Rowland M, Warhurst G. Functional modeling of tight junctions in intestinal cell monolayers using polyethylene glycol oligomers. Am J Physiol-Cell Ph. 2001; 281:C388–97. https://doi.org/10.1152/ajpcell.2001.281.2.C388
32. Watson CJ, Hoare CJ, Garrod DR, Carlson GL, Warhurst G. Interferon-gamma selectively increases epithelial permeability to large molecules by activating different populations of paracellular pores. J Cell Sci. 2005; 118:5221–30. https://doi.org/10.1242/jcs.02630 PMID: 16249235
33. Van Itallie CM, Holmes J, Bridges A, Gookin JL, Coccaro MR, Proctor W, et al. The density of small tight junction pores varies among cell types and is increased by expression of claudin-2. J Cell Sci. 2008; 121:298–305. https://doi.org/10.1242/jcs.021485 PMID: 18198187
34. Van Itallie CM, Fanning AS, Bridges A, Anderson JM. ZO-1 Stabilizes the Tight Junction Solute Barrier through Coupling to the Perijunctional Cytoskeleton. Mol Biol Cell. 2009; 20:3930–40. https://doi.org/10.1091/mbc.E09-04-0320 PMID: 19605556
35. Van Itallie CM, Holmes J, Bridges A, Anderson JM. Claudin-2-dependent changes in noncharged solute flux are mediated by the extracellular domains and require attachment to the PDZ-scaffold. Ann NY Acad Sci. 2009; 1165:82–7. https://doi.org/10.1111/j.1749-6632.2009.04052.x PMID: 19538292
36. Linnankoski J, Mäkelä J, Palmgren J, Mauriala T, Vedin C, Ungell A, et al. Paracellular Porosity and Pore Size of the Human Intestinal Epithelium in Tissue and Cell Culture Models. J Pharm Sci. 2010; 99:2166–75. https://doi.org/10.1002/jps.21961 PMID: 19827099
37. Amasheh S, Meiri N, Gitter AH, Schöneberg T, Mankertz J, Schulzke JD, et al. Claudin-2 expression induces cation-selective channels in tight junctions of epithelial cells. J Cell Sci. 2002; 115:4969–76. https://doi.org/10.1242/jcs.00165 PMID: 12432083
38. Pitkänen L, Ranta VP, Moilanen H, Urtti A. Permeability of retinal pigment epithelium: effects of permeant molecular weight and lipophilicity. Invest Ophth Vis Sci. 2005; 46:641–6. https://doi.org/10.1167/iovs.04-1051
39. Rajasekaran SA, Hu J, Gopal J, Gallemore R, Ryazantsev S, Bok D, et al. Na,K-ATPase inhibition alters tight junction structure and permeability in human retinal pigment epithelial cells. Am J Physiol-Cell Ph. 2003; 284:C1497–507. https://doi.org/10.1152/ajpcell.00355.2002
40. Ma TY, Hollander D, Krugliak P, Katz K. PEG 400, a hydrophilic molecular probe for measuring intestinal permeability. Gastroenterology. 1990; 98:39–46. https://doi.org/10.1016/0016-5085(90)91288-H PMID: 2293598
41. He YL, Murby S, Warhurst G, Gifford L, Walker D, Ayrton J, et al. Species differences in size discrimination in the paracellular pathway reflected by oral bioavailability of poly(ethylene glycol) and D-peptides. J Pharm Sci. 1998; 87:626–33. https://doi.org/10.1021/js970120d PMID: 9572915

42. Shen L, Weber CR, Raleigh DR, Yu D, Turner JR. Tight junction pore and leak pathways: a dynamic duo. Annu Rev Physiol. 2011; 73:283–309. https://doi.org/10.1146/annurev-physiol-012110-142150 PMID: 20936941

43. Capaldo CT, Nusrat A. Claudin switching: Physiological plasticity of the Tight Junction. Semin Cell Dev Biol. 2015; 42:22–9. https://doi.org/10.1016/j.semcdb.2015.04.003 PMID: 25957515

44. Krug SM, Günzel D, Conrad MP, Lee IFM, Amasheh S, Fromm M, et al. Charge-selective claudin channels. Ann N Y Acad Sci. 2012; 1257(1):20–28. https://doi.org/10.1111/j.1749-6632.2012.06555.x PMID: 22671585

45. Buschmann MM, Shen L, Rajapakse H, Raleigh DR, Wang Y, Wang Y, et al. Occludin OCEL-domain interactions are required for maintenance and regulation of the tight junction barrier to macromolecular flux. Mol Biol Cell. 2013; 24:3056–68. https://doi.org/10.1091/mbc.E12-09-0688 PMID: 23924897

46. Sasaki H, Matsui C, Furuse K, Mimori-Kiyosue Y, Furuse M, Tsukita S. Dynamic behavior of paired claudin strands within apposing plasma membranes. P Natl Acad Sci USA. 2003; 100:3971–6. https://doi.org/10.1073/pnas.0630649100

47. Guo P, Weinstein AM, Weinbaum S. A dual-pathway ultrastructural model for the tight junction of rat proximal tubule epithelium. Am J Physiol-Renal. 2003; 285:F241–57. https://doi.org/10.1152/ajprenal.00331.2002

48. Anderson JM, Van Itallie CM, Fanning AS. Setting up a selective barrier at the apical junction complex. Curr Opin Cell Biol. 2004; 16:140–5. https://doi.org/10.1016/j.ceb.2004.01.005 PMID: 15196556

49. Shen L, Weber CR, Turner JR. The tight junction protein complex undergoes rapid and continuous molecular remodeling at steady state. J Cell Biol. 2008; 181:683–95. https://doi.org/10.1083/jcb.200711165 PMID: 18474622

50. Van Itallie CM, Tietgens AJ, Anderson JM. Visualizing the dynamic coupling of claudin strands to the actin cytoskeleton through ZO-1. Mol Biol Cell. 2017; 28:524–34. https://doi.org/10.1091/mbc.E16-10-0698 PMID: 27974639

51. Zeissig S, Burgel N, Gunzel D, Richter J, Mankertz J, Wahnschaffe U, et al. Changes in expression and distribution of claudin 2, 5 and 8 lead to discontinuous tight junctions and barrier dysfunction in active Crohn's disease. Gut. 2007; 56:61–72. https://doi.org/10.1136/gut.2006.094375 PMID: 16822808

52. Rosenthal R, Milatz S, Krug SM, Oelrich B, Schulzke JD, Amasheh S, et al. Claudin-2, a component of the tight junction, forms a paracellular water channel. J Cell Sci. 2010; 123:1913–21. https://doi.org/10.1242/jcs.060665 PMID: 20460438

53. Rosenthal R, Günzel D, Krug SM, Schulzke JD, Fromm M, Yu ASL. Claudin-2-mediated cation and water transport share a common pore. Acta Physiol. 2017; 219:521–36. https://doi.org/10.1111/apha.12742

54. Fanning AS, Van Itallie CM, Anderson JM. Zonula occludens-1 and -2 regulate apical cell structure and the zonula adherens cytoskeleton in polarized epithelia. Mol Biol Cell. 2012; 23:577–90. https://doi.org/10.1091/mbc.E11-09-0791 PMID: 22190737

55. Gong Y, Renigunta V, Zhou Y, Sunq A, Wang J, Yang J, et al. Biochemical and biophysical analyses of tight junction permeability made of claudin-16 and claudin-19 dimerization. Mol Biol Cell. 2015; 26:4333–46. https://doi.org/10.1091/mbc.E15-06-0422 PMID: 26446843

56. Weber CR, Liang GH, Wang Y, Das S, Shen L, Yu ASL, et al. Claudin-2-dependent paracellular channels are dynamically gated. Elife. 2015; 4:e09906. https://doi.org/10.7554/eLife.09906 PMID: 26568313

57. Conrad MP, Piontek J, Günzel D, Fromm M, Krug SM. Molecular basis of claudin-17 anion selectivity. Cell Mol Life Sci. 2015; 73:185–200. https://doi.org/10.1007/s00018-015-1987-y PMID: 26194246

58. Fredriksson K, Itallie CMV, Aponte A, Gucek M, Tietgens AJ, Anderson JM. Proteomic analysis of proteins surrounding occludin and claudin-4 reveals their proximity to signaling and trafficking networks. PLoS ONE. 2015; 10:e0117074. https://doi.org/10.1371/journal.pone.0117074 PMID: 25789658

59. Ho NFH, Raub TJ, Burton PS, Barsuhn CL, Adson A, Audus KL, et al. Quantitative Approaches to Delineate Passive Transport Mechanisms in Cell Culture Monolayers. In: Amidon GL, Lee PI, Topp EM, editors. Transport Processes in Pharmaceutical Systems. Marcel Decker, Inc; 2000. p. 219–316.

60. Saitoh R, Sugano K, Takata N, Tachibana T, Higashida A, Nabuchi Y, et al. Correction of permeability with pore radius of tight junctions in Caco-2 monolayers improves the prediction of the dose fraction of hydrophilic drugs absorbed by humans. Pharm Res. 2004; 21:749–55. https://doi.org/10.1023/B:PHAM.0000026423.48583.e2 PMID: 15180329

61. Avdeef A. Leakiness and size exclusion of paracellular channels in cultured epithelial cell monolayers-interlaboratory comparison. Pharm Res. 2010; 27:480–9. PMID: 20069445

62. Diecke FP, Cacace VI, Montalbetti N, Ma L, Kuang K, Iserovich P, et al. Comparative permeabilities of the paracellular and transcellular pathways of corneal endothelial layers. J Membrane Biol. 2011; 242:41–51. https://doi.org/10.1007/s00232-011-9375-5

63. Yu ASL, Cheng MH, Angelow S, Günzel D, Kanzawa SA, Schneeberger EE, et al. Molecular basis for cation selectivity in claudin-2-based paracellular pores: identification of an electrostatic interaction site. J Gen Physiol. 2009; 133:111–27. PMID: 19114638

64. Tervonen A, Vainio I, Nymark S, Hyttinen J. Prediction of Passive Drug Permeability Across the Blood-Retinal Barrier. Pharm Res. 2014; 31:2297–311. https://doi.org/10.1007/s11095-014-1325-3 PMID: 24623477

65. Weber CR. Dynamic properties of the tight junction barrier. Ann NY Acad Sci. 2012; 1257:77–84. https://doi.org/10.1111/j.1749-6632.2012.06528.x PMID: 22671592

66. Weber CR, Turner JR. Dynamic modeling of the tight junction pore pathway. Ann NY Acad Sci. 2017; 1397:209–18. https://doi.org/10.1111/nyas.13374 PMID: 28605031

67. Washiyama M, Koizumi N, Fujii M, Kondoh M, Yagi K, Watanabe Y. Percolation analysis in electrical conductivity of madin-darby canine kidney and caco-2 cells by permeation-enhancing agents. Biol Pharm Bull. 2013; 36:384–9. https://doi.org/10.1248/bpb.b12-00786 PMID: 23449326

68. Usansky HH, Sinko PJ. Estimating Human Drug Oral Absorption Kinetics from Caco-2 Permeability Using an Absorption-Disposition Model: Model Development and Evaluation and Derivation of Analytical Solutions for k a and F a. J Pharmacol Exp Ther. 2005; 314(1):391–399. https://doi.org/10.1124/jpet.104.076182 PMID: 15833900

69. Adson A, Raub TJ, Burton PS, Barsuhn CL, Hilgers AR, Ho NFH, et al. Quantitative approaches to delineate paracellular diffusion in cultured epithelial cell monolayers. J Pharm Sci. 1994; 83(11):1529–1536. https://doi.org/10.1002/jps.2600831103 PMID: 7891269

70. Dechadilok P, Deen WM. Hindrance Factors for Diffusion and Convection in Pores. Ind Eng Chem Res. 2006; 45:6953–9. https://doi.org/10.1021/ie051387n

71. Ruddy SB, Hadzija BW. Iontophoretic permeability of polyethylene glycols through hairless rat skin: application of hydrodynamic theory for hindered transport through liquid-filled pores. Drug design and discovery. 1992; 8:207–24. PMID: 1525303

72. Balda MS, Whitney JA, Flores C, González S, Cereijido M, Matter K. Functional dissociation of paracellular permeability and transepithelial electrical resistance and disruption of the apical-basolateral intramembrane diffusion barrier by expression of a mutant tight junction membrane protein. J Cell Biol. 1996; 134:1031–49. https://doi.org/10.1083/jcb.134.4.1031 PMID: 8769425

73. Jou TS, Schneeberger EE, Nelson WJ. Structural and functional regulation of tight junctions by RhoA and Rac1 small GTPases. J Cell Biol. 1998; 142:101–15. https://doi.org/10.1083/jcb.142.1.101 PMID: 9660866

74. Furuse M, Furuse K, Sasaki H, Tsukita S. Conversion of zonulae occludentes from tight to leaky strand type by introducing claudin-2 into Madin-Darby canine kidney I cells. J Cell Biol. 2001; 153:263–72. https://doi.org/10.1083/jcb.153.2.263 PMID: 11309408

75. Colegio OR, Van Itallie CM, Rahner C, Anderson JM. Claudin extracellular domains determine paracellular charge selectivity and resistance but not tight junction fibril architecture. Am J Physiol-Cell Ph. 2003; 284:C1346–54. https://doi.org/10.1152/ajpcell.00547.2002

76. Kaufmann R, Piontek J, Grüll F, Kirchgessner M, Rossa J, Wolburg H, et al. Visualization and quantitative analysis of reconstituted tight junctions using localization microscopy. PLoS ONE. 2012; 7:e31128. https://doi.org/10.1371/journal.pone.0031128 PMID: 22319608

77. Sonoda N, Furuse M, Sasaki H, Yonemura S, Katahira J, Horiguchi Y, et al. Clostridium perfringens Enterotoxin Fragment Removes Specific Claudins from Tight Junction Strands: Evidence for Direct Involvement of Claudins in Tight Junction Barrier. J Cell Biol. 1999; 147:195–204. PMID: 10508866

78. Capaldo CT, Farkas AE, Hilgarth RS, Krug SM, Wolf MF, Benedik JK, et al. Proinflammatory cytokine-induced tight junction remodeling through dynamic self-assembly of claudins. Mol Biol Cell. 2014; 25:2710–9. https://doi.org/10.1091/mbc.E14-02-0773 PMID: 25031428

79. Tamura A, Tsukita S. Paracellular barrier and channel functions of TJ claudins in organizing biological systems: Advances in the field of barriology revealed in knockout mice. Semin Cell Dev Biol. 2014; 36:177–85. https://doi.org/10.1016/j.semcdb.2014.09.019 PMID: 25305579

80. Van Itallie CM, Tietgens AJ, Krystofiak E, Kachar B, Anderson JM. A complex of ZO-1 and the BAR Domain Protein TOCA-1 Regulates Actin Assembly at the Tight Junction. Mol Biol Cell. 2015; 26:2769–87. https://doi.org/10.1091/mbc.E15-04-0232 PMID: 26063734

81. Schindelin J, Arganda-Carreras I, Frise E, Kaynig V, Longair M, Pietzsch T, et al. Fiji: an open-source platform for biological-image analysis. Nat Methods. 2012; 9:676–82. https://doi.org/10.1038/nmeth.2019 PMID: 22743772

82. Schneider CA, Rasband WS, Eliceiri KW. NIH Image to ImageJ: 25 years of image analysis. Nat Methods. 2012; 9:671–5. https://doi.org/10.1038/nmeth.2089 PMID: 22930834

83. Van Itallie CM, Fanning AS, Holmes J, Anderson JM. Occludin is required for cytokine-induced regulation of tight junction barriers. J Cell Sci. 2010; 123:2844–52. https://doi.org/10.1242/jcs.065581 PMID: 20663912

84. Gekle M, Wünsch S, Oberleithner H, Silbernagl S. Characterization of two MDCK-cell subtypes as a model system to study principal cell and intercalated cell properties. Pflugers Arch. 1994; 428(2):157–162. https://doi.org/10.1007/BF00374853 PMID: 7971172

85. Marchiando AM, Shen L, Vallen Graham W, Weber CR, Schwarz BT, Austin JR, et al. Caveolin-1-dependent occludin endocytosis is required for TNF-induced tight junction regulation in vivo. J Cell Biol. 2010; 189(1):111–126. https://doi.org/10.1083/jcb.200902153 PMID: 20351069

86. Al-Sadi R, Khatib K, Guo S, Ye D, Youssef M, Ma T. Occludin regulates macromolecule flux across the intestinal epithelial tight junction barrier. Am J Physiol Gastrointest Liver Physiol. 2011; 300(6):G1054–G1064. https://doi.org/10.1152/ajpgi.00055.2011 PMID: 21415414

87. Krug SM, Bojarski C, Fromm A, Lee IM, Dames P, Richter JF, et al. Tricellulin is regulated via interleukin-13-receptor $\alpha 2$, affects macromolecule uptake, and is decreased in ulcerative colitis. Mucosal Immunol. 2018; 11(2):345–356. https://doi.org/10.1038/mi.2017.52 PMID: 28612843

88. Tokuda S, Furuse M. Claudin-2 Knockout by TALEN-Mediated Gene Targeting in MDCK Cells: Claudin-2 Independently Determines the Leaky Property of Tight Junctions in MDCK Cells. PLoS ONE. 2015; 10:e0119869. https://doi.org/10.1371/journal.pone.0119869 PMID: 25781928

89. Umeda K, Ikenouchi J, Katahira-Tayama S, Furuse K, Sasaki H, Nakayama M, et al. ZO-1 and ZO-2 Independently Determine Where Claudins Are Polymerized in Tight-Junction Strand Formation. Cell. 2006; 126:741–54. https://doi.org/10.1016/j.cell.2006.06.043 PMID: 16923393

90. Cereijido M, González-Mariscal L, Contreras G. Tight Junction: Barrier Between Higher Organisms and Environment. Physiology. 1989; 4:72–5. https://doi.org/10.1152/physiologyonline.1989.4.2.72

91. Hopkins AM, Li D, Mrsny RJ, Walsh SV, Nusrat A. Modulation of tight junction function by G protein-coupled events. Adv Drug Deliver Rev. 2000; 41:329–40. https://doi.org/10.1016/S0169-409X(00)00050-8

92. Rizzolo LJ. Development and role of tight junctions in the retinal pigment epithelium. Int Rev Cytol. 2007; 258:195–234. https://doi.org/10.1016/S0074-7696(07)58004-6 PMID: 17338922

93. Friend DS, Gilula NB. Variations in tight and gap junctions in mammalian tissues. J Cell Biol. 1972; 53:758–76. https://doi.org/10.1083/jcb.53.3.758 PMID: 4337577

PUBLICATION
III

Sensitivity Distribution of Electrical Impedance Epithelial Measurement Systems

Tervonen, A. & Hyttinen, J.

"Click here and type Original publication, vol, number and pages"
https://doi.org/10.1007/978-981-10-5122-7_156

Sensitivity Distribution of Electrical Impedance Epithelial Measurement Systems

A. Tervonen[1] and J. Hyttinen[1]

[1] BioMediTech Institute and Faculty of Biomedical Sciences and Engineering, Tampere University of Technology, Tampere, Finland

Abstract— **Epithelia are essential tissues that separate body compartments from each other and are affected by a plethora of diseases and conditions. Electrical properties are a convenient method to study the state of these tissues. There are various measurement setups for studying these properties. However, there has been no studies on how the setup of the electrodes affects the sensitivity distribution of the measurement system. We created a computational model of 4-electrode electrical impedance measurement system to study how the placement of the electrode as well as defects in the epithelium affect the sensitivity distribution. Our results show that the sensitivity is highly dependent on the frequency as well as on the distance between the electrodes and the epithelium. The sensitivity become more concentrated to areas between the electrodes when they were moved closer to the epithelium. The sensitivity should be taken into account when developing measurement systems to study localized phenomena with the electrodes placed close to the epithelium.**

Keywords— **Epithelium, electrical impedance, sensitivity distribution**

I. INTRODUCTION

Epithelial tissues separate body compartments from each other and govern the permeation between them. There is a plethora of diseases that affect the epithelial tissues, usually disrupting their barrier function [1]. Therefore the barrier function is an important indicator of the state of the epithelia.

A convenient method to study the epithelial barrier function is to measure the electrical resistance that the epithelium imposes on ion current flowing through it. This resistance can be measured either as a low-frequency transepithelial electrical resistance (TER) or as a frequency-dependent transepithelial electrical impedance (TEZ). With TEZ, the capacitive component is formed by the transcellular pathway through the cells and the resistive component is formed by both the transcellular pathway and the paracellular pathway between the cells [2]. Traditionally, TER and TEZ are measured with systems such as Ussing chamber in which the electrodes are placed relatively far away from the epithelium [3]. Also simpler system that measure TER and TEZ with electrodes positioned around cell culture inserts in well plates have been used [4]. These methods aim to measure the epithelium-wide properties. Four-electrode setups are common in these methods [3, 4], because the current injection is separated from the measurement electrodes, removing the effect of electrode polarization from the measurements.

The placement of the electrodes in the measurement system affects what part of the epithelium is actually measured. The electrode configuration produces a sensitivity distribution that can be determined computationally. The concept of sensitivity distribution is tightly connected to the lead field theory [5, 6]. A lead can be considered as a pair of electrodes connected to the system and when an unit current is flowing through the lead, it produces an current density in the system that is equal to the lead field. The lead fields produced by both the current injection and the voltage measurement electrodes can be used to calculate the sensitivity distribution of the electrode setup in question. This method has been used to study e.g. electrocardiography and electroencephalography measurement systems [7, 8].

We created a finite element method model of a 4-electrode TEZ measurement system for epithelia on inserts to study how the placement of the electrodes affects the results. The aim was to see the how suitable this kind of systems are for trying to measure local areas of epithelium. Further, we used the model to simulate how different local heterogeneities or defects in the epithelia affect the sensitivity distribution.

II. METHODS

The model was constructed as a cylindrical system for a cell culture insert with the diameter of 12 mm (12-well plate inserts, Corning Inc. [9]). The basic model geometry is shown in Fig. 1. The height of the chambers above and below the inserts was 5 mm. The cylindrical electrodes all had the radius of 0.5 mm. Electrodes 1 and 3 were the current injection electrodes and electrodes 2 and 4 the voltage measurement electrodes.

By assuming that there were no sources in the systems, the governing equation was Laplace's equation:

$$(\sigma + i\omega\varepsilon_0\varepsilon_r)\nabla^2 V = 0, \qquad (1)$$

where σ is the conductivity (S m^{-1}), ω is the angular frequency (Hz), ε_0 is the vacuum permittivity (8.8542×10^{12} F m^{-1}), ε_r is the relative permittivity and V is the electric

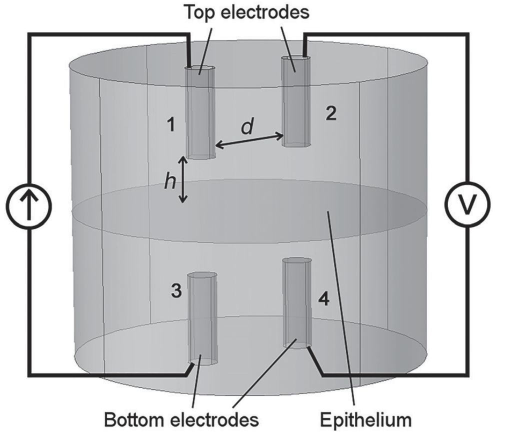

Fig. 1: Model geometry. The electrodes are shown in blue and the epithelium in green. Electrodes 1 and 3 are for current injection and 2 and 4 for voltage measurement. *h* = electrode-epithelium distance, *d* = distance between electrodes.

potential field (V). Zero current flux was assumed at all the boundaries except at the electrodes, whose boundary conditions depended on the case to be modeled. For the pair used to inject current, a Neumann boundary condition with a value of I_{unit} and a Dirichlet boundary condition with a value of 0 V were used for the top and bottom electrodes, respectively. The other electrode pair was set to zero flux.

The epithelium was simplified to a boundary having a impedance of

$$Z = \frac{1}{1/R + i\omega C}, \tag{2}$$

where Z is the impedance (Ω cm^2), R is the resistance (Ω cm^2) and C is the capacitance (F cm^{-2}).

The sensitivity distribution was determined by injecting unit current I_{unit} through the current injection and the voltage measurement electrode pairs in separate simulations and then by calculating the sensitivity from equation

$$S = J_{LI} \cdot J_{LE}, \tag{3}$$

where J_{LI} and J_{LE} are the lead fields of the current injection and voltage measurement electrodes, respectively [5, 7].

To study the effect of electrode placement we varied the electrode locations and calculated the sensitivity distribution for each configuration. In all of the simulated cases, the electrodes were positioned along the same axis and mirrored between the top and the bottom compartments as shown in Fig. 1. The two parameters that were varied where the electrode distance from the epithelium (*h*) and the distance between the electrodes in a pair (*d*). The four simulated cases are shown in Table 1. In addition to the sensitivity distribution, we also calculated the impedance measurement result for each of the electrode configurations.

Table 1: Cases to be modeled.

Case	1	2	3	4
electrode-epithelium distance, *h* (mm)	2	4	2	1
electrode-electrode distance, *d* (mm)	4	4	8	4

Next, we simulated three cases to see how defects in the epithelium affect the sensitivity distribution. These cases were simulated with Case 1 electrode configuration of the setup simulations (*h* = 2 mm and *d* = 4 mm). In these three cases we applied 90 % of the normal resistance to certain areas of the epithelium: (1) circular area (r = 1 mm) in the middle, (2) circular area (r = 1 mm) between one of the electrode pairs, and (3) area at the edges of the epithelium with the thickness that produces the same defected area as with cases 1 and 2 (thickness = 0.084 mm).

The parameters needed were the electrical properties of the epithelium and the medium. The epithelial parameters were based on the fitted results by Onnela et al. [4] for human embryonic stem cell derived retinal pigment epithelium cells. The resistance was $R = 390\ \Omega$ cm^2 and the capacitance $C = 7.1\ \mu$F cm^{-2}. The conductivity and the relative permittivity of the culture medium were taken as 1.6 S m^{-1} and 80 [10], respectively. The model was implemented with the electric currents module of Comsol Multiphysics® (v. 5.2a. www.comsol.com. COMSOL AB, Stockholm, Sweden).

III. RESULTS

The results of the simulations studying the effect of the electrode placement onto the sensitivity distributions and TEZ measurements are presented in Fig. 2 as lead fields at the boundary representing the epithelium (green in Fig. 1). As can be seen from the figure, the sensitivity distribution profile changed drastically with the changing frequency. The major changes happened at around 10^3 Hz for all of the simulations. The changes began around the frequency corresponding to the reciprocal of the time constant for the system ($1/(2\pi RC) = 57.48$ Hz). Generally, the highest points of sensitivity were between the electrodes in each pair, i.e. between electrodes 1 and 3 as well as electrodes 2 and 4. The major changes in the sensitivity occured between the electrode pairs in the middle of the insert. There, at low frequencies the

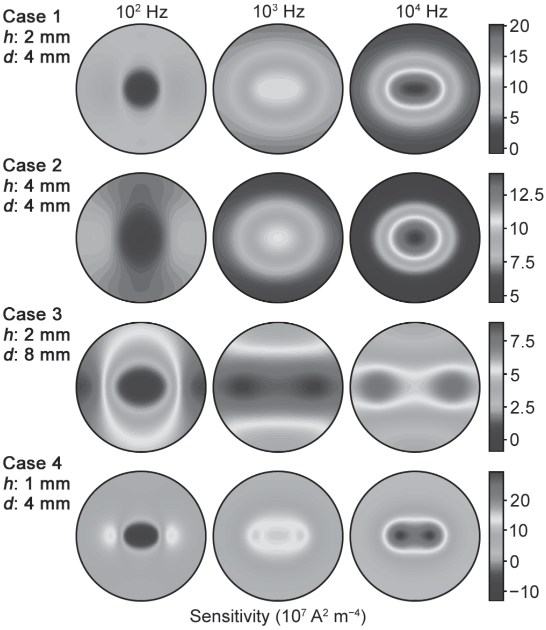

Fig. 2: Results of the simulations of changing the electrode placement as lead fields at the epithelium boundary (green in Fig. 1). Sensitivity distribution is shown for frequencies 10^2, 10^3, and 10^4 Hz as they describe the results best. Note that the scaling of the color is different between cases.

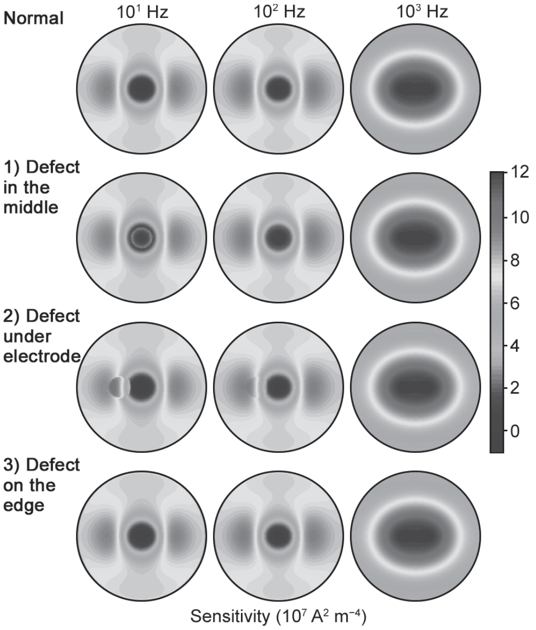

Fig. 3: Results of the simulations with three different defects in the epithelium as lead fields at the epithelium boundary (green in Fig. 1). 1) Circular defect in the middle with a radius of 1 mm. 2) Circular deferct under one of the electrodes with a radius of 1 mm. 3) Defect on the edge of the insert with a thickness of 0.084 mm. The normal case on top for comparison. Sensitivity distribution is shown for frequencies 10^1, 10^2, and 10^3 Hz as they describe the results best.

sensitivity was low or even negative, but at the transition frequency of 10^3 Hz the sensitivity increased rapidly to values even above the one between the electrodes in a pair. When the sensitivity is negative, the small changes in the electrical properties have the opposite effect on the measurement. For example, small decrease in resistance leads to increase in resistive part of the TEZ. The changes in the sensitivity distribution on the peripheral part of the inserts caused by the change in frequency were minute compared to changes in the middle of the insert. Also, the differences in the sensitivity throughout the epithelium became smaller when the electrodes were moved further away from the epithelium and from each other. The case with the distance of 1 mm had 4.38 times larger difference between the lowest and highest sensitivity values compared to the case with the distance 4 mm. There were no significant differences between the TEZ results between these simulated electrode placements.

The effects the three defects introduced into the epithelium had on the sensitivity distribution profile can be seen in Fig. 3. The defects were clearly seen only at frequencies lower than 10^3 Hz because of the transition to capacitance dominated domain beyond that limit. The influence of the defects was mainly restricted near them and the change in sensitivity at the defect was towards positive in all cases. Also, in case 3 there was a small decrease in sensitivity just outside the defect especially at low frequencies. With the edge defect, the effects were quite minor and limited to the edges. The defects produced an identical and small decrease in the measured TEZ.

IV. DISCUSSION

The ability to determine the sensitivity distribution for a measurement system makes it possible to easily study what the system actually measures which helps in the design of these systems. Defining the lead fields experimentally is extremely difficult if not impossible, and therefore computational methods provide a convenient and fast way to determine the sensitivity distributions.

The most striking finding from our study was the dramatic change in the sensitivity distribution caused by the change in frequency. Thus, in essence different frequencies measure different areas of the epithelium. At low frequencies the current spreads to a wide area because of the high resistance compared to the capacitive component of TEZ. The negative or low sensitivity in the middle is formed because of this spread. Especially when the electrodes were close the epithelium (Case 4), the horizontal components of the current vectors are large compared to the vertical ones. This led to negative values in the middle of the insert because of the dot product between two almost antiparallel vectors. As the frequency increased and the capacitive component became more significant, the current spread reduced and the current passed the epithelia more directly. This led to positive sensitivity also between the electrodes pairs. In addition, the distance of the electrodes from the epithelium has a considerable effect on the sensitivity.

While the negative sensitivity means that the changes in the epithelium are inversed in the measurement, these same changes also change the lead fields. This is emphasized as the epithelium is the defining factor resisting the current flow in the system. This is reflected by the result that similar defects located at areas of widely different sensitivity in the homogeneous case led to identical TEZ results. Thus, decrease of resistivity in the negative sensitivity area does not lead to increase in the measured TEZ. Clearly the effect of the negative sensitivity on changes in the epithelium is observable only with changes that do not affect the lead fields significantly.

The significance of the sensitivity distribution to a measurement largely depends on what is measured. If the aim is to monitor the condition of the epithelium in general, sensitivity might not be a relevant to consider. However, especially when more specific studies are done e.g. the similar placement of the electrodes in the system between different measurements becomes more important. Also, it is good to note that the formation of cell junctions during the epithelial maturation leads to increasing resistance and thus changes in the sensitivity distribution. Furthermore, the sensitivity is not an issue with systems such as the Ussing chambers, in which the electrodes are farther away from the epithelium than what was simulated here and the sensitivity distribution is basically homogeneous. The sensitivity becomes influential when designing measurement systems that aim to study the local resistive properties of the epithelia by bringing the electrodes extremely close the epithelium.

V. CONCLUSIONS

The placement of the electrodes in a TEZ measurement systems as well as the heterogeneity of the epithelium itself affect the sensitivity distribution during the measurements. The sensitivity becomes important as the electrodes are placed close to the epithelium and when local phenomena are to be studied and thus it should be taken into account when developing measurement systems for this use.

CONFLICT OF INTEREST

The authors declare that they have no conflict of interest.

ACKNOWLEDGMENTS

This study was funded by the Rector's Graduate School of Tampere University of Technology and Academy of Finland (grant number 298638).

REFERENCES

1. Mullin JM, Agostino N, Rendon-Huerta E, Thornton JJ. Keynote review: Epithelial and endothelial barriers in human disease *Drug Discov Today.* 2005;10:395–408.
2. Krug SM, Fromm M, Günzel D. Two-path impedance spectroscopy for measuring paracellular and transcellular epithelial resistance *Biophys J.* 2009;97:2202-2011.
3. Clarke LL. A guide to Ussing chamber studies of mouse intestine *Am J Physiol Gastrointest Liver Physiol.* 2009;296:G1151–G1166.
4. Onnela N, Savolainen V, Juuti-Uusitalo K, Vaajasaari H, Skottman H, Hyttinen J. Electric impedance of human embryonic stem cell-derived retinal pigment epithelium *Med Biol Eng Comput.* 2011;50:107–116.
5. Malmivuo J, Plonsey R. *Bioelectromagnetism - Principles and Applications of Bioelectric and Biomagnetic Fields*. New York: Oxford University Press 1995.
6. Geselowitz DB. An Application of Electrocardiographic Lead Theory to Impedance Plethysmography *IEEE Trans Biomed Eng.* 1971;18:38–41.
7. Kauppinen PK, Hyttinen JA, Kööbi T, Malmivuo J. Lead field theoretical approach in bioimpedance measurements: towards more controlled measurement sensitivity *Ann N Y Acad Sci.* 1999;873:135–142.
8. Wendel K, Narra NG, Hannula M, Kauppinen P, Malmivuo J. The influence of CSF on EEG sensitivity distributions of multilayered head models *IEEE Trans Biomed Eng.* 2008;55:1454–1456.
9. Corning Inc . Transwell Permeable Supports Selection and User Guide . Accessed 26th January, 2017. `http://csmedia2.corning.com/LifeSciences/Media/pdf/transwell_guide.pdf`.
10. Cho S, Becker S, Briesen H, Thielecke H. Impedance Monitoring of Virus-Induced Cytopahtic Effects in Cells in *IFMBE Proc, World Congress on Med. Phys. & Biomed. Eng.*;14(Seoul, Korea):695–698 2006.

Author: Aapo Tervonen
Institute: Tampere University of Technology
Street: Korkeakoulunkatu 6
City: Tampere
Country: Finland
Email: aapo.tervonen@tut.fi

PUBLICATION
IV

The effect of substrate stiffness on tensile force transduction in the epithelial monolayers

Tervonen, A., Korpela, S., Nymark, S., Hyttinen, J. & Ihalainen, T.O.

Manuscript

The effect of substrate stiffness on tensile force transduction in the epithelial monolayers

Aapo Tervonen[1*], Sanna Korpela[1], Soile Nymark[1], Jari Hyttinen[1], Teemu O Ihalainen[1]

1 BioMediTech, Faculty of Medicine and Health Technology, Tampere University, Tampere, Finland

* aapo.tervonen@tuni.fi

Abstract

In recent years, the importance of mechanical signaling and the cellular mechanical microenvironment in affecting cellular behavior has been widely accepted. Cells in epithelial monolayers are mechanically connected to each other and the underlying extracellular matrix (ECM), forming a highly connected mechanical system subjected to various mechanical cues from their environment, such as the ECM stiffness. Changes in the ECM stiffness have been linked to many pathologies, including tumor formation. However, our understanding of how ECM stiffness and its heterogeneities affect the transduction of mechanical forces in epithelial monolayers is lacking. To investigate this, we used a combination of experimental and computational methods. The experiments were conducted using epithelial cells cultured on an elastic substrate and applying a mechanical stimulus by moving a single cell by micromanipulation. To replicate our experiments computationally and quantify the forces transduced in the epithelium, we developed a new model that described the mechanics of both the cells and the substrate. Our model further enabled the simulations with local stiffness heterogeneities. We found the substrate stiffness to distinctly affect the force transduction as well as the cellular movement and deformation following an external force. Also, we found that local changes in the stiffness can alter the cells' response to external forces over long distances. Our results suggest that this long-range signaling of the substrate stiffness depends on the cells' ability to resist deformation. Furthermore, we found that the cell's elasticity in the apico-basal direction provides a level of detachment between the apical cell-cell junctions and the basal focal adhesions. Our simulation results show potential for increased ECM stiffness, e.g. due to a tumor, to modulate mechanical signaling between cells also outside the stiff region. Furthermore, the developed model provides a good platform for future studies on the interactions between epithelial monolayers and elastic substrates.

Author summary

Cells can communicate using mechanical forces, which is especially important in epithelial tissues where the cells are highly connected. Also, the stiffness of the material under the cells, called the extracellular matrix, is known to affect cell behavior, and an increase in this stiffness is related to many diseases, including cancers. However, it remains unclear how the stiffness affects intercellular mechanical signaling. We studied this effect using epithelial cells cultured on synthetic deformable substrates and developed a computational model to quantify the results better. In our experiments and simulations, we moved one cell to observe how the substrate stiffness impacts the deformation of the neighboring cells and thus the force transduction between the cells. Our model also enabled us to study the effect of local stiffness changes on the force transduction. Our results showed that substrate stiffness has an apparent impact on the force transduction within the epithelial tissues. Furthermore, we found that the cells can communicate information on the local stiffness changes over long distances. Therefore, our results indicate that the cellular mechanical signaling could be affected by changes in the substrate stiffness which may have a role in the progression of diseases such as cancer.

1 Introduction

Our understanding of the importance of mechanical forces and microenvironment in cellular processes and signaling alongside biochemistry has drastically improved during the last decades [1–3]. Biomechanics has a vital role in embryogenesis, stem cell differentiation, tissue homeostasis, and migration [4–10]. In addition, abnormal changes in the biomechanics of the cells and the extracellular matrix (ECM) are linked to many pathological processes, including tumor- and carcinogenesis [11–15]. While the research on the effect of physical cues and the role of the mechanical environment on cell functions and signaling is active, the understanding of this mechanical system is not complete. In epithelial tissues, the cellular mechanical microenvironment is formed by the neighboring cells and the ECM on the basal side of the cells. In some instances, the apical side of the cells is subjected to shearing forces from fluid flow [16]. Thus, epithelial cells are exposed to various physical cues rising from their environment. The high interconnectivity of the epithelial tissues enables the cells to distribute exogeneous mechanical energy and transmit endogenous forces to their environment [17, 18]. Here, we investigated how the propagation of tensile forces in the epithelial monolayer is affected by the stiffness of the substrate under the cells.

Cells can use their actomyosin cytoskeleton to generate contractile forces that enable cells to change their shape and move [18, 19]. Since the actomyosin cytoskeletons of neighboring epithelial cells are connected via adherens junctions, these contractile forces can be transmitted between cells over distances [20]. Cells have various responses to these exogenous forces, behaving elastically over a short time scale by deforming and viscously over sustained stress by dissipating the stress via various processes [21–24]. Endo- and exogenous forces can also alter the structural state of different proteins, which may lead to the conversion of forces to biochemical signals via a process known as mechanotransduction [3, 25]. Furthermore, mechanical forces have been indicated to have an even more direct effect on the cell behavior since they are transmitted directly to the cell nucleus along the actin stress fibers, where they have been shown to be able to modulate gene expression [26–29]. Therefore, understanding how forces are transmitted between cells is essential to understand the mechanical system formed by the epithelial tissues.

Epithelial cells are connected to the ECM on their basal side via focal adhesions, which connect the actomyosin cytoskeleton to the basal lamina. The focal adhesions contain mechanosensitive proteins that enable the cells to sense the external forces and ECM stiffness [30–32], which has been shown to affect many cell functions during development, homeostasis, and diseases. For example, ECM stiffness has been heavily linked to cell differentiation [6, 33] and the metastatic potential of tumors [34–36]. It is well established that tumor stroma, the adjacent tissue surrounding the tumor, is often considerably stiffer than native tissue [37, 38]. In tissues, this leads to stiffness gradients and interfaces between the stroma and the surrounding healthy tissue, which can influence cellular mechanosignaling, especially during cancer invasion [14, 39]. However, we do not fully understand how the ECM stiffness or stiffness gradients affect the mechanical signaling between cells in confluent epithelial monolayers.

There is a plethora of computational methods that can describe the mechanical system formed by the epithelial monolayer. Vertex models are a relatively simplistic approach that reduces the mechanical properties of the cells to only a few parameters [40–42]. Methods such as the subcellular element method [43, 44] and immersed-boundary method [45–47] provide a more nuanced description of the cells and their mechanical properties but differ on how they describe the cells and solve the cellular movement. Only a few cell-based models have included a description of a deformable substrate under the cells [42, 43].

This study aimed to describe how strain and forces propagate in an elastic mechanical system formed by the epithelial monolayer and a deformable substrate with different stiffnesses. The work was conducted experimentally using Madin-Darby canine kidney (MDCK) II cell model on polyacrylamide (PAA) hydrogel substrates and computationally using a cell-based model we developed. To investigate the propagation of tensile forces between the neighboring cells and the cells and the ECM, we, experimentally and in the computational model, moved a single cell, causing a local stretching in the epithelium. Furthermore, we used our computational model in combination with data from the literature to study the mechanics related to subcellular changes in cell shapes.

Results

Micromanipulation of epithelial monolayers on substrates with varying stiffness

To experimentally study the effect of environmental stiffness on the propagation of forces and deformation in epithelial tissue, we used an *in vitro* model of MDCK II cells expressing tight junction marker mEmerald-Occludin cultured on PAA hydrogel substrates with embedded fluorescent beads. We used collagen-I-coated PAA substrates with four stiffnesses (Young's moduli): 1.1, 4.5, 11, and 35 kPa. We manipulated a single cell with a sharp pipette attached to a piezo-driven micromanipulator as a mechanical stimulus. The pipette was brought into contact with the cell, and the micromanipulator was used to move the pipette 30 μm parallel to the surface in 1 second (speed 30 μm/s) while simultaneously imaging both the mEmerald-Occludin and the fluorescent beads.

The micromanipulation led to large deformation of the epithelium and displacement of the cells and the PAA substrate. We visualized the movement by comparing the images of the epithelium and the substrate before and following the micromanipulation (Fig. 1). It is clear from the movement of the cell boundaries (Fig. 1A) that the PAA stiffness profoundly affects the distance that the mechanical strain spreads around the manipulated cell. For example, the movement of the cell boundaries along the axis of the pipette movement (Fig. 1B, dashed lines in Fig. 1A) showed that for the 1.1-kPa substrate, the cell boundary at the edge of the imaged field (approximately 80 μm from the initial pipette position) moves 3.3 μm. This was in stark contrast with the 11-kPa and the 35-kPa substrates, for which the discernible cell boundary movement happened only at the distance of approximately 50 μm along the axis of its movement (Fig. 1B).

Similar to the cells, the displacement of the substrate was naturally affected by their stiffness. There was deformation in the whole imaged field for both the 1.1- and 4.5-kPa substrates (Fig. 1C) in the direction parallel to the pipette movement. However, the displacement in the perpendicular direction was more limited with the 4.5-kPa substrate than with 1.1 kPa. The deformation was even smaller with the stiffer (11 and 35 kPa) substrates (Fig. 1C).

Fig 1. Displacements of MDCK II cells and substrate with different stiffnesses. (A) Representative examples of mEmerald-Occludin-expressing MDCK II cell movement on polyacrylamide (PAA) hydrogel substrates with stiffnesses of 1.1, 4.5, 11, and 35 kPa following the movement of the micromanipulated pipette for 30 μm in 1 s (pipette movement shown by the white arrow). The boundaries of cells were indicated using mEmerald-Occludin and shown in green before the micromanipulation and in magenta following the 30 μm pipette movement. The cell displacement on the right side of the pipette (white arrow) is partly due to the pipette affecting part of the image. (B) Line plot along the dashed lines for cell boundaries in A in arbitrary units (AU) before (green) and following the micromanipulation (magenta) for each gel stiffness to better show the magnitude of the cell movement along the pipette movement axis. The data was smoothed using 10 pixel moving average. The pipette movement is indicated by the black arrows. (C) The movement of the fluorescent beads embedded in the PAA hydrogel substrates with the corresponding stiffness underlying the epithelia shown in A. The pipette movement of 30 μm is shown by the white arrow and the bead locations before and following the micromanipulation in green and magenta, respectively. The pipette shadow was affecting the results on the right side of the white arrow. Scale bar, 20 μm.

To quantify the cell displacements, we segmented the cell imaging data before and following the micromanipulation to obtain the cell outlines. Using the outlines, we defined a geometrical cell center, which we then used to measure the displacement of the individual cell during the micromanipulation. This provided us with a spatial map of the cell center movements in relation to their distance and direction from the initial position of the pipette (p_0). We then interpolated the cell center movement data over the whole imaging area to obtain a continuous distribution for each measurement and calculated the average distribution for each substrate stiffness (Fig. 2A and B). In order to do the same for the substrate data, we used particle image velocimetry (PIV) analysis to find the displacement of the substrate beads between images taken before and following the micromanipulation. Similar to the cell data, this was averaged and plotted in relation to p_0 (Fig. 2C and D).

Interestingly, the 30-μm pipette movement translated to a cell center movement of a similar range independent of the substrate stiffness with values of 15.4 ± 3.2, 15.8 ± 2.3, 14.5 ± 2.6, and 14.8 ± 3.1 μm (mean ± SD), from the softest to the stiffest substrate. This difference between the pipette movement and the cell displacement can be explained by the deformation and stretching of the manipulated cell. The pipette movement caused substantial deformation to the adjacent cells in the direction of the movement, and thus the displacement of these cells was difficult to quantify. Therefore, we mainly concentrated our analysis on the area where the pipette pulled and stretched the cells and present the results mainly as a function of the location on the negative y-axis from p_0. Parallel to the pipette movement (Fig. 2B, along the red, dashed line in 2A), the cell centers move 5 μm or more within a distance of 47, 34, 26, and 20 μm from p_0 respectively for 1.1, 4.5, 11, and 35-kPa substrates. Interestingly, the three stiffest substrates have the same amount of cell center displacement perpendicular to the pipette movement. In contrast, with the softest substrate, the displacement of at least 5 μm extends to approximately 1.5 times farther away than the rest (Fig. 2B).

The amount of displacement of the substrate was considerably smaller than that of the cells (Fig. 2D). The maximum displacements, located near p_0, were, from the softest to the stiffest, 8.9 ± 0.8, 7.6 ± 2.5, 2.7 ± 1.0, and 2.6 ± 1.1 μm. Therefore, the relative magnitude of the maximum substrate displacement compared to that of the cells corresponding to the stiffnesses from 1.1 to 35 kPa were 0.58, 0.48, 0.19, and 0.17. This difference in the maximum displacements partly originated from the facts that the

Fig 2. Displacement fields of the MDCK II cells and polyacrylamide (PAA) hydrogel substrates. (A) Average displacement of the segmented MDCK II cell centers as function of location of the original cell positions in relation to the initial pipette position (p_0) for the stiffnesses 1.1 (n = 11), 4.5 (n = 7), 11 (n = 11), and 35 kPa (n = 7). The field is limited to the left of micromanipulation axis since the movement was symmetric on either side of the axis. The area of the shown displacement field varies between the stiffnesses since p_0 in relation to the imaging area varied between measurements. (B) The cell center displacement along the y-axis (red dashed line in A) away from the direction of the pipette movement (left) and along x-axis (red dotted line in A) perpendicular to the pipette movement direction (right) for each stiffness. (C) Average displacement of PAA hydrogel substrates based on the particle image velocimetry (PIV) analysis as function of location in relation to p_0 for the stiffnesses 1.1 (n = 11), 4.5 (n = 7), 11 (n = 11), and 35 kPa (n = 7). The field is limited to the left of micromanipulation axis since the movement was symmetric on either side of the axis and the pipette causes artefacts in the PIV data on the right side of the pipette. The area of the shown displacement field varies between the stiffnesses since the pipette position in relation to the imaging area varied between measurements. Note that maximum displacement is different than with the cells. (D) The PAA substrate displacement along the red dashed line in C away from the direction of the pipette movement (left) and along the red dotted line in C perpendicular to the pipette movement direction (right) for each stiffness. The shaded region represents the SD for each stiffness. (E) Distance of pipette movement before cells detached from the substrate estimated from the live imaging data for the different stiffnesses 1.1 (n = 11), 4.5 (n = 7), 11 (n = 11), and 35 kPa (n = 7). The indicated cases with the distance to detachment of 30 μm did not detach from the substrate during the experiment.

cell-cell junctions are near the cells' apical surface and the substrate-binding focal adhesions are on the basal side, and that the cell height provides some elasticity. The measured substrate displacements close to p_0 were affected in the PIV analysis by the shadow of the pipette and a slight out-of-focus indentation caused by the pipette pushing the cells.

We also observed cells around the pipette detaching from the substrate in 28 % of the measurements with the 4.5-kPa substrate, in almost all the cases for the 11-kPa substrate, and in all the cases for the stiffest 35-kPa substrate (Fig. 2E and S3 Video). The detachments occurred late in the movement on the 4.5-kPa substrate, whereas those for the two stiffer substrates occurred much earlier. In addition, interestingly, there was more variance in the detachment distance for the 11-kPa substrate compared to the others. The detachment with the two stiffer substrates explained the minuscule difference between the substrate displacements in these measurements.

Computational modeling of force propagation in the epithelium

In order to further understand the force propagation in the epithelial monolayers, we developed a cell-based computational model of the epithelial cell-cell and cell-substrate force transduction. The cells were represented by closed polygons, and the model was evolved by calculating forces between the polygon vertices similar to Tamulonis et al. [48]. We described the deformable substrate under the cells as a triangular grid of points whose movement was solved similar to that of the cell vertices. For a detailed explanation of the model, the fitting, and the simulations, see the description in S2 Text. We used the experimental results from our *in vitro* cell model and data from the literature to fit the model parameters. The computational model was first used to grow virtual epithelia, followed by the simulation of single-cell mechanical manipulation.

During the simulated manipulation, we restricted the remodeling of the cell properties to describe the purely elastic properties of the experimental time scale.

We fitted the model parameters by comparing the cell center and substrate displacements between the *in vitro* experiments and the computational model. Due to the similarity of the experimental 11 and 35-kPa results in cellular displacements (Fig. 2B and D) and detachment distances (Fig. 2E), we decided to omit the 35-kPa substrate from our simulations. We assumed that the elastic properties of the epithelium are similar between the substrates, and therefore we used the same cell parameter values for each substrate stiffness in the fitting process. However, the only exception was the focal adhesion strength parameter, which we assumed to depend on the substrate stiffness and was thus altered accordingly. Similar to the experiments, in the simulation data analysis, we focused on the area of the epithelium under tension (i.e., $y < 0$). The most drastic movement of the cell boundaries during the micromanipulation was visible for the softest substrate (Fig. 3A). We measured the average cell and substrate displacements, which show highly similar behavior to the experiments (Fig. 3C-E).

Fig 3. Computational model fitting results. (A) Representative figures showing the cell displacement in the simulations during the micromanipulation for the 1.1, 4.5, and 11-kPa substrates highlighting the cell shapes before (green) and following the micromanipulation (magenta). The white arrow indicates the micromanipulator movement. The scale bars are 20 μm. (B) Description of the axis the results were plotted on in C-H. Comparison between the experimental cell and substrate displacement with the fitted computational model for (C) 1.1, (D) 4.5, and (E) 11-kPa substrates. The top row for each stiffness shows the fit for cell displacement in vertical (left, dashed line in B) and horizontal (right, dotted line in B) directions and the bottom row shows the same for the substrate displacements. (F) The focal adhesion, (G) the cortical, and (H) the junction forces parallel the pipette movement (dashed line in A) for the cells on 1.1, 4.5, and 11-kPa substrates in arbitrary units (AU). The force magnitudes are comparable between each other. The shaded region represents the SD. For each set of simulation parameters, n = 5.

The values obtained for the focal adhesion strengths were 0.5, 0.8, and 1.0 g s^{-2} μm^{-2} for 1.1, 4.5, and 11-kPa substrates, respectively. Since we described the focal adhesions by springs, the units include the unit of the spring constant (g s^{-2}). In addition, the strength depends on the length of the membrane (μm) that each focal adhesion spring represents. Furthermore, it is essential to note that since the cell polygons represent the apical surface of the cells, the focal adhesion springs that connect the apical polygon vertices to the basal substrate also include the cell elasticity in the apico-basal axis. However, the increase in the focal adhesion strength as a function of substrate stiffness still reflects the stronger binding of the cell to a stiff substrate.

We analyzed the computational cell displacements similar to the experimental results by calculating the average cell center movement distributions in relation to p_0. The substrate displacement, on the other hand, was defined directly from the substrate point movement. We transformed the results so that they were in relation to p_0 and averaged over multiple simulations. The fitted model captured extremely well the general behavior of the *in vitro* micromanipulation (Fig. 3A), especially in the region parallel to the pipette movement (left side plots of Fig. 3C-E). However, the model produced higher cell displacement near p_0 for all stiffnesses, most likely due to the difficulty of cell segmentation in the *in vitro* data in this area. Also, since these areas were affected in the PIV analysis, the substrate displacements here differ between the experiments and the model. The model was unable to accurately describe the displacement perpendicular to the pipette movement direction with the 1.1-kPa substrate. Furthermore, the substrate deformations remained higher over longer distances for the 4.5 and 11-kPa substrates in the model for both the cells and the substrate (left side plots in Fig. 3D and E). This may indicate that cellular structures near the pipette are damaged, therefore dampening the transmission of forces between the cells. Interestingly, the variabilities in the displacement between the computationally manipulated epithelia were small even though we ran each simulation using a different epithelial system.

The model was then used to compare the propagation of different forces depending on the substrate stiffness. To describe the forces following the micromanipulation as a function of position in relation to the p_0, we averaged the forces over the vertices of each cell and assigned them to the original cell center positions. Next, we interpolated the averaged force magnitudes between the cell centers to obtain continuous spatial distributions and then averaged over multiple simulations.

We concentrated on the forces that arise from the interactions between the cells and the substrate (focal adhesion forces, Fig. 3F), the mechanical tension and deformation of the cell itself (cortical force, Fig. 3G), and the mechanical connection between the cells (junction forces, Fig. 3H). The substrate stiffness had an apparent effect on the maximum magnitudes of each of the three forces. The average maximum focal adhesion forces near p_0 were 19.7, 27.6, and 24.6 AU (arbitrary units) from the softest 1.1 to the stiffest 11 kPa substrate (Fig. 3F). The maximum value for the 11-kPa substrate is lower due to the cell detachment near p_0. The corresponding average maximum values for the cortical forces were 83.5, 127.7, and 152.1 AU (Fig. 3G) and for the junction forces 133.2, 208.2, and 272.5 AU (Fig. 3H). There were only minor differences in the junction forces between the two stiffest substrates beyond the distance of 25 μm from p_0. Interestingly, the cortical force became highest for the 4.5-kPa substrate farther than approximately 50 μm away. Both the junction and cortical forces remained marginally lower for the softest 1.1-kPa substrate compared to the stiffer substrates until approximately the distance of 50 μm. On the other hand, the focal adhesion forces showed an apparent effect of the stiffness over the whole range of the simulated distance. For example, the focal adhesion force level sensed by the cells on 1.1-kPa substrate at 25 μm from p_0 extended on average to 40 and 47 μm for 4.5 and 11 kPa, respectively (Fig. 3F).

The results indicate that the stiffness of the substrate had an apparent effect on the propagation of cell movement following an external tensile force. However, while the forces between cells and cell deformation in the apical plane, as indicated by the increased cortical force, were higher near the manipulated cell on stiffer substrates, there were only minor differences in the forces at longer distances. On the other hand, the focal adhesion forces on the softest substrate remained lower over the simulated distance.

Propagation of cell-cell and cell-substrate forces over substrate stiffness gradients

Next, we investigated how stiffness gradients – describing those between stiff tumorous tissues and healthy soft tissue – affect the transduction of tensile forces between the cells. Our computational model enabled the generation of epithelial monolayers attached to substrates with stiffness gradients with different slopes. We first concentrated on studying strain propagation from a soft substrate to an area of a stiff substrate. To do this, we simulated the pipette micromanipulations with substrates that included one of the following three different types of stiffness gradients between 1.1 and 11 kPa: a stiffness interface (change in stiffness in 2 μm, Fig. 4H), a sharp or a shallow gradient (changes in stiffness in 10 μm or 50 μm, respectively, Fig. B in S1 Appendix). The pipette was moved only 20 μm in these simulations to minimize the cell detachment from the substrate. We also simulated the 20-μm micromanipulations with the uniform stiffnesses of 1.1 and 11 kPa for comparison (Fig. A and B in S1 Appendix). We analyzed the results by calculating how the cell and substrate displacements and the focal adhesion, cortical, and junction forces changed compared to the situation with a uniform 1.1-kPa substrate under the cells. Therefore, we calculated how much the displacements and forces changed by comparing results from simulations with a stiffness gradient against those with a uniform stiffness. This absolute difference was defined by subtracting the latter from the first at each distance from p_0. We also calculated the relative difference between the two cases for the forces by dividing the results with the stiffness changes by those with the uniform stiffness at each distance. An example visualizes these steps in Fig. 4A. We used the relative differences for the forces to visualize better the large relative changes in the forces independent of magnitude, especially the focal adhesion forces, that are not as clearly shown with an absolute difference.

Fig 4. Differences in vertical cell displacement and focal adhesion, cortical, and junction force propagations caused by an interface gradient from soft to stiff substrate. The results are calculated towards the negative y-direction from the initial pipette position (p_0) based on their average difference compared to the case where the substrate stiffness was the same as below the manipulated cell. (A) Example of the results calculations' using the focal adhesion force for the stiffness interfaces at $y = -40$ μm (blue dashed line in H). The orange striped areas correspond to each other in the figure. The difference is either calculated as absolute difference (by subtracting the results with uniform substrate from those with a gradient at each distance from p_0) or as relative difference (by dividing the results with a gradient by those with the uniform stiffness at each distance from p_0). The absolute difference in (B) cell and (C) substrate displacement compared to the uniform 1.1-kPa displacement for stiffness interfaces at 20, 40, 60, and 80 μm. The relative (top) and absolute (bottom) differences in the average focal adhesion, cortical, and junction forces for the stiffness interfaces at (D) 20, (E) 40, (F) 60, or (G) 80 μm compared to the forces in the corresponding position with 1.1-kPa substrate. (H) The stiffness interfaces for displacement and forces shown in B-G. The magnitudes of the displacement and forces are shown in Fig. A in S1 Appendix. The vertical striping shows the positions of cell boundaries for average sized cells and the positions of the interfaces are shown with the arrowheads of corresponding colors at the bottom of each figure. For each set of parameters, n = 15. AU, arbitrary unit.

Compared to the 1.1-kPa uniform substrate, the rapid increase in stiffness at the various distances from p_0 led to a reduced cell displacement with the most prominent effect near the stiffness interface (Fig. 4B). While larger when the interface was closer to p_0, the reduction still occurred even when the interface was up to 80 μm away. However, with the interface farther away, the difference in displacement remained smaller than 1 μm. The difference in the substrate displacement was slightly higher but otherwise similar to that of the cells (Fig. 4C). Interestingly, the substrate was displaced more at p_0 when the stiffness interface was farther away.

The decreased cell and substrate displacement was accompanied by increased forces (Fig. 4D-G). The cortical and junction forces were generally increased between p_0 and the interface and some distance beyond the interface when closer to p_0. However, only minor changes were visible near the interface at 80 μm away. On the other hand, the focal adhesion forces showed no differences between p_0 and about one cell layer (indicated by the vertical striping) before the interface. However, these forces were greatly increased around the interface, as indicated by the peaks that continue for 3-5 cell layers on the stiff substrate. These difference peaks were most prominent in absolute terms when the interface was 20 μm from p_0 (Fig. 4D) and in relative terms when the interface at 60 μm with an over 5-fold increase in the force compared to the uniform 1.1-kPa substrate (Fig. 4F). While the higher focal adhesion strengths can partly explain the increase following the interface on the stiffer substrate, the peak values were also higher than the focal adhesion forces at this distance on a uniform 11-kPa substrate (Fig. A in S1 Appendix). Our results suggest that cells situated on a soft island move less and are subjected to larger cortical and junction forces if one cell experiences a substantial deformation or movement. In addition, the cells near the stiffness interface sense high focal adhesion forces.

The observed behavior was similar with the shallow and sharp stiffness gradients compared to the interface gradients in equal distances from p_0 (Fig. B in S1 Appendix). These gradients also produced similar relative peaks in the focal adhesion forces; however, the wider the stiffness gradient was, the more spread out and lower the peak was.

Next, we wanted to investigate how the force transduction is altered when the substrate stiffness gradient is oriented from stiff to soft. Thus, we simulated the 20-μm micromanipulation of a single cell with the stiffness profiles mirroring those in the previous section. Here, the cell and substrate movements were considerably increased in comparison to uniform 11-kPa substrate (Fig. 5, Fig. D in S1 Appendix). The cell displacements were increased at the stiffness interface gradients (Fig. 5A), with the largest difference with the interfaces closer to p_0. Interestingly, the displacement was increased well before the interface itself, also for those farther away from p_0. The general behavior of the difference in the substrate displacement was similar to that of the cells but with slightly higher peak values (Fig. 5B). The substrate displacement was also increased at p_0, unlike with the cells.

Fig 5. Differences in vertical cell displacement and focal adhesion, cortical, and junction force propagations caused by an interface gradient from stiff to soft substrate. The absolute difference in (A) cell and (B) substrate displacement compared to the uniform 11-kPa displacement for stiffness interface gradients at 20, 40, 60, and 80 μm. The relative (top) and absolute (bottom) differences in focal adhesion, cortical, and junction forces for the stiffness interfaces at (C) 20, (D) 40, (E) 60, or (F) 80 μm compared to the average cell forces in the corresponding position with 11-kPa substrate. (G) The stiffness interfaces for displacement and forces shown in A-F. The magnitudes of the displacement and forces are shown in Fig. C in S1 Appendix. The vertical striping shows the positions of cell boundaries for average sized cells and the positions of the interfaces are shown with the arrowheads of corresponding colors at the bottom of each figure. For each set of parameters, n = 15. AU, arbitrary unit. See Fig. 4A for explanation of how the absolute and relative differences were calculated.

In terms of absolute values, there are only minor differences in the forces farther than approximately 50 μm from p_0 compared to the uniform case independent of the interface gradient location (Fig. 5C-F). The cortical and junction forces were decreased close to p_0 with the interface at 20 μm (Fig. 5C). On the other hand, focal adhesion forces were increased near p_0 but showed generally reduced values at longer distances. Furthermore, following the interfaces at 20 and 40 μm, there were inverse peaks in these forces compared to the uniform substrate (Fig. 5C and D), which were not as clearly visible with the farther interfaces. The data indicates that the single-cell movement within a stiff substrate island causes larger deformations in the neighboring cells than on a uniform stiffness. Thus, the changes in the stiffness can be sensed farther away.

Again, the differences in the cell displacements and forces were similar with the shallow and sharp gradients compared to the interface gradients in similar locations (Fig. D in S1 Appendix). The reduced focal adhesion forces were also visible following the decrease in stiffness similar to those in Fig. 5C and D.

The effect of substrate stiffness on small changes in cell shapes

Our computational model indicated that the substrate stiffness and especially stiffness gradients influence the strain distribution after a large single-cell movement. Next, we wanted to investigate how minute changes in cell-cell junctions are transmitted to the surrounding substrate. To correlate the simulations to experimental data, we simulated an optogenetic experiment, where actomyosin contractility is increased by light activation. Therefore, we implemented the optogenetic activation into our model based on the experimental and theoretical work by Staddon et al. [24]. We obtained the model parameters either directly from Staddon et al. or by fitting as described in S2 Text. We did not consider the strain-based remodeling of the cortical tension since we wanted to concentrate on the effect of the substrate stiffness on the local movement of cell boundaries, and the tension remodeling primarily affects the reduced junction length following the optogenetic activation [24]. We also allowed the remodeling of the cell structures in these simulations due to the long experiment duration compared to the micromanipulation. We increased the contractility of cell vertices forming the junctions between two cells to observe how the length of this junction reduced following the activation (Fig. 6A). We ran the simulations on substrates with uniform stiffnesses of 1.1, 4.5, or 11 kPa.

Fig 6. Reduction of the cell-cell junction length and substrate displacement during optogenetic activation. (A) To simulate the increased cortical contractility due to light activation, a rectangular area enclosing the cell-cell junctions between two cells (the red rectangle) was selected for activation. We then monitored the change in the junction length (L) from the initial state (L_0) as a function of time. (B) We used a single activation of 20 minutes (grey area between 2 and 22 minutes) and calculated the relative junction length (L/L_0) during this activation and the following relaxation. This was done for the stiffnesses 1.1, 4.5, and 11 kPa. For each stiffness, n = 20. The shaded area indicates standard deviation. (C) Representative plots of the displacement of the substrate with the three stiffnesses along the axis of the junctions (the dashed line in A) in relation to the junction center point (indicated in A). (D) Maximum substrate displacement as a function of half of the change in the junction length for each simulation for the three stiffnesses. The maximum substrate displacement was calculated as mean of the peaks on each side of the junction center point shown in C. The lines show linear fit for each set of points.

During the simulated 20-min activation, the increased cortical contractility reduced the junction length the most with the softest 1.1-kPa substrate with the final relative length of around 0.63 ± 0.08 (mean ± SD) (Fig. 6B). The relative junction length was reduced to similar values for the two stiffer substrates with the values of 0.66 ± 0.07 and 0.67 ± 0.07 for 4.5 and 11 kPa, respectively (Fig. 6B). However, the initial length reduction was faster with the 4.5-kPa substrate than the 11-kPa, with a similar slope to the 1.1-kPa substrate.

Next, we studied how the shortening of the cell-cell junction deformed the substrate under the cells via the focal adhesions. We defined the maximum displacement of the substrate field between the moment before the activation (time = 2 min) and the end of the activation (time = 22 min) along a line defined by the activated section of junctions between two cells (the dashed line in Fig. 6A) for each simulation. Fig. 6C shows a representative displacement plot for each stiffness centered on the junction center point shown in Fig. 6A. To quantify the results, we took the average displacement peak values on each side of the junction center point. We plotted them as a function of half of the change in the junction length between the two time points for each simulation (Fig. 6D). Half of the length change was used since one of the displacement peaks in Fig.

6B resulted from half of the total junction length reduction. To compare these relative displacements with those from the micromanipulations, we calculated the mean maximum substrate displacement in relation to the corresponding half of the junction length reductions. The obtained values were 0.093, 0.035, and 0.018 respectively for 1.1, 4.5, and 11-kPa substrates, which were considerably smaller than the corresponding values in the 30-μm micromanipulations, indicating a nonlinear relationship between the cell and substrate displacements.

The simulation results show that the substrate stiffness has only a minor direct effect on the small cellular morphological changes. In addition, these small changes in the cell morphology could not deform the substrates at a visible level, especially with the higher stiffnesses.

Discussion

The role of mechanical forces in cellular communication and in the regulation of cell functions has been widely accepted [1, 2, 19, 29, 49]. Moreover, the stiffness of the cellular microenvironment is known to affect the cells' mechanical properties and behavior, and an increase in the stiffness has been linked to many diseases. Most notably, in tumor formation and cancer progression, the ECM stiffness increases [11, 15, 34, 50–52], affecting how mechanical strains are transmitted between the cells. Tightly packed epithelial monolayers on deformable substrates form an excellent platform for studying how forces propagate between cells and what is the effect of the substrate stiffness in this process. To this end, we developed a computational model to describe the propagation of forces in the cell monolayer on deformable substrates based on our own experimental data and that from the literature.

We first studied how a substrate with a uniform stiffness affected the propagation of cell displacements and strain, and therefore forces, following an exogenous 30-μm movement of a single cell within one second. Logically, both the cell and the substrate displacement spanned over longer distances with soft substrates. The higher substrate stiffnesses, on the other hand, greatly reduced both displacements. The high cell displacement perpendicular to the pipette movement with the soft 1.1-kPa substrate can be explained by the reported stiffnesses of the MDCK monolayers, that are between 1 and 5 kPa, when measured with atomic force microscopy [53–55]. This means that the stiffness of the epithelial monolayer in this system has a similar or slightly higher stiffness than the softest substrate and, therefore, can more readily displace the substrate than the monolayers on the stiffer substrates. We observed only minor differences between the cell displacements on the stiffer substrates, suggesting that the propagation of forces began to saturate. Therefore, having a substrate stiffer than 35 kPa would most likely not have a further effect on the cell displacements.

The difference between the maximum cell and substrate displacements can be explained by the different displacements of the apical and basal surfaces of the cell. Both our imaging of the mEmerald-Occludin-expressing MDCK cells and our computational model describe the cells by their apical surface. The displacement of the basal substrate-binding surface is more related to that of the substrate. This suggests that the cell shape in the apico-basal axis is heavily distorted, especially near the micromanipulated cell. Furthermore, the variabilities in the displacements of both the cells and the substrate predicted by our computational model were considerably smaller than those seen in the experimental results. Therefore, the variability in the epithelial morphology – i.e., the cell sizes and shapes – was not enough to explain the experimental displacement variability, and our simulation results thus only reflect an average epithelium. In reality, the mechanical properties are more varied.

We used our computational model to study the cortical, cell-cell, and cell-substrate forces during the micromanipulations. It is noteworthy to mention that the focal adhesion forces describe both the tension in the focal adhesions and the apico-basal axis of the cell. We found that all of these forces were increased by the increase in substrate stiffness. This was expected because the cells were subjected to the same external strain on the stiffer, less deformable substrates as those on the soft substrates. Therefore, the smaller substrate deformation meant that the cells were subjected to a larger portion of this strain, which led to larger cell deformation in the apical plane and higher cell strain in the apico-basal cells axis. These changes corresponded to the increases in the cortical and focal adhesion forces. Importantly, for the apical cell deformation to occur, the next cell opposite to the incoming strain must resist movement or deformation. If the next cell can be readily moved, less of the mechanical energy goes to cell deformation since it is easier to transmit onward. Therefore, the cortical and junction forces depend on each other since higher resistance against deformation leads to higher junction forces as less of the mechanical energy is absorbed by the cell cortex. However, the differences in the cortical and junction forces between the stiffnesses disappeared beyond the distance of 50 μm, indicating that the bulk of the mechanical energy is absorbed closer to p_0 on the stiff substrates.

The focal adhesion forces remained higher for the cells on stiffer substrates due to the more considerable difference between the cell and substrate displacement and the higher focal adhesion strength. Similar results were found by Goodwin et al. [56] in the developing *Drosophila* embryos, as they showed that the amount, and thus the strength, of basal cell-ECM adhesions was inversely correlated with the displacement of the apical surface. They hypothesized that the increased apical displacement was the result of more efficient apical force transmission. On the other hand, our results indicated higher forces transmitted between cells with stronger focal adhesions and smaller apical displacements in an elastic system with an exogenous mechanical stimulus.

We also studied how local changes in the substrate stiffness affect the propagation of forces in the epithelium. Stiffness interfaces have been shown to affect the integrity of endothelial monolayers and impact their behavior over a distance of more than a hundred micrometers [57]. Similarly, we found that the cell displacement was affected near p_0 even if the stiffness interface was at a distance of 80 μm. Interestingly, when the forces propagate from soft to stiff substrate, the more distant interfaces led to a higher substrate displacement near p_0. The origin of this effect is unclear. The cortical and junction forces on the soft region between the stiffness interfaces and p_0 were increased, indicating that they experience more strain than on a substrate with a uniform stiffness. This is because the cells on the stiff region were more difficult to displace due to their stronger binding to the substrate and the stiffer substrate itself. A similar effect occurred for the force propagation from stiff to soft since the cells on the soft region were easier to move, meaning that more of the strain could be transmitted to them. Thus, this led to decreased cortical and junction forces in the stiff region.

The predicted peaks in the focal adhesion forces near the interface gradients with the increases in stiffnesses were a combination of two factors. First, the cells on the stiff substrate near the interface were subjected to a larger apical displacement from their close neighbors from the soft side. Second, the focal adhesion strength of these cells was higher due to the stiffer substrate under them. This combination thus led to the high relative increase in the focal adhesion forces. The situation was similar when the forces were transmitted from the stiff to the soft substrate. In this case, the cells on the soft side of the interface sensed smaller focal adhesion forces compared to the stiff uniform substrate due to the lower focal adhesion strength. However, since the cell displacement was already diminished at more distant interfaces, this effect was not as visible. Furthermore, we observed only minor differences in the cell displacement or forces in relation to the slope of the increase or decrease in stiffness. Therefore, whether the change in stiffness occurs within 2 or 50 μm, the main factors that affected the cells were the change in stiffness and its distance.

We also studied how the substrate stiffness affects the small local changes in cell shape by implementing an optogenetic control of the myosin activation into our computational model. The results suggested that the substrate stiffness has only a minor effect on the small changes in the cell-cell junction elastic behavior. This can be explained by the cellular apico-basal connections, as small morphological changes in the apical side were not greatly restricted by the substrate-binding in the basal side of the cells. The observed difference in the relative substrate and cell displacement between the optogenetic and micromanipulation simulations show that the displacement of the apical side of the cells has to be extensive enough to visibly deform the substrate due to the compliance provided by the cells' apico-basal axis.

The factors affecting the displacement and deformation of cells following some external force can be summarized as follows (Fig. 7). First, the stiffness of the substrate to which the cell is attached – together with the strength of this attachment – modulates the apical displacement. The second factor is the ability of the cells farther away from the external force to displace or deform. The cells move easily on a soft uniform substrate, as do the cells farther away. Therefore, the cell deformations are limited as it is easier to transmit the strain to the neighboring cells. On the other hand, the cell positions are more fixed on a stiffer substrate, making their movement more difficult, which leads to increased cell deformation. Furthermore, for example in the case with a stiffness increase opposite to the incoming force, the displacement of a cell in the soft region is limited by the less movable cells in the stiff region, leading to the more apical deformation. This further indicates that the information of the limited displacement farther away is transmitted as forces between the cells.

Fig 7. A 2D crosscut abstraction of the effect of substrate stiffness and stiffness interfaces on cell displacement and deformation upon mechanical stimulus. (A) On a uniform soft substrate, the cells are easily moved and do not substantially deform since the neighboring cells can also be readily moved. (B) A uniform stiff substrate is challenging to deform, leading to limited cell displacement, that is further limited by the stronger focal adhesion forces compared to the soft substrate. This leads to large deformation of the cells due to the limited ability of the neighboring cells to move. (C) When there is an increase in stiffness at a distance, the movement of cells on the stiff side of the stiffness interface is suppressed by the limited movement of the cells. This leads to more deformation of the cells on soft side of the interface compared to the uniform soft substrate. (D) With a decrease in stiffness at a distance, the cells on the soft substrate can readily move, enabling large cell movement also on the stiff substrate and thus less cell deformation compared to the uniform stiff substrate. The lengths in the figures are not to scale.

This communication of the forces and the information of the mechanical properties of the substrate is highly dependent on the cells' resistance against deformation. If an external force can readily deform the cell's apical surface, no force is left to transmit to the neighboring cells. Tension in the cytoskeleton has been shown to enable longer distance mechanical communication within cells compared to homogeneous solids [32, 58, 59], but it seems to be important also in the long-range mechanical signaling within an epithelial monolayer. This same effect is seen with fibrous substrates since separate cells have been shown to be able to communicate via the substrate over long distances [60–62].

The developed computational model forms a platform to complement the existing cell-based methods, by, to our knowledge, for the first time describing in detail the mechanics of the epithelial monolayer in combination with those of the underlying substrate. Compared to the common vertex model, our approach describes the cells and their interactions in more detail while being computationally considerably heavier. Furthermore, the model provides an additional level of complexity and dynamics compared to the previous closed-polygon-based models, e.g., Tamulonis et al. [48], since the cells are allowed to divide during growth and change their size and perimeter, and the junctions between the cells are allowed to remodel. A similar model to ours was recently published [63], building on the work by Tamulonis and coworkers with more dynamic cell functions and properties. However, like many other computational cell-based epithelial models, this model excluded the description of a deformable substrate under the epithelial monolayer. The few models that describe the substrate have not considered the effect of its mechanical properties in relation to the epithelial mechanics [42, 43]. In addition to the simulations presented here, the developed computational platform enables the description of further typical mechanical experiments conducted with epithelia, e.g., lateral substrate compression or stretching. Furthermore, we developed a graphical user interface for the simulations and data analysis to improve the platform's usability.

While our modeling approach generally describes the system formed by the epithelial monolayer and the substrate well, there are limitations. First, the model cannot correctly describe the force propagation perpendicular to the micromanipulation on soft substrates, which can be explained by the rotation of the cell-cell junction interactions in relation to the cell membranes. Secondly, based on the slightly higher cell displacement at longer distances with the stiffer substrate predicted by the model compared to the experimental data, it seems that the elastic springs' ability to describe the cell mechanics might be limited to cases with smaller strains. Furthermore, the description of the focal adhesion forces is challenging since they included both the focal adhesions themselves as well as the stiffness of the cell in the apico-basal axis. Separating these two components into their own forces could better describe the mechanics during the micromanipulation.

In summary, results from our *in vitro* cell model and computational simulations suggest that the mechanical properties of the substrate have a significant effect on the distance over which forces are transmitted in the epithelium. Furthermore, we found that the cells can communicate information of the substrate stiffness over long distances based on their ability to resist deformations. This indicates that, for example, the increased ECM stiffness in tumors can affect the mechanical signaling also outside the tumor itself. However, further studies are needed to better understand the role of each component in this phenomenon. The computational cell-based model presented here forms a valuable platform for futures studies on epithelial mechanics. In the future, the model would benefit from adding the tension remodeling described by Staddon et al. [24] and the inclusion of the cell nuclei. The latter would also allow the study of the forces felt by the nucleus and thus their possible role in regulating gene expression [29, 49, 64]. Furthermore, since the more fibrous nature of the natural ECM has been shown to transmit forces over longer distances [60–62], it would be interesting to study the ability of a fibrous substrate to propagate strain in the epithelial monolayer.

Materials and methods

Cell maintenance and establishment of MDCK mEmerald-Occludin-expressing cells

We used MDCK II (ATCC CCL-34) cells as an *in vitro* epithelial model tissue. The cells were cultivated in standard conditions in a humidified cell incubator (+37 °C, 5 % CO_2) and maintained in Modified Eagle's medium (#51200046, Thermo Fisher Scientific, Waltham, MA, USA) supplemented with 1 % (vol/vol) antibiotic (#15140122, Thermo Fisher Scientific) and 10 % fetal bovine serum (#10500064, Thermo Fisher Scientific). The MDCK cells used in the micromanipulation experiments stably expressed mEmerald-Occludin to highlight the cell-cell junctions with fluorescence. mEmerald-Occludin was a gift from Michael Davidson (Addgene plasmid #54212; http://n2t.net/addgene:54212; RRID: Addgene_54212). The MDCK mEmeral-Occludin cell line was established by first transfecting the MDCK cells with the mEmerald-Occludin plasmid using Neon Transfection system (Thermo Fisher, Waltham, USA). One day after the transfection, we started the positive cell selection with a medium where we replaced P/S with 0.75 mg/ml G418 antibiotic (#Gnl-41-01, Thermo Fisher Scientific). We picked positive colonies approximately two weeks later using a fluorescent microscope situated in the sterile cell culture hood. The MDCK mEmerald-Occludin cells were maintained in Modified Eagle's medium (#51200046, Thermo Fisher Scientific, Waltham, MA, USA) supplemented with 0.25 mg/ml G418 antibiotic (#Gnl-41-01, Thermo Fisher Scientific) and 10 % fetal bovine serum (#10500064, Thermo Fisher Scientific).

Polyacrylamide hydrogels and cell culturing

The polyacrylamide hydrogels were cast on 18 × 18 mm glass coverslips. First, coverslips were cleaned by immersing them in 2 % Helmanex for 1 h in +60 °C, followed by washes with excess water and ethanol. The coverslips were then let to dry in a fume hood or dried with a nitrogen stream. The cleaned coverslips were stored in a desiccator.

Before gel casting, the surfaces of the coverslips were amino-modified with 3-(Trimethoxysilyl)propyl methacrylate (#M6514, Sigma-Aldrich, Saint-Louis, USA) to allow firm gel attachment. The 3-(Trimethoxysilyl)propyl methacrylate and glacial acetic acid were mixed with 95 % ethanol yielding final concentrations of 0.3 % (vol/vol) and 5 % (vol/vol), respectively. The solution was let to react with a glass coverslip for 3 min at RT. Next, the coverslips were washed with excess ethanol and air-dried in a fume hood. The activated coverslips were stored in a desiccator.

The different gel rigidities were achieved by mixing different ratios of gel precursors acrylamide (AA) (stock 40 %, #1610140, Bio-Rad Laboratories, Hercules, USA) and bis-acrylamide (Bis) (stock 2 %, #1610142, Bio-Rad Laboratories, Hercules, USA) with PBS in 15 ml falcon tube [65]. The following mixing ratios were used: for 1.1 kPa gel final concentrations of AA and Bis were 3 % and 0.10 %, respectively; for 4.5 kPa 5 % and 0.15 %; for 11 kPa 10 % and 0.10 %; and for 35 kPa 10 % and 0.30 %. The gel precursor solution was then degassed with a vacuum. Next, 2 ml of this solution was pipetted into a new 15 ml falcon tube, and 2 % (vol/vol) fluorescent beads (0.2 μm diameter, red fluorescent, #F8810, Thermo-Fisher, Waltham, USA) were added and mixed without bubble formation.

The gel polymerization was initiated by adding TEMED (#1610800, Bio-Rad Laboratories, Hercules, USA) and APS (10 % (weight/vol) stock solution in PBS, #A3678-100G, Merck, Kenilworth, USA) to a concentration of 0.2 % (vol/vol) and 1 % (vol/vol). The gel was mixed by tilting the tube 3–5 times, and immediately afterward, 13 μl of gel solution was pipetted on an activated coverslip. Next, 13 mm cleaned but unactivated coverslip was carefully placed on top, sandwiching the polymerizing gel between the two coverslips. Gels were allowed to polymerize for 45 min in a moist chamber at RT. After polymerization, the gel-coverslip sandwiches were placed on 6-well plates, immersed in PBS, and kept o/n at +4 °C. On the following day, the 13 mm coverslips were carefully removed using a sharp scalpel, yielding approximately 100 μm thick PAA gels on 18 × 18 mm coverslips.

Finally, the gels were coated with collagen-I to facilitate cell adhesion and growth. The coating was conducted by using 3,4-Dihydroxy-L-phenylalanine (L-DOPA) (#D9628, Sigma-Aldrich) according to Wouters et al. [66]. L-DOPA was dissolved in the dark to 10 mM Tris buffer, pH 10, with a final concentration of 2 mg/ml. The gel samples were incubated with L-DOPA solution for 30 min at RT in the dark. Next, the samples were washed twice with PBS and collagen-I in concentration of 50 μg/ml in PBS was added on top of the gel and incubated for 1 h at RT. Finally, the cells were washed twice with PBS, and cell seeding was conducted immediately.

MDCK II cells stably expressing mEmerald-Occludin were maintained in 75 cm^2 cell culture flasks. The protein-coated gels were placed on a sterile 6-well plates with PBS and sterilized in the laminar under UV light for 15 min. The cells were trypsinated and suspended into 10 ml of cell culture medium, and 100 μl of the cell suspension was then pipetted on each gel, and 2 ml of medium was added to the well. Cells were cultured for 7 d prior to the micromanipulation experiments.

Imaging and micromanipulation

We imaged the epithelial mechanics during micromanipulation using Nikon FN1 upright microscope (Nikon Europe BV, Amsterdam, Netherlands) with CFI Apo 40x/0.8 water-dipping objective. The mEmerald-Occludin was excited with 470 nm LED and beads with 580 nm LED from pE-4000 light source (CoolLED Ltd., Andover, UK). The system was equipped with W-VIEW GEMINI image splitting optics (Hamamatsu, Sunayama-cho, Japan), allowing simultaneous capturing of mEmerald-Occludin and fluorescent bead channels. The camera used in imaging was sCMOS ORCA-Flash 4.0 v2 (Hamamatsu, Sunayama-cho, Japan), which yielded an image pixel size of 330 nm. The used exposure time was 50 ms. During timelapse imaging, the frame rate was 13.4 frames per second.

Micromanipulation was conducted using uMp-3 triple-axis micromanipulator with uMp-TSC controller and uMp-RW3 rotary wheel interface (Sensapex, Oulu, Finland). The cells were manipulated by using a glass micropipette, similar to those used in patch-clamp recordings. The pipettes were constructed with P-1000 micropipette puller (Sutter Instruments, Novato, USA) and afterward closed with micro forge MF-830 (Narishige, Tokyo, Japan).

In the epithelium micromanipulation, the micropipette was brought in contact with a cell. The contact was visible in the microscopy images as a small indentation of the cell membrane. We started timelapse imaging and subsequently moved the micropipette 30 μm with a speed of 30 μm/s perpendicular to the pipette orientation. The movement was controlled via uMx Software (Sensapex, Oulu, Finland) using its macro commands. This yielded rapid mechanical manipulation of the cell and a movement of approximately 15 μm of its center.

Data analysis

The experimental imaging data before and after the micromanipulation pipette movement was initially segmented using the Trainable Weka Segmentation [67] plugin of ImageJ Fiji [68]. We randomly selected six images from the imaging data set to train the classifier to segment the cells based on the mEmerald-Occludin data to obtain the cell boundaries. Next, the probability maps were converted to binary masks using Find maxima and then skeletonized. We manually fixed any errors in the skeleton images based on comparison with the original images. Finally, BioVoxxel Toolbox's Extended Particle Analyzer [69] was used to analyze the final segmented binary images. We tracked the movement of the cell centers between the segmented images before and after the pipette movements using a custom, semi-automated MATLAB script (R2020b, The MathWorks Inc., Natick, Massachusetts). The movement data was then used to interpolate the cell movement in relation to the original pipette position to obtain a cell movement map. Finally, we averaged the movement maps over the data from each gel stiffness.

We analyzed the gel deformation based on the fluorescent microbead data using Fiji's particle image velocimetry (PIV) analysis plugin between the images before and after the micromanipulation. Similar to the cell data, the gel deformation maps were centered on the original pipette position and averaged over the same stiffnesses.

Computational modeling

A detailed description of the model, the fitting, and the simulations are available in S2 Text. In our model, the epithelium was described as a two-dimensional monolayer, with each cell represented by a closed polygon (Fig. 8A). The model was based mainly on the boundary-based model by Tamulonis et al. [48] but borrowed features from the vertex models [40–42]. Cell structures and processes were incorporated into the model as forces affecting the polygon vertices. These include cortical actomyosin, cell-cell junction dynamics, intracellular pressure, cell division, focal adhesions, and membrane elasticity. Some of these forces are depicted in Fig. 8B. Furthermore, the cortical dynamics included the actomyosin prestress, described by a constant force component and a perimeter-dependent tension component. The number of the cell vertices was not static: new vertices were added to divide long membrane sections, and vertices were removed if a section between two vertices became too short. In addition, the cell-cell junctions were dynamic and constantly remodeled during the simulation.

The top surface of the underlying substrate was represented by a two-dimensional triangular grid of points (Fig. **??**). As with the cells, the substrate mechanics were represented by forces acting on the grid points. The forces were related to the internal mechanics of the substrate as well as to the focal adhesions.

Fig 8. Depiction of the model. (A) Basic structure of the model. The cells were described by closed polygons and the cell structures and processes were included as forces affecting the polygon vertices. The cell-cell junctions and cortical actomyosin are depicted. The substrate was described by a triangular grid of points whose internal mechanics were defined by the forces between the grid points. The cell vertices were connected to the substrate via focal adhesion connections. (B) Example of forces that determine the cell vertex movements: cell-cell junction forces (F_{junc}), cortical forces (F_{cort}), membrane forces (F_{mem}), and intracellular pressure or area force (F_{area}). An additional cortical force component is added to the concave vertices, since the cortical link between its neighboring vertices runs behind it pushing it outwards (unfilled arrow). Note that the forces are calculated for every vertex but for simplicity, all forces are not shown for all vertices here. (C) Time series showing the growth of epithelial cell cluster from a single cell over a period of 10 days.

Equation of motion was used to evolve the model system during the simulation. The system was assumed to be overdamped, enabling the omission of inertial effects. This simplification is commonly done as the importance of inertia is small in biological systems [40, 41, 70]. The movement of cell vertex i and substrate point m were calculated as

$$\eta \frac{d\vec{r}_i}{dt} = \vec{F}_{i,tot} \tag{1}$$

$$\eta \frac{d\vec{s}_m}{dt} = \vec{F}_{m,tot} \tag{2}$$

where η is the dampening coefficient (kg s^{-1}), r_i is the position of the cell vertex i (m), s_m is the position of the substrate point m (m), t is time (s), and $F_{i,tot}$ is the total force acting on cell vertex i (N) and $F_{m,tot}$ that on the substrate point m (N). The total force for each cell vertex i was calculated as the sum of these component forces:

$$\vec{F}_{i,tot} = \vec{F}_{i,cort} + \vec{F}_{i,junc} + \vec{F}_{i,area} + \vec{F}_{i,div} + \vec{F}_{i,fa} + \vec{F}_{i,mem} + \vec{F}_{i,cont} + \vec{F}_{i,edge} \tag{3}$$

where $\vec{F}_{i,cort}$ is the cortical actomyosin force, $\vec{F}_{i,junc}$ the cell-cell junction force, $\vec{F}_{i,area}$ the area force that describes the internal pressure, $\vec{F}_{i,div}$ the division force, $\vec{F}_{i,fa}$ the focal adhesion force, $\vec{F}_{i,mem}$ the membrane force, $\vec{F}_{i,cont}$ the contact force, and $\vec{F}_{i,edge}$ is the edge force. The last two forces had an auxiliary role: the contact force described contact between cells and prevented cell overlap, and the edge force described the continuity of the epithelium outside the simulated area.

The substrate mechanics were divided into three forces: a central force between neighboring points, a repulsive force between a point and the connection between two of its neighbors, and a restorative force that sought to move a point to its original location. The second force was included to prevent the collapse of the substrate during large deformations [71], and the third to describe the fact that the substrate was attached to rigid glass at its bottom surface in our experiments. Furthermore, a fourth force component was included to depict the cell-substrate connection via the focal adhesions. Now, the total force affecting each substrate point was calculated as

$$\vec{F}_{m,tot} = \vec{F}_{m,cent} + \vec{F}_{m,rep} + \vec{F}_{m,rest} + \vec{F}_{m,fa} \tag{4}$$

where $\vec{F}_{m,cent}$ is the central force between closest neighboring points, $\vec{F}_{m,rep}$ is the repulsive force to prevent material collapse, $\vec{F}_{m,rest}$ is a restorative force, and $\vec{F}_{m,fa}$ is the force from the focal adhesions.

The model was used to simulate epithelial growth and the tissue response to two different mechanical stimuli: 1) pointlike micromanipulation in a short time scale and 2) a local increase in actomyosin tension by optogenetics over a longer time scale.

We used the model to grow epithelia from a single cell (Fig. 8C) to produce epithelium of sufficient size without the substrate. The randomness in the tissue was produced by normally distributed times between divisions and cell area distribution based on our *in vitro* MDCK cell data. The size of the grown epithelium was chosen based on the assumed effect of each mechanical stimulus to minimize the impact of the tissue edges. Following the growth, the epithelia were given time to relax without division to remove any stresses. Next, the grown epithelia were placed on the substrate, and the focal adhesions were defined between the two.

Corresponding to our micromanipulation experiments, we moved a single cell by an external force with a known speed over a distance. Since we wanted to describe the elastic behavior, we prohibited any changes in the number of cell vertices and cell-cell junctions in these simulations, justified by the short time scale of these measurements. The values of the model parameters governing the cell mechanics were fitted using our *in vitro* micromanipulation data with the uniform 1.1, 4.5, and 11-kPa substrates by iteratively changing the parameter values and comparing the cell center and substrate displacements between the experimental data and simulations results. The fitted model was then used to study the force propagation on the uniform substrates and those with stiffness interfaces and gradients. The interfaces and the gradients were defined along the direction of the virtual pipette movement and characterized by the gradient slope and distance from the initial pipette position.

In the optogenetic activation simulations, the contractility of the cortex in a section between two randomly chosen cells was increased to describe the experimental myosin activation. This was done by increasing the value of cortical tension constants for the cortical forces within the activation region. The parameters for these simulations were obtained from Staddon et al. [24] and by fitting our model to their data.

The model was solved using either 2nd or 4th order Runge-Kutta methods with variable time steps. During the growth simulations when the substrate was excluded, 2nd order Runge-Kutta was used since it was sufficiently accurate. These simulations also omitted the focal adhesion and the cell edge forces. During the simulations that included the substrate, 4th order Runge-Kutta was used to evolve the system.

The model is implemented in MATLAB, where we also created a graphical user interface for the model platform. The model code is available in GitHub (https://github.com/atervn/epimech).

Supporting information

S1 Appendix. Supporting figures. Figures showing the cell and substrate displacement data and the force data from which the stiffness interface gradient results were calculated (Figs. A and C). Figures show the cell and substrate displacement data and the force data, and the difference results for the sharp and shallow stiffness gradients (Figs. B and D). An example of the forces affecting the cell vertices and substrate points following 30-μm micromanipulation of a single cell (Fig. E).

S2 Text. Description of the EpiMech model. A detailed description of the model, the included cell components and processes, the forces, the simulations, and the parameter values.

S3 Video. Experimental micromanipulation. Representative examples of the micromanipulation experiments showing both the cell boundaries and the fluorescent microbeads of the hydrogel substrates for the stiffnesses 1.1, 4.5, 11, and 35 kPa.

S4 Video. Simulated micromanipulation. Representative examples of the micromanipulation simulations showing both the cell boundaries and the substrate points for the stiffnesses 1.1, 4.5, and 11 kPa. The purple cross represents the micromanipulator position.

S5 Video. Simulated growth. Representative example of an epithelium growth simulation from a single cell over 14 hours.

S6 Video. Optogenetics simulation. Representative example of an optogenetic activation simulation showing both the cell boundaries and the substrate points. The simulation was run with a substrate with a stiffness of 1.1 kPa. The purple region shows the activated area during the light activation from 2 to 22 minutes.

Acknowledgments

The authors acknowledge the Biocenter Finland (BF), Tampere Imaging Facility (TIF), and Tampere facility of Electrophysiological Measurements for the service. Michael Davidson is kindly acknowledged for the mEmerald-Occludin plasmid (Addgene plasmid #54212).

References

1. Eyckmans J, Boudou T, Yu X, Chen CS. A Hitchhiker's Guide to Mechanobiology. Developmental Cell. 2011;21(1):35–47. doi:10.1016/j.devcel.2011.06.015.

2. Paluch EK, Nelson CM, Biais N, Fabry B, Moeller J, Pruitt BL, et al. Mechanotransduction: Use the force(s). BMC Biology. 2015;13(1):1–14. doi:10.1186/s12915-015-0150-4.

3. Wang N. Review of cellular mechanotransduction. Journal of Physics D: Applied Physics. 2017;50(23). doi:10.1088/1361-6463/aa6e18.

4. Bosveld F, Markova O, Guirao B, Martin C, Wang Z, Pierre A, et al. Epithelial tricellular junctions act as interphase cell shape sensors to orient mitosis. Nature. 2016;530(7591):495–498. doi:10.1038/nature16970.

5. Brugués A, Anon E, Conte V, Veldhuis JH, Gupta M, Colombelli J, et al. Forces driving epithelial wound healing. Nature Physics. 2014;10(9):683–690. doi:10.1038/nphys3040.

6. Engler AJ, Sen S, Sweeney HL, Discher DE. Matrix Elasticity Directs Stem Cell Lineage Specification. Cell. 2006;126(4):677–689. doi:10.1016/j.cell.2006.06.044.

7. Guillot C, Lecuit T. Mechanics of Epithelial Tissue Homeostasis and Morphogenesis. Science. 2013;340(6137):1185–1189. doi:10.1126/science.1235249.

8. Trepat X, Wasserman MR, Angelini TE, Millet E, Weitz DA, Butler JP, et al. Physical forces during collective cell migration. Nature Physics. 2009;5(6):426–430. doi:10.1038/nphys1269.

9. Wolfenson H, Yang B, Sheetz MP. Steps in Mechanotransduction Pathways that Control Cell Morphology. Annual Review of Physiology. 2019;81(1):585–605. doi:10.1146/annurev-physiol-021317-121245.

10. Wozniak MA, Chen CS. Mechanotransduction in development: A growing role for contractility. Nature Reviews Molecular Cell Biology. 2009;10(1):34–43. doi:10.1038/nrm2592.

11. Broders-Bondon F, Ho-Bouldoires THN, Fernandez-Sanchez ME, Farge E. Mechanotransduction in tumor progression: The dark side of the force. Journal of Cell Biology. 2018;217(5):1571–1587. doi:10.1083/jcb.201701039.

12. Ingber DE. Mechanobiology and diseases of mechanotransduction. Annals of Medicine. 2003;35(8):564–577. doi:10.1080/07853890310016333.

13. Jaalouk DE, Lammerding J. Mechanotransduction gone awry. Nature Reviews Molecular Cell Biology. 2009;10(1):63–73. doi:10.1038/nrm2597.

14. Kalli M, Stylianopoulos T. Defining the role of solid stress and matrix stiffness in cancer cell proliferation and metastasis. Frontiers in Oncology. 2018;8(MAR). doi:10.3389/fonc.2018.00055.

15. Kumar S, Weaver VM. Mechanics, malignancy, and metastasis: The force journey of a tumor cell. Cancer and Metastasis Reviews. 2009;28(1-2):113–127. doi:10.1007/s10555-008-9173-4.

16. Sadeghipour E, Garcia MA, Nelson WJ, Pruitt BL. Shear-induced damped oscillations in an epithelium depend on actomyosin contraction and E-cadherin cell adhesion. eLife. 2018;7:1–16. doi:10.7554/eLife.39640.

17. Angulo-Urarte A, van der Wal T, Huveneers S. Cell-cell junctions as sensors and transducers of mechanical forces. Biochimica et Biophysica Acta - Biomembranes. 2020;1862(9):183316. doi:10.1016/j.bbamem.2020.183316.

18. Chen T, Saw TB, Mege RM, Ladoux B. Mechanical forces in cell monolayers. Journal of Cell Science. 2018;131(24). doi:10.1242/jcs.218156.

19. Ladoux B, Mège RM. Mechanobiology of collective cell behaviours. Nature Reviews Molecular Cell Biology. 2017;18(12):743–757. doi:10.1038/nrm.2017.98.

20. Serra-Picamal X, Conte V, Vincent R, Anon E, Tambe DT, Bazellieres E, et al. Mechanical waves during tissue expansion. Nature Physics. 2012;8(8):628–634. doi:10.1038/nphys2355.

21. Cavanaugh KE, Staddon MF, Munro E, Banerjee S, Gardel ML. RhoA Mediates Epithelial Cell Shape Changes via Mechanosensitive Endocytosis. Developmental Cell. 2020;52(2):152–166.e5. doi:10.1016/j.devcel.2019.12.002.

22. Khalilgharibi N, Fouchard J, Asadipour N, Barrientos R, Duda M, Bonfanti A, et al. Stress relaxation in epithelial monolayers is controlled by the actomyosin cortex. Nature Physics. 2019;15(8):839–847. doi:10.1038/s41567-019-0516-6.

23. Mao Y, Baum B. Tug of war–The influence of opposing physical forces on epithelial cell morphology. Developmental Biology. 2015;401(1):92–102. doi:10.1016/j.ydbio.2014.12.030.

24. Staddon MF, Cavanaugh KE, Munro EM, Gardel ML, Banerjee S. Mechanosensitive Junction Remodeling Promotes Robust Epithelial Morphogenesis. Biophysical Journal. 2019;117(9):1739–1750. doi:10.1016/j.bpj.2019.09.027.

25. Martino F, Perestrelo AR, Vinarský V, Pagliari S, Forte G. Cellular mechanotransduction: From tension to function. Frontiers in Physiology. 2018;9(JUL):1–21. doi:10.3389/fphys.2018.00824.

26. Dahl KN, Ribeiro AJS, Lammerding J. Nuclear shape, mechanics, and mechanotransduction. Circulation Research. 2008;102(11):1307–1318. doi:10.1161/CIRCRESAHA.108.173989.

27. Elosegui-Artola A, Oria R, Chen Y, Kosmalska A, Pérez-González C, Castro N, et al. Mechanical regulation of a molecular clutch defines force transmission and transduction in response to matrix rigidity. Nature Cell Biology. 2016;18(5):540–548. doi:10.1038/ncb3336.

28. Hwang Y, Barakat AI. Dynamics of mechanical signal transmission through prestressed stress fibers. PLoS ONE. 2012;7(4). doi:10.1371/journal.pone.0035343.

29. Ihalainen TO, Aires L, Herzog FA, Schwartlander R, Moeller J, Vogel V. Differential basal-to-apical accessibility of lamin A/C epitopes in the nuclear lamina regulated by changes in cytoskeletal tension. Nature Materials. 2015;14(12):1252–1261. doi:10.1038/nmat4389.

30. del Rio A, Perez-Jimenez R, Liu R, Roca-Cusachs P, Fernandez JM, Sheetz MP. Stretching Single Talin Rod Molecules Activates Vinculin Binding. Science. 2009;323(5914):638–641. doi:10.1126/science.1162912.

31. Plotnikov SV, Pasapera AM, Sabass B, Waterman CM. Force fluctuations within focal adhesions mediate ECM-rigidity sensing to guide directed cell migration. Cell. 2012;151(7):1513–1527. doi:10.1016/j.cell.2012.11.034.

32. Wang N, Tytell JD, Ingber DE. Mechanotransduction at a distance: mechanically coupling the extracellular matrix with the nucleus. Nature Reviews Molecular Cell Biology. 2009;10(1):75–82. doi:10.1038/nrm2594.

33. Kumar A, Placone JK, Engler AJ. Understanding the extracellular forces that determine cell fate and maintenance. Development (Cambridge). 2017;144(23):4261–4270. doi:10.1242/dev.158469.

34. Dong Y, Zheng Q, Wang Z, Lin X, You Y, Wu S, et al. Higher matrix stiffness as an independent initiator triggers epithelial-mesenchymal transition and facilitates HCC metastasis. Journal of Hematology and Oncology. 2019;12(1):1–15. doi:10.1186/s13045-019-0795-5.

35. Nisticò P, Bissell MJ, Radisky DC. Epithelial-mesenchymal transition: General principles and pathological relevance with special emphasis on the role of matrix metalloproteinases. Cold Spring Harbor Perspectives in Biology. 2012;4(2):1–10. doi:10.1101/cshperspect.a011908.

36. Ribatti D, Tamma R, Annese T. Epithelial-Mesenchymal Transition in Cancer: A Historical Overview. Translational Oncology. 2020;13(6):100773. doi:10.1016/j.tranon.2020.100773.

37. Clark AG, Vignjevic DM. Modes of cancer cell invasion and the role of the microenvironment. Current Opinion in Cell Biology. 2015;36:13–22. doi:10.1016/j.ceb.2015.06.004.

38. Emon B, Bauer J, Jain Y, Jung B, Saif T. Biophysics of Tumor Microenvironment and Cancer Metastasis - A Mini Review. Computational and Structural Biotechnology Journal. 2018;16:279–287. doi:10.1016/j.csbj.2018.07.003.

39. Acerbi I, Cassereau L, Dean I, Shi Q, Au A, Park C, et al. Human breast cancer invasion and aggression correlates with ECM stiffening and immune cell infiltration. Integrative Biology (United Kingdom). 2015;7(10):1120–1134. doi:10.1039/c5ib00040h.

40. Barton DL, Henkes S, Weijer CJ, Sknepnek R. Active Vertex Model for cell-resolution description of epithelial tissue mechanics. PLoS Computational Biology. 2017;13(6):1–34. doi:10.1371/journal.pcbi.1005569.

41. Fletcher AG, Osterfield M, Baker RE, Shvartsman SY. Vertex Models of Epithelial Morphogenesis. Biophysical Journal. 2014;106(11):2291–2304. doi:10.1016/j.bpj.2013.11.4498.

42. Schaumann EN, Staddon MF, Gardel ML, Banerjee S. Force localization modes in dynamic epithelial colonies. Molecular Biology of the Cell. 2018;29(23):2835–2847. doi:10.1091/mbc.E18-05-0336.

43. Jamali Y, Azimi M, Mofrad MRK. A sub-cellular viscoelastic model for cell population mechanics. PLoS ONE. 2010;5(8). doi:10.1371/journal.pone.0012097.

44. Nematbakhsh A, Sun W, Brodskiy PA, Amiri A, Narciso C, Xu Z, et al. Multi-scale computational study of the mechanical regulation of cell mitotic rounding in epithelia. PLoS Computational Biology. 2017;13(5):1–22. doi:10.1371/journal.pcbi.1005533.

45. Battista NA, Strickland WC, Miller LA. IB2d: A Python and MATLAB implementation of the immersed boundary method. Bioinspiration and Biomimetics. 2017;12(3). doi:10.1088/1748-3190/aa5e08.

46. Rejniak KA. An immersed boundary framework for modelling the growth of individual cells: An application to the early tumour development. Journal of Theoretical Biology. 2007;247(1):186–204. doi:10.1016/j.jtbi.2007.02.019.

47. Tanaka S, Sichau D, Iber D. LBIBCell: A cell-based simulation environment for morphogenetic problems. Bioinformatics. 2015;31(14):2340–2347. doi:10.1093/bioinformatics/btv147.

48. Tamulonis C, Postma M, Marlow HQ, Magie CR, de Jong J, Kaandorp J. A cell-based model of Nematostella vectensis gastrulation including bottle cell formation, invagination and zippering. Developmental Biology. 2011;351(1):217–228. doi:10.1016/j.ydbio.2010.10.017.

49. Sankaran J, Uzer G, van Wijnen AJ, Rubin J. Gene regulation through dynamic actin control of nuclear structure. Experimental Biology and Medicine. 2019;244(15):1345–1353. doi:10.1177/1535370219850079.

50. Butcher DT, Alliston T, Weaver VM. A tense situation: forcing tumour progression. Nature Reviews Cancer. 2009;9(2):108–122. doi:10.1038/nrc2544.

51. Riehl BD, Kim E, Bouzid T, Lim JY. The Role of Microenvironmental Cues and Mechanical Loading Milieus in Breast Cancer Cell Progression and Metastasis. Frontiers in Bioengineering and Biotechnology. 2021;8(January):1–22. doi:10.3389/fbioe.2020.608526.

52. Stowers RS, Shcherbina A, Israeli J, Gruber JJ, Chang J, Nam S, et al. Matrix stiffness induces a tumorigenic phenotype in mammary epithelium through changes in chromatin accessibility. Nature Biomedical Engineering. 2019;doi:10.1038/s41551-019-0420-5.

53. Fujii Y, Ochi Y, Tuchiya M, Kajita M, Fujita Y, Ishimoto Y, et al. Spontaneous Spatial Correlation of Elastic Modulus in Jammed Epithelial Monolayers Observed by AFM. Biophysical Journal. 2019;116(6):1152–1158. doi:10.1016/j.bpj.2019.01.037.

54. Nehls S, Nöding H, Karsch S, Ries F, Janshoff A. Stiffness of MDCK II Cells Depends on Confluency and Cell Size. Biophysical Journal. 2019;116(11):2204–2211. doi:10.1016/j.bpj.2019.04.028.

55. Pietuch A, Brückner BR, Fine T, Mey I, Janshoff A. Elastic properties of cells in the context of confluent cell monolayers: impact of tension and surface area regulation. Soft Matter. 2013;9(48):11490. doi:10.1039/c3sm51610e.

56. Goodwin K, Ellis SJ, Lostchuck E, Zulueta-Coarasa T, Fernandez-Gonzalez R, Tanentzapf G. Basal Cell-Extracellular Matrix Adhesion Regulates Force Transmission during Tissue Morphogenesis. Developmental Cell. 2016;39(5):611–625. doi:10.1016/j.devcel.2016.11.003.

57. VanderBurgh JA, Potharazu AV, Schwager SC, Reinhart-King CA. A discrete interface in matrix stiffness creates an oscillatory pattern of endothelial monolayer disruption. Journal of Cell Science. 2020;133(18). doi:10.1242/jcs.244533.

58. Hu S, Chen J, Butler JP, Wang N. Prestress mediates force propagation into the nucleus. Biochemical and Biophysical Research Communications. 2005;329(2):423–428. doi:10.1016/j.bbrc.2005.02.026.

59. Na S, Collin O, Chowdhury F, Tay B, Ouyang M, Wang Y, et al. Rapid signal transduction in living cells is a unique feature of mechanotransduction. Proceedings of the National Academy of Sciences of the United States of America. 2008;105(18):6626–6631. doi:10.1073/pnas.0711704105.

60. Humphries DL, Grogan JA, Gaffney EA. Mechanical Cell–Cell Communication in Fibrous Networks: The Importance of Network Geometry. Bulletin of Mathematical Biology. 2017;79(3):498–524. doi:10.1007/s11538-016-0242-5.

61. Ma X, Schickel ME, Stevenson MD, Sarang-Sieminski AL, Gooch KJ, Ghadiali SN, et al. Fibers in the extracellular matrix enable long-range stress transmission between cells. Biophysical Journal. 2013;104(7):1410–1418. doi:10.1016/j.bpj.2013.02.017.

62. Reinhart-King CA, Dembo M, Hammer DA. Cell-cell mechanical communication through compliant substrates. Biophysical Journal. 2008;95(12):6044–6051. doi:10.1529/biophysj.107.127662.

63. Conradin R, Coreixas C, Latt J, Chopard B. PalaCell2D: A framework for detailed tissue morphogenesis. Journal of Computational Science. 2021; p. 101353. doi:10.1016/j.jocs.2021.101353.

64. Lammerding J, Kirby TJ. Emerging views of the nucleus as a cellular mechanosensor. Nature Cell Biology. 2018;20(4):373–381. doi:10.1038/s41556-018-0038-y.Emerging.

65. Tse JR, Engler AJ. Preparation of hydrogel substrates with tunable mechanical properties. Current Protocols in Cell Biology. 2010;(SUPPL. 47):1–16. doi:10.1002/0471143030.cb1016s47.

66. Wouters OY, Ploeger DTA, van Putten SM, Bank RA. 3,4-Dihydroxy-L-Phenylalanine as a Novel Covalent Linker of Extracellular Matrix Proteins to Polyacrylamide Hydrogels with a Tunable Stiffness. Tissue Engineering Part C: Methods. 2016;22(2):91–101. doi:10.1089/ten.tec.2015.0312.

67. Arganda-Carreras I, Kaynig V, Rueden C, Eliceiri KW, Schindelin J, Cardona A, et al. Trainable Weka Segmentation: A machine learning tool for microscopy pixel classification. Bioinformatics. 2017;33(15):2424–2426. doi:10.1093/bioinformatics/btx180.

68. Schindelin J, Arganda-Carreras I, Frise E, Kaynig V, Longair M, Pietzsch T, et al. Fiji: An open-source platform for biological-image analysis. Nature Methods. 2012;9(7):676–682. doi:10.1038/nmeth.2019.

69. Brocher J. The BioVoxxel Image Processing and Analysis Toolbox. European BioImage Analysis Symposium. 2015;8(2):67112.

70. Fletcher AG, Osborne JM, Maini PK, Gavaghan DJ. Implementing vertex dynamics models of cell populations in biology within a consistent computational framework. Progress in Biophysics and Molecular Biology. 2013;113(2):299–326. doi:10.1016/j.pbiomolbio.2013.09.003.

71. Cooper L, Maddock S. Preventing Collapse Within Mass-Spring-Damper Models of Deformable Objects. In: The 5th Int. Conf. in Central Europe on Comput. Graphics and Vis. 1; 1997. p. 196–204.

Figures

Figure 1

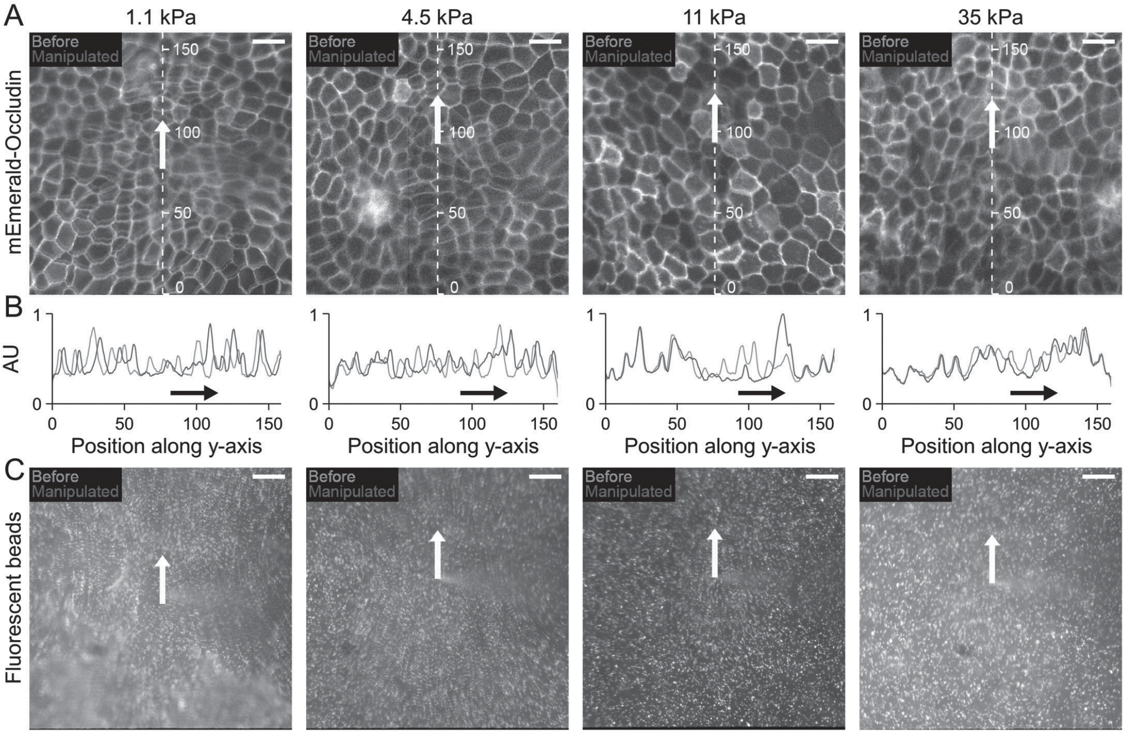

Figure 2

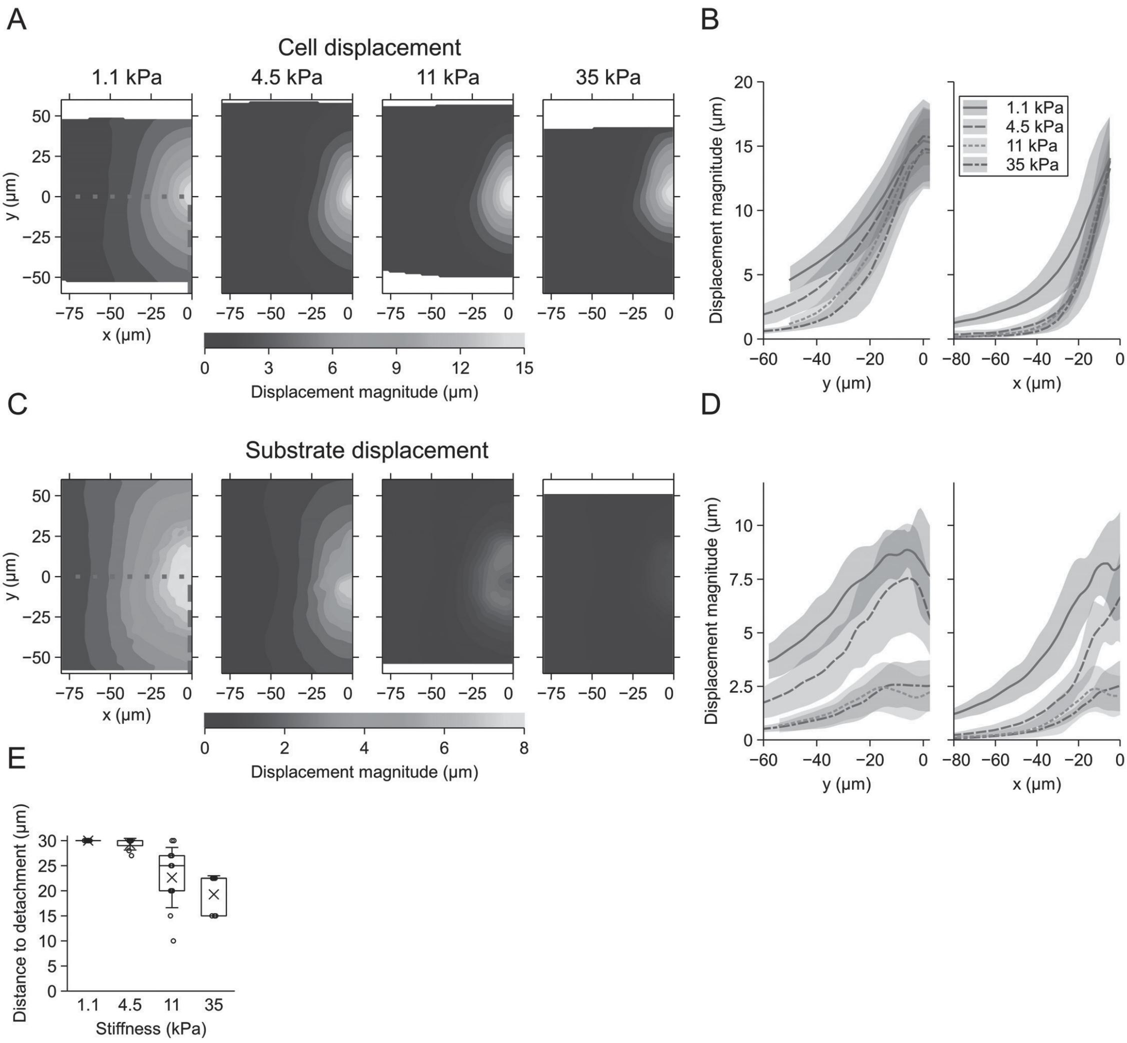
A
Cell displacement
1.1 kPa
4.5 kPa
11 kPa
35 kPa
y (µm)
x (µm)
50
25
0
−25
−50
−75
Displacement magnitude (µm)
0
3
6
9
12
15
B
Displacement magnitude (µm)
20
15
10
5
0
1.1 kPa
4.5 kPa
11 kPa
35 kPa
y (µm)
x (µm)
−60
−40
−20
−80
C
Substrate displacement
Displacement magnitude (µm)
0
2
4
6
8
D
Displacement magnitude (µm)
10
7.5
5
2.5
E
Distance to detachment (µm)
30
25
20
15
10
5
0
1.1
4.5
11
35
Stiffness (kPa)

Figure 3

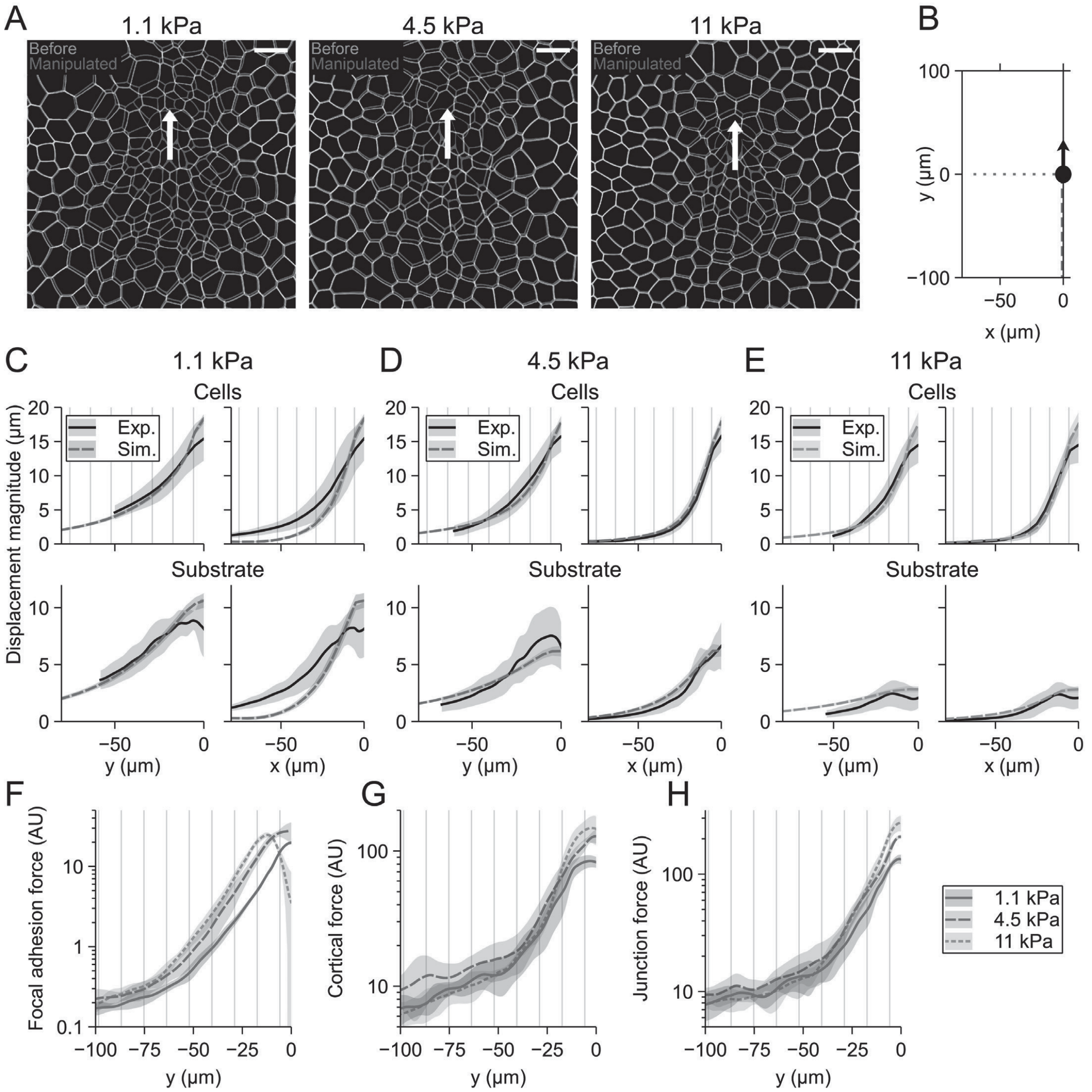
A
1.1 kPa
4.5 kPa
11 kPa
Before
Manipulated
B
100
0
−100
y (μm)
−50
0
x (μm)
C
1.1 kPa
D
4.5 kPa
E
11 kPa
Cells
Substrate
Exp.
Sim.
Displacement magnitude (μm)
20
15
10
5
0
−50
0
y (μm)
x (μm)
F
Focal adhesion force (AU)
0.1
1
10
G
Cortical force (AU)
10
100
H
Junction force (AU)
10
100
−100
−75
−50
−25
0
y (μm)
1.1 kPa
4.5 kPa
11 kPa

Figure 4

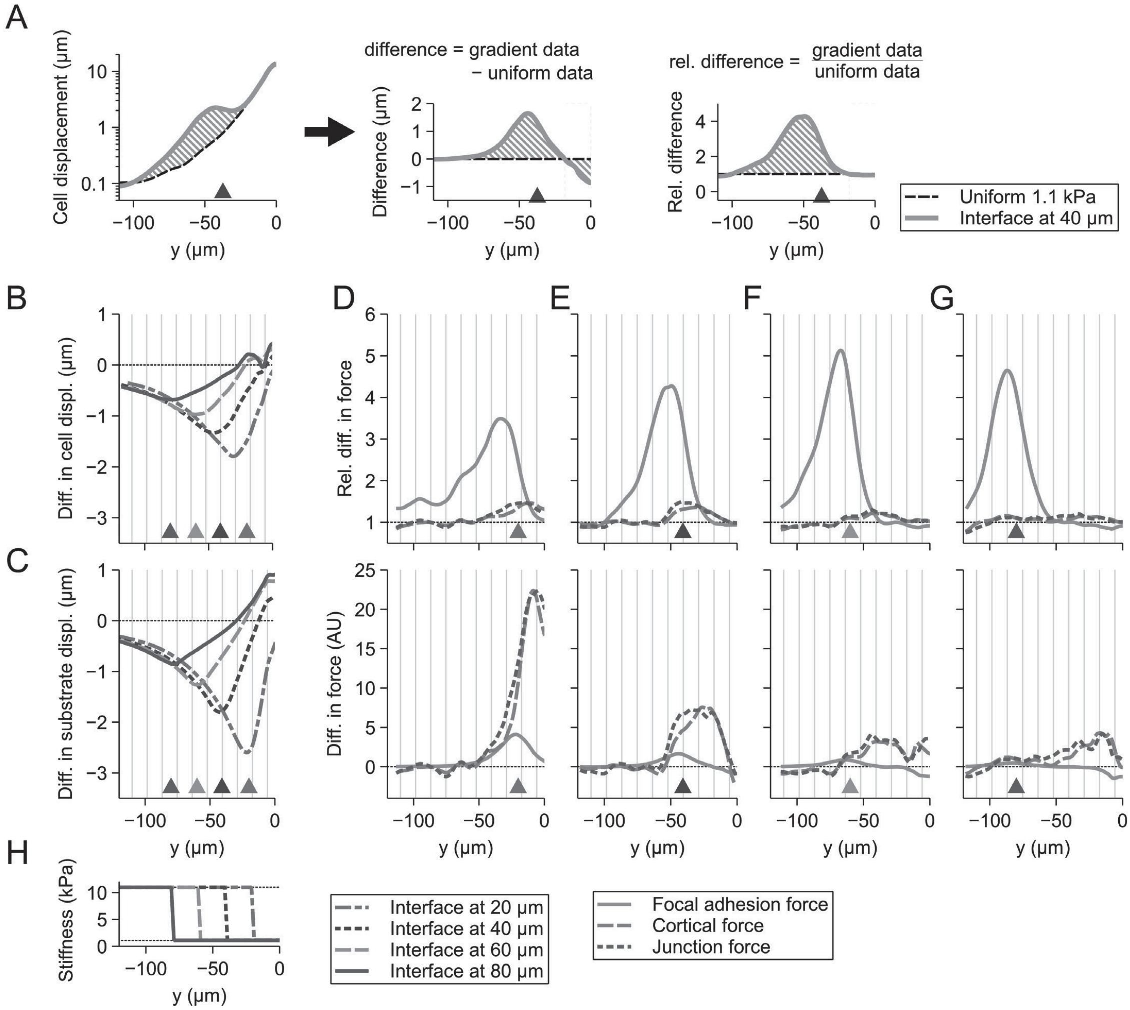
A
Cell displacement (µm)
10
1
0.1
−100
−50
0
y (µm)
difference = gradient data − uniform data
Difference (µm)
2
1
0
−1
rel. difference = gradient data / uniform data
Rel. difference
4
2
0
Uniform 1.1 kPa
Interface at 40 µm
B
Diff. in cell displ. (µm)
1
0
−1
−2
−3
C
Diff. in substrate displ. (µm)
D
E
F
G
Rel. diff. in force
6
5
4
3
2
1
Diff. in force (AU)
25
20
15
10
5
0
H
Stiffness (kPa)
10
5
0
Interface at 20 µm
Interface at 40 µm
Interface at 60 µm
Interface at 80 µm
Focal adhesion force
Cortical force
Junction force

Figure 5

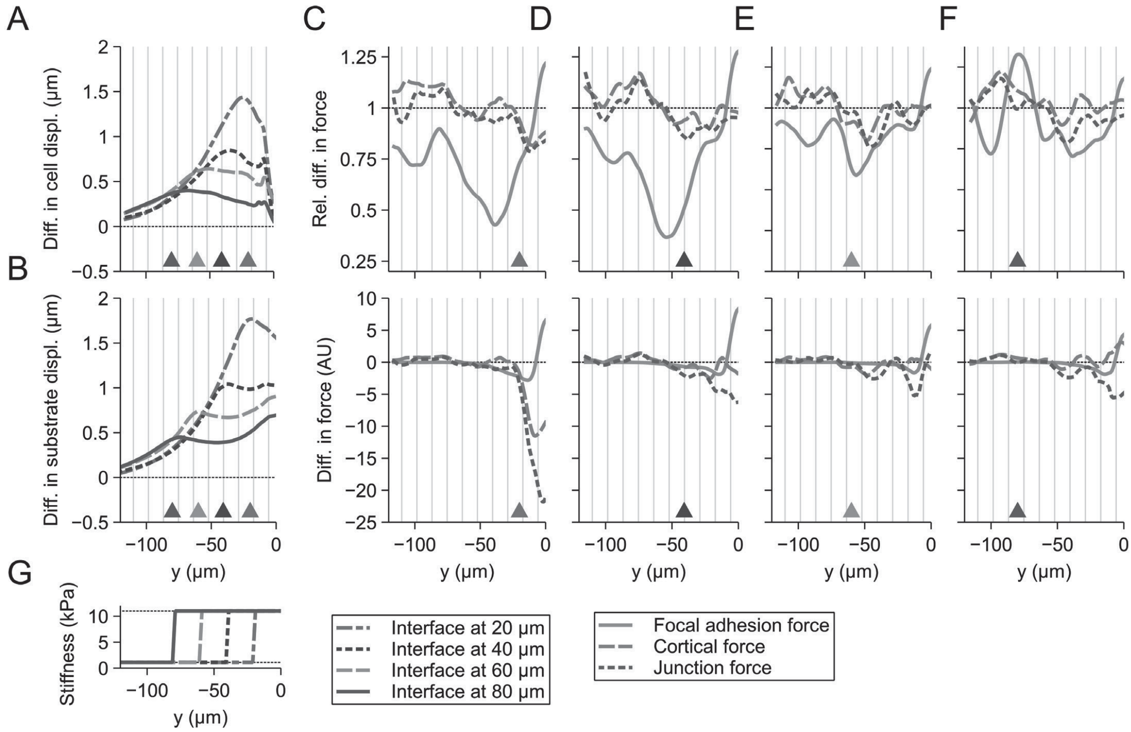
A
B
C
D
E
F
G
Diff. in cell displ. (µm)
Diff. in substrate displ. (µm)
Rel. diff. in force
Diff. in force (AU)
Stiffness (kPa)
2
1.5
1
0.5
0
−0.5
1.25
0.75
0.25
10
5
−5
−10
−15
−20
−25
−100
−50
y (µm)
Interface at 20 µm
Interface at 40 µm
Interface at 60 µm
Interface at 80 µm
Focal adhesion force
Cortical force
Junction force

Figure 6

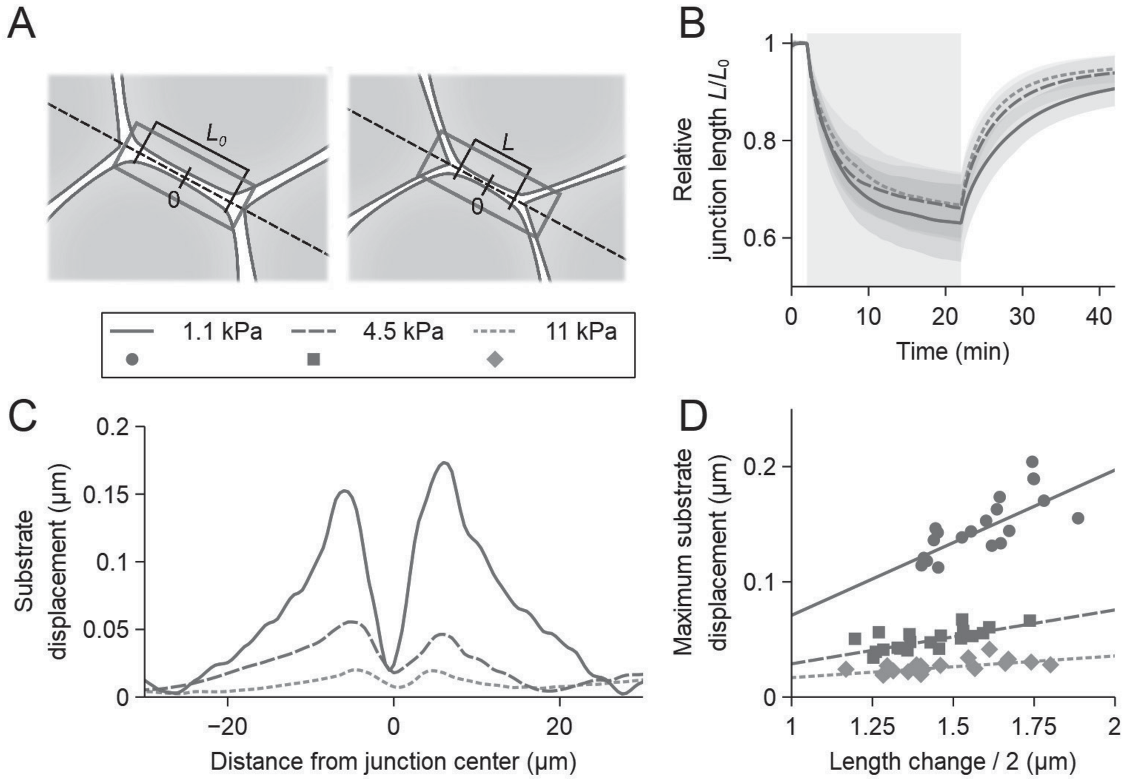
A
L0
0
L
0
B
1
0.8
0.6
Relative junction length L/L0
0
10
20
30
40
Time (min)
1.1 kPa
4.5 kPa
11 kPa
C
0.2
0.15
0.1
0.05
0
Substrate displacement (μm)
−20
0
20
Distance from junction center (μm)
D
0.2
0.1
0
Maximum substrate displacement (μm)
1
1.25
1.5
1.75
2
Length change / 2 (μm)

Figure 7

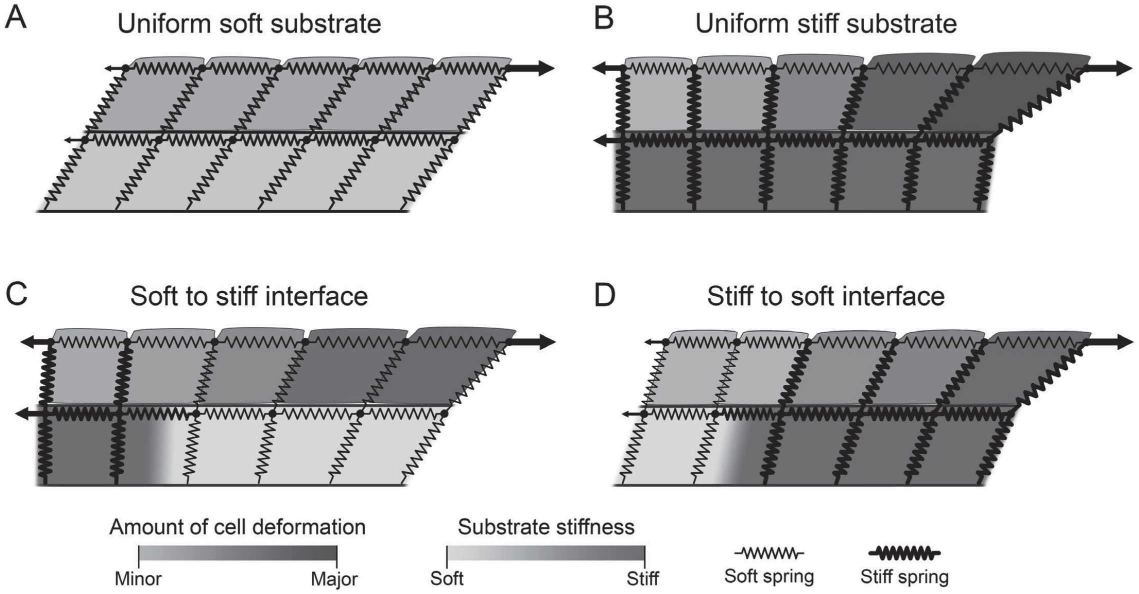
A
Uniform soft substrate
B
Uniform stiff substrate
C
Soft to stiff interface
D
Stiff to soft interface
Amount of cell deformation
Minor
Major
Substrate stiffness
Soft
Stiff
Soft spring
Stiff spring

Figure 8